Roma Tre University
Department of Mathematics and Physics

Doctoral School in Mathematics and Physics - XXVIII Cycle

Structural behavior and phase stability of Uranium at high pressure and high temperature

Dissertation submitted in partial fulfillment of the requirements for the degree of Doctor of Philosophy in Physics

by

Federico Brazzi

Tutor Prof. Wolfango Plastino

Contents

Introduction

Over the last three decades there has been an incredible effort in studying the dynamics of earthquake, mostly to be able to predict them. Of course, a comprehension of such a complex phenomenon passes through the knowledge of the physics and the chemistry involved. To improve this field it is necessary to relate the physics of seismic source to the data now available and to develop some numerical model somehow connected to any geological observation. The understanding of the physics of seismic source is a challenging issue not only because it is a relatively recent subject but also because it requires a multiple approach: e.g. in order to include in a model all the physical processes happening during faulting, we need to take into account all the rheological/physical/chemical properties of the medium. The aim of building up a constituent law of earthquake is a challenging goal especially because many of the mechanisms involved can interact and/or compete with each other, since they happen on similar time and space scales. Not to mention that there is still a lack of knowledge about the state of the art of the Earth crust and the mantle. So the whole picture seems to have to be completed. Faulting episodes have been studied under an incredible amount of mechanisms: such as flash heating, chemical influences and permeability.

In order to develop a valid phenomenological model for seismic source, there is also need to consider radioactivity: in fact we know that many radioactive processes occur inside the Earth and the radiogenic heat sources distribution influences the geodynamic and the thermal behavior of the planet. We know that the total heat flux at the Earth surface is $\sim$ 47 TW, 70% of which comes from the radioactive decay of uranium, thorium and potassium. Uranium accounts for 11 TW itself and is present in the mantle although we do not know the exact distribution. And it is not the only element present: its concentration is around 0.025 p.p.m. by weight compared to that of potassium that is around 70 p.p.m. by weight. This means that we're starting here in this work the study of uranium itself, to be followed up in the future by the same analysis for K and Th. Not only this,

but we are aware of the fact that U in the crust finds itself more likely in compounds than alone, such as dioxide and silicide and that many experiments with these elements have been carried out to study their elastic and mechanical behavior up to the pressure range we are going to investigate here. But since radioactive processes have never been considered when studying the processes related to the physics of seismic source, we are now focusing on the first one of these elements requiring a deeper analytical understanding itself: uranium.

Besides, all the phenomena studied so far have always considered mechanisms happening on a time scale between $\sim 10^{-6}$ s and $\sim 10^{14}$ s and on a spatial scale between μm and $\sim 10^{6}$ km.

The study of uranium behavior over a wide range of temperature and pressure is the subject of this thesis. The phenomena we are going to investigate happen over a time scale between $\sim 10^{-11}$ s and $\sim 10^{-9}$ s and over a space scale of up to 10^{-1} Å and we want to check whether or not they can contribute to make the picture more clear.

After reviewing the theory of seismic sources and its complex scenario in Chapter 1, we mainly aim to study a cluster of uranium in a region of space and in a well established configuration. Uranium has a very complex phase diagram with three allotropic structures, as it will be explained in Chapter 2, showing a crystallization in a face-centered orthorhombic structure named α-U; at temperature T $\sim$ 935 K and zero pressure it then transforms to the tetragonal β-U and at T $\sim$ 1045 K it transforms to the bcc γ-U, finally melting at T $\sim$ 1406 K.

To study such a complex system we choose to implement a Classical Molecular Dynamics (MD) set of simulations with the LAMMPS software through which we mean to calculate its structural, elastic an polycrystalline properties. LAMMPS is an open-source software written in C++ whose output are processed by Python scripts. Unlike first principles calculations treated with density functional theory (DFT) based on *ab initio* calculations, in classical simulations atoms are considered to be point-like spheres interacting through many-body interactions that is governed by a potential. MD is a reliable method to acquire some knowledge about metals at non-zero temperature. It is very powerful, showing in a wide range of scenarios a robustness when comparing its results to sets of surveys. In fact *ab initio* methods have been very successful in describing many properties of uranium, but they are computationally limited to study systems up to $\sim 10^{2}$ atoms. MD allows us to study the evolution of a set of atoms under conditions we can control and it is widely used when it comes to study high temperature and high pressure behavior of a physical system. But a very critical issue

is the choice of the potential one uses: when doing such a choice it must be taken into consideration its accuracy in reproducing known properties of the system under study, and its computational efficiency. Our choice is the Embedded-Atom-Method (EAM) that has been shown to predict and reproduce the properties of metals and alloys and is valid over a wide range of pressure and temperature: with this potential the many body effect of interaction is taken into account with a so-called embedding function and each atom is then embedded in an electron gas caused by all the neighboring atoms. It is a semi-empirical potential used in many calculations such as those of fractures, energies and melting. In this *ansatz* the total energy is expressed as $E = \sum_i F_i(\rho) + \frac{1}{2}\sum_{j\neq i}\phi_{ij}(r_{ij})$, where F is the embedding energy providing the energy necessary to place an atom in the electron density ρ it is surrounded by, and the ϕ term is an electrostatic two-body term. This will be done in Chapter 3.

Once the potential choice is made we also have to check its reliability: to do that we need to reproduce some known elastic properties, and this will be done in Chapter 4. So we will create a box of uranium with 2000 atoms and will perform a simulation that will lead it to its equilibrium state: such a microcanonical ensemble with number of atoms N, volume V and energy E conserved can be reached through a so-called *NVE* simulation. We want to check that we are able to let the system evolve and get to a predictable state. After making sure that all the parameters such as temperature, volume, pressure and energy are under control we will compute the elastic constants to be linked to the data we do have: to check the robustness of the potential we choose, we want to quantify how accurately we can predict the bulk modulus, shear modulus and Young modulus of an uranium box. We will also need to check if such a structure is stable and to do that every time, we will control that some stability criteria are satisfied.

In Chapter 4, once the potential is corroborated by phenomenological constrains, to go further than this we also want to compute elastic constants and all the polycrystalline properties related, over a wide range of temperature and pressure. We will compare our results with previous calculations and/or different theoretical approaches when there are available works/data. We want to study the isothermal and isobar behavior of the elastic constants and of the bulk modulus of uranium over a wide range of temperature from 100 K up to 1000 K and pressure from 0 GPa up to 100 GPa.

We then aim to study the system in a more complex scenario: we want to expose the box with different volumes to an external pressure (1 GPa, 20 GPa and 100 GPa) in the temperature range 100 K-400 K-700 K. To do so we run a *NPT* simulation that performs an isothermal-isobaric integration

following the Nosé-Hoover algorithm: the positions and velocities of the atoms are updated while the energy and forces are minimized at each time step. In fact we want to study the behavior of such a region of space under these conditions to connect quantitatively a change in the bulk modulus to be used as a marker and in the pressure of the system in such an extreme environment. We will be interested hence in the *transient states* between equilibrium configurations, to investigate these variations.

Chapter 1

The mechanics of seismic sources

Understanding the dynamic of earthquakes is one of the most challenging goal in geophysics and might lead us to a prediction of such phenomena and a comprehension of the physics involved. Instrumentally based seismology is in fact a relatively young subject compared to the time involved in seismogenic fault formation even though, if we knew the exact initial conditions of the problem, we could technically be able to solve the equations involved. One of the main limitations we come to face is that *we do not completely understand the earthquakes source physics*: several models have been proposed and we want to briefly analyze the most important among them. Before going through that, let us review the main concepts of the theory of elasticity we might use [1].

1.1 Elasticity and stiffness

Let us focus on elasticity in solids and more precisely in crystals. It is used a fixed system of Cartesian coordinates, and points of Euclidean space are identified with their coordinate triples $(x, y, z) = \mathbf{x} \, \epsilon \, \mathbb{R}^3$. An elastic body is then associated with a domain $\Omega \subset \mathbb{R}^3$ which is the set of all the interior points of the body. We shall use:

- bold notation for vectors, e.g. $\mathbf{v}$
- v_i are the components of the vector
- the covariant derivative is $v_{i,j} = \partial v_i / \partial x_j$

- $\dot{v}_i = \partial v_i / \partial t$ is the time derivative
- it is used the notation of Cartesian tensor analysis to describe the physical quantities associated with elastic bodies: tensors of various orders are denoted by subscript and Einstein summation convention is used

Let a point coordinates in a crystal be $\mathbf{r} = (x, y, z)$. If we deform the solid we can define a new set of coordinates $\mathbf{r}'$ and a *deformation* vector $\mathbf{u}(\mathbf{r})$

$$\mathbf{u}(\mathbf{r}) = \mathbf{r}' - \mathbf{r} = u_x(\mathbf{r})\hat{x} + u_y(\mathbf{r})\hat{y} + u_z(\mathbf{r})\hat{z} \tag{1.1}$$

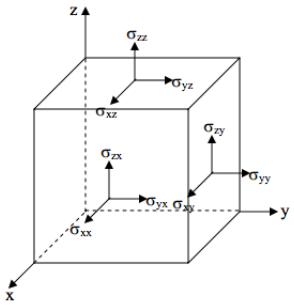

Figure 1.1: Stress vectors in a solid

Such a vector defines the displacement of any atom (or point if we are in continuum approximation) in a strained body from its original unstrained position to the new position in the strained state. If an external force acts on a solid, it will lead to a deformation: internal forces acting within the solid try to resist this deformation and when external forces are removed the solid will try and return to its original form. If this is the case the solid is said to be elastic. We can describe the law relating applied force to deformation in terms of **strain** and **stress**. Consider a force $\mathbf{F}$ acting on a solid and its surface vector $\mathbf{A}$: they both have 3 components, namely F_x, F_y, F_z and A_x, A_y, A_z, the latter being oriented in the direction normal to the surface. The component F_i acting normal to the surface A_i gives a *normal stress* σ_{ii}, whereas *shear stresses* are defined as e.g.

$$\sigma_{yx} = \lim_{A_x \to 0} \frac{F_y}{A_x} \tag{1.2}$$

A stress σ_{ij} is the force acting on the surface of an element of the body, i.e. the force per area and is considered as acting on the i-plane and being

oriented in the j-direction. If the solid is in static equilibrium the sum of all stress components acting in the x, y, z direction and the total momentum is zero. The tensor is defined as

$$\sigma_{ij} = \begin{pmatrix} \sigma_{xx} & \sigma_{xy} & \sigma_{xz} \\ \sigma_{yx} & \sigma_{yy} & \sigma_{yz} \\ \sigma_{zx} & \sigma_{zy} & \sigma_{zz} \end{pmatrix} \tag{1.3}$$

If stress has positive values it is directed outward from faces and called tensional stress; if it assumes negative values it's called compressional stress. In the SI unit we use Pa $= N/m^2$.

The strain e is then defined as a nine-components tensor given in terms of the first derivatives of the displacement components, and is a dimensionless quantity

$$e_{ij} = \begin{pmatrix} e_{xx} & e_{xy} & e_{xz} \\ e_{yx} & e_{yy} & e_{yz} \\ e_{zx} & e_{zy} & e_{zz} \end{pmatrix} \tag{1.4}$$

where e.g.

$$e_{xx} = \frac{\partial u_x}{\partial x} \quad e_{yy} = \frac{\partial u_y}{\partial y} \quad e_{zz} = \frac{\partial u_z}{\partial z} \tag{1.5}$$

Since the tensor is symmetric there are six independent components and we have

$$e_{ij} = e_{ji} = \frac{1}{2}\left(\frac{\partial u_i}{\partial j} + \frac{\partial u_j}{\partial i}\right) = \frac{1}{2}(u_{i,j} + u_{j,i}) \tag{1.6}$$

where $i, j = x, y, z$ and $i \neq j$ and where we have used the notation $u_{i,j} = \partial u_i / \partial x_j$. The strain tensor measures the change of distance between any two points in a solid.

1.1.1 Elastic constants

Hooke's Law describes linear elasticity in which stress is related linearly to a consequent strain [2]

$$\sigma_{ij} = C_{ijkl} e_{kl} \tag{1.7}$$

The fourth-rank C_{ijkl} tensor is known as the *elastic modulus tensor*: each of the 81 entries is called *elastic constant* and measures how hard this solid is, i.e. high values of those constants mean it takes more force per unit area

to deform such a solid. Every index i, j, k takes three values according to the spatial components $x, y, z = 1, 2, 3$. The tensor links the deformation to an applied stress. Due to the symmetry of stress and strain the number of its independent components reduces to 21: $C_{ijkl} = C_{jikl} = C_{ijlk} = C_{jilk}$ an $C_{ijkl} = C_{klij}$. According to each crystal symmetry then the number of independent components can be reduced, as is shown in Figure 1.2 and Figure 1.3.

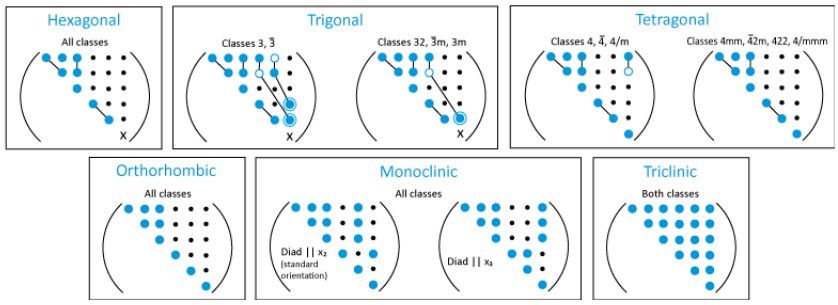

Figure 1.2: Elastic constant tensors according to the kind of solid: black dots are zero components; blue dots are non-zero components; blue dots bounded by a line are equal components; blue dots bounded by a line to circled-blue dots are components numerically equal but opposite in sign. All tensors are symmetrical about the leading diagonal.

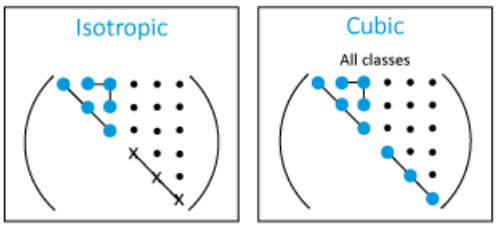

Figure 1.3: Another example of elastic constant tensors according to the kind of solid in exam.

Beyond a certain value of the stress, the solid can still be elastic but Hooke's law doesn't hold anymore and the strain-shear relationship becomes non-linear. So materials can show *elastic* behavior when no permanent deformation results when removing the force acting on them; if the body is stressed beyond a certain point, it will not return as it was before the force was applied: this is called *elastic limit*, and beyond that the deformation

is said to be *plastic*. Sometimes the applied stress exceeds the strength of the material and failure occurs: materials showing abrupt failure within the elastic range are said to show a *brittle* behavior. The opposite of brittle behavior is *ductile* behavior. Figure 1.4 shows the stress-strain relationship for solid up to the proportionality limit: under the elastic range Hooke's law holds and the material deforms elastically until the elastic limit, after which we see plastic deformation and then failure can occur. Elastic materials are deformed if a stress is applied and then return to their original state if the stress is removed; anelastic materials show a gradual strain that reaches a stable value over a time interval; plastic materials are deformed permanently by a stress and the strain increases as long as stress is acting.

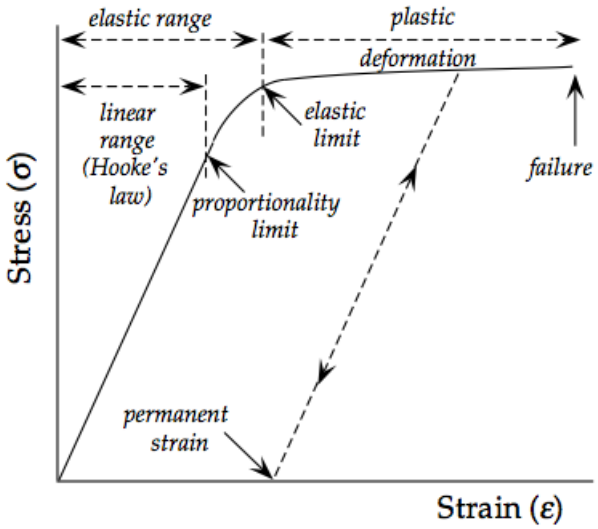

Figure 1.4: Stress-strain (ideal) relationship for a solid

1.1.2 Elastic moduli

The ratio of stress to strain defines the elastic moduli of a body: *Young's modulus* E is the constant of proportionality between stress and longitudinal strain, i.e.

$$E = \frac{\sigma_{ii}}{e_{ii}} \tag{1.8}$$

with $i = x, y, z$. Its physical unit in SI is Pa. The *shear modulus* μ is the constant of proportionality between shear strain and the shear stress, namely

$$\mu = \frac{1}{2}\frac{\sigma_{xy}}{e_{xy}} \quad \mu = \frac{1}{2}\frac{\sigma_{yz}}{e_{yz}} \quad \mu = \frac{1}{2}\frac{\sigma_{zx}}{e_{zx}} \tag{1.9}$$

its physical units is Pa. *Poisson's ratio* ν is defined as the negative ratio between transverse and axial strain:

$$\nu = -\frac{e_{yy}}{e_{xx}} \quad \nu = -\frac{e_{zz}}{e_{xx}} \tag{1.10}$$

and its a dimensionless quantity. The *bulk modulus* B determines how much a solid will compress under a given amount of external pressure

$$B = -V\frac{\partial P}{\partial V} \tag{1.11}$$

and its unit is Pa.

This quantity can be related to Young's modulus and Poisson's ratio. Consider a volume element subjected to normal stress σ_{xx}, σ_{yy}, σ_{zz}. Consequently it will experience longitudinal strain ϵ_{xx}, ϵ_{yy}, ϵ_{zz} because of a mixed effect of the three normal stress components: for example if we stretch a bar parallel to the x-axis it becomes thinner parallel to the y-axis and to the z-axis as well, as perfectly described by Poisson's ratio. Therefore

$$e_{xx} = \frac{\sigma_{xx}}{E} - \nu\frac{\sigma_{yy}}{E} - \nu\frac{\sigma_{zz}}{E} \tag{1.12}$$

and same holds for e_{yy} and e_{zz}

$$e_{yy} = \frac{\sigma_{yy}}{E} - \nu\frac{\sigma_{xx}}{E} - \nu\frac{\sigma_{zz}}{E} \tag{1.13}$$

$$e_{zz} = \frac{\sigma_{zz}}{E} - \nu\frac{\sigma_{xx}}{E} - \nu\frac{\sigma_{yy}}{E} \tag{1.14}$$

Adding together (1.12), (1.13) and (1.14) we get

$$E(e_{xx} + e_{yy} + e_{zz}) = (1 - 2\nu)(\sigma_{xx} + \sigma_{yy} + \sigma_{zz}) \tag{1.15}$$

If we set a hydrostatic pressure $\sigma_{xx} = \sigma_{yy} = \sigma_{zz} = -p$, defining dilatation θ as $\theta = e_{xx} + e_{yy} + e_{zz}$ so that the bulk modulus can be written as $B = -p/\theta$, we can write

$$B = \frac{E}{3(1 - 2\nu)} \tag{1.16}$$

Now we rearrange equation (1.12) as

$$Ee_{xx} = (1+\nu)\sigma_{xx} - \nu(\sigma_{xx} + \sigma_{yy} + \sigma_{zz}) \tag{1.17}$$

and (1.15) as

$$(\sigma_{xx} + \sigma_{yy} + \sigma_{zz}) = \frac{E}{(1-2\nu)}(e_{xx} + e_{yy} + e_{zz}) = \frac{E}{(1-2\nu)}\theta \tag{1.18}$$

Now we substitute this last equation in (1.17) and we get

$$\sigma_{xx} = \frac{\nu E}{(1+\nu)(1-2\nu)}\theta + \frac{E}{(1+\nu)}e_{xx} \tag{1.19}$$

and we define *Lamé constant*

$$\lambda = \frac{\nu E}{(1+\nu)(1-2\nu)} \tag{1.20}$$

related to the elastic constants of the solid, and we can write equation (1.19) in a more elegant form

$$\sigma_{xx} = \lambda\theta + 2\mu e_{xx} \tag{1.21}$$

We can also rearrange all the elastic parameters we studied so far in terms of Lamé constant: consider equation (1.21) for all σ_{ii} and add them together

$$\sigma_{xx} + \sigma_{yy} + \sigma_{zz} = 3\lambda\theta + 2\mu(e_{xx} + e_{yy} + e_{zz}) \tag{1.22}$$

Using hydrostatic pressure $\sigma_{xx} = \sigma_{yy} = \sigma_{zz} = -p$ and $B = -p/\theta$ we get

$$B = \lambda + \frac{2}{3}\mu \tag{1.23}$$

About Young's modulus we have seen that it is defined as the longitudinal strain of a material when a uniaxial normal stress is applied. Let us consider a uniaxial σ_{xx} stress applied so that $\sigma_{yy} = \sigma_{zz} = 0$. We can write Hooke's law as

$$\sigma_{xx} = \lambda\theta + 2\mu e_{xx} \tag{1.24}$$

$$0 = \lambda\theta + 2\mu e_{yy} \tag{1.25}$$

$$0 = \lambda\theta + 2\mu e_{zz} \tag{1.26}$$

If we add these last three equations we get

$$\sigma_{xx} = (3\lambda + 2\mu)\theta \tag{1.27}$$

and we can substitute this in (1.24) leading to

$$\sigma_{xx} = \lambda \frac{\sigma_{xx}}{(3\lambda + 2\mu)} + 2\mu e_{xx} \tag{1.28}$$

which withe a little bit of algebra becomes

$$\sigma_{xx} = \mu \left(\frac{3\lambda + 2\mu}{\lambda + \mu} \right) e_{xx} \tag{1.29}$$

Recalling that Young's modulus is defined as $E = \sigma_{xx}/e_{xx}$ equation (1.29) becomes

$$E = \mu \left(\frac{3\lambda + 2\mu}{\lambda + \mu} \right) \tag{1.30}$$

And lastly we defined Poisson's ratio as $\nu = -e_{yy}/e_{xx} = -e_{zz}/e_{xx}$. We can use equation (1.31) and use (1.23) and (1.30) to get

$$B = \frac{E}{3(1 - 2\nu)} \tag{1.31}$$

$$\frac{3\lambda + 2\mu}{3} = \mu \frac{1}{3(1 - 2\nu)} \left(\frac{3\lambda + 2\mu}{\lambda + \mu} \right) \tag{1.32}$$

And substituting Lamé constant we obtain

$$\nu = \frac{\lambda}{2(\lambda + \mu)} \tag{1.33}$$

1.2 Seismic source models

Our understanding of the processes leading to earthquakes derives from many years of observation of the zones where earthquakes have occurred. We then study **faults** that are planar fractures in a volume along which displacement happen due to the rock movement, e.g. the San Andreas fault in California. Faults can be considered as surfaces of discontinuity: according to the modern tectonic theory there are adjacent blocks in relative motion across a fault causing an amount of strain over time, see Figure 1.5. If due to motion the rocks reach their breaking point there is a violent displacement on the fault plane within a few seconds. Seismic waves propagate taking all the energy accumulated with the strain.

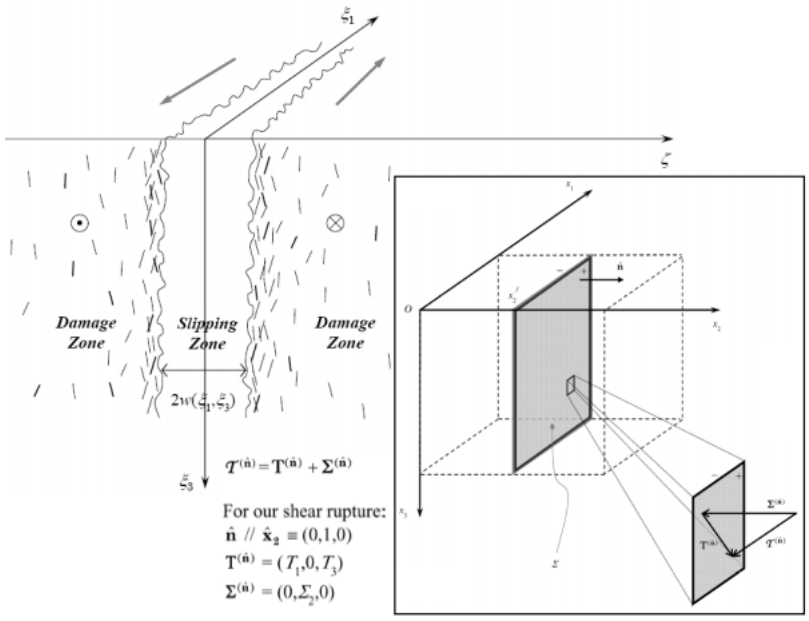

Figure 1.5: Fault structure with slipping zone and damage zones. $\mathbf{T}$ is the shear traction, Σ the normal stress vector, $\mathsf{T} = \mathbf{T} + \Sigma$ is the total traction, $\hat{n}$ is the normal vector to the plane $x_3 = 0$. The fault is vertical and parallel to the x_2 -axis.

1.2.1 Fault kinematics

We now want to describe faulting sources of earthquake that can cause seismic waves. Seismic waves can have both external (e.g. volcanic explosions, ocean waves, atmospheric explosions) and internal sources (e.g. earthquakes, underground explosions). A faulting source is an event related to an internal surface like a slip across a fracture plane. If we want to study fault mechanics, we need to define this physical entity in a mathematical way, for equations to hold. So as a basic definition, a fault is a mathematical object: an infinitesimally thin surface of all the points deviating from the elastic behavior [4]; or as in [5] a fault zone is a system of related fault segments that interact and link and are restricted to a relatively narrow band or volume. Nevertheless we must recall that when we consider faults as mathematical objects with no thickness we're using an approximation, whereas fault zones can be as wide as 200 m. But even in those cases this value is still less than the wavelengths of detectable seismic radiation.

So we're going to describe the mathematical framework of dynamic elasticity in terms of mechanic of motion and of *displacement field* [7]. A comprehensive theory of fault mechanics must include the following steps:

- a mathematical description of seismic source (e.g. fault mechanics)
- equations of motions of the fault
- the relationship between the source(s) and the equations of motion, provided some boundary conditions we need to specify

In fact not only do we need to analyze a possible set of seismic sources and how the motion propagates, but in order to make a powerful theory we also need to determine a set of boundary conditions at the Earth's surface to uniquely establish the resulting motion at the receivers. We want to focus here only on spontaneous fault motion, studying the state of the art and trying to understand how faulting sources can be an internal source of seismic waves. We will see how this simple model can be used to constrain the physics of earthquakes.

1.2.2 Mathematical formulation of motion

An elastic body in an Euclidean space can be associated with a domain $\Omega \subset \mathbb{R}^3$. We shall consider a Lagrangian approach in which we describe the motion of a particle at some point and time and its evolution in terms of all the quantities we're interested in. This approach is actually useful as it turns out to be fairly simple and accurate: in fact a seismogram records the motion of the particles to which it is attached. The basic problem of elastodynamic is to determine the *displacement*

$$\mathbf{u} = \mathbf{u}(\mathbf{x}, t) \tag{1.34}$$

as the vector distance of a particle at time t from the position $\mathbf{x}$ it occupies at time $t_0 = 0\ s$. We will denote the particle velocity as $\dot{\mathbf{u}} = \frac{\partial \mathbf{u}}{\partial t}$. So we describe a particle being in position $\mathbf{x}$ moved to a new position $\mathbf{x}+\mathbf{u}$ and use the relation $\mathbf{u} = \mathbf{u}(\mathbf{x})$ to denote the *displacement field*. We want to analyze the distortion of the medium in which the particle is inserted, so we need to look at the neighbor of the particle position at $t = 0\ s$, namely $\mathbf{x} + \delta\mathbf{x}$ and at the neighbor of the new position $\mathbf{x} + \delta\mathbf{x} + \mathbf{u}(\mathbf{x} + \delta\mathbf{x})$, $\delta\mathbf{x}$ and $\delta\mathbf{u}$ being arbitrarily small. Considering $\delta\mathbf{u} = \mathbf{u}(\mathbf{x} + \delta\mathbf{x}) - \mathbf{u}(\mathbf{x})$ we can write

$$\delta\mathbf{x} + \delta\mathbf{u} = \mathbf{x} + \delta\mathbf{x} + \mathbf{u}(\mathbf{x} + \delta\mathbf{x}) - \mathbf{x} - \mathbf{u}(\mathbf{x}) \tag{1.35}$$

We can now expand

$$\mathbf{u}(\mathbf{x}+\delta\mathbf{x}) \cong \mathbf{u}(\mathbf{x}) + (\delta\mathbf{x}\cdot\nabla)\mathbf{u} + \mathcal{O}(\delta\mathbf{x}^2) \tag{1.36}$$

So we can write

$$\delta\mathbf{x} + \delta\mathbf{u} \cong \delta\mathbf{x} + \mathbf{u}(\mathbf{x}) + (\delta\mathbf{x}\cdot\nabla)\mathbf{u} - \mathbf{u}(\mathbf{x}) \tag{1.37}$$

and we have found that

$$\delta\mathbf{u} = (\delta\mathbf{x}\cdot\nabla)\mathbf{u} \tag{1.38}$$

or in terms of its components

$$\delta u_i = \frac{\partial u_i}{\partial x_j}\delta x_j \tag{1.39}$$

and we have a direct relationship between $\delta\mathbf{u}$ and $\delta\mathbf{x}$ and the gradient of $\mathbf{u}$. Using vector product properties it is easy to re-write eq. (1.39) in terms of a distortion of the neighbor of $\mathbf{x}$ and one concerning a rigid-body rotation, i.e.

$$\delta\mathbf{u}_i = \frac{1}{2}(\mathbf{u}_{i,j} + \mathbf{u}_{j,i}) + \frac{1}{2}(\nabla\times\mathbf{u}\times\delta\mathbf{x})_i \tag{1.40}$$

We now have an explicit term taking care of the infinitesimal rigid-body rotation $\nabla\times\mathbf{u}$, although this does not affect the length of the element displaced. This means we do not need all 9 components of the tensor u_{ij}, since they're not all independent. So neglecting terms of $\mathcal{O}(\delta\mathbf{u}^2)$, using eq. (1.6) and that $(\nabla\times\mathbf{u}\times\delta\mathbf{x})\cdot\delta\mathbf{x} = 0$ we get

$$\begin{aligned} |\delta\mathbf{x}+\delta\mathbf{u}| &\cong \sqrt{\delta\mathbf{x}\cdot\delta\mathbf{x} + 2\delta\mathbf{u}\cdot\delta\mathbf{x}} + \mathcal{O}(\delta\mathbf{u}^2) \\ &= \sqrt{\delta x_i\delta x_i + 2e_{ij}\delta x_i\delta x_j} \\ &\cong |\delta x|(1 + e_{ij}\nu_i\nu_j) \end{aligned} \tag{1.41}$$

where ν is the unit vector indicating $\delta\mathbf{x}/|\delta\mathbf{x}|$ and the extensional strain of a line element in the ν direction is now $e_{ij}\nu_i\nu_j$.

1.2.3 Internal Forces

We now want to analyze the internal forces acting within a continuum. In order to define the dynamic of a particle within a medium we need to describe the forces to which it is subject. We can start up with the **traction**

vector: it is the internal force vector on a cross section divided by that cross section's area and quantifies the contact force per unit area with which particles on one side of the surface act upon particles on the other side

$$\mathbf{T} = \frac{\mathbf{F}_{int}}{\mathbf{A}} \tag{1.42}$$

it has unit of stress, but it's a vector.

So we have a *contact force* between adjacent particles; but there are also forces among *non-adjacent* particles and forces that are external to the medium affecting the internal part of the body. Clearly the last two kinds of force are non-contact forces and are referred to as **body forces**. We now want to describe these. Let us consider a particle inside a solid at a point $\mathbf{x}$ being subject to a body force per unit volume $f(\mathbf{x}, t)$ at time t. Let the force be impulsive and acting on a particle in position ξ at $t = \tau$: we can now give an explicit expression to it acting in the x_n-axis

$$f_i(\mathbf{x}, t) = A\ \delta^{(3)}(\mathbf{x} - \xi)\ \delta(t - \tau)\ \delta_{in} \tag{1.43}$$

where $\delta^{(3)}(\mathbf{x}-\xi)$ and $\delta(t-\tau)$ are respectively a three-dimensional and a one-dimensional Dirac delta[1], specifying the force is acting only on the particle in the ξ position at time $t = \tau$; A is a constant giving the strength of the impulsive force; δ_{in} is a Kronecker delta indicating the force is acting only in the direction of x_n-axis. From a dimensional point of view we have that the left side of eq. (1.43) is a [force/volume], whereas the right side is the product of the A term which is a [force $\times$ time], the spatial Dirac delta which is [1/volume], the temporal delta which is [1/time] and the Kronecker delta which is dimensionless.

Now consider a particle with mass m: its momentum is $q = mv = m\dot{u} = \rho V \partial u/\partial t$ where ρ is the density and V is the volume. We need to remember that the time derivative of momentum gives the force, so we can now link this quantity to all the forces the particle is subject to in the volume V

$$\frac{\partial}{\partial t} \int_V \rho\, \frac{\partial \mathbf{u}}{\partial t}\, dV = \int_V \mathbf{f}\, dV + \int_S \mathbf{T}(\mathbf{n})\, dS \tag{1.44}$$

where S is the surface bounding the volume V, and $\mathbf{T}$ is the traction acting on the surface. We have connected all the non-contact forces (body forces) represented by the $\int_V \mathbf{f}$ and the forces with which particles on one side of

[1] remember that in a three-dimensional space for example the Dirac delta is defined such as $\int \delta^{(3)}(\mathbf{x})\ d^3x = 1$

an internal surface act on each other (represented by the traction integrated over the whole surface), to the dynamic of the particle itself.

It is now possible to find through this result the equation of motion of the particle. Let us first express the traction vector in terms of the stress tensor through the relation

$$T_i = \sigma_{ij} n_j \tag{1.45}$$

where $\hat{n}$ is the unit vector normal to the surface, or in a more straightforward way

$$\begin{aligned} T_x &= \sigma_{xx} n_x + \sigma_{xy} n_y + \sigma_{xz} n_z \\ T_y &= \sigma_{yx} n_x + \sigma_{yy} n_y + \sigma_{yz} n_z \\ T_z &= \sigma_{zx} n_x + \sigma_{zy} n_y + \sigma_{zz} n_z \end{aligned} \tag{1.46}$$

Let's now consider the integral $\int_S \mathbf{T(n)}\ dS$ in eq. (1.44): using Gauss's divergence theorem

$$\int_S T_i\ dS = \int_S \sigma_{ij}\ n_j\ dS = \int_V \frac{\partial \sigma_{ij}}{\partial X_j}\ dV \tag{1.47}$$

with $\mathbf{X} = \mathbf{x} + \mathbf{u}$, so we can write equation (1.44) as

$$\int_V (\rho\ \ddot{u}_i - f_i - \sigma_{ij,j})\ dV = 0 \qquad \forall dV \tag{1.48}$$

Since this relationship must hold $\forall V$ it is possible to write the following **equation of motion**

$$\rho\ \ddot{u}_i = f_i + \sigma_{ij,j} \tag{1.49}$$

This equation is the fundamental elastodynamic equation or **Cauchy's momentum balance law**. Since we are interested in seismology it is necessary to emphasize that spatial fluctuations in the displacements, strains, stresses all have wavelengths much greater than the amplitude of particle displacements, which means it makes almost no difference to evaluate the spatial gradient for a single particle or in a fixed position, i.e. $\nabla X \cong \nabla x$.

1.2.4 Theorem of Uniqueness and Reciprocity

By extrapolating the equation of motion (1.49) we have settled a link between the application of body forces (non-contact) throughout a volume V,

the application of traction on the surface S and the consequent displacement field, ruled by Cauchy's law. We now want to give a general result: once we have specified the body forces through the volume and the traction over the surface it is possible to determine *uniquely* the displacement field that will develop, provided some initial conditions that need to be specified. This result is known as "Uniqueness Theorem".

Theorem 1.2.1 (Uniqueness Theorem)**.**
It is possible to uniquely determine the displacement $\boldsymbol{u}(\boldsymbol{x}, t)$ *throughout the volume* V *with surface* S *provided the following conditions are known:*

- *at* $t = t_0$ *the initial values of displacement and particle velocity*
- *for* $t \geq t_0$ *the values of the non-contact forces and the heat* $\mathcal{Q}$ *supplied through* V*, the tractions over any part* $\Omega_1 \subset S$*, and the displacement over the remainder* Ω_2 *of* S *so that* $\Omega_1 + \Omega_2 = S$

Proof. Let $\mathbf{u}$ and $\mathbf{v}$ be two solutions satisfying the same initial conditions and assume the same values for all the hypothesis of the theorem. We can build up a new solution $\mathbf{U} = \mathbf{u} - \mathbf{v}$: this new displacement field set up by linearity has zero initial conditions, has zero body forces, zero heating, zero traction on Ω_1 (since $\mathbf{u}$ and $\mathbf{v}$ assume the same value on Ω_1) and $\mathbf{U} = 0$ on Ω_1 (since for hypothesis we know the values of $\mathbf{u}$ and $\mathbf{v}$ on Ω_2). So it's left to prove that $\mathbf{U} = 0$ throughout V for $t \geq t_0$. To do that we can write the rate of mechanical work

$$\int_V \mathbf{f} \cdot \dot{\mathbf{U}} \, dV + \int_S \mathbf{T} \cdot \dot{\mathbf{U}} \, dS \tag{1.50}$$

Notice all integrand terms have physical dimensions of a time derivative of work. Recall that $T_i = \sigma_{ij} n_j$; using Gauss's divergence theorem we get

$$\int_V (f_i \dot{U}_i + (\sigma_{ij} \dot{U}_i)_{,j}) \, dV \tag{1.51}$$

Consider the equation of motion (1.49) multiplied for $\dot{U}_i$

$$\rho \, \ddot{U}_i \dot{U}_i = f_i \dot{U}_i + \sigma_{ij,j} \dot{U}_i \tag{1.52}$$

and $(\sigma_{ij} \dot{U}_i)_j = \sigma_{ij,j} \dot{U}_i + \sigma_{ij} \dot{U}_{i,j}$ and (1.51) becomes

$$\int_V (\rho \, \ddot{U}_i \dot{U}_i + \, \sigma_{ij} \dot{U}_{i,j}) \, dV \tag{1.53}$$

We can rewrite these two terms reminding that $e_{ij} = \frac{1}{2}(U_{i,j} + U_{j,i})$ and that σ_{ij} is symmetric

$$\frac{\partial}{\partial t}\int_V \frac{1}{2}\rho\, \dot{U}_i \dot{U}_i dV + \int_V \sigma_{ij}\dot{e}_{ij}\, dV \tag{1.54}$$

The rate of mechanical work for $\mathbf{U}$ is zero throughout V and on Ω_1 and Ω_2. We can integrate the rate over time to get

$$\int_V \frac{1}{2}\rho\, \dot{U}_i \dot{U}_i dV + \int_V c_{ijkl}U_{i,j}U_{k,l}\, dV \tag{1.55}$$

the former term being the kinetic energy and the latter the strain energy of the displacement field solution, and they both are positive definite quadratic form (since our system is stable). We got that $\dot{U}_i = 0$ for $t \geq t_0$ and $U_i = 0$ for $t = t_0$, so $\mathbf{U} = 0\ \forall t$.

1.2.5 The Reciprocal Theorem

We now want to show another powerful result due to Betti [6]: it establishes a relationship between two different stress and displacement fields for an elastic body.

Theorem 1.2.2 (Reciprocal Theorem)**.**
Let $\boldsymbol{u}(\boldsymbol{x}, t)$ be a displacement field due to body forces $\boldsymbol{f}$, and $\boldsymbol{v}(\boldsymbol{x}, t)$ another displacement field due to body forces $\boldsymbol{g}$ with (in the general case) different initial conditions. Then the following equality holds

$$\int_V (\boldsymbol{f} - \rho\ddot{\boldsymbol{u}}) \cdot \boldsymbol{v}\, dV + \int_S \boldsymbol{T}(\boldsymbol{u}, \boldsymbol{n}) \cdot \boldsymbol{v}\, dS = \int_V (\boldsymbol{g} - \rho\ddot{\boldsymbol{v}}) \cdot \boldsymbol{u}\, dV + \int_S \boldsymbol{T}(\boldsymbol{v}, \boldsymbol{n}) \cdot \boldsymbol{u}\, dS \tag{1.56}$$

Proof. The left-side of the equality can be rewritten using eq. (1.49) as

$$-\int_V \sigma_{ij,j} v_i\, dV + \int_S T_i v_i\, dS \tag{1.57}$$

$$-\int_V \sigma_{ij,j} v_i\, dV + \int_S \sigma_{ij} n_j v_i\, dS \tag{1.58}$$

Notice that the traction vectors $\mathbf{T}(\mathbf{u}, \mathbf{n})$ and $\mathbf{T}(\mathbf{v}, \mathbf{n})$ indicates the different tractions due to the $\mathbf{u}$ displacement and $\mathbf{v}$ displacement respectively on normal surfaces. Then using again Gauß's divergence theorem on the surface integral, symmetry relationships and the definition of strain tensor we get

$$- \int_V \sigma_{ij,j} v_i \, dV + \int_V (\sigma_{ij} v_i)_{,j} \, dV \tag{1.59}$$

$$\int_V (-\sigma_{ij,j} v_i + \sigma_{ij,j} v_i + \sigma_{ij} v_{i,j}) \, dV \tag{1.60}$$

$$\int_V c_{ijkl} \, e_{kl} v_{i,j} \, dV = \int_V c_{ijkl} \, u_{k,l} v_{i,j} \, dV \tag{1.61}$$

The right-hand side of (1.56) can be written following the same path as $\int_V c_{ijkl} \, v_{i,j} u_{k,l}$ also using the symmetry $c_{ijkl} = c_{klij}$.

Betti's theorem stands that the work done by external forces ($\mathbf{f}$) and surface traction ($\mathbf{T}(\mathbf{u}, \mathbf{n})$) moving through the displacement $\mathbf{v}$ due to ($\mathbf{g}$) and $\mathbf{T}(\mathbf{v}, \mathbf{n})$ is equal to the work done by the external forces ($\mathbf{g}$) and surface traction ($\mathbf{T}(\mathbf{v}, \mathbf{n})$) moving through displacement $\mathbf{u}$ due to $\mathbf{f}$ and $\mathbf{T}(\mathbf{u}, \mathbf{n})$.

1.2.6 Displacement field representation: Green's function for elastodynamic

We have seen from the equation of motion (1.49) that body forces through an elastic body volume and applied tractions over a surface originate the motion. We have also established a unique relationship between the displacement field and these quantities, so the next step is to develop the appropriate expression for the displacement suitable for the problem we're interested in, namely seismology. This representation will also depend on the boundary conditions that are set, whose change will lead to different solutions for different problems in exam. For earthquake faulting the seismic source is complicated and an appropriate description of it would involve finite fault plane constantly varying in space and time, so we're going to describe the simplest of sources which perfectly synthesized a more realistic source and whose solution we're able to find in an appropriate mathematical environment.

So we want to study a seismic source with **unidirectional unit impulse, localized in space and time**, i.e. a source due to an impulse like the one described in equation (1.43): this impulse is applied at $\mathbf{x} = \xi$ at time $t = \tau$ in the $n-$direction with $i-$components. The displacement field from such a source is the **elastodynamic Green function**: we denote the

$i-$th component of displacement in $(\mathbf{x}, t)$ as $G_{in}(\mathbf{x}, t; \xi, \tau)$. As we know from partial derivative equation theory [8], we shall use Green function as a solution of the equation of motion with a source described by a Dirac delta, depending on both the source and the receiver coordinates

$$\rho \frac{\partial^2}{\partial t^2} G_{in} = \delta_{in}\, \delta(\mathbf{x} - \xi)\, \delta(t - \tau) + \frac{\partial}{\partial x_j} \left(c_{ijkl} \frac{\partial}{\partial x_l} G_{kn} \right) \tag{1.62}$$

Clearly the Green function is itself a tensor. Without any loss of generality we can set initial conditions such as $G_{in}(\mathbf{x}, t; \xi, \tau) = 0$ and $\partial G_{in}(\mathbf{x}, t; \xi, \tau)/\partial t = 0$ for $t \leq \tau$ and $x \neq \xi$. Of course there is an infinite number of Green functions, each of them being determined by some boundary condition on the surface S, so according to the different problem we would like to study we shall specify it. But what we're interested in right now is to find an explicit solution for our displacement field, and we're able to do it with the representation theorem studied in section 1.2.4: in fact using Betti's theorem for $\mathbf{u}$ and $\mathbf{v}$ fields with quiescent past (so that they were both zero up to a certain time), it is easy to prove the relation

$$\begin{aligned} &\int_{-\infty}^{+\infty} dt \int_V (\mathbf{u}(\mathbf{x}, t) \cdot \mathbf{g}(\mathbf{x}, \tau - t) - \mathbf{v}(\mathbf{x}, \tau - t) \cdot \mathbf{f}(\mathbf{x}, t))\, dV = \\ &\int_{-\infty}^{+\infty} dt \int_S (\mathbf{v}(\mathbf{x}, \tau - t) \cdot \mathbf{T}(\mathbf{u}, \mathbf{n}) - \mathbf{u}(\mathbf{x}, t) \cdot \mathbf{T}(\mathbf{v}(\mathbf{x}, \tau - t), \mathbf{n}))\, dS \end{aligned} \tag{1.63}$$

where we have integrated over time because the displacement is also defined to take place over a time interval. Now if we substitute in this equation the body force $g_i = \delta_{in}\delta(\mathbf{x} - \xi)\delta(t)$ with corresponding solution $G_{in}(\mathbf{x}, t; \xi, 0)$ we can find an expression for u: the first integrand term becomes

$$\int d^4x\, \mathbf{u}(\mathbf{x}, t) \cdot \mathbf{g}(\mathbf{x}, \tau - t) = \int dt \int_V u_i\, \delta_{in}\delta(\mathbf{x} - \xi)\delta(\tau - t) = u_n(\xi, \tau) \tag{1.64}$$

where we used the notation $d^4x = dt\, d^3x$. So we can write equation (1.63) as

$$\begin{aligned} u_n(\xi, \tau) = &\int_{-\infty}^{+\infty} dt \int_V f_i(\mathbf{x}, t) G_{in}(\mathbf{x}, \tau - t; \xi, 0)\, dV + \\ &\int_{-\infty}^{+\infty} dt \int_S (G_{in}(\mathbf{x}, \tau - t; \xi, 0) T_i(\mathbf{u}, \mathbf{n}) - u_i(\mathbf{x}, t) c_{ijkl} n_j G_{kn,l}(\mathbf{x}, \tau - t; \xi, 0))\, dS \end{aligned} \tag{1.65}$$

We shall interchange the variables $(\mathbf{x}, \xi)$ and (t, τ) to better understand this equation: $(\mathbf{x}, t)$ then becomes the general position at which the displacement is to be evaluated and ξ is the point of observation

$$\begin{aligned} u_n(\mathbf{x},t) = &\int_{-\infty}^{+\infty} d\tau \int_V f_i(\xi,\tau) G_{in}(\xi, t-\tau; \mathbf{x}, 0)\, dV(\xi) + \\ &\int_{-\infty}^{+\infty} d\tau \int_S (G_{in}(\xi, t-\tau; \mathbf{x}, 0) T_i(\mathbf{u}(\xi,\tau), \mathbf{n}))\, dS(\xi) + \\ &\int_{-\infty}^{+\infty} d\tau \int_S -(u_i(\xi,\tau) c_{ijkl} n_j G_{kn,l}(\xi, t-\tau; \mathbf{x}, 0))\, dS(\xi) \end{aligned} \tag{1.66}$$

We have used the representation theorem to find this result which allows us to find a representation of the displacement field: it is possible to have an explicit equation describing $\mathbf{u}(\mathbf{x}, t)$ that relates all the contributions due to the **f** force and the traction and the displacement itself on the surface. Equation (2.9) states that **the displacement in a generic point x at time** t **is the sum of three different contribution: one due to the force f through the volume V, one due to the traction over the surface S** an one to the displacement itself on S, even though it doesn't specify how every contribution is weighted. Now depending on which boundary condition on S we take, we'll get different solutions for the equation of motion. But the important result we have built here states that we can have an explicit representation of the **u**. It is often useful to take boundary conditions such as S to include two adjacent surfaces inside the volume, in order to describe a buried fault.

1.2.7 Representation of a seismic source: faulting source

So far we have described in a mathematical way a fault surface. Then we have found the equation of motion, establishing how a displacement field can occur. Equation (2.9) is an implicit expression of the displacement since we would need to specify some Green function. We now want to show a simple case in which we know exactly the analytical expression of the Green function: the case of a homogeneous, unbounded, isotropic medium. Even though this is a much simpler scenario than reality, we shall find out an important result concerning the motion of a fault throughout the medium.

We have seen that there are both external and internal sources to the Earth that can cause seismic waves: external source can be explosions or volcanic eruptions. We're now focusing on **internal seismic sources** which

can be divided into two types: **faulting sources** and volume sources. The former happen inside a certain volume V (a *domain*) covering a surface S where there's a fracture plane across which a slip can occur; the latter are associated with a volume V where a sudden explosion may happen in a source region. It is possible to demonstrate a unified theory including both sources: we shall consider a volume and its surface across which discontinuities can occur in displacement or in strain. As we have done before we want to present a mathematical environment for the appropriate equations to hold. So we can describe internal seismic sources through two different descriptions: a medium containing the source on which some kind of non-contact forces are applied; some kind of discontinuities in displacement or strain. And it is possible to show that different body forces can be equivalent to the same displacement discontinuity, i.e. we'll find body force equivalents.

Let's then analyze the process of slip on a buried fault using the representation theorem, to get a general result about displacement. Let us consider a finite elastic body in a domain V with external surface S. A buried fault will be an internal surface and will be indicated as Σ: this surface will be divided into two parts Σ^+ and Σ^- on which different displacement can occur, so that $\mathbf{u}(\xi,\tau)|_{\Sigma^+} - \mathbf{u}(\xi,\tau)|_{\Sigma^-} \equiv [\mathbf{u}(\xi,\tau)] \neq 0$. Σ^+ and Σ^- will be opposite faces of a fault. If slip happens across Σ we face a discontinuity in the displacement field there: in order for the equation of motion to hold we must consider a whole surface with no discontinuity and we'll refer to $S+\Sigma^+ +\Sigma^-$, then S can be looked at as the surface of the Earth and we shall compute the quantities we want on Σ. In absence of body forces, assuming the Green function and its derivatives are continuous on that surface, the simplest representation for the displacement at any point x at time t is

$$u_n(\mathbf{x},t) = \int_{-\infty}^{+\infty} d\tau \int_{\Sigma} ([u_i(\xi,\tau)] c_{ijpq} \nu_j G_{np,q}(\mathbf{x}, t-\tau; \xi, 0))\, d\Sigma \qquad (1.67)$$

What we have found here is that displacement on the fault can determine displacement everywhere $(\mathbf{x},t)$. Setting up the appropriate Green function with the right boundary conditions it is possible to evaluate with this formula the motion starting up with the slip function, and this is an important result. This is in fact an example of earthquake model describing waves propagating from a source when a slip on a surface occurs, propagating through a medium. Of course this model can be more complex but it is impressive we got such a result with such a simple example. Since equation (1.67) bounds the displacement $u(x,t)$ to a set of the Green functions set up by a body force, we can think of the fault surface as a surface distribution of body

forces (non contact forces). Let's write equation (2.9) including all the body forces terms

$$\begin{aligned} u_n(\mathbf{x},t) = &\int_{-\infty}^{+\infty} d\tau \int_V f_p(\eta,\tau) G_{np}(\mathbf{x},t-\tau;\eta,0)\ dV(\eta) + \\ &\int_{-\infty}^{+\infty} d\tau \int_\Sigma -[T_p(\mathbf{u}(\xi,\tau),\nu)] G_{np}(\mathbf{x},t-\tau;\xi,0)\ d\Sigma(\xi) + \\ &\int_{-\infty}^{+\infty} d\tau \int_\Sigma ([u_i(\xi,\tau)] c_{ijpq}\nu_j G_{np,q}(\mathbf{x},t-\tau;\xi,0))\ d\Sigma(\xi) \end{aligned} \tag{1.68}$$

where we have a discontinuity inside the volume V. Since we want to find a body force equivalent of all the discontinuities inside the surface let's start up with the traction term. The integrand $[T \times d\Sigma]$ has the dimensions of [force/surface $\times$ surface], i.e. [force]. Body forces are [force/volume], so we can evaluate them as $[T\ \delta^3(\eta-\xi)\ d\Sigma]$, and now this term is a body force as η varies inside the volume V. So to compute the contribution of this force to the displacement we need to compute the integral:

$$\int_{-\infty}^{+\infty} d\tau \int_V \left(\int_\Sigma -[T_p(\mathbf{u}(\xi,\tau),\nu)] \delta^3(\eta-\xi) d\Sigma \right) G_{np}(\mathbf{x},t-\tau;\eta,0)\ dV \tag{1.69}$$

and here it is possible to isolate the body force equivalent of a traction discontinuity on Σ

$$f^{[T]}(\eta,\tau) = \int_\Sigma -[\mathbf{T}(\mathbf{u}(\xi,\tau),\nu)] \delta^3(\eta-\xi)\ d\Sigma \tag{1.70}$$

We can find the body force equivalent of displacement discontinuity as well using the Dirac delta property

$$\frac{\partial}{\partial \xi_q} G_{np}(\mathbf{x},t-\tau;\xi,0) = -\int_V \frac{\partial}{\partial \eta_q} \delta^3(\eta-\xi) G_{np}(\mathbf{x},t-\tau;\eta,0)\ dV(\eta) \tag{1.71}$$

so that the displacement discontinuity in terms of forces is

$$\int_{-\infty}^{+\infty} d\tau \int_V \left(\int_\Sigma -[u_i(\xi,\tau)] c_{ijpq}\nu_j \frac{\partial}{\partial \eta_q} \delta^3(\eta-\xi) d\Sigma \right) G_{np}(\mathbf{x},t-\tau;\eta,0)\ dV \tag{1.72}$$

The body force equivalent of a displacement discontinuity on Σ is then

$$f_p^{[\mathbf{u}]}(\eta,\tau) = \int_\Sigma -[u_i(\xi,\tau)]c_{ijpq}\nu_j \frac{\partial}{\partial \eta_q}\delta^3(\eta-\xi)d\Sigma \tag{1.73}$$

So we have seen a mathematical approach to internal seismic sources concerning a simple fault source model. It has been shown that if the displacement discontinuity across a fault surface has a functional form we 're able to find in terms of space and time variables, then motions throughout the medium is set. Besides, we have described this model in terms of discontinuities in displacement or strain across the surface of a volume source where waves start to propagate and we incorporated this strategy into a description of the same phenomenon in terms of body forces, finding body forces equivalents to discontinuities in displacement and strain.

1.3 The slider-block model for earthquakes

We now want to explain a simple mechanical model for an earthquake cycle. In this model the plates move along the lithosphere causing shear stress to build up on a locked fault until failure stress is reached: the accumulated stress is then released and the earthquake occurs, propagating along the fault and generating seismic waves through the surrounding rocks. Seismic waves carry the elastic energy stored in the slipping rocks. To better explain such a machinery we present the so-called *slider-block model* through which the earthquake mechanism is explained. Let us consider then a block of rock of mass m resting on a surface with a contact area A which represents the fault that will fracture causing the earthquake. On the mass a normal force acts, namely F_n pressing it,

$$F_n = \rho g h A \tag{1.74}$$

where ρ is the density $\rho = m/V$ (so that $m = \rho A^{3/2}$), g is the gravitational acceleration and h is the mean depth of the fault, see Figure 1.6. We imagine there is a constant velocity driver plate pulling the block along the surface with velocity u_0, bound to the block through a spring of constant k exerting a force $F = kx$ where x is the extension of the spring. A shear force F_σ resist the spring force. We use a spring because it models the accumulation of elastic strain in the rock close to the fault. The slip of the block represents the occurrence of an earthquake: the block sticks to the ground while the force in the spring increases until a critical value when it equals the frictional resistance to slide, namely F_σ. When this value is reached the stored energy

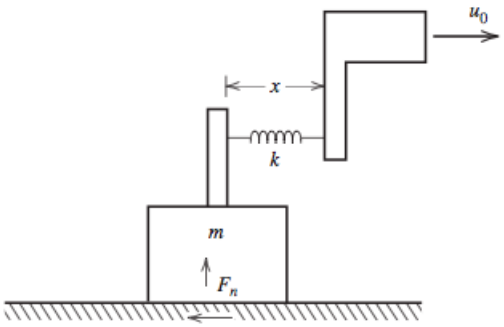

Figure 1.6: Slider-block model and the quantities involved.

is released. As long as the block sticks to the ground the shear stress on the fault is

$$\sigma = \frac{\mu x}{2b} \tag{1.75}$$

where b is the distance from the fault where the uniform velocity is applied and we assume it is $b = A^{1/2}$ and μ is the shear modulus. Since velocity is constant we also know that $u_0 = x/t$ where x is the spring extension. The shear force can be expressed as

$$F_\sigma = \sigma A = \frac{\mu x A}{2b} = \frac{\mu x A^{1/2}}{2} \tag{1.76}$$

So from the expression of the surface shear force that resists the spring force we can find the constant k as

$$\frac{F_\sigma}{x} = k = \frac{\mu A^{1/2}}{2} \tag{1.77}$$

We now invoke Amonton's law that stands that the greater the normal stress the harder it is to initiate sliding, i.e. $\sigma_{fs} = f_s \sigma_n$ where σ_{fs} is the static frictional stress and f_s is the coefficient of friction. So the static condition for the onset of sliding is the equality between the surface shear force and the normal force

$$k x_s = f_s F_n = f_s \rho g h A \tag{1.78}$$

where x_s is the extension required to initiate the slip. So we can find x_s which is the accumulated displacement on the fault

$$x_s = \frac{2f_s\rho g h A^{1/2}}{\mu} \tag{1.79}$$

Once the block starts to slip there is a frictional force contrasting the motion: as long as the block sticks to the surface the static coefficient of friction f_s will be greater than the dynamic coefficient of friction f_d. Sliding will start instead at the velocity u_0 when $f_d > f_s$ so we can write the following equation of motion

$$m\ddot{x} = -kx + f_d F_n \tag{1.80}$$

To solve this second order linear differential equation we need a few substitutions

$$\begin{aligned} m\ddot{x} + \frac{\mu A^{1/2} x}{2} - f_d \rho g h A = 0 \\ \frac{2\rho A}{\mu}\frac{d^2x}{dt^2} + x - \frac{2f_d\rho g h A^{1/2}}{\mu} = 0 \end{aligned} \tag{1.81}$$

Let's now introduce the following auxiliary variables

$$\phi = \frac{f_s}{f_d} \tag{1.82}$$

$$T = t\left(\frac{\mu}{2\rho A}\right)^{1/2} \tag{1.83}$$

$$X = \frac{x\mu}{2f_s\rho g h A^{1/2}} \tag{1.84}$$

$$U = \frac{u}{f_s g h}\left(\frac{\mu}{2\rho}\right)^{1/2} \tag{1.85}$$

so that equation (1.80) becomes

$$\frac{d^2X}{dT^2} + X = \frac{1}{\phi} \tag{1.86}$$

with the initial condition $X = 1$ at $T = 0$ corresponding to the condition (1.79) when slip occurs. We now have a Cauchy problem whose solution is easily found to be

$$X = \frac{1}{\phi} + \left(1 - \frac{1}{\phi}\right)\cos(T) \tag{1.87}$$

and the slip velocity is

$$U = \frac{dX}{dT} = -\left(1 - \frac{1}{\phi}\right)\sin(T) \tag{1.88}$$

So where $dX/dT = 0$ sliding ends and this happens for $T = \pi$. The position of the block at the end of slip is then $X(\pi) = -1 + 2/\phi$ and the whole displacement of the block will be

$$\Delta X = X(\pi) - X(0) = 2\left(\frac{1}{\phi} - 1\right) \tag{1.89}$$

We can compute the total time of the cycle

$$\Delta T = \frac{\Delta X}{U} = \frac{2}{U}\left(\frac{1}{\phi} - 1\right) \tag{1.90}$$

so slip occurs periodically. We now want to relate the displacement of the slider-block to the displacement w on a fault during an earthquake, the latter corresponding to (1.79) so that

$$\Delta w = \frac{2 f_s \rho g h A^{1/2}}{\mu} \Delta X \tag{1.91}$$

We can also compute how much elastic energy is involved in this process. This is important because the energy released can be related to the intensity of the earthquake. The elastic energy for the spring is then

$$E_s = \frac{1}{2} k x_s^2 = \frac{f_s^2 \rho^2 g^2 h^2 A^{3/2}}{\mu} \tag{1.92}$$

Whereas right after the earthquake this energy can be modified as

$$E_f = \frac{1}{2} k (x_s - \Delta w)^2 = \frac{f_s^2 \rho^2 g^2 h^2 A^{3/2}}{\mu} \left(\frac{2 f_d}{f_s} - 1\right)^2 \tag{1.93}$$

And then the total energy released in this model by the earthquake is

$$\begin{aligned} \Delta E =& \frac{f_s^2 \rho^2 g^2 h^2 A^{3/2}}{\mu} - \frac{f_s^2 \rho^2 g^2 h^2 A^{3/2}}{\mu} \left(\frac{2 f_d}{f_s} - 1\right)^2 = \\ &= \frac{f_s^2 \rho^2 g^2 h^2 A^{3/2}}{\mu} \left(1 - (2\phi - 1)^2\right) = \\ &= \frac{4 f_s f_d \rho^2 g^2 h^2 A^{3/2}}{\mu} \left(1 - \frac{f_d}{f_s}\right) \end{aligned} \tag{1.94}$$

This quantity though does not take into account all the energy involved in the process: in fact part of the energy release in the slip goes into seismic waves and heat throughout the fault.

1.4 Seismic source physics

So far we have seen mechanics seismic source models of faults based on many investigations on the internal structure of fault zones where a core is surrounded by highly fractured materials named damage zone, surrounded by undamaged rocks, the host rock. But of course the whole scenario is way more complicated than explained so far. In fact the need of a governing law linking the components of the stress tensor to all the physical/chemical observables arise. We know that [9] we can relate the magnitude τ of the shear traction to the effective normal stress on the fault σ_n^{eff} through the internal friction coefficient μ_f as

$$\tau = \mu_f \sigma_n^{eff} \tag{1.95}$$

where σ_n^{eff} is the difference between the normal stress and the pore fluid pressure on the fault p_{fluid}, namely

$$\sigma_n^{eff} = \sigma_n - p_{fluid} \tag{1.96}$$

Once all the parameters and the boundary conditions are set we can study all the phases of pre-seismic cycle governed by the traction evolution equation. In order to include in a model all the physical processes happening during faulting a more realistic equation must be specified, taking into account the rheological/physical/chemical properties of the medium. So equation (1.95) can be thought as

$$\tau = \mu_f(w_1 O_1, \ldots, w_n O_n; p_1, \ldots, p_M)\sigma_n^{eff} \tag{1.97}$$

where $O_{i=1,\ldots,N}$ are the dynamical variables of the problem (the observables), $w_{i=1,\ldots,N}$ are the weights with which every observable occur in the process and $P_{i=1,\ldots,M}$ are the parameters of the theory. This governing equation for seismic source finally takes into account several mutually influencing (and sometimes competing) mechanisms that can happen. In Figure 1.7 we can see a scheme of such a complex phenomenon, where each colored-path corresponds to a possible evolutionary stage of a faulting episode. Each phenomenon we're studying might have different parameters like the fault dimension and the weights in equation (1.97) can change according to each

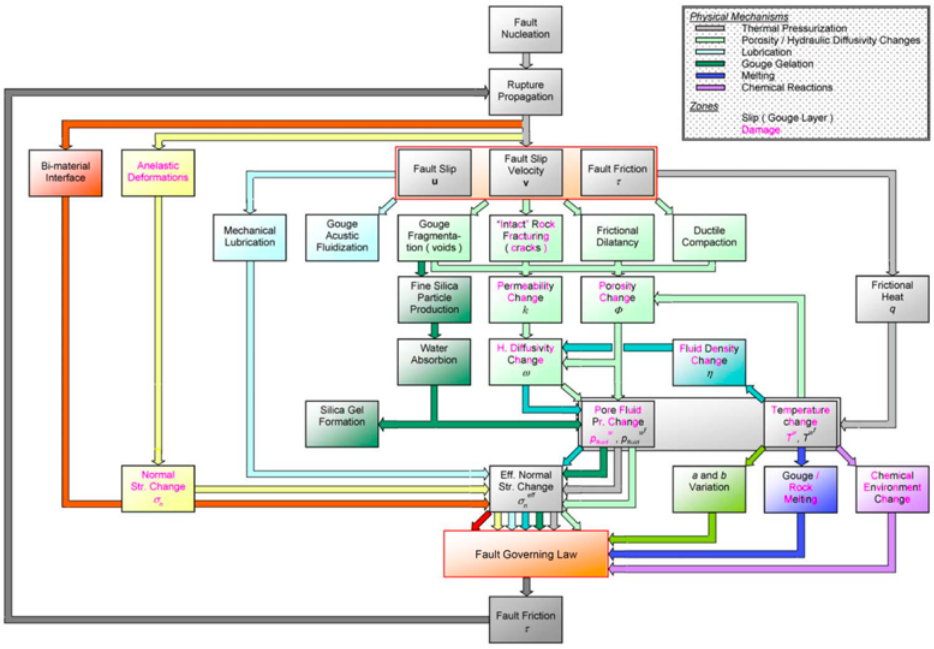

Figure 1.7: Scheme of most of the possible mechanisms occurring during a faulting episode that can lead to fault traction [9]

case so it is important to phenomenologically constrain the model. Each path in Figure 1.7 represents a possible mechanism occurring during a faulting episode. Let's see more in detail.

1.4.1 Fluids in the fault

Fluids and pore pressure relaxation play an important role in faulting episodes for they influence the mechanics of earthquakes, e.g. affecting the earthquake nucleation or triggering aftershocks. For example the permeability k which is the capacity of a porous material to allow fluids to pass through it, is three order of magnitudes greater in the damage zone than it is in the fault core [10]. Fluids then tend to flow in the direction perpendicular to the fault. It is possible [11] to determine the full equations for temperature and pressure variations due to friction, including them into equation (1.97) getting

$$\tau = \left[\mu_* + a \ln\left(\frac{v}{v_*}\right) + b \ln\left(\frac{\psi v_*}{L}\right)\right] \sigma_n^{eff} \tag{1.98}$$

where a, b, L are constitutive parameters, μ_* and v_* are reference values for friction coefficient and sliding velocity [12] and ψ represents all the state variables. When one considers fluids as well, the fault behavior compared to the dry case changes: rupture acceleration, instability, stress drop can occur and a few models have been developed, see e.g. [13].

1.4.2 Flash heating

Another phenomenon that can cause a variation of the evolution equation when coupling with a faulting episode is flash heating. The temperature on an asperity contact changes faster than the average temperature of the fault, so the heating rate is locally higher. Flash heat is activated if sliding velocity is greater than a critical value v_{fh} which can be calculated. The governing law can change this time as [14]

$$\tau = \left[\mu_* + a \ln\left(\frac{v}{v_*}\right) + \Theta\right] \sigma_n^{eff} \tag{1.99}$$

where Θ represents the state variable of this model including the value of v_{fh} that can be computed. This variation though only holds when high slip rates occur. As shown for example in [14] flash heating increases the instability causing: stress drop, self-heating of the fault, early melting and a decrease of the sliding resistance.

1.4.3 Melt in earthquake faulting

The issue of melt occurring during coseismic slip is still in debate: in fact even though melting should probably occur due to the heat conditions, there's still little evidence for such a process coming from exhumed rocks. Nevertheless both experimental evidence in laboratory and theoretical model simulations have shown that melt in earthquake faulting is an important factor to be taken into account [15]. For example in the models performed in [11]-[16] it has been shown that for thin slipping zone melting temperature can be achieved during motion. In [17] a constituent law for friction when melting occurs is derived which has the form

$$\tau = \frac{K}{R}\sqrt{\frac{\ln\left(\frac{2v}{v_m}\right)}{\frac{2v}{v_m}}}(\sigma_n^{eff})^{1/4} \tag{1.100}$$

where K is a normalizing constant, R is the radius of the fault and v_m is a characteristic slip rate.

1.4.4 Chemical influences

Chemical environment changes have influence on fault friction and must be taken into account. Laboratory experiments such as [18] have shown from analyses of gouge particles that processes like the release of structural water in serpentine can take place. Not only, it has also been proved for example in [19] that thermally activated decomposition of calcite can happen in a very early stage of slip of the fault: this is important in that natural gouges often contain sheet silicate minerals which can decompose and leave a signature of seismic slip. Nevertheless nowadays there is no model of earthquake including such chemical effects in the governing law. Even though the puzzle is still to be completed.

1.4.5 Porosity

Porosity ϕ also plays an important role in controlling fluid migration on wet faults. In fact during an earthquake the frictional sliding can open cracks and pores and the pore fluid pressure will decrease. An equation governing the evolution of porosity in time has been introduced [20] in the form

$$\frac{d}{dt}\phi = \frac{v\beta\mu_*}{2w} - \frac{\sigma_n^{eff}}{C(\phi_{sat} - \phi)^m} \tag{1.101}$$

where β is a dimensionless factor, C is a viscosity parameter, the exponent m contains effects on nonlinear rheology and percolation theory, w is the width of the fault and ϕ_{sat} is a limit value porosity can't exceed (it would in fact lead to a vanishing denominator). During an earthquake though there are both frictional slip processes on fault surfaces and shear fracture of rocks. So new voids can create in such an event, and the fracturing will cause a change in porosity. An increase of porosity can be related to the displacement of the fault. Starting from this point several evolution laws for porosity have been proposed, see e.g. [21]-[22], all stating that porosity evolution is concurrent with breakdown processes since they involve the evolution of the state variables of the problem. Nevertheless we must say that there is a lack of experimental surveys about porosity in the fault structure: so far we only have numerical models.

1.4.6 Permeability

Permeability k as well undergoes changes within different type of rocks because of their thermal state [23]. As noted in [24] there is a relationship between k and σ_n^{eff}

$$k = k_0 e^{-\frac{\sigma_n^{eff}}{\sigma_*}} \tag{1.102}$$

where k_0 is the permeability at zero effective normal stress, and σ_* is a constant. This means that as σ_n^{eff} changes during an earthquake, permeability can increase up to a factor 2. Besides, k also depends on porosity [25]

$$k = K\frac{\phi^3}{(1-\phi)^2}d^2 \tag{1.103}$$

where d is the grain size, K is a constant. It is clear now from this picture that temporal changes in ϕ governed by the above mentioned equations can influence permeability too and both enter in the equation for the pressure of fluids in the fault.

1.4.7 Mechanical lubrication

We have to consider mechanical lubrication too, i.e. a phenomenon due to the pore fluids within the fault asperities flowing in the direction perpendicular to the fault surface, whose effect is to cause a lubrication pore fluid pressure [26], [27]. The fluid pressure in the lubrication model is

$$P_{fluid}^{lub}(\xi) = p_r + \frac{3}{2}\eta v \int_0^{\xi} \frac{w^* - w}{w^3} d\xi' \tag{1.104}$$

where p_r is the initial reservoir pressure, w^* is the dimension of the fault evaluated in the lubricated zone where the P_{fluid}^{lub} is constant, v is the relative velocity between two faults, ξ is the variable identifying the lubrication zone L, η is the viscosity. So the total effect is that the effective normal stress on the fault is reduced by the pore fluid pressure and the pressure lubrication, i.e. equation (1.96) has to be modified

$$\sigma_n^{eff} = \sigma_n - p_{fluid} - P_{fluid}^{lub} \tag{1.105}$$

So the net effect of lubrication is to reduce the fault traction, increasing the fault slip velocity, reducing asperity collisions. Nevertheless it's been noticed [28] that when effective traction vanishes $\sigma_n^{eff} \to 0$ if fluids are present in the fault, the hydrodynamic regime holds: friction will then only depend on fault separation surfaces, the fault velocity and the viscous resistance being included in the P_{fluid}^{lub}. So depending on what kind of fluid there will be inside the fault, different effects can occur in the model: thermal pressurization and/or hydrodynamical lubrication.

1.4.8 Dissimilar materials

There is no general consensus on the role of dissimilar materials in normal stress. For example: [29] suggested that if slip between bi-materials occur there will be a reduction in the normal stress σ_n influencing the dynamic fault weakening; [30] showed if asperity failure occurs in such a material σ_n will then change in time; whereas [31] demonstrated inhomogeneous slip between bi-materials can cause a change in σ_n^{eff}.

1.4.9 Challenges of such a model

Building up a constituent law of earthquake source is a challenging goal according to our knowledge nowadays. The scheme presented here in Figure 1.7 states that there can be several different physical/chemical mechanisms concurring to an earthquake phenomenon. Most of these mechanisms can interact and/or compete with each other [32]. One of the main lack we come to face in geophysical observation is that the scale of the laboratory is rather different than the real fault scale: so when we're able to infer some parameters to be included in the model, there is the issue of how to rescale these values to the fault scale. Not to forget that, when considering all the up mentioned factors in an earthquake model, a computational simulation can be too severe. Besides, there still is lack of knowledge of the state of the art of the Earth crust and the mantle.

We have described so far a lot of mechanisms that can occur during a fault episode, all of which involve macroscopic averaged variables: e.g. the fault friction described by equation (1.97) is then obtained averaging all the effects happening on each single asperity. *So there is a strong need of connecting atomic properties of the materials involved in the process to a macrophysical description of them.* Another limitation is that we don't know which (if there is one) mechanism is dominant in controlling the friction evolution. *So, Figure 1.7 can be looked at as a description -still to be completed- of the links among existing phenomena, and as a complex puzzle of the rupture process made up of several variables to be taken into account. Only a multiple approach to source mechanics including numerical simulation, geophysical surveys, data analyses can lead to a real model for earthquake.*

It then seems to us there is a lack in the scheme in Figure 1.7 , for radioactivity is missing. In order to corroborate a sophisticated and phenomenological model for seismic sources, radiogenic sources must be taken into account, for we have strong evidence of radioactive elements presence inside the Earth and of their importance as heat sources. Which means

these elements produce energy inside the crust and the mantle. So far we have never considered the radioactive processes occurring inside the Earth: in fact the radiogenic heat sources distribution strongly influences the geodynamic and the thermal behavior of the Earth. The heat coming from the inside of the planet has basically two sources: the cooling of the planet and the heat produced by the decay of the long-lived isotopes. We now know that the total heat flux at the Earth surface is 47 ± 1(stat.) TW [33], 70% of which comes from the radioactive decay of uranium, thorium and potassium, with 11 TW ($\sim$ 25%) accounting for uranium alone. Uranium is mainly present in the mantle [23] but the location of all these heat sources is still to be constrained. In order to be a source of heat a radioactive isotope has to fulfill a few conditions: it must have a half-life comparable to the age of the Earth and it must be sufficiently abundant. ^{238}U, ^{235}U, ^{232}Th and ^{40}K all fulfill these requirements with half-lives and decay constants as shown in Figure 1.8. ^{238}U is the most abundant in nature ($\sim$ 99.28%), ^{235}U being $\sim$ 0.71%. It is possible to compute the rates of radioactive heat produced by these elements in a rock multiplying the average heat per second produced by each element times the concentration in a rock.

Parent isotope	Daughter isotope	Decay constant [10^{-10} yr^{-1}]	Half-life [Ga]
^{40}K	89.5% ^{40}Ca 10.5% ^{40}Ar	5.543	1.25
^{87}Rb	^{87}Sr	0.1420	48.8
^{147}Sm	^{143}Nd	0.0654	106.0
^{232}Th	^{208}Pb	0.4948	14.01
^{235}U	^{207}Pb	9.8485	0.704
^{238}U	^{206}Pb	1.5513	4.468

Figure 1.8: Main radioactive isotopes inside the Earth with decay constants and half-lives [2].

So in order to consider a new point of view to add (i.e. radioactivity) to the scheme in Figure 1.7, let's start up with describing uranium geochemistry.

1.5 Uranium geochemistry

We now want to see a few geochemical properties of the radionuclide U and its aquifer chemistry and behavior. Aquifer parameters are hard to sample since direct measurement is not always possible, this is why this kind

of information is integrated with laboratory experiments on aquifer materials. Nevertheless by measuring waters alone it is possible to find out those water-rock interaction parameters thanks to the decay series of nuclides in groundwater, and many information can be obtained from those decay series: in fact the main source of groundwater nuclides are those in aquifer rocks whose relative proportions are known [34]; besides each radionuclide has more than one isotope each with a different time-life so we can distinguish among different processes occurring over different time scale. To constrain the behavior of an element in groundwater an important process is α-recoil [35]: when an element of the U/Th-series undergoes an α-decay, the daughter nuclide is boosted in a random direction about 20 nm, and can stop in groundwater. This process is unaffected by groundwater chemistry so it allows to gain more physical knowledge about the elements involved. Groundwater concentration from U/Th-series can be found for example in [36], [37], [38] and [39]. In groundwater the main isotope of U is ^{238}U forming

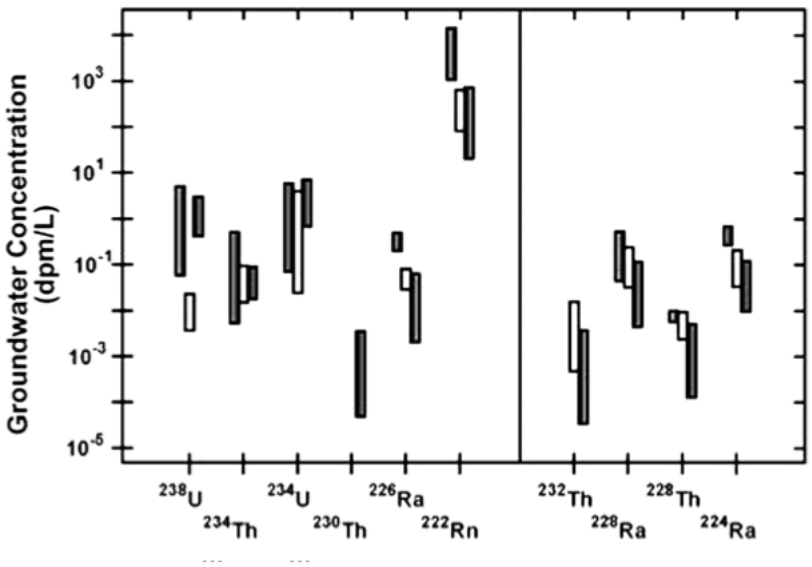

Figure 1.9: Groundwater concentrations of U series (left) and Th series (right) as in [36], [37], [38] and [39].

soluble complexes with carbonate and phosphate or with sulfate and fluorides, with typical concentrations about 1 ppb [40]. ^{238}U is released from the host aquifer only by weathering: zircon minerals and micas mainly contain U and it is possible to find its trace in groundwater flows. About sorption in-

stead, clays and carbonates for example as well as organic matter can adsorb it [41]. Also iron minerals are important in controlling nuclides migration; ferrihydrite sorbs U too. It can be incorporated in monazite, sphene, apatite and magnetite [42]. But the distribution of U in host rocks has to be constrained by some kind of direct study of the aquifer rocks.

1.5.1 Nuclide transport in aquifers

We now want to describe a general model for U series transport following [34] and [43]. The radionuclides in an aquifer include: groundwater species obtained through direct sampling; populations in the host aquifer rock; adsorbed atoms on host rocks surfaces. It is possible to write an equation [44] for transport along groundwater flow paths and relate all the processes involved, i.e.: advection, weathering, recoil, desorption, precipitation, production, decay, adsorption. See Figure 1.10. For an isotope i with groundwater molar concentration i_W and parent molar concentration p_W the following equation for time evolution holds

$$\begin{aligned}\frac{\partial i_W}{\partial t} =& v\left(\frac{\partial i_W}{\partial x}\right) + bw_i i_R + b\epsilon_i \lambda_P p_R + i_{AD} k_{-1}^i + f_i \lambda_P p_{AD} \\ &+ \lambda_P p_W - Q_i i_W - \lambda_i i_W - k_1^i i_W\end{aligned} \tag{1.106}$$

where: b is the ratio of the mass of aquifer rock to the mass of water, i_R (p_R) is the host rock nuclide i (parent) molar concentration, i_{AD} (p_{AD}) is the adsorbed nuclide (parent) molar concentration, v is the groundwater velocity, x is the distance along a flow line in groundwater, w_i is a constant for weathering release of nuclide i, ϵ_i is the recoil release fraction, λ_i and λ_P are the decay constants of nuclide i and parent p, k_{-1} is the bulk desorption rate constant, k_1 the adsorption rate constant, Q_i is the rate of precipitation of nuclide i, f_i fraction of nuclide i produced by adsorbed parents and recoiled into water.

Each term of equation (1.106) represents a process in Figure 1.10. The first term $\frac{\partial i_W}{\partial t}$ represents the time variation of isotope molar concentration i along a flow which is constant so this term would vanish; the second term $v\left(\frac{\partial i_W}{\partial x}\right)$ represents advection (horizontal current) which is the concentration gradient for i times the flow velocity v; the term $bw_i i_R$ is the input by weathering: host rocks (minerals) with molar concentrations i_R release radionuclides at rate w_i; the recoil term $b\epsilon_i \lambda_P p_R$ represents the release of a fraction of daughter by direct recoil by a parent nuclide population in the

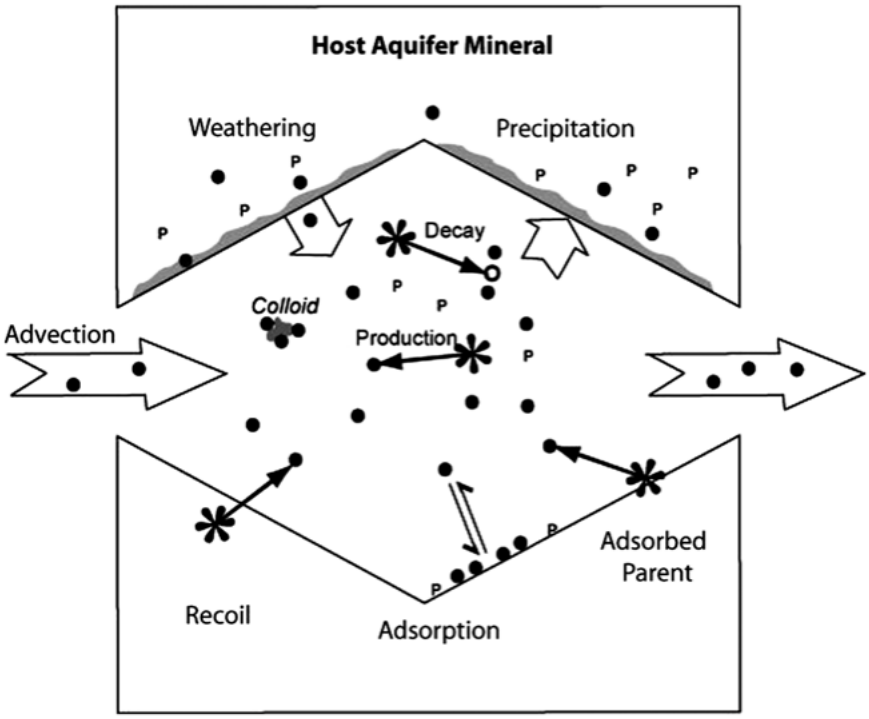

Figure 1.10: In the model depicted here there are three populations of radionuclides in an aquifer: groundwater species, populations in the host rocks, and adsorbed atoms on host rock surfaces. The image contains all processes involved in U transport along a flow path: P indicates parent atoms, large asterisks are recoil from sites of decay of parent atoms in the aquifer minerals.

aquifer solids with molar concentration p_R; then there is the input by desorption $i_{AD}k^i_{-1}$ of adsorbed nuclides of molar concentration i_{AD}; the input by production $f_i\lambda_P p_{AD}$ from sorbed parent atoms of molar concentration p_{AD}; input by production from decay of dissolved parent $\lambda_P p_W$ with molar concentration p_W; removal by precipitation $Q_i i_W$; removal by decay of radionuclide i in water, $\lambda_i i_W$; and removal by adsorption $k^i_1 i_W$. It is assumed that all parameters in equation (1.106) are constants and the equation is a model to describe concentrations in groundwater along a flow path.

The analytical solution of equation (1.106) for nuclide distribution along a flow path in this one-dimensional model can be very complex. This is why a few assumptions are made for each radionuclide considered in order

to gain some information [45]. For example, it is assumed that a constant concentration over a characteristic distance $\bar{x}_i$ is achieved

$$\bar{x}_i = \frac{v}{\lambda_i(1+K_i)+Q_i} \tag{1.107}$$

K_i being the ratio of atoms adsorbed to atoms in solution, i.e.

$$K_i = \frac{i_{AD}}{i_W} = \frac{k_1^i}{k_{-1}^i + \lambda_i} \tag{1.108}$$

Since uranium is a long-lived isotope, far beyond the distance $\bar{x}_i$ the advection term in equation (1.106) can be ignored. Besides it is expected that $\lambda_P p_R = \lambda_i i_R$ which means the radionuclides are expected to be in equilibrium. The dominant factors controlling groundwater concentrations for ^{238}U are weathering, adsorption and precipitation [34]. The equation becomes

$$(^{238}U)_W = (^{238}U)_{W0} e^{-x/\bar{x}_{238}} + \frac{b w_{238} (^{238}U)_R}{\lambda_{238}(1+K_{238})+Q_U}(1-e^{-x/\bar{x}_{238}}) \tag{1.109}$$

where $(^{238}U)_W$ is the groundwater ^{238}U activity concentration (so $(^{238}U)_{W0}$ is the initial concentration), and $(^{238}U)_R$ is the host rock activity concentration. But for example the extent of ^{238}U adsorption and precipitation vary according to the model assumptions, depending on which aspect one considers to be more relevant. To constrain the equation of time evolution data are needed too. In [46] it is reported that in groundwaters clusters around a concentration of $\sim$ 1 ppb U can be found. It is important to highlight that gathering data from different aquifer environments would be an important tool to study all these processes and making all the approximations done more reliable.

A complete picture of all these processes has to take into account uranium from a more physical point of view, i.e. studying its microscopic structure/behavior and how this is linked to its macroscopic properties. It still seems pretty unlikely though that the mechanisms for groundwater aquifer transport described so far may act as a trigger for seismic sources: there's still need to constrain uranium under pressure and temperature conditions appropriate for the inside of the Earth. This is why uranium itself and its structure are now going to be presented before studying it under these conditions.

1.6 Open issues and questions

The understanding of the physics of earthquake source is still incomplete, even though there has been a significant growth in this research field lately: we went from simple models to much more powerfully predictive ones that can describe quantitatively the physics involved during faulting. We can now simulate an extended fault zone and this implies that we understand an increasing amount of chemical and physical phenomena occurring.

We have already pointed out how it seems to us that the scheme in Figure 1.7 shows some lack in not considering any radioactive process that we now know for sure happen in the crust and in the mantle. Let us now look at Figure 1.11 from [47]: this scheme represents the spatial and temporal scales of the most important processes occurring in a fault structure as those described in the previous sections, and as can be found as well in [48]. The scales refer to the single phenomenon. *It is clearly visible that around and*

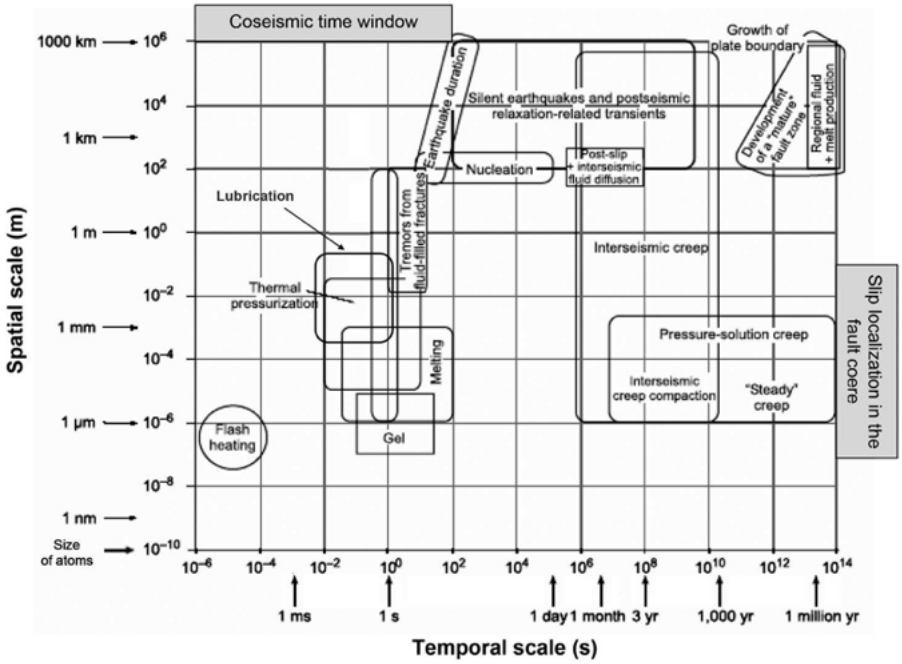

Figure 1.11: The scheme represents the most important processes occurring in a fault structure: on the x axis here is the temporal scale in s, while on the y axis the spatial scale of the mechanisms involved [47].

below the temporal scale of μs and spatial scale of Å *there is nothing reported.*

So either this region of time and space scale does not contribute to the physics phenomena involved, or it has just not been studied yet. This is where this work aims. The processes we will now illustrate involve regions of space filled with a certain number of uranium atoms: **we are going to study for the first time the behavior of such systems over a wide range of temperature and pressure typical of the mantle and the crust. These phenomena occur on space scales of** $\sim 10^{-1}$ Å **and on time scales of** $\sim 10^{-11} s \div 10^{-9}$ s which means that they can contribute to make this scheme even more complex: in fact most of these chemical and physical mechanisms occurring during an earthquake happen over the same spatial and/or temporal scale so that we can not find a non-interacting model for each of them.

Chapter 2

The physics of Uranium

Uranium element was first discovered in 1789 by German scientist Martin Klaproth and named after the planet Uranus. It took over a hundred years to find out by accident its radioactive properties by Antoine Henri Becquerel and it was only in the 1930's that the first artificial uranium nuclear fission were performed by Otto Hahn. It is a member of the heaviest naturally occurring elements [56] and has a number of unique properties [57] . It has received a lot of attention because of its nuclear properties but there are important issues related to uranium metal strongly determined by its electron distribution. It is considered a complex metal in which the f electrons participate in the bonding such as other actinide elements with $90 \leq Z \leq 94$: these metals have narrow-band $5f$ electrons with bandwidths of $1 - 3$ eV in comparison to transition metals with d bandwidths of $3 - 10$ eV. Uranium metal shows narrow-band $5f$ electrons near the Fermi level leading to a symmetry breaking mechanism that lowers the energy and results in an open low-symmetry ground-state structure. It also presents a complex phase diagram showing unusual properties at high and normal pressure conditions we will now describe.

2.1 Uranium properties

Metallic uranium in pure form is a solid silvery metal. It has a complex phase diagram: it crystallizes [58] in the face-centered (fcc) orthorhombic structure (α-U) with space group Cmcm below 935 K, above which, at ambient pressure, it transforms to the tethragonal β-phase (bct) and to the γ-phase (bcc cubic) above 1045 K [59]. To study its structure both theoretical and experimental investigations were made: there are early *ab*

initio calculations on uranium metal performed in e.g. [60], [61], [62], [63]; as well as more recents papers [64], [65], [66], [67], [68], and experimental works [71], [72], [73]. Uranium in nature has three isotopes ^{238}U, ^{235}U and ^{234}U in relative abundances (Figure 2.1). The isotope ^{238}U is the parent

Abundance (at%)		
Mass number	*Range*	*'Best' value*
234	0.0059–0.0050	0.005 ± 0.001
235	0.7202–0.7198	0.720 ± 0.001
238	99.2752–99.2739	99.275 ± 0.002

Figure 2.1: Natural abundance of uranium isotopes [56]

of the natural $4n + 2$ radioactive series and the isotope ^{235}U is the parent of the natural $4n + 3$ radioactive series: ^{235}U is also important because it undergoes fission with slow neutrons. In Figure 2.2 we can see the uranium series and the actinium series. Complete fission of ^{235}U gives rise to an energy

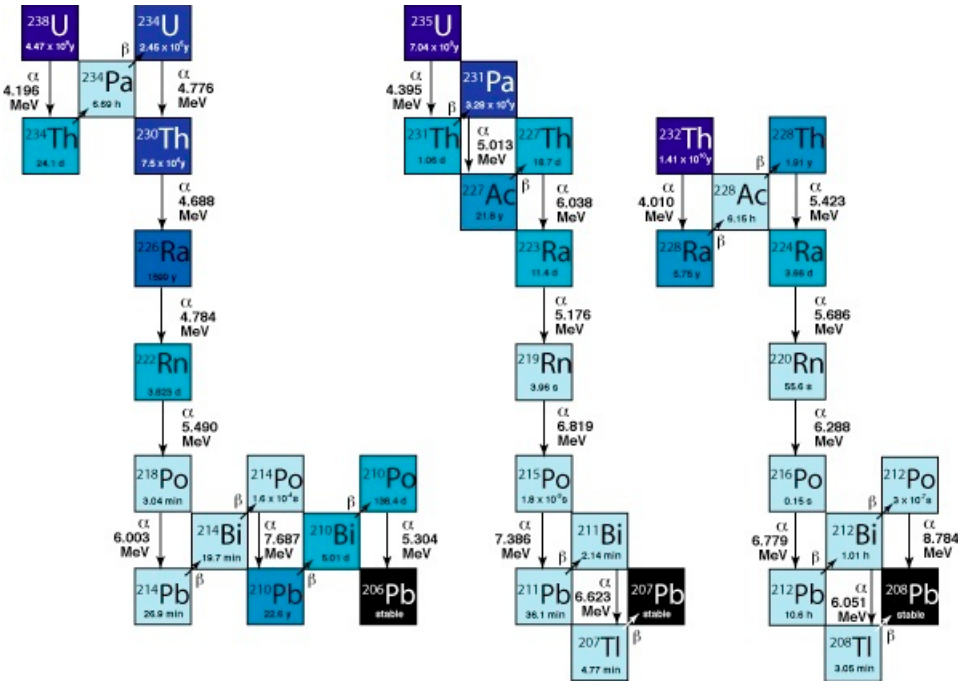

Figure 2.2: Uranium and actinium series

equivalent of about 200 MeV per fission. ^{238}U is a natural radioactive element with a mean life time of about 4.5 Gy. Uranium can be used in nuclear reactors to generate neutrons: ^{235}U is fissioned creating fission products and a neutron excess that can be captured by other natural isotopes to produce plutonium:

$$^{235}\mathsf{U} + n \rightarrow \mathsf{products} + \mathsf{energy} + 2.5n$$

$$^{238}\mathsf{U} + n \rightarrow \ ^{239}\mathsf{U}$$

$$^{239}\mathsf{U} \rightarrow \ ^{239}\mathsf{Np} \rightarrow \ ^{239}\mathsf{Pu}$$

About its chemical and physical properties in Figure 2.3 several properties are shown. Relevant to this work we notice that its mechanical properties are very sensitive to the pre-history of the sample and are strongly dependent on crystal orientation and heat treatment.

2.2 Uranium structure

Uranium has $Z = 92$ and its atomic weight is 238.0289 ± 0.0001 u [56]. There are mainly two different approaches to numerical modeling of crystal properties: Density Functional Theory and Classic Molecular Dynamics (MD) with which we're now able to calculate structural parameters, elastic moduli and chemical-mechanical properties. The former approach is a first-principle calculation and is quantum mechanics based, whereas the latter uses a classical approach to describe the interatomic potential. Both will be explained in more details in the next chapter. Thanks to the late success of both experimental and theoretical works for uranium, it is now possible to use classical interatomic potential to compute and foresee dynamical behavior with molecular dynamics simulation softwares. MD simulation is a reliable method to gain some knowledge about many metals at non-zero temperature. The reliability of such calculation is related to its capability of reproducing existing data. This is why a few interatomic potentials have been developed. Despite electronic structure calculation being successful in describing uranium complex structure, there also have been a few obstacles in performing elastic constant calculations and in reproducing β-U structure: the former being very model-dependent and the latter having 30 atom per unit cell. In fact full-potential calculations can reproduce most of the mechanical properties of uranium crystal in the orthorhombic structure but

melting point	(1408 ± 2) K
vapor pressure	
1720–2340 K	$\log p(\text{atm}) = -(26210 \pm 270)\, T^{-1}$
(Pattoret *et al.*, 1964)	$+ (5.920 \pm 0.135)$
1480–2420 K	$\log p(\text{atm}) = -(25230 \pm 370)\, T^{1}$
(Ackerman and Rauh, 1969)	$+ (5.71 \pm 0.17)$
X-ray density (α-uranium)	19.04 g cm^{-3}
(Lander and Müller, 1970)	
enthalpy of sublimation	
$\Delta_f H^\circ$(U, g, 298.15 K)	(533 ± 8) kJ mol^{-1}[a]
enthalpy	
$H^\circ(298.15\text{ K}) - H^\circ(0\text{ K})$	6364 J mol^{-1}
entropy	
S°(298.15 K)	(50.20 ± 0.20) J K^{-1} mol^{-1}[a]
heat capacity	
C_p°(298.15 K)	(27.669 ± 0.050) J K^{-1} mol^{-1}
transformation points	
α to β	(942 ± 2) K
β to γ	(1049 ± 2) K
enthalpies of transformation	
$\Delta_{trs}H$ (α to β)	2791 J mol^{-1}
$\Delta_{trs}H$ (β to γ)	4757 J mol^{-1}
$\Delta_{fus}H$ (γ to liq)	9142 J mol^{-1}
enthalpy and specific heat functions	
α-uranium (298–942 K)	$H_T - H_{298} = 26.920T - 1.251 \times 10^{-3}T^2 + 8.852 \times 10^{-6}T^3 + 0.7699 \times 10^5 T^{-1} - 8407.828$ (J mol^{-1}) $C_p = 26.920 - 2.502 \times 10^{-3}T + 26.556 \times 10^{-6}T^2 - 0.7699 \times 10^5 T^{-2}$ (J K^{-1} mol^{-1})
β-uranium (942–1049 K)	$H_T - H_{298} = 42.920T - 14326.020$ (J mol^{-1}) $C_p = 42.92$(J K^{-1} mol^{-1})
γ-uranium (1049–1408 K)	$H_T - H_{298} = 38.280T - 4698.690$ (J mol^{-1}) $C_p = 38.28$ (J K^{-1} mol^{-1})
uranium (liquid)	$H_T - H_{298} = 48.650T - 10137.120$ (J mol^{-1}) $C_p = 48.65$ (J K^{-1} mol^{-1})
thermal conductivity at 298.15 K (Ho *et al.*, 1972)	27.5 J m^{-1} s^{-1} K^{-1}
electrical resistivity (300 K) (Arajs and Colvin, 1964)	28×10^{-8} Ω m

[a] CODATA key value (Cox *et al.*, 1989).

Figure 2.3: Physical and chemical properties of uranium [56]

they're not powerful enough to perform more complex calculations that are computationally expensive.

Uranium metal has three allotropes solid structure, namely α-U, β-U and γ-U. The α phase has a face-centered fcc orthorhombic structure with four atoms in the unit cell, A20 *Strukturbericht* designation, space group 63 Cmcm and is shown in Figure 2.4 and Figure 2.5. It is stable up to 935 K [74]. The structure consists of corrugated sheets of atoms parallel to the ac-plane and perpendicular to the b-axis. a, b, c are the unit cell parameters and y is the so-called "position parameter": it is related to the degree of corrugation (y=0 corresponds to no-corrugation). Their experimental values

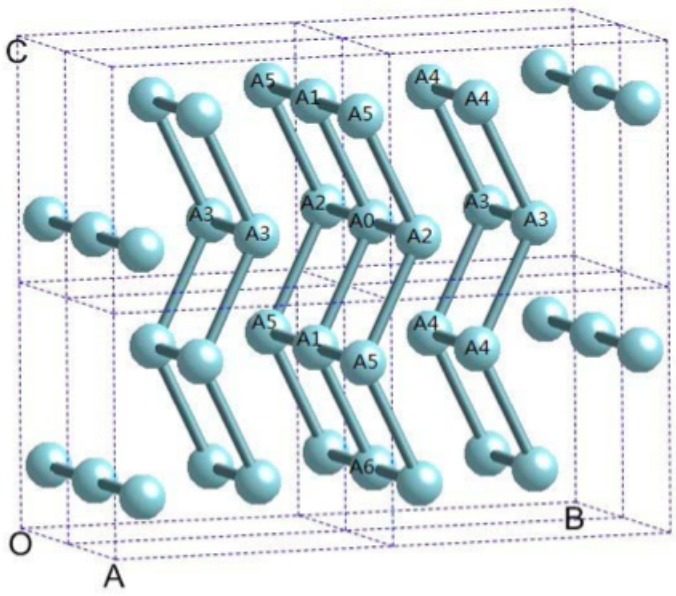

Figure 2.4: α-U structure in a 2x2x2 supercell. OA is the $\hat{x}$-direction, OB the $\hat{y}$-direction and OC the $\hat{z}$-direction. Atoms are labelled according to their distances as calculated in the text.

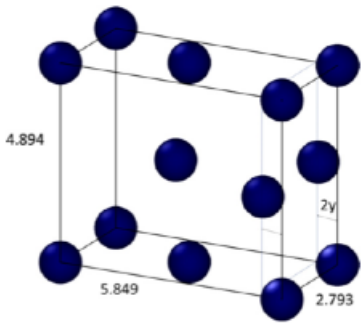

Figure 2.5: Lattice parameters of α-U: a, b, c, y in Å, as explained in the text

at room temperature [58] are: $a = 2.853$ Å, $b = 5.869$ Å, $c = 4.954$ Å, $y = 0.102$ Å. The neighbor-distance among the first six atoms are calculated

as the following [75]:

$$d_1 = \frac{1}{2}\sqrt{(4yb)^2 + c^2} \tag{2.1}$$

$$d_2 = a \tag{2.2}$$

$$d_3 = \frac{1}{2}\sqrt{a^2 + b^2} \tag{2.3}$$

$$d_4 = \frac{1}{2}\sqrt{a^2 + (1-4y)^2 + c^2} \tag{2.4}$$

$$d_5 = \sqrt{a^2 + 4y^2b^2 + c^2/4} \tag{2.5}$$

$$d_6 = c \tag{2.6}$$

The β-phase of uranium has a tetragonal structure with 30 atoms in the unit cell, $D8_b$ *Strukturbericht* designation, $P4_2/mnm$ space group as shown in Figure 2.6. It is stable in a narrow range of temperature between $935-1045$

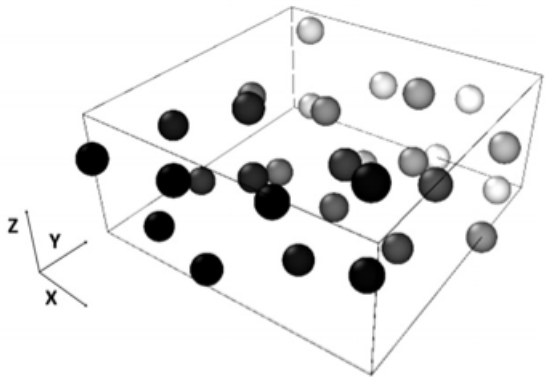

Figure 2.6: β-uranium structure unit cell

K [76] and up to 3 GPa [72]. The experimental values of lattice constants are [77]: $a = 10.759$ Å, $c = 5.653$ Å. Since this structure is very complex, it is very computationally expensive to analyze so it is often approximated with a body-centered tetragonal (bct) structure instead [78]: this structure has 2 atoms per unit cell. A comparison of the energy per atom [67] of the bct and the β-phase shows that the latter is more energetically favored but the values are very close one to each other: $E_{bct} = -11.1489$ eV/atom and $E_\beta = -11.1867$ eV/atom. γ-U has a body centered cubic structure (bcc) stable between 1045 K up to the melting point 1406 K [74]. The experimental value of the lattice parameter is [79]: $a = 3.47$ Å. Experimental investigation

of this phase is hard due to the low temperature mechanical instability. In Table 2.1 we report a comparison of the internal parameters of α-uranium among different (recent to the present date) calculation approaches: DFT theory [67], classic MD calculation [80] and experimental values [58].

	Beeler et al. [67]	Yangzhong et al. [80]	Experimental [58]
a	2.793	2.778	2.836
b	5.849	6.152	5.867
c	4.894	4.797	4.936

Table 2.1: The internal parameters in Å for α-uranium: comparison with a density functional theory framework employing Perdew generalized gradient approximation PBE-GGA [67], a COMB moleculars dynamic simulation [80] and experimental values [58].

2.3 Elastic moduli

In Chapter 1 we introduced elastic constants for a solid system relating stress to strain. They can be defined for example as

$$C_{ij} = \frac{1}{V_0}\left(\frac{\partial^2 E}{\partial e_i \partial e_j}\right) \tag{2.7}$$

where E is the energy of the crystal, V_0 is the equilibrium volume and e_i is the strain. For an orthorhombic crystal there are only nine independent constants: C_{11}, C_{12}, C_{13}, C_{22}, C_{23}, C_{33}, C_{44}, C_{55}, C_{66}. Thanks to necessary and sufficient elastic stability conditions [81], representing the fact that when a solid is deformed its internal energy will increase so that when the force is removed the system will try and return to its initial condition, it is possible to set a few elastic stability criteria according to the crystal symmetry. For example for an orthorhombic crystal this criteria come into ten equations

$$C_{ii} > 0 \tag{2.8}$$
$$C_{11}C_{22} - C_{12}^2 > 0 \tag{2.9}$$
$$C_{22}C_{33} - C_{23}^2 > 0 \tag{2.10}$$
$$C_{11}C_{33} - C_{13}^2 > 0 \tag{2.11}$$
$$C_{11}C_{22}C_{33} + 2C_{12}C_{23}C_{13} - C_{11}C_{23}^2 - C_{22}C_{13}^2 - C_{33}C_{12}^2 > 0 \tag{2.12}$$

with $i = 1, \ldots, 6$. We can see in Figure 2.7 the matrix expression of the constants. These equations reduce to the three Born stability criteria for

$$\boldsymbol{C}_{\text{ortho}} = \begin{pmatrix} C_{11} & C_{12} & C_{13} & & & \\ . & C_{22} & C_{23} & & & \\ . & . & C_{33} & & & \\ & & & C_{44} & & \\ & & & & C_{55} & \\ & & & & & C_{66} \end{pmatrix}$$

Figure 2.7: Elastic matrix with independent elastic constants for an orthorhombic crystal

cubic system.

$$C_{11} + 2C_{12} > 0 \tag{2.13}$$
$$C_{11} - C_{12} > 0 \tag{2.14}$$
$$C_{44} > 0 \tag{2.15}$$

In Figure 2.8 we can see the elastic matrix for a cubic system. As for the

$$\boldsymbol{C}_{\text{cubic}} = \begin{pmatrix} C_{11} & C_{12} & C_{12} & & & \\ . & C_{11} & C_{12} & & & \\ . & . & C_{11} & & & \\ & & & C_{44} & & \\ & & & & C_{44} & \\ & & & & & C_{44} \end{pmatrix}$$

Figure 2.8: Elastic matrix with independent elastic constants for a cubic crystal

case of lattice dimensions we want to report in Table 2.2 this constants for α-uranium to be compared with experimental values: in [82] all calculations are performed in an *ab initio* framework neglecting spin-orbit coupling; in [67] the projector augmented wave PAW method is used [83]; and in [80] a COMB potential in a MD simulation framework.

2.4 Equations of state for solids

A few important elastic properties of a solid can be found through its equation of state (EOS), which is a relationship connecting two or more variables describing the thermodynamic state of a system, like pressure P,

	Beeler *et al.* [67]	COMB [80]	Adak *et al.* [82]	Experiment [58]
C_{11}	299	257	230	214
C_{22}	231	222	196	198
C_{33}	364	298	312	267
C_{12}	59	99	70	46
C_{23}	144	66	134	107
C_{13}	30	45	38	21
C_{44}	100	99	130	124
C_{55}	150	61	93	73
C_{66}	132	89	82	74
B_0	151	133	133	135.5

Table 2.2: Comparison of the elastic constants and bulk modulus B_0 for α-uranium obtained in different works. All units are in GPa.

temperature T and density ρ. It is possible to extract the EOS parameters fitting experimental or simulated data. For ideal gases the best known EOS states

$$PV = nRT \tag{2.16}$$

where n is the number of moles and R is the ideal gas constant [85]. When it comes to solid state physics though we can extrapolate many extra information we might be interested in. In the case of a compositional Earth model we come to face density and elastic moduli values inferred from the inversion of seismic waves travel times and velocities at different pressures: this is why we need to compare these values with those of the minerals composing the Earth's interior. This is why we need to study EOSs for solid systems which will allow to gain important physical information: the energy and volume per atom, the bulk modulus and its first derivative with respect to the volume. In the case of solids though the effect of temperature is much less than for gases, this is why only isothermal EOSs will be introduced here [86]. The simplest equation of state we can build up is given by the definition of *bulk modulus* we already gave in Chapter 1, i.e.

$$B = -\frac{dP}{d\ln V} = \frac{dP}{d\ln \rho} \tag{2.17}$$

where $\rho = m/V$. Let's solve this separable differential equation with $K = K_0$ (which means we're considering the linear elasticity regime when the bulk modulus is constant) and initial pressure $P_0 = 0$

$$\int_{V_0}^{V} K_0 \frac{dV'}{V'} = -\int_0^P dP' \tag{2.18}$$

$$V = V_0 e^{-\frac{P}{K_0}} \tag{2.19}$$

We're considering here the case of a system that is initially unstressed that undergoes some infinitesimal strains due to pressure application, so we cannot use this equation for high pressure, since the bulk modulus increases with increasing pressure: as we study seismic waves propagating through media inside the Earth we must take into account ΔP, since the finite strain applied will modify the elastic moduli of the medium.

2.4.1 Murnaghan equation of state

So let's now consider a pressure P causing infinitesimal strains applied to a solid that is already compressed to a finite strain by the pressure P_0. Recalling equation (1.23) that relates Lamé constant, the shear modulus μ and the dilatation θ Murnaghan showed [87] that the bulk modulus can be written as

$$B = \lambda + \frac{2}{3}\mu + \frac{1}{3}P_0 \tag{2.20}$$

where λ and μ depend on the initial pressure as $\lambda(P)|_{P_0} = \lambda_0$ and $\mu(P)|_{P_0} = \mu_0$. Assuming that λ and μ are linear function of P_0 so that also B is linear in P_0 we can write the bulk modulus as

$$B = \frac{1}{3}(3\lambda_0 + 2\mu_0) + kP_0 \tag{2.21}$$

where k is a constant. Using equation (2.17)

$$d\ln\rho = \frac{dP}{B_0 + kP_0} \tag{2.22}$$

where $B_0 = \frac{1}{3}(3\lambda_0 + 2\mu_0)$. Since P_0 is arbitrary we can get the following integration

$$\int d\ln\rho = \int \frac{dP}{B_0 + kP} \tag{2.23}$$

$$\ln\left(\frac{\rho}{\rho_0}\right) = \frac{1}{k}\ln\left(\frac{B_0 + kP}{B_0}\right) \tag{2.24}$$

$$P = \frac{B_0}{k}\left[\left(\frac{\rho}{\rho_0}\right)^k - 1\right] \tag{2.25}$$

Assuming that the dependance of B on P_0 is the same as that of B_0 on pressure about $P = 0$, which means we assimilate $k \sim B_0^{'} = dB/dP|_{P=0}$ so that equation (2.21) becomes $B \sim B_0 + B_0^{'}P$, equation (2.25) can be written as

$$P = \frac{B_0}{B_0^{'}}\left[\left(\frac{\rho}{\rho_0}\right)^{K_0^{'}} - 1\right] \tag{2.26}$$

which is known as *Murnaghan Equation of State* [88].

2.4.2 Finite strain and Birch-Murnaghan equation of state

Nevertheless, in order to introduce a more complex form of this last result, i.e. the so-called Birch-Murnaghan equation of state, we need to first get some background about finite strain. Recall that if in a solid system we consider two points P of coordinates x_i and Q of coordinates $x_i + dx_i$ that undergo a displacement u, causing $P(x_i) \rightarrow P^{'}(x_i + u_i)$ and $Q(x_i + dx_i) \rightarrow Q^{'}(x_i + dx_i + u_i + du_i)$, it means strain is applied, see Figure 2.9. The distance

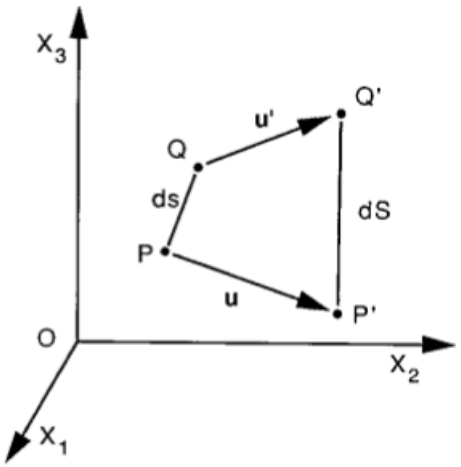

Figure 2.9: Displacement of points P and Q in a solid due to strain.

between PQ, namely $ds^2 = \sum_i dx_i^2$, will be different than that between $P^{'}Q^{'}$, i.e. $dS^2 = \sum_i dX_i^2$ where $X_i = x_i + u_i$ since it is not a rigid-body translation. Writing $du_i = \sum_j \frac{du_i}{dX_j} dX_j$ we get

$$dS^2 - ds^2 = 2e_{ij}dX_i dX_j \tag{2.27}$$

e_{ij} being the usual strain tensor. If we now consider isotropic compressional strain due to hydrostatic pressure

$$\frac{\partial u_1}{\partial X_1} = \frac{\partial u_2}{\partial X_2} = \frac{\partial u_3}{\partial X_3} = \frac{\theta}{3} \tag{2.28}$$

and we can write $\theta = \sum_i \partial u_i/\partial x_i$ and get

$$e_{ij} = e\delta_{ij} \tag{2.29}$$

where

$$e = \frac{\theta}{3} - \frac{1}{18}\theta^2 \tag{2.30}$$

Let's consider an infinitesimal cube of strained volume $(dX_1)^3$ that originally had a volume in the unstrained state $V_0 = \left[dX_1\left(1 - \frac{\partial u_1}{\partial X_1}\right)\right]^3$ then the ratio V_0/V becomes

$$\frac{V_0}{V} = \frac{\left[dX_1\left(1 - \frac{\partial u_1}{\partial X_1}\right)\right]^3}{(dX_1)^3} = \left(1 - \frac{\theta}{3}\right)^3 \tag{2.31}$$

Now

$$\begin{aligned} \frac{V_0}{V} = &\frac{\rho}{\rho_0} = \left[\left(1 - \frac{\theta}{3}\right)^2\right]^{3/2} = \left(1 + \frac{\theta^2}{9} - 2\frac{\theta}{3}\right)^{3/2} = \\ &= \left[1 - 2\left(\frac{\theta}{3} - \frac{\theta^2}{18}\right)\right]^{3/2} = (1 - 2e)^{3/2} \end{aligned} \tag{2.32}$$

We can define compression f to be the same as dilation e with opposite sign and the last equation becomes

$$\frac{V_0}{V} = \frac{\rho}{\rho_0} = (1 + 2f)^{3/2} \tag{2.33}$$

which for an infinitesimal strain becomes

$$\frac{V_0}{V} = \frac{\rho}{\rho_0} = (1 + 2f)^{3/2} = \left(1 - \frac{\theta}{3}\right)^3 \sim 1 - \theta \tag{2.34}$$

Let's now introduce the isothermal bulk modulus for $P = 0$ indicated as $B|_{P=0,T} = B_{0,T}$

$$B_{0,T} = -\lim_{P\to 0} \frac{PV}{\Delta V} = -\lim_{P\to 0} \frac{P}{\theta} \tag{2.35}$$

because $\theta = \Delta V/V_0$. Now using the function of state F, namely Helmholtz free energy defined as $dF = -SdT - pdV$ where S is the entropy, we can write for an isothermal transformation $P = -(\partial F/\partial V)_T$ so that equation (2.35) becomes

$$B_{0,T} = \lim_{P\to 0} \frac{1}{\theta} \frac{\partial F}{\partial V} \tag{2.36}$$

Now to the first order we have

$$V \sim V_0(1 - 3f) \tag{2.37}$$

and $dV \sim -3V_0 df$; and always to the first order

$$f = -e \sim -\frac{\theta}{3} \tag{2.38}$$

So equation (2.35) becomes

$$B_{0,T} = \lim_{P\to 0} \frac{1}{9V_0} \frac{1}{f} \frac{\partial F}{\partial f} \tag{2.39}$$

Let's now expand the free energy F in powers of f, recalling that elastic strain energy is quadratic for infinitesimal strains (and taking the energy of the unstrained state as zero)

$$F \sim a(T)f^2 + b(T)f^3 + c(T)f^4 + \dots \tag{2.40}$$

where we are expanding in power of

$$f = \frac{1}{2}\left[\left(\frac{V_0}{V}\right)^{2/3} - 1\right] \tag{2.41}$$

To derive the second-order Birch-Murnaghan equation of state let's now consider the expansion (2.42) up to the second order

$$F = a(T)f^2 + \mathcal{O}(f^3) \tag{2.42}$$

where using (2.39) we recognize that $a = \frac{9}{2}K_{0,T}V_0$. Now let's get equation (2.34) and differentiate it

$$dV = -3V_0(1+2f)^{-5/2} \tag{2.43}$$

so that it is possible to write

$$\frac{df}{dV} = -\frac{1}{3V_0}(1+2f)^{5/2} \tag{2.44}$$

and recalling that

$$P = -\left(\frac{\partial F}{\partial V}\right)_T = -\left(\frac{\partial F}{\partial f}\right)_T \frac{df}{dV} \tag{2.45}$$

we have

$$P = 3B_{0,T} f(1+2f)^{5/2} \tag{2.46}$$

Now using (2.41) to be inserted in (2.46) we obtain the *second order Birch-Murnaghan equation fo state*

$$P = \frac{3B_{0,T}}{2}\left[\left(\frac{\rho}{\rho_0}\right)^{7/3} - \left(\frac{\rho}{\rho_0}\right)^{5/3}\right] \tag{2.47}$$

And the bulk modulus will then be

$$B = -V\frac{dP}{dV} = \frac{\rho}{\rho_0}\frac{dP}{d(\rho/\rho_0)} = \frac{B_{0,T}}{2}\left[7\left(\frac{\rho}{\rho_0}\right)^{7/3} - 5\left(\frac{\rho}{\rho_0}\right)^{5/3}\right] \tag{2.48}$$

or in terms of f

$$\begin{aligned} B =& \frac{B_{0,T}}{2}\left[7\left((1+2f)^{3/2}\right)^{7/3} - 5\left((1+2f^{3/2})\right)^{5/3}\right] = \\ &= B_{0,T}(1+2f)^{5/2}(1+7f) \end{aligned} \tag{2.49}$$

It is possible to go on with the calculation to a higher order in the expansion of F up to the third order, getting

$$P = 3B_{0,T} f(1+2f)^{5/2}\left(1 + \frac{3bf}{2a}\right) \tag{2.50}$$

and then setting appropriate boundary conditions expressed through the coefficients a and b yields to the *third order Birch-Murnaghan equation of state*

$$P(\rho/\rho_0) = \frac{3B_{0,T}}{2}\left[\left(\frac{\rho}{\rho_0}\right)^{7/3} - \left(\frac{\rho}{\rho_0}\right)^{5/3}\right]\left[1 + \frac{3}{4}(B_0^{'} - 4)\left(\left(\frac{\rho}{\rho_0}\right)^{2/3} - 1\right)\right] \tag{2.51}$$

Connecting the energy to the pressure it is possible to obtain the same equation but for $E(V)$ [89], e.g.

$$E = E_0 + \frac{9B_0V_0}{2}\left[\frac{1}{2}\left[\left(\frac{V_0}{V}\right)^{2/3} - 1\right]^2\right]\left[1 + (B_0^{'} - 4)\left(\frac{1}{2}\left[\left(\frac{V_0}{V}\right)^{2/3} - 1\right]\right)\right] \tag{2.52}$$

It must be said that these equations are empirical ones. There are other possibilities like [90], [91] in agreement with one other. Birch-Murnaghan is derived from strain theory and has shown [92] very good agreement in describing the compressional behavior of solids at high pressure, even though not for all existing measurements of elastic moduli: it is numerically stable and shows good agreement with experimental data. This is why we choose to use it to first fit existing data which we will now show and then to fit the obtained with MD simulations, which will be explained in the next chapter.

2.5 Fit of EOS parameters from existing data

The first step of our analysis is to fit existing data from the curve $E(V)$ to test the reliability of the third order Birch-Murnaghan equation of state. From the relationship (2.52) the information we're able to get are

1. the bulk modulus B_0
2. the unit cell volume per atom V_0
3. the equilibrium energy per atom E_0
4. the first pressure derivative of the bulk modulus $B_0^{'}$

To perform the fit of these quantities we therefore used the data of $E(V)$ taken from [82]. In [82] all calculations performed were static at 0 K, up to $\sim$ 100 GPa, neglecting spin-orbit coupling for an α-U. Our fit was done with Mathematica [93] and is reported in Figure 2.10. The parameters of the fit are reported in Table 2.3 together with those found in [82] and two

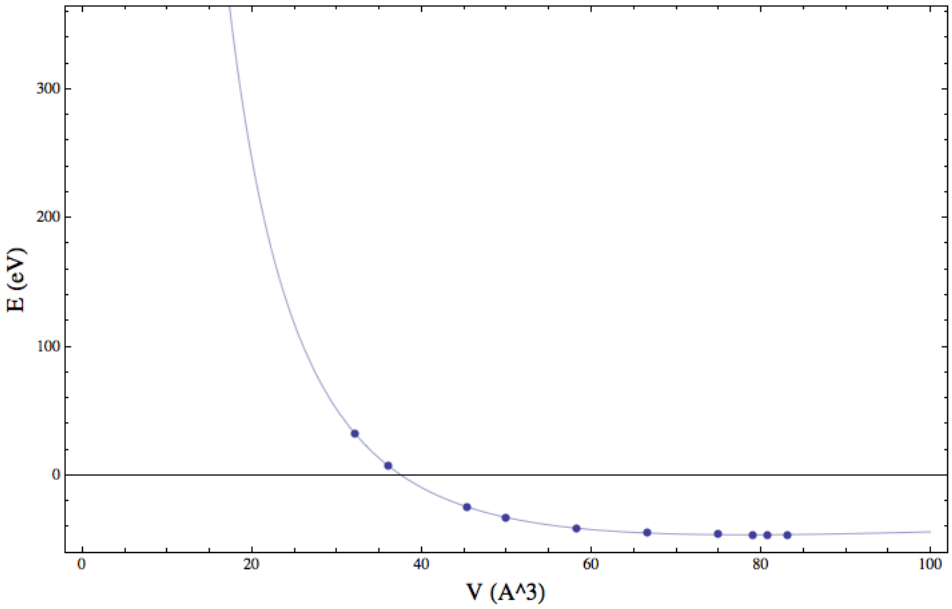

Figure 2.10: E(V) data (points) from [82] with fit curve as in eq. (2.52). Units are: eV for energy and $Å^3$ for the volume.

experimental values [72] and [73]. As we can see our calculated value for the bulk modulus is $B_0 = 95$ GPa as obtained from the fit of the $E(V)$ curve with a standard error of 16.6. No error is available from the data so Mathematica [93] gives a standard error as the standard deviation divided by the square root of the sample size. We notice that our value is in agreement with the experimental values reported in [72], [73] and [94]: it shows a $\sim 20\%$ difference from the value of [72], a $\sim 10\%$ difference from [73] and less than a $\sim 10\%$ from [94]. The difference though between our fit parameter B_0 and Adak *et al.* [82] from which the data are taken is $\sim 30\%$, and we notice the latter value is almost $\sim 30\%$ higher than the experimental one found in [73]. Comparing the energy/atom and the volume/atom between our fit and Adak *et al.* [82] we find very good agreement, both lying within the range reported in literature [58]-[98]. As for the pressure derivative of the bulk modulus $B_0^{'}$ it is also within the range reported in literature and $\sim 10\%$ distant from [82].

	Fit	St. Error	Adak *et al.* [82]	Experiment [72]	[73]
E_0 (eV)	-11.566	0.049	-11.576	-	-
V_0 (Å^3)	19.50	0.45	20.19	24.33	-
B_0 (GPa)	95.0	16.6	135.5	113.3	104
$B_0^{'}$	4.35	0.23	4.97	3.37	6.2

Table 2.3: Comparison of the EoS parameters as obtained from the fit of the energy-volume data taken from [82]. The last two columns are experimental values.

Chapter 3

Molecular dynamics simulation

Describing accurately the electronic ground state of actinide metals is challenging: uranium under ambient conditions shows a complex orthorhombic structure with four atoms per unit cell, as a consequence of its itinerant $5f$ electrons. Its basic elastic properties and phase stability have been studied experimentally using ultrasound techniques e.g. [73], [72], [95], [96] and theoretically [67], [68], [80], [82], [97] with molecular dynamics (MD) simulations. MD simulations can have a quantum mechanics based approach, namely Density Functional Theory (DFT) through first principle calculations or a classical approach where the most important issue is the choice of the potential one uses. It is highly desirable to develop a classical interatomic potential for MD simulations in order to compare the results from *ab initio* calculations with an effective method capable of characterizing atomic dynamics even at non-zero temperature. After briefly reviewing the basic concepts of DFT theory and those of classical MD, a sketch of the simulations we have run together with the problem of the choice of the most reliable potential will be presented in details.

3.1 Density functional theory

Studying a solid system means one is dealing with a many body problem: if there are N nuclei there are N + ZN interacting particles so we shall develop some methods that can be applied to study the structure of many-electron atoms. The starting point is the description of the exact Hamiltonian of the problem:

$$
\begin{aligned}
H = & \sum_i \left(-\frac{\hbar^2}{2m}\nabla_{r_i}^2 - \frac{\hbar^2}{2M}\nabla_{R_i}^2 \right) - \frac{1}{4\pi\epsilon_0}\sum_{i,j}\frac{e^2 Z_i}{|\mathbf{R}_i - \mathbf{r}_j|} \\
& + \frac{1}{8\pi\epsilon_0}\sum_{i\neq j}\frac{e^2}{|\mathbf{r}_i - \mathbf{r}_j|} + \frac{1}{8\pi\epsilon_0}\sum_{i\neq j}\frac{e^2 Z_i Z_j}{|\mathbf{R}_i - \mathbf{R}_j|}
\end{aligned}
\tag{3.1}
$$

where the first two terms represent the kinetic terms for the electrons (of mass m and vector position $\mathbf{r}_i$) and the nuclei (of mass M and vector position $\mathbf{R}_i$), the last three terms are respectively the Coulomb interaction between nuclei and electrons, electrons-electrons and nuclei-nuclei [99]. Solving Schrödinger's equation for the Hamiltonian (3.1) would be overwhelming, and it would be even more considering that we are already neglecting spin-orbit interactions, relativistic effects, radiative corrections, spin-spin interaction and nuclear corrections. So some approximations are in order.

The first one is the *Born-Oppenheimer* approximation: considering that the ratio m/M is in the range 10^{-3} to 10^{-5} while the forces to which the electrons and the nuclei are submitted are of comparable magnitude, the motion of the nuclei is much slower than that of electrons. So the electronic and nuclear motions can be treated independently and the nuclei are considered fixed as we determine the electronic states. The problem is extremely simplified because now the kinetic term for the nuclei in (3.1) vanishes and the last one becomes constant. We are left with NZ interacting electrons moving in the external potential of the nuclei: the Hamiltonian is now made up of a kinetic term for the electrons, the potential energy due to electron-electron interactions and the potential energy of the electron in the external potential of nuclei $H = T + V + V_{ext}$. This problem is still too complicated to be solved directly. There are several powerful methods in literature used to treat this problem, such as Hartree-Fock, or Density Functional Theory which is the one we're going to describe.

Density Functional Theory is based upon the results of Hohenberg and Kohn [100]-[101] and it is a successful approach to finding the solutions of the time-independent Schrödinger equation

$$
H\psi = E\psi \tag{3.2}
$$

where H is the Hamiltonian operator, $\psi(\mathbf{r}_1 \dots \mathbf{r}_N)$ is a set of eigenstate (the electronic wave function) function of the spatial coordinates of each of the NZ electrons, and E is a set of eigenvalues associated. Even though it is possible to approximate $\psi(\mathbf{r}_1 \dots \mathbf{r}_N)$ as the product of the individual wave

functions $\psi = \psi(\mathbf{r}_1)\ldots\psi(\mathbf{r}_N)$ (the so-called *Hartree product*) the problem is still overwhelming since there are $3N$ variables. So it is possible to introduce the *density of electrons at a particular position in space*

$$n(\mathbf{r}) = 2\sum_i \psi_i^*(\mathbf{r})\psi_i(\mathbf{r}) \tag{3.3}$$

representing the sum of probability that an electron with wave function $\psi_i(\mathbf{r})$ is located at position $\mathbf{r}$. The asterisk represents a complex conjugate term and the 2 factor appears to take the spin into account because of Pauli exclusion principle. This new quantity is a function of only 3 variables since we do not care which electron is where. Two important theorems, due to Hohenberg and Kohn, come in handy now.

Theorem 3.1.1 (First theorem)**.**
There is a one-to-one correspondance between the ground state density $n(\boldsymbol{r})$ of a many electron system and the external potential V_{ext}. The ground state expectation value of any observable $\mathcal{O}$ is a unique functional of the exact ground state electron density

$$\langle\psi|\mathcal{O}|\psi\rangle = \mathcal{O}[n] \tag{3.4}$$

The theorem states that the ground state energy of Schrödinger's equation is a unique functional of the electron density. This means we could possibly find the ground state energy by finding the appropriate functional.

Theorem 3.1.2 (Second theorem)**.**
For $\mathcal{O}$ being the Hamiltonian H, the ground state total energy functional has the form

$$H[n] \equiv E[n] = \langle\psi|T + V|\psi\rangle + \langle\psi|V_{ext}|\psi\rangle \tag{3.5}$$

where the first term is a universal functional for any many-electron system and the second one reaches its minimal value (corresponding to the ground state total energy) for the ground state density corresponding to the right potential describing the system.

The second theorem states that the electron density minimizing the energy of the overall functional is the true electron density corresponding to the full solution of the Schrödinger's equation. So if the true functional form were known, we could use the variational principle of Rayleigh-Ritz to vary the electron density until the energy from the functional is minimized. In terms of a single electron wave function $\psi_i(\mathbf{r})$ the energy functional would be

$$E[\psi_i] = E_{known}[\psi_i] + E_{XC}[\psi_i] \tag{3.6}$$

where the known contributions correspond to the kinetic term, the Coulomb interactions between electrons-nuclei, electrons-electrons, nuclei-nuclei in the Hamiltonian H, whereas E_{XC} is the exchange correlation functional to include all the quantum mechanics effects. Kohn and Sham also showed that to find the electron density it is necessary to solve a set of equations for the single-electron wave functions

$$\left(-\frac{\hbar^2}{2m}\nabla_i^2 + \frac{1}{8\pi\epsilon_0}\int\frac{e^2\rho(\mathbf{r}')}{|\mathbf{r}-\mathbf{r}'|} + V_{XC} + V_H\right)\psi_i(\mathbf{r}) = \epsilon_i\psi_i(\mathbf{r}) \tag{3.7}$$

There is no summation here involved. The term V_H is the Coulomb repulsion between the electron considered in one of the Kohn-Sham equations and the total density defined by all electrons in the problem. The exchange correlation potential is the functional derivative $V_{XC} = \delta E_{XC}/\delta n$. Both these terms depend on density which in turn depends on the wave functions we're searching for. This is a self-consistent problem: we first have to define a trial electron density $n(\mathbf{r})$, then solve Khan-Sham equations to find single-particle wave functions $\psi_i(\mathbf{r})$, calculate the electron density $n'(\mathbf{r})$ using the solutions just found, compare the two densities and if they are the same that is the ground state electron density and can be used to compute the total energy otherwise we would just start up again. The problem about this technique is that the form of the exchange correlation functional is simply not known: the theorem seen above only guarantees its existance. And so we are forced to use some kind of approximation.

Approximations. One of the main areas of active research involves the development of functionals that more faithfully represent the problem we're studying. In fact there are a few numbers of functionals that have been found to give good results in a variety of physical contexts and for this reason are very used. Here are some of these.

- **Local Density Approximation (LDA)**. In the Local Density Approximation the exchange-correlation potential at each position is set to be the known exchange-correlation potential from a uniform electron gas at the electron density observed at that position. In other words, the exchange-correlation energy due to a particular density could be found by dividing the physical system under study in infinitesimally small volumes with constant density: and each volume contributes to

the total exchange correlation energy by an amount equal to the contribution of a homogeneous electron gas with the same volume. This approach works fine for all those materials showing slowly varying density.

- **Generalized Gradient Approximation (GGA)**. To include some more physical information, it is possible to also make the exchange-correlation contribution depend on the density of the neighboring volumes. The gradient of the electron density can be included. Two of the most widely used functionals for solid state physics are the Perdew-Wang functional (PW91) [102] and the Perdew-Burke-Ernzerhof functional (PBE) [103].

To solve the time-independent Schrödinger equations set of the type (3.7) in the LDA, GGA or any other approximation, the exchange-correlation operator is treated approximately. The ψ_i are single particle orbitals. In order to get to know these functions we need to find some coefficients with which we can express them in terms of a given basis set

$$\psi_i(\mathbf{r}) = \sum_\alpha c_{i\alpha}\phi_\alpha(\mathbf{r}) \tag{3.8}$$

The wave functions live in a function space of infinite dimension, but since we need a limited basis to describe the ψ_i the aim of the theory is to find a basis that can generate functions close the real ψ_i. A good choice of basis set has to be kept as simple as possible and in the lowest possible dimension, for the programming to stay easy. This stimulated a lot of literature like the *Pseudopotential method*, the *Augmented Plane Wave*, or the *Linearized Augmented Plane wave* that can be found e.g. in [104], [105], [106], [107].

What we can calculate. DFT theory showed throughout its history to be powerfully successful in calculating and forsee a lot of issues. For example it is possible to calculate the total energy of the ground state, which can be used to get structures, elastic moduli, adsorption energies, diffusion barriers etc. We can also find nuclei forces particularly easily with plane wave basis, properties at finite temperature and vibrational frequencies. It can compute magnetic properties using Local Spin Density Approximation. And the overall positive side is that we can calculate the properties of many-electron system from first principles, no empiric input is needed but still great accuracy is achieved.

However it must be kept in mind that DFT calculations are not exact solutions of Schrödinger equation so there is an intrinsic uncertainty between what we calculate with the DFT and the experimental values. This is why it is often necessary to phenomenologically compare DFT calculations with experimental data. Besides, DFT calculation is not as accurate in calculating electronic excited states as it is for ground state energies: in fact the theorems we cited above only apply to ground state energy. Another situation where it gives inaccurate results is associated with weak van der Waals attractions between atoms and molecules. And overall, DFT is computationally expensive and therefore it is limited to small length or time scales.

3.2 Molecular dynamics simulation

Molecular dynamics simulation (MD) is a method of studying the evolution of a set of atoms under conditions we can control [108]. It is especially useful when one comes to study high temperature and high pressure behavior of a physical system. An assembly of N particles is considered with their trajectories generated by numerical integration of Newton's equations of motion thanks to the definition of a *potential* describing the mutual interaction of the atoms and to some boundary conditions. In MD each particle is treated like a single classical particle. There is also a quantum mechanics based approach describing atoms and electrons and taking into account a wave function for the latter, and it is very well documented e.g. here [109]. We now want to focus on *classical molecular dynamics*.

If we have N particles moving in a volume V, their coordinates being $\mathbf{r}(t)$, we have a set of $3N$ coordinates and their velocities: namely $\mathbf{r}^{3N}(t)$ and $\dot{\mathbf{r}}^{3N}(t)$, with initial conditions specified to be $\mathbf{r}^{3N}(t_0)$ and $\dot{\mathbf{r}}^{3N}(t_0)$. The simulation proceeds through a series of discrete *time step*

$$\mathbf{r}^{3N}(t_0) \to \mathbf{r}^{3N}(t_1) \to \cdots \to \mathbf{r}^{3N}(t_L) \tag{3.9}$$

with $t_k = t_0 + k\Delta t$, $k = (1, 2, \ldots, L)$, and Δt is the time step and L is the number of steps. The total energy of the system is given by a kinetic term and a potential one, the former being related to the velocities of the atoms and the latter being linked to the interatomic potential, namely $U = U(\mathbf{r}^{3N}(t))$. The main key of MD is to find the appropriate potential describing the interactions within the atoms, and it will be described in details in the next section. To find the trajectories of the atoms it is necessary to solve Newton's equations of motion which for a system on N particles with potential energy U states

$$m\frac{d^2 r_i}{dt^2} = -\nabla_{r_i} U(r^{3N}) \tag{3.10}$$

with $i = (1, \ldots, N)$ and m is the mass of the particles assumed to be the same for all of them. These highly complicated equations are then solved numerically. There are several methods to do so. One of these is due to Verlet [110]. If we divide the time period in L time steps of size Δt we proceed to the integration $\mathbf{r}^{3N}(t_0) \rightarrow \mathbf{r}^{3N}(t_1) \rightarrow \cdots \rightarrow \mathbf{r}^{3N}(t_L)$. To find $\mathbf{r}^{3N}(t)$ we use a Taylor expansion for $\mathbf{r}_i(t_0 \pm \Delta t)$

$$\mathbf{r}_i(t_0 + \Delta t) = \mathbf{r}_i(t_0) + \dot{\mathbf{r}}_i(t_0)\Delta t + \frac{1}{2}\ddot{\mathbf{r}}_i(t_0)(\Delta t)^2 \tag{3.11}$$

Adding the expansion for $\mathbf{r}_i(t_0 - \Delta t)$ we get

$$\mathbf{r}_i(t_0 + \Delta t) = -\mathbf{r}_i(t_0 - \Delta t) + 2\mathbf{r}_i(t_0) + \ddot{\mathbf{r}}_i(t_0)(\Delta t)^2 \tag{3.12}$$

The term $\ddot{\mathbf{r}}_i$ is then needed to find the particle position at time step $t_0 + \Delta t$ and it can be found by substituting it with the $F_i(\mathbf{r}^{3N}(t_0))/m$ taken from equation (3.10). We're now left with a discrete equation (3.12) that has the potential U involved, whose form we can actually choose. The part of the simulation that is more computationally demanding is the calculation of the force which is related to the potential. So we need to specify a potential that is at the same time accurate but efficient.

3.2.1 Simulation settings

To perform an MD simulation we generally need to set a few parameters that now we want to look at in details. These are the most common features.

- We need to set a *supercell*, where atoms are placed, made up of unit cells where a minimum number of particles is placed.
- The number of particles N in the volume of the supercell is set through the specification of the supercell itself. This determines the density as well
- We use periodic boundary conditions (PBC) so that particles cannot be lost or created
- In case we used a pair potential we need to set which pair is interacting. So a *neighbor cutoff distance* is provided to define the possible couples

- A *force cutoff distance* is introduced defining the range of action of the force so that if two atoms are at distance $r > r_{cutoff}$ they don't interact

- A useful tool is the *neighbor list* which is a list tacking track of who are the neighbors of each particle, so that we don't have to check every atom every time a calculation is made

What we can calculate. The main issue that is regarded as being of paramount importance is that no approximation in treating this N-body problem is required. We can study a system and its time evolution keeping track of the atoms in the simulation volume without requiring any limitations. With a MD simulation it is possible to obtain thermodynamic, structural, mechanical properties in solid, liquid or gas. With this method we can follow the atomic motions according to the Hamiltonian mechanics principles. Besides, a lot of particles can be treated at the same time (provided there is a sufficiently powerful computer) and still all the thermodynamic properties like the equation of state are perfectly accurate. And there is always a direct control over input, initial and boundary conditions that are set by the user. MD simulations are very accurate in describing high temperature and high pressure system properties as well: random velocities are generated according to a Maxwell distribution probability in an infinitesimal volume d^3x proportional to $\sim (m/2\pi k_B T)^{3/2} e^{-m(v_x^2+v_y^2+v_z^2)/2k_B T} d^3x$, where k_B is Boltzmann constant, v_i are the particle velocity components and T is the temperature. We now understand how complementary DFT and MD simulations are, providing different tools and different advantages and disadvantages. In fact MD simulations also show some limitations that has to be taken in mind: the definition of the potential describing the interaction between atoms is of crucial importance and is not trivial. In the past years a lot of different forms for these functions have been developed and one of the main problems is that there is not just one potential suitable for all the elements. Another challenge MD has to face is the computational capability: since we're dealing with such a great number of atoms at the same time, we do not have infinite power and time to do all the calculations. But great progress has been made in these fields. Let's now introduce the principal interatomic potentials used in MD simulations.

3.3 Interatomic potentials

It is clear from what we have seen so far that the choice of the potential is the most critical point of an MD simulation: in fact a simulation has to keep its fidelity (the physical description has to be accurate) but at the same time it has to also be computationally efficient [111]. When choosing a potential one should consider then its accuracy in reproducing known properties of the physical system under study and its computational speed. The potential function $U(\mathbf{r}_1, \ldots, \mathbf{r}_N)$ describes the potential energy of the system and then depends on the coordinates $\mathbf{r}^{3N}(t)$. It is involved since the forces are defined as

$$\mathbf{F}_i = -\nabla_{\mathbf{r}_i} U(\mathbf{r}_1, \ldots, \mathbf{r}_N) \tag{3.13}$$

All simulations are based on the Born-Oppenheimer approximation. In classical MD Schrödinger equation is replaced by Newton equation of motion, which is a good approximation for all atoms except for the lightest ones. It is then considered an expansion of the total energy of the N atoms in terms of many-body interactions, i.e.

$$U(\mathbf{r}_1, \ldots, \mathbf{r}_N) = \sum_{i=1}^{N} U_1(\mathbf{r}_i) + \sum_{i<j}^{N} U_2(\mathbf{r}_i, \mathbf{r}_j) + \sum_{i<j<k}^{N} U_3(\mathbf{r}_i, \mathbf{r}_j, \mathbf{r}_k) + \ldots \tag{3.14}$$

where U_1 is the one-body term and represents the interaction of the atoms with an external field (it is usually absent); the U_2 is the two-body term or *pair potential* and is the contribution of any pair of atoms not affected by the presence of other atoms; the U_3 term represents an interaction between one pair and another atom. Among the pair potential models, the Lennard-Jones [112] is widely used and is considered a good description of the van der Waals interactions between closed shell atoms. The potential has the form

$$U(r_{ij}) = 4\epsilon \left[\left(\frac{\sigma}{r_{ij}} \right)^{12} - \left(\frac{\sigma}{r_{ij}} \right)^{6} \right] \tag{3.15}$$

where $r_{ij} = |r_i - r_j|$ is the interatomic distance. It has two parameters that are fixed by fitting to selected data, ϵ and σ [113] which also set the scale for energy and separation distance respectively. The term $\sim (1/r_{ij})^{12}$ represents the repulsion between atoms at short distance: when electronic clouds overlap the energy of the system increases. The term $\sim (1/r_{ij})^{6}$ dominates at large distance and is related to the cohesion of the system. The value 12 for the first exponent has no special meaning and is sometimes replaced by and exponential whereas the exponent 6 comes from quantum

mechanical calculation. To make the simulation more efficient reducing the computational effort, only nearest neighbors are considered to interact: a cutoff radius is then defined as the maximum value of the modulus of the radius vector. Lennard-Jones potential is an example of pair potential and not the only one, nevertheless it is not adequate to describe covalent bond or metal interaction.

Another popular potential was introduced by Morse [114] to describe the vibrational spectrum of diatomic molecules. It is an empirical potential whose expression states

$$U(r) = D\left[e^{-2\alpha(r-r_0)} - 2e^{-\alpha(r-r_0)}\right] \tag{3.16}$$

where r_0, α, D are positive constants for a given diatomic molecule. This potential provides attraction at large distance and has a minimum at equilibrium distance r_0. Born and Mayer then extended this potential to describe the energy of ionic crystal including van der Waals and ionic interactions in the form

$$U(r) = Ae^{-\alpha r} - \frac{C}{r^6} \tag{3.17}$$

with A, α, C specific parameters to be set. It can be as well found with a Coulombic term added

$$U(r) = Ae^{-\alpha r} - \frac{C}{r^6} + \frac{q_i q_j e^2}{4\pi\epsilon_0 r} \tag{3.18}$$

where q_i are the charge of the atoms, e is the electron charge and ϵ_0 is the permettivity. All the potentials we discussed so far cannot describe closed-shell materials though and many-body potentials have to be introduced like Stilliner-Weber [115], Tersoff [127]-[117], REBO [118], Finnis-Sanclair [119], COMB [120] and EAM [121]-[122].

COMB potential. The COMB formalism [120],[123],[124] in its most recent formulation named COMB3 [125] can be used to develop a potential for α-U as well. It depends on both the charge of the atom and its position $\mathbf{r}$ and is made up of three terms

$$U(q, r) = U^{self} + U^{coul} + U^{sr} \tag{3.19}$$

where U^{self} is the self energy of the atom, U^{coul} describes the Coulombic interaction between electron-electron and electron-core, U^{sr} stands for

short range many-body bonding interaction. We already see how more complex this formulation is compared to the pair potential. The first term in equation (3.20) is expressed in terms of a set of parameters to be fitted $\chi, J, K, L, P_{ij}^{\chi}, P_{ij}^{J}$

$$U^{self} = \sum_i \left(\chi_i q_i + J q_i^2 + K_i q_i^3 + L_i q_i^4 + \frac{1}{2\pi\epsilon_0} \sum_{j<i} \frac{P_{ij}^{\chi} q_j}{r_{ij}^3} \frac{P_{ij}^{J} q_j^2}{r_{ij}^5} \right) \tag{3.20}$$

where the first four terms represent the ionization energy and the last summation is the electronegativity and atomic hardness in a charged environment. The Coulombic interaction describes the force between electron-electron (qq) and electron-core (qZ) and is defined for the atomic charge as a spherically distributed density ρ

$$\rho_i(q_i, \mathbf{r}) = Z_i \delta(|\mathbf{r} - \mathbf{r}_i|) + (q_i - Z_i) f_i(|\mathbf{r} - \mathbf{r}_i|) \tag{3.21}$$

where $f_i = \xi^3/\pi e^{-2\xi|\mathbf{r}-\mathbf{r}_i|}$ (ξ is a fitting parameter), and $\delta(|\mathbf{r} - \mathbf{r}_i|)$ is the Dirac delta. This density is a function of the charge q, its core point charge Z and the position $\mathbf{r}$ with respect to the atom position $\mathbf{r}_i$. The U^{coul} term can then be written following [126] as

$$\begin{aligned} U^{coul} =& U^{qq} + U^{qZ} = \sum_i \sum_{j<i} q_i q_j \int \frac{f_i(\mathbf{r}_1) f_j(\mathbf{r}_2)}{|\mathbf{r}_1 - \mathbf{r}_2|} d^3\mathbf{r}_1 d^3\mathbf{r}_2 + \\ & \sum_i \sum_{j<i} q_i Z_j \left(\int \frac{f_i(\mathbf{r})}{|\mathbf{r} - \mathbf{r}_i|} d^3\mathbf{r} - \int \frac{f_i(\mathbf{r}_1) f_j(\mathbf{r}_2)}{|\mathbf{r}_1 - \mathbf{r}_2|} d^3\mathbf{r}_1 d^3\mathbf{r}_2 \right) + \\ & \sum_i \sum_{j<i} q_j Z_i \left(\int \frac{f_j(\mathbf{r})}{|\mathbf{r} - \mathbf{r}_j|} d^3\mathbf{r} - \int \frac{f_i(\mathbf{r}_1) f_j(\mathbf{r}_2)}{|\mathbf{r}_1 - \mathbf{r}_2|} d^3\mathbf{r}_1 d^3\mathbf{r}_2 \right) \end{aligned} \tag{3.22}$$

The short range interaction is made of a repulsion part V^R and an attraction part V^A in the analytical form

$$U^{sr} = \sum_i \sum_{j<i} F_c(r_{ij}) \left(V^R - \beta V^A \right) \tag{3.23}$$

where F_c is a cutoff function determining the short interaction range; the expressions of V^R and V^A are derived for example in [127], and β is a bond-order parameter considering the effect of all the neighbors of atom i on the bonding between atoms i and j. Of course this kind of potential needs a parametrization using DFT or experimental data.

EAM potential. A widely used potential for metals is the Embedded-Atom Method (EAM) [121]-[122] through which the many-body effect is taken into account with an embedding function. This approach is based on the concept of local density: each atom is embedded in a host electron gas due to all the neighboring atoms. In this *ansatz*

$$E_{tot} = \sum_i E_i = \sum_i F_i(\rho_i) + \frac{1}{2}\sum_{j\neq i} \phi_{ij}(r_{ij}) \tag{3.24}$$

where F is the embedding energy providing the energy associated with placing an atom in the electronic environment described by ρ which is the spherically averaged atomic electron density and is $\rho_i = \sum_{i\neq j} \rho_j(r_{ij})$; the ϕ term is an electrostatic two-body term: so the total energy is then found embedding an atom in the electronic density due to the atoms of the system. The background density for each atom is calculated by considering the superposition of atomic density tails from the other atoms at its nucleus. Such a description is way more complex than the one in the pair model as it provides a many-body interaction environment. The main advantage is the ability to describe the variation of the bond strength with coordination. So the energy is made up of two parts: a pair potential ϕ which is the electrostatic core-core repulsion and a cohesive term specified by the function F which is the energy the ion core gets when embedded in the electron sea. The latter is also function of the local electron density. The EAM formulation was preceded by the work found in [128] and [129], but Daw and Baskes [121]-[122] renewed the whole EAM *ansatz* proposing that the cohesive energy of a metallic system is made of these two contributions of the embedding energy plus the electrostatic interaction and they also obtained the functions needed by fitting the properties of bulk metals allowing calculations of complex metallic structures. So in this scheme the many-body interaction, neglected in the pair potential, is incorporated without making the calculation computationally expensive. The EAM potential works well for systems where the kinetic energy and the correlation-exchange functionals can be approximated with semi-local functional and for which the electron density can be approximated with a linear superposition of single-atom densities. Following [130] and starting from DFT theory it is possible to derive heuristically the expression in equation (3.24). We consider the electron density of a solid $\rho(\mathbf{r})$ and we assume that the kinetic, exchange-correlation functional that we'll call F is semilocal i.e. is given by a function of the local electron density and its derivatives

$$F[\rho] = \int g(\rho(\mathbf{r}), \nabla\rho(\mathbf{r}), \nabla^2\rho(\mathbf{r}), \dots)d^3r \tag{3.25}$$

g being the density function. The electron density is assumed to be a linear superposition of the densities of the individual atoms $\rho_s = \sum_i \rho_i^a(\mathbf{r} - \mathbf{R}_i)$ where R_i is the coordinate of the i-th nucleus. This is because in many metals it has been observed that the electron distribution is close to the superposition of the atomic densities. The cohesive energy of the solid can then be written as

$$\begin{aligned} E_{coh} = F[\rho] + \frac{1}{2}\sum_{i\neq j}\frac{Z_iZ_j}{R_{ij}} - \sum_i \int d^3r \frac{Z_i\rho}{|\mathbf{r} - \mathbf{R}_i|} + \\ \frac{1}{2}\int \frac{\rho(\mathbf{r}_1)\rho(\mathbf{r}_2)}{r_{12}} d^3r_1 d^3r_2 - E_{atoms} \end{aligned} \tag{3.26}$$

where the summation over i and j goes over the nuclei of the solid, Z_i is the charge of the i-th nucleus, E_{atoms} is the total energy of the isolated atoms. If now we substitute in equation (3.26) the expression of the density $\rho_s = \sum_i \rho_i^a(\mathbf{r} - \mathbf{R}_i)$ we get

$$E_{coh} = F[\sum_i \rho_i^a] - \sum_i F[\rho_i^a] + \frac{1}{2}\sum_{i\neq j} U_{ij}^a \tag{3.27}$$

with

$$U_{ij}^a = \int \frac{(\rho_i^a(\mathbf{r} - \mathbf{R}_i)) - Z_i\delta(\mathbf{r} - \mathbf{R}_i))(\rho_j^a(\mathbf{r} - \mathbf{R}_j) - Z_j\delta(\mathbf{r} - \mathbf{R}_j))}{r_{12}} d^3r_1 d^3r_2 \tag{3.28}$$

representing the electrostatic energy of the overlapping charge distributions. The first two terms in equation (3.27) represent the difference in considering the kinetic and exchange-correlation functionals between isolated atoms and the whole solid. When looking at atom i we can say that it is embedded in a background density that can be considered constant (and named $\bar{\rho}$) since it varies slowly compared to ρ_i^a. So the embedding energy of an atom in the electron gas of constant density $\bar{\rho}$ will be $F_i(\bar{\rho}_i) \equiv F[\rho_i^a + \bar{\rho}_i] - F[\rho_i^a] - F[\bar{\rho}_i]$ and the cohesive energy becomes

$$E_{coh} = \sum_i F_i[\bar{\rho}_i] + \frac{1}{2}\sum_{i\neq j} U_{ij}^a + E_{err} \tag{3.29}$$

where $E_{err} = F[\sum_i \rho_i^a] - \sum_i F[\rho_i^a + \bar{\rho}_i] + \sum_i F[\bar{\rho}_i]$. And setting $E_{err} = 0$ provides the optimal background densities, even though for example if the

system is homogeneous $\bar{\rho}_i \equiv \bar{\rho}$. In the case of inhomogeneous solid we need an equation for each ρ_i which depends locally on the neighboring of atom i.

3.4 Embedded-atom method potential for uranium

In order to set up an MD simulation for uranium metal we need to pick a potential that is appropriate for a bcc configuration and is valid for a wide range of pressures and temperatures. There are a few calculations of U EAM potential such as [131], [132], [155], [134]. The most recent work we followed is by Smirnova *et al.* [135] where it is developed an interatomic potential for the α-U, γ-U and liquid uranium fitted to the quantities obtained from *ab initio* calculations. In fact in order to tune the potential parameter there is the need of first of all create a fitting database with *ab initio* calculations and experimental data. When the tuning is performed only on the latter the approach is called force-matching method, which is the one Smirnova *et al.* used. *Ab initio* techniques have been widely used in literature to find several properties of uranium. Nevertheless this approach has strong limitations in terms of time and size due to the computational effort: typical time scales and size are respectively about picoseconds and $\sim 10^2$ atoms. *Thanks to MD simulation a wider range can be studied, especially useful for phase transition for example, and several new properties can then be studied and discovered.* Clearly these discoveries are based on the reliability of the interatomic potential which is then a delicate issue and a powerful tool. This is why a building procedure involving a comparison with known properties of uranium is needed.

To first build the database containing the values of atomic forces, stresses and energies for several configurations *ab initio* DFT calculations are performed; then the optimization of the EAM potential is made, requiring that the deviations between the reference values and their EAM approximations are minimized. Through this minimization iteration the result is a potential that best fit the data: this is a standard procedure, starting from e.g. in [137]. In [135] to create the reference database, α-U, γ-U and liquid U structures are created and a short MD simulation is performed with a trial potential [155] at temperature T so that after the simulation has run the atomic arrangement represents the required configuration. Then an *ab initio* calculation is made to compute the created energy, stress and force reference set. And a complete reference database with $\sim$ 12054 values is built. In order to find a reliable potential it is then mandatory to fit the potential to the reference data found so far. With an EAM potential there are three

functions to be found, namely F, ϕ, ρ. The right fit is obtained by minimizing the deviations between the database values and those obtained with the EAM potential, e.g. the average fitting errors for the forces in each reference configuration are

$$\Delta = \frac{1}{N}\sum_{i=1}^{N}\sqrt{\frac{(F^i_{EAM} - F^i_{DFT})^2}{(F^i_{DFT})^2}} \tag{3.30}$$

To further corroborate the process, the resulting potential is verified by comparing several properties of uranium with existing data. The agreement is not satisfying, then the whole procedure is repeated changing some parameter. In Figure 3.1 we can see the shape of the functions as found in [135]: these three functions constitute the EAM potential developed in there, the dots being the spline knots. The potential in [131]-[132] was fitted to the

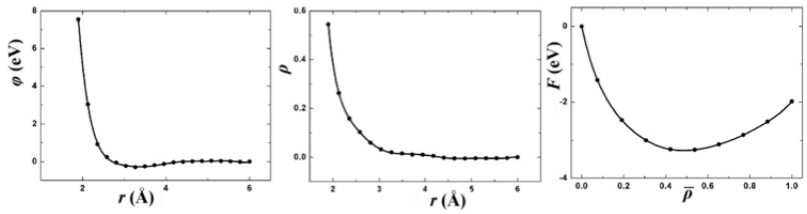

Figure 3.1: EAM potential functions: ϕ is the pair potential, ρ is the effective electron density, and F is the embedding function responsible for the many-body effects.

lattice constants, bulk modulus, cohesion energy and equilibrium atomic volume and is valid for α-U at normal conditions. The potential found in [155] was fitted to the data of liquid uranium and well represents the bcc structure but it is not valid for α-U at low temperature. The potential built in [134] does not consider liquid uranium. Whereas in [135] the properties of α, γ and liquid U are considered at the same time. To verify the potential a few MD calculations are made for the thermodynamic parameters of the element, basically involving structural and elastic properties: in particular lattice parameters a, b, c, y, atomic volume V_0^{at}, atomic energy of cohesion E_{coh}, elastic constants c_{ij} and the bulk modulus of α and γ-U at zero pressure are calculated with the EAM potential and reported in Figure 3.2.

		α-U	
a	2.8361	2.845	2.800
b	5.7604	5.818	5.896
c	4.9551	4.996	4.893
y	0.1015	0.103	0.097
V_0^{at}	20.238	20.674	20.194
E_{coh}	−4.20	—	—
c_{11}	151	300	296
c_{22}	218	220	216
c_{33}	330	320	367
c_{12}	109	50	60
c_{13}	130	5	29
c_{23}	108	110	141
B	149	133	149
		γ-U	
a	3.493	—	3.430
V_0^{at}	21.309	—	20.180
B	95.0	—	176.0

Figure 3.2: EAM values for lattice parameters (a, b, c, y) in Å, atomic volume V_0^{at} in Å^3, atomic energy of cohesion E_{coh} in eV, elastic constants c_{ij} in GPa and the bulk modulus in GPa of α ($T = 300$ K) and γ-U ($T = 900$ K) at zero pressure. From the left: in the first column the values from [135], the second and the third (both *ab initio* calculations) from respectively [63] and [64].

3.5 Molecular dynamics simulation software: LAMMPS

All the simulations performed in this work run using the Large-scale Atomic Molecular Massively Parallel Simulator LAMMPS [138], an open-source software developed at Sandia National Labs for classical molecular dynamics codes written in C++. LAMMPS output are then processed by Python [139] scripts we wrote to study the properties we are interested in. This software can in fact model a lot of systems from biological material to solid metals, it also contains all the force fields and boundary conditions and can perform simulations including up to millions or billions of particles.
To optimize performances LAMMPS is implemented using the MPI message passing library for parallel processing in which the simulation region is divided in smaller domains each assigned to a different processor. Complex geometries of atoms can be created and we used our own code to create atomic configurations. The structure of a typical simulation run will be explained in the next chapter, so first of all let's give a sketch of an input file

for LAMMPS.
To run the simulation we need the modules:

1. +Initialize System
2. +Define Potential
3. +Molecular Dynamics Evolution
4. +Files and Output

We split the first module into two parts:

1. +Initialize System:

   - in the first part we initialize the system (see Figure 3.3) by setting the appropriate units[1], specifying a three-dimensional simulation ("dimension") with periodic boundary conditions in all directions ("boundary"), defining which style of atoms is used for the appropriate system you want to study.

```
# ---------- Initialize Simulation -------------
clear
units metal
dimension 3
boundary p p p
atom_style atomic
atom_modify map array
```

Figure 3.3: Example of a simulation initialization.

   - in the second part we can create the simulation box with the desired dimension and structure (fcc, bcc,..) and then create the atoms on the lattice, e.g. Figure 3.4: the "lattice" command specifies what type of lattice is used, the "region" command sets the simulation cell ("latconst" has the grammar of a parameter); the "replicate" command duplicates the simulation domain in each direction according to the settings.

   With these modules we can create structures like the one shown in Figure 3.5 as an example.

[1] the units command determines the units of all quantities specified in the input and output script. For "metal" style distance is in Angstrom, energy in eV, temperature in Kelvin, pressure in bars.

```
# ---------- Create Atoms -----------------
lattice     bcc ${latconst}
region      box block 0 10 0 10 0 10
create_box  1 box

create_atoms 1 box
replicate 1 1 1
```

Figure 3.4: The create atoms command.

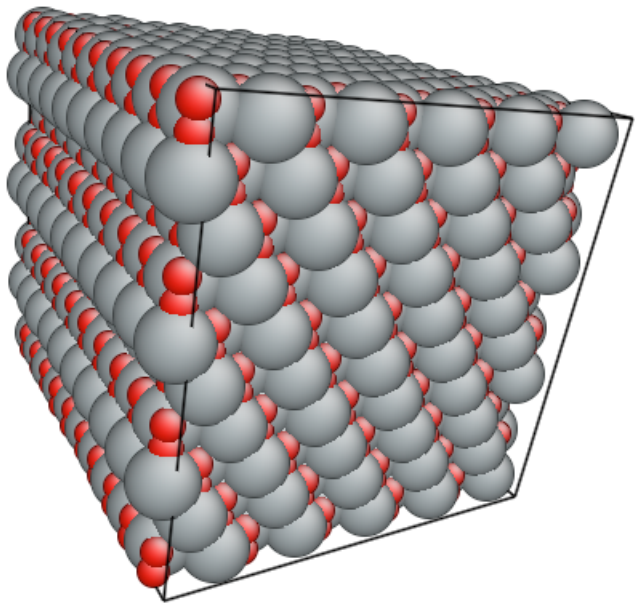

Figure 3.5: Example of a structure that can be created with these modules.

2. in the second module it is necessary to set up the physical quantities for the system we mean to study, see Figure 3.6, the first of which is the potential. The "pair-style" command specifies what kind of potential is used: our choice is "eam/alloy" that computes pairwise interaction reading a file through the string "U.eam.sss2012.alloy U" where spe-

cific tabulated values for alloy interactions are stored. There is an

```
# ---------- Define Interatomic Potential -------------
pair_style eam/alloy
pair_coeff * * U.eam.sss2012.alloy U
neighbor 0.3 bin
neigh_modify delay 10 check yes
```

Figure 3.6: Definition of the potential.

interatomic potential repository project [140] which is a source for interatomic potentials where the files submitted by the authors like [135] are available. EAM potentials for use with LAMMPS are in the format *setfl* and give all the values for embedding energy, electron density and interatomic potential. In Figure 3.7 we can see the beginning of

```
EAM potential for uranium in LAMMPS setfl format
Smirnova D.E., Starikov S.V., Stegailov V.V.
[see J. Phys.: Cond. Mat. 24 (2012) 015702]
produced using VASP and PotFit
 2 U U2
962 0.0010395010395 1462 0.0041041041041 6.0
92  238.03  3.493   BCC
0.0
-0.1078624
-0.1286982
-0.1494877
-0.1702299
-0.1909235
```

Figure 3.7: The setfl file for uranium potential from [135].

the file for uranium potential. The file is built as following: we have three optional comments line; in the fourth line there is the number of elements with the symbol (e.g. U); then in the fifth alpha-numeric line there are

Nrho : number of points at which electron density is evaluated

drho : the distance between two points where the electron density is evaluated

Nr : the number of points at which the interatomic potential and embedding function are evaluated

dr : the distance between points where interatomic potential and embedding function are evaluated

cutoff : the cutoff distance for all functions

Here the body of the file starts with two sections: in the atomic section for each element we have

atomic number, mass, lattice constant, lattice type (fcc, bcc ,..)

embedding function $F(\rho)$ for Nrho values

density function $\rho(r)$ for Nr values

Then the potential section begins:

interatomic potential of element 1 interacting with element 1

interatomic potential between element 1 interacting with element 2

interatomic potential between element 2 interacting with element 1

To define the force between any pair of particles there are short range pair forces which are functions of the displacement vector separating them, so a cutoff distance needs to be set up. Every pair feels a set of forces whose effect needs to take into account all the contributions. To do so a data structure that lists interacting pairs, *the neighbor list*, has to be employed [138], [141], [142]. The list has already been calculated and contains j particles at a distance $r_j < r_{max}$ from particle i, with $r_{max} \geq r_{cutoff}$. All the entries of the neighbor list are then stored in a matrix NBL where every particle i has a list of neighbors (the column index of the matrix keeps record of this). Since for every list the number of neighbors can vary because each particle can have a different amount of neighbors, there is another structure called NN storing the number of neighbors of particle i. Normally a linked list is used instead, but a matrix in this case is necessary. To calculate all the forces acting on the N particles in the simulation Newton's third law increments to the forces on particles i and j at the same time reducing by half the number of floating point calculations. But since we increase the memory accesses the result is a drop of performance.

In our simulation the cutoff distance is specified by the "pair-coeff" command, see Figure 3.6. The "neighbor" command sets the parameter affecting the building of pairwise neighbor list. The "bin" style means the list is created by binning, an operation scaling linearly with

the total number of atoms divided by the number of processors. The "neigh-modify" command controls how often neighbor lists are built and which pairs are stored in the list.

EAM potential is the most widely used potential for metals and alloy [143], as it offers major advantages in terms of physical reliability and computational efficiency, avoiding some unphysical constraints other approaches show. This is why EAM-based classical molecular researches are abundant [144]. Nevertheless it still has issues that have to be improved: for example when computing the elastic constants it gives unphysical results such as $C_{12} > C_{44}$ for cubic systems, $C_{13} > C_{44}$ and $3C_{12} - C_{11} > 2(C_{13} - C_{44})$ for hexagonal close packed crystals [144]-[145] in contrast with experimental existing data. In addition, EAM potentials do not describe accurately the inward and outward relaxations of surface layers [146], as in the simulation results do not agree with phenomenology.

3. A molecular dynamics simulation is run using the *"run"* command.
Of course we have to set some physics on the system before starting the simulation. A lot of commands are available in LAMMPS and also the user can personalize the settings. A list of all the commands can be found on LAMMPS website [138] and we will focus here on those used in this work.
We mainly used three commands: "fix nve", "fix npt", "minimize". So let's see them in details.
Our first goal is to create a system of uranium at a given temperature which can be done following different procedures. We chose to use the "fix nve" command: a "fix" operation in LAMMPS is any procedure applied during a time integration, like changing velocities of the particles, setting the temperature or rescaling the atoms positions.

   fix nve. The simplest simulation for a crystal is the NVE which corresponds to a microcanonical ensemble where the number of particles N, cell volume V and total energy of the system E are conserved. This simulation is usually run to ensure that we are able to let the system be in equilibrium with the right amount of timestep, and to check if the numerical integrator works fine.

   fix npt. The NPT indicates an isothermal-isobaric ensemble. In this case the fix command computes a time integration following the Nosé-Hoover [147]-[148] algorithm[2] by updating the position and the velocity

[2]The Nosé-Hoover algorithm allows to control the temperature of a simulated sys-

```
# ---------- Dynamics ---------------------
fix 1 all nve
run ${runpar}
```

Figure 3.8: A "fix nve" command example.

of the atoms. To perform this operation some dynamic variables are coupled to the domain dimension, allowing to reach a given external temperature/pressure through some specific parameters.

```
# ---------- Dynamics ---------------------
fix 1 all npt temp ${tempconst} ${tempconst} 100.0 iso 0.0 ${pressconst} 1000.0
run ${runpar}
```

Figure 3.9: A "fix npt" command example.

minimize. The minimization procedure changes the atom coordinates iteratively in order to find the configuration corresponding to a local potential energy minimum. A time step is required. It is possible to set a few parameters as stopping criteria for the iterations. It is necessary to check whether or not the system is found to be in a local minimum.

```
# ---------- Dynamics ---------------------
minimize  1e-7 1e-15 5000 5000
```

Figure 3.10: A "minimize" command example.

time step. We highlight that through all these calculations a *time step* is always used. LAMMPS has a "timestep" command which allows to set the time units. **However the unit "metal" which is set at the start of the simulation has a default value of** 0.001 **ps**. As we shall show in the simulations this is the appropriate time step for an

tem. The temperature fluctuates about an average value and with a damping factor the oscillations are controlled.

uranium cluster and since it is also linked to the potential, the choice is coherent with the simulation of the properties of such a system.

4. The last module regards the chance to write files, we briefly describe: in LAMMPS both data and graphics files are available, for our goal we have used data files allowing us to restart the simulation right where it had previously stopped. We have used this approach since the system under study, namely uranium crystal, is very complex and writing data files makes it possible to always control the environment. The price is that we lose a bit of performance.

All the modules described so far are rearranged in the sketch in Figure 3.11.

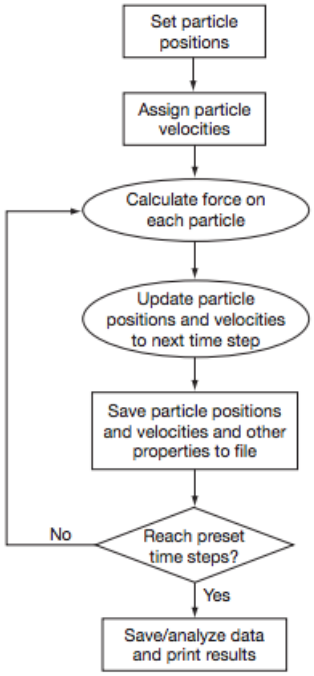

Figure 3.11: A sketch of a simulation run.

Chapter 4

Results and discussion

Our aim is to study the structural behavior and evolution at high pressure and high temperature of an uranium crystal during mechanical deformation. The first step is to validate the potential found in the previous chapter: as a standard procedure in molecular dynamics, it is important to check the reliability of the potential one uses. So we first of all check the elastic properties of the system by reproducing with computer simulations its elastic constants whose values have to be compared both with experimental and theoretical works. We then run a set of NVE simulations: this allows us to see that we are able to let the system reach the equilibrium and we shall study the system in such a configuration at different values of temperature. We will then perform NPT simulations varying the temperature and the pressure. Through this pattern we can find an equilibrium configuration with the NVE run, save it in a data file and then start up the NPT run from it, in order to have the widest control on the system under study and to make sure that as it undergoes any variation of pressure and/or temperature it is still predictable. We will then study how a region of space filled with uranium atoms behaves under high pressure and temperature conditions. Hence we will build up such a configuration and let it evolve to a predictable state and will establish how many time steps are needed. Therefore we will expose such a structure to an environment where an external pressure is applied through a NPT simulation and study how the created box evolve under different physical conditions. We shall examine the pressure, energy, volume and temperature behavior of such a structure over a wide range of temperature and pressure.

4.1 Elastic behavior of uranium in a wide range of pressure and temperature

In the previous chapter we have explained how a few potentials have been developed and what a delicate issue the choice of the adequate one for the system under study is. Not only is it necessary to pick a potential with no general rule, but it is also mandatory to check its reliability. To do that we have to perform a simulation trying to reproduce some known properties to quantify how accurate the potential is. So the first simulation we run concerns the elastic constants of an uranium crystal, for which experimental data and some previous *ab initio* calculations are available.

The simulations are performed for a three-dimensional cell for a total of 2×10^3 atoms with periodic boundary conditions. The potential used [135] is set for a bcc cubic crystal of uranium with lattice constant $a = 3.493$ Å, so we first adjust those parameters and create a box, Figure 4.1. However

```
boundary     p p p

lattice         bcc $a
lattice         bcc 3.4929999999999998828
Lattice spacing in x,y,z = 3.493 3.493 3.493
region              box prism 0 10.0 0 10.0 0 10.0 0.0 0.0 0.0
create_box   1 box
Created triclinic box = (0 0 0) to (34.93 34.93 34.93) with tilt (0 0 0)
  1 by 1 by 1 MPI processor grid
create_atoms 1 box
Created 2000 atoms
```

Figure 4.1: The orthorhombic region created for a bcc uranium with lattice constant $a = 3.493$ Å to satisfy [135].

to apply any compression or dilatation along any axis we need to create a triclinic region (non-orthogonal): this will be useful because we want to compute the elastic constants of the system and so compression inward and outward of the box will be applied in any direction. The "tilt" command allows to perform a stretching of the box along any axis.

Once the simulation region is created, we want to compute the elastic constants of such a system by compressing and dilating it at a given temperature and external pressure: *in other words we need a system whose parameters we are able to handle. So we perform a NVE simulation to let the system reach a given equilibrium state and then a NVP simulation as if we were diving the region in an external pressure the system would eventually come to equilibrium with.* Of course as the NVP simulation is performed the temperature of the crystal is allowed to change. **Our goal is in fact to**

compute the elastic constants for a fixed temperature at several values of the pressure and then for a fixed pressure at different temperature values[1].

The next step is to let the program read the file with the appropriate configuration of atoms at T = *const* and P = *const* and then start the minimization procedure: the energy and forces minimization are performed by changing iteratively the atom coordinates until any of the stopping criteria is reached. The atoms can move as far as they want within 0 and a maximum value, namely *dmax*. The Polak-Ribiere conjugate gradient algorithm is then used[2]. During the iterations of the minimizer a displacement is applied to the region: the prism region creates a parallelepiped starting from the origin, being defined through 3 edge vectors (in our case $(0,0,0)$Å $\rightarrow (34.93, 34.93, 34.93)$Å, see Figure 4.2), and then we can apply

```
Lattice spacing in x,y,z = 3.493 3.493 3.493
Created triclinic box = (0 0 0) to (34.93 34.93 34.93) with tilt (0 0 0)
  1 by 1 by 1 MPI processor grid
Created 2000 atoms
Setting up minimization ...
```

Figure 4.2: The created triclinic box before the first minimization starts.

the displacement each time along one axis at a time once to dilate the region and once to compress it. This procedure is repeated separately for all the components of the stress tensor, i.e. xx, yy, zz, xy, xz, yz, see Figure 4.3. Once the displacement and the minimization have been performed along all

```
triclinic box = (0.5535 0.5535 0.5535) to (34.3765 34.3765 34.3765) with tilt (0 0 0)
  1 by 1 by 1 MPI processor grid
2000 atoms
Changing box ...
triclinic box = (0.5535 0.5535 0.5535) to (34.7293 34.3765 34.3765) with tilt (0 0 0)
Setting up minimization ...
```

Figure 4.3: The created triclinic box after the first minimization starts, when the first displacement is applied.

the six independent directions the elastic constants are computed using

$$C_{ijkl} = \frac{\partial \sigma_{ij}}{\partial e_{kl}} \tag{4.1}$$

[1] A full description of these kinds of simulation is reported in the next sections

[2] with the conjugate gradient method for every iteration a search direction perpendicular to the previous one is found; with the Polak-Ribiere algorithm the whole method is restarted when within a search direction no new information is added.

where σ_{ij} is the applied stress and e_{kl} the strain tensor. We compute the elastic constants over the following values for the temperature

- T = 10 K
- T = 100 K
- T = 200 K
- T = 300 K
- T = 400 K
- T = 450 K
- T = 500 K
- T = 550 K
- T = 600 K
- T = 650 K
- T = 700 K
- T = 750 K
- T = 800 K
- T = 850 K
- T = 900 K
- T = 950 K
- T = 1000 K

and for each temperature for the following pressure values

- P = 0 GPa
- P = 1 GPa
- P = 10 GPa
- P = 20 GPa
- P = 30 GPa

- P = 35 GPa
- P = 40 GPa
- P = 45 GPa
- P = 50 GPa
- P = 55 GPa
- P = 60 GPa
- P = 70 GPa
- P = 90 GPa
- P = 100 GPa

It is used the "stress-strain technique" [149] in which the stress is computed as a function of the strain as the internal coordinates are optimized for each strain. This procedure allows us to calculate the elastic constants for each temperature and each pressure to be compared with experimental and theoretical (where available) data. Symmetry imposes that an orthorhombic crystal has nine independent elastic constants: C_{11}, C_{22}, C_{33}, C_{12}, C_{23}, C_{13}, C_{44}, C_{55}, C_{66}. To further investigate mechanical stability we will also check that our values satisfy the stability criteria:

$$C_{11} > 0 \tag{4.2}$$
$$C_{22} > 0 \tag{4.3}$$
$$C_{33} > 0 \tag{4.4}$$
$$C_{11}C_{22} - C_{12}^2 > 0 \tag{4.5}$$
$$C_{22}C_{33} - C_{23}^2 > 0 \tag{4.6}$$
$$C_{11}C_{33} - C_{13}^2 > 0 \tag{4.7}$$
$$C_{11}C_{22}C_{33} + 2C_{12}C_{23}C_{13} - C_{11}C_{23}^2 - C_{22}C_{13}^2 - C_{33}C_{12}^2 > 0 \tag{4.8}$$
$$C_{44} > 0 \tag{4.9}$$
$$C_{55} > 0 \tag{4.10}$$
$$C_{66} > 0 \tag{4.11}$$

4.1.1 Comparison of the elastic constants at T = 300 K with the experimental data

In Table 4.1 all values of elastic constants we computed for a cubic bcc uranium crystal with $a = 3.493$ Å at T = 300 K and P = 0 GPa are reported. To corroborate the potential we chose, the values we have found are compared with two previous works, namely [150] and [135], and with the experimental values from [151]. About the two theoretical works the latter uses a COMB potential, and the former the same EAM potential we used. These are the most recent works to our knowledge on this subject, even though they both refer to α-U. In Table 4.2 we report the deviations (% errors) from

	this work	Li *et. al.* [150]	Smirnova *et al.* [135]	Exp. [151]
C_{11}	204.713	257.57	151	214.7
C_{22}	204.001	222.64	218	198.6
C_{33}	208.130	298.87	330	267.1
C_{12}	69.417	99.05	109	46.5
C_{23}	69.070	66.47	108	107.6
C_{13}	68.528	45.98	130	21.8
C_{44}	51.437	99.97	-	124.5
C_{55}	51.224	61.72	-	73.4
C_{66}	51.708	89.24	-	74.3

Table 4.1: Comparison of elastic constants for uranium among this work (first column) and two other theoretical works [150] (using COMB potential) and [135] (using EAM) and the experimental values found in [151]. All units are in GPa.

experimental values at T = 300 K. The elastic constants we calculated along the principle axes C_{11}, C_{22}, C_{33} are in good agreement with experimental data with highest deviation of $\sim$ |20|%, although we notice that since we only deal with a potential for a cubic bcc crystal the elastic constants found here show such a symmetry, being $C_{11} \sim (C_{22}, C_{33})$, $C_{44} \sim (C_{55}, C_{66})$ and $C_{12} \sim (C_{23}, C_{13})$. The constants C_{12}, C_{23}, C_{13} show larger deviations: this is probably due to the fact that their phenomenological value is small compared to the others so any deviation from it will end up in a bigger percentage error. But such a behavior is shown in any other theoretical work. Nevertheless looking at the Root-Mean-Square (RMS) found in previous works we realize that this calculation is itself complicated: Smirnova [135] reported a 211 % RMS deviation and Li [150] 56 %. We have found a 38 % RMS which is even smaller than the one reported in [150] and more than 4 times smaller than

	this work	Li *et al.* [150]	Smirnova *et al.* [135]
C_{11}	-5%	20 %	-
C_{22}	3 %	12%	-
C_{33}	-23%	12%	-
C_{12}	34%	113%	-
C_{23}	-36%	-38%	-
C_{13}	70%	111%	-
C_{44}	-60%	-20%	-
C_{55}	-31%	-16%	-
C_{66}	-32 %	20 %	-
RMS err.	38 %	56 %	211 %

Table 4.2: Deviation of the elastic constants and Root-Mean-Square (RMS) from the experimental values at 300 K [151], found in this work and in [150] and [135] (this calculation is reported in [150] as well, although it refers to [135]).

the value in [135] with the EAM potential, albeit these results are higher than typical potential fitting.

A further check of the system stability is the calculation of equations (**??**): so we compute these equations and compare the results with the same works. These are reported in Table 4.3. Each equation is computed individually and we found that the criteria are satisfied, i.e. **the system is stable**. Then we calculate the deviation from the experimental values and the Root-Mean-Square as well. We notice that the most critical quantities are those involving the constants C_{12}, C_{13}, C_{23} showing the largest deviation. Nevertheless our values are comparable with previous calculations and all criteria are satisfied which means that the system is stable under these conditions. This is also a good test of robustness for the simulations we run and for the next results, for which there are no available data.

Once we have shown the stability of the system and checked that the potential we have used is reliable, we now want to study the system under more critical conditions: we shall compare our results with previous studies where available.

4.1.2 Isothermal elastic constants at high pressure

We then want to check uranium stability at higher pressure. So we perform a set of NPT simulations to let the system reach the desired pressure, then we apply the same technique explained in the last section to calculate

Stability Equation	Exp [151]	Li *et al.* [150] (GPa)	% Error	Smirnova *et al.* [135]	% Error	This work	% Error
Eqn (4.1)	214.7	257.57	20 %	151	-30 %	204.71	-5 %
Eqn (4.2)	198.6	222.64	12 %	218	10 %	204.00	3 %
Eqn (4.3)	267.1	298.87	12 %	330	24 %	208.13	-23 %
Eqn (4.4)	40477	47534	17 %	21037	-48 %	36492	-10 %
Eqn (4.5)	41468	62122	50 %	60276	45 %	37688	-10 %
Eqn (4.6)	56871	74866	32 %	32930	-42 %	37911	-34 %
Eqn (4.7)	8.449×10^6	1.320×10^7	56 %	4.557×10^6	-46 %	6.41×10^6	25 %
RMS	-	-	30 %	-	37 %	-	24 %

Table 4.3: Calculation of the stability criteria for uranium compared among experimental values [151], the theoretical work with the COMB potential found in [150] (and the percentage error in there), the theoretical work with the EAM potential from [135] (and the percentage error in there) and our work with the relative deviation. The last line is the Root-Mean-Square (RMS).

the elastic constants. The values of pressure we spann are the ones mentioned before. As we can see, we have more values around $30, 40, 50$ GPa because we noticed around that interval an inflection of the curve we wanted to highlight. All the calculations are isothermal.

Comparison with [68] at T $\sim$ 0 K.
First we compute the values of elastic constants at[3] T $\sim$ 6 K for increasing P and compare them with those found in [68] (T = 0 K). In Table 4.4 the results are shown.

The constants we calculate **always meet the stability criteria (??): this means that such a bcc uranium is mechanically stable up to** 100 **GPa.** Looking at the values in Table 4.4 when comparing them with [68] we notice that the trend is the more we increase the pressure the higher discrepancy we have. Besides, the agreement results vary once again with which elastic constant is computed. This might be due to the different potential one uses and the different approach: in fact in [68] density functional theory with a projector augmented wave (PAW) method is used.

We then plot in Figure 4.4 the elastic constant C_{11} as a function of increasing pressure at T $\sim$ 6 K compared with the one obtained in [68]. In Figure 4.5 we can see the comparison for C_{12}. In Figure 4.6 we can see the comparison for C_{55}. Then in Figure 4.7 we show the behavior of the elastic constants along the principal axis, namely C_{11}, C_{22} and C_{33} compared to those found in [68] under the same conditions; in Figure 4.8 we show C_{12}, C_{23} and C_{13} and in Figure 4.9 C_{44}, C_{55} and C_{66}. From Table 4.4

[3] T = 0 K is a critical value for the simulation so the temperature is kept below 10 K which is very close to 0 K.

P (GPa)	C_{11}	C_{22}	C_{33}	C_{12}	C_{23}	C_{13}	C_{44}	C_{55}	C_{66}
0	249.175	251.721	262.863	104.976	93.991	93.418	82.687	82.191	84.989
0 [68]	294.877	215.018	346.893	67.557	149.040	24.816	143.027	130.205	101.661
10	264.096	262.785	327.141	198.809	168.220	169.272	86.370	88.903	73.825
10 [68]	378.715	279.169	452.915	88.337	191.707	48.064	180.719	149.182	123.133
20	357.417	410.568	370.787	290.022	248.167	247.6494	91.866	85.824	123.963
20 [68]	479.927	347.805	528.812	112.264	230.251	71.858	202.353	165.917	146.132
30	442.301	479.805	479.062	373.495	332.589	331.878	103.356	109.132	104.503
30 [68]	585.723	408.995	595.999	144.853	272.230	98.056	219.110	182.123	166.473
40	482.595	587.162	427.681	406.747	366.587	349.186	104.929	92.094	143.335
40 [68]	683.963	462.629	668.488	172.675	315.062	125.139	233.685	195.407	180.031
50	520.238	659.872	448.006	449.472	411.774	378.405	123.265	99.656	155.307
50 [68]	769.190	508.081	736.067	196.263	357.707	152.538	248.619	204.912	197.843
60	551.9648	630.630	525.760	470.676	445.870	421.657	114.269	92.288	114.885
60 [68]	847.016	550.627	790.780	219.531	401.328	183.573	263.511	211.638	213.990
70	646.679	963.569	539.065	594.920	564.729	490.280	188.119	117.804	202.379
70 [68]	927.370	584.431	838.587	252.147	449.029	212.302	278.565	215.092	226.204
90	850.154	955.226	932.667	697.264	694.478	690.756	142.163	152.642	157.744
90 [68]	1133.613	683.559	950.335	307.889	533.009	247.780	303.275	212.794	250.219
100	1134.130	1233.124	899.039	784.789	741.159	704.061	245.009	186.169	248.852
100 [68]	1220.698	731.327	1008.587	336.862	577.792	256.993	312.200	212.264	265.607

Table 4.4: Elastic constants as computed in this work at T $\sim$ 6 K in the pressure range $0 - 100$ GPa compared with [68].

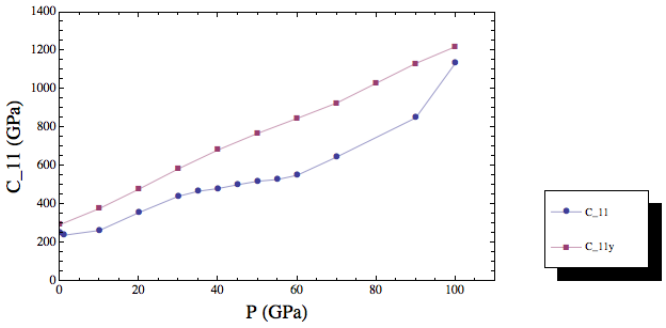

Figure 4.4: Isothermal elastic constant C_{11} as a function of the pressure compared between this work (namely C_{11}) at T $\sim$ 10 K and [68] (namely C_{11y}) at T = 0 K.

we notice that: almost all constants rise with increasing pressure, but we notice around $P \sim 30$ GPa some of them decrease, this is why we have investigated more accurately around those values. We notice that although our system is stable, the agreement with the previously calculated values of these constants depends on which constant we are computing. This might be due to the fact that a cubic symmetry such as the one we use flattens some of the values, causing a better agreement result with some calculations

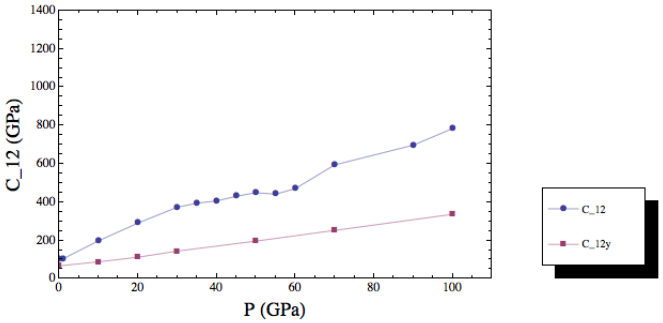

Figure 4.5: Isothermal elastic constant C_{12} as a function of the pressure compared between this work (namely C_{12}) at T $\sim$ 10 K and [68] (namely C_{12y}) at T = 0 K.

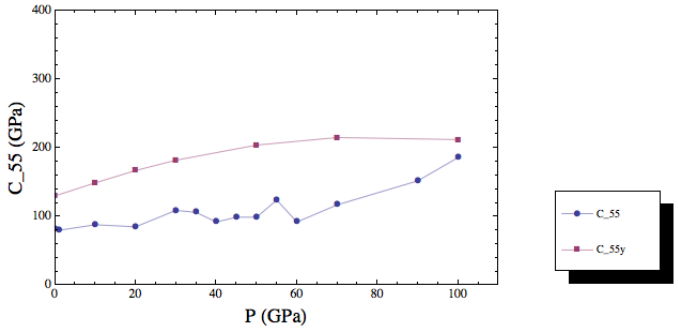

Figure 4.6: Isothermal elastic constant C_{55} as a function of the pressure compared between this work (namely C_{55}) at T $\sim$ 10 K and [68] (namely C_{55y}) at T = 0 K.

and a worse one with some others. However, in [68] the values found are compared with another theoretical work ([152]) using a different approach and a discrepancy is noticed as well: the definition of elastic constants seems to be very model-dependent since they are computed as differences between physical quantities. Hence it seems to us that a good criterium to establish the robustness of such a calculation is the deviation from the experimental values which has been proved in the previous sections. Unfortunately there are no available data yet in this range of temperature and pressure.

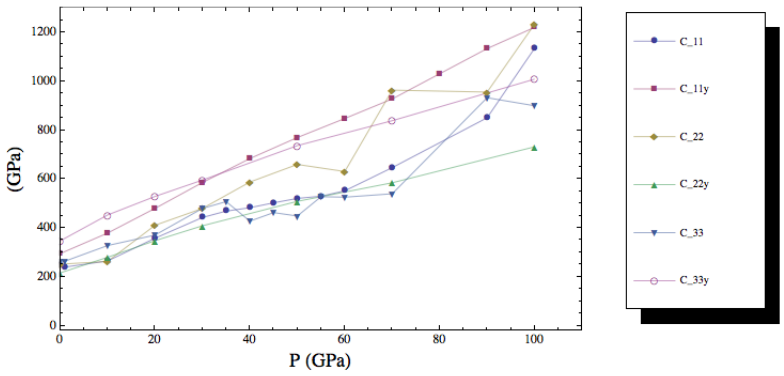

Figure 4.7: Isothermal elastic constants along the principal axis C_{11}, C_{22} and C_{33} as a function of the pressure at T $\sim$ 10 K compared with [68] (namely C_{iiy}) at T = 0 K.

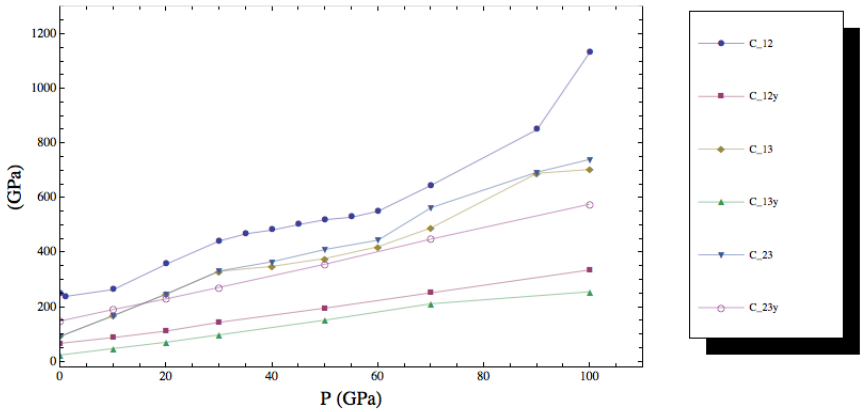

Figure 4.8: Isothermal elastic constants C_{12}, C_{23} and C_{13} as a function of the pressure at T $\sim$ 10 K compared with [68] (namely C_{ijy}) at T = 0 K.

4.1.3 Isothermal behavior of elastic constants in the range of temperature 300 K-1000 K

We hence went further than this. To study uranium stability under more extreme new conditions, we raise the temperature. In fact in [68] the temperature is kept below T $\leq$ 300 K. We spann and evaluate the elastic constants as a function of the pressure for T = 300 K, T = 400 K, T = 450 K, T =500 K, T= 550 K, T =600 K, T = 650 K, T = 700 K, T=750 K,

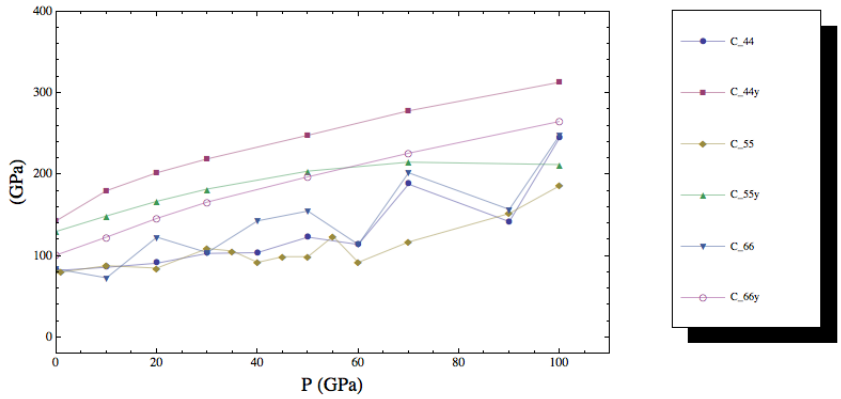

Figure 4.9: Isothermal elastic constants C_{44}, C_{55} and C_{66} as a function of the pressure at T $\sim$ 10 K compared with [68] (namely C_{jjy}) at T = 0 K.

T=800 K, T=850 K, T =900 K, T=950 K and T= 1000 K. We can see a sample of these values reported in Table 4.5 and Table 4.6 for T = 300 K and T = 400 K. All the values are then tabulated in Appendix A.

	C_{11} (GPa)	C_{22} (GPa)	C_{33} (GPa)	C_{12} (GPa)	C_{13} (GPa)	C_{23} (GPa)	C_{44} (GPa)	C_{55} (GPa)	C_{66} (GPa)
T=300 K									
P=0 GPa	204.713	204.001	208.130	69.417	68.528	69.070	51.437	151.224	51.708
P=10 GPa	240.005	264.903	266.290	176.488	176.738	159.265	61.345	68.370	68.404
P=20 GPa	347.356	303.552	344.364	271.511	252.600	273.353	75.402	69.058	72.892
P=30 GPa	411.918	422.674	407.888	322.047	319.915	328.621	75.590	77.476	71.557
P=35 GPa	456.337	425.993	459.236	347.802	361.134	351.750	80.735	87.171	77.568
P=40 GPa	446.858	473.718	471.851	372.565	377.398	384.899	83.034	76.585	74.101
P=45 GPa	456.919	550.976	486.596	389.842	369.250	396.620	126.722	77.395	101.663
P=50 GPa	464.737	535.978	516.155	406.698	405.941	413.621	80.434	82.006	79.875
P=55 GPa	517.340	521.470	536.673	424.996	433.181	424.448	81.717	86.131	89.181
P=60 GPa	518.742	552.030	636.877	396.253	421.064	477.419	108.317	101.632	76.842
P=70 GPa	782.020	783.321	557.986	486.252	520.247	524.197	102.127	105.539	74.364
P=90 GPa	972.157	886.612	904.527	648.939	648.897	668.144	153.793	112.315	112.893
P=100 GPa	1136.578	977.614	895.198	736.351	716.491	643.826	131.021	219.866	227.417

Table 4.5: Computed isothermal elastic constants as a function of the pressure at T = 300 K in the pressure range $0 - 100$ GPa.

To look through more details, we show in Figure 4.10 the isothermal behavior of the elastic constant C_{11} as a function of the pressure through all the values of the temperature: each curve is an isothermal curve. The elastic constant increases with the increasing pressure as expected. At a given pressure the lower the temperature is the higher the constant value is: for example at P = 0 GPa the constant evaluated at T = 200 K is the highest versus all the other temperature values. This is actually a tendency, showing some fluctuations over the pressure interval we study, as one can

	C_{11} (GPa)	C_{22} (GPa)	C_{33} (GPa)	C_{12} (GPa)	C_{13} (GPa)	C_{23} (GPa)	C_{44} (GPa)	C_{55} (GPa)	C_{66} (GPa)
T=400 K									
P=0 GPa	191.815	193.827	193.282	70.591	70.699	69.831	47.253	47.813	47.786
P=10 GPa	231.663	242.968	242.619	168.872	169.469	157.395	51.527	56.677	56.522
P=20 GPa	326.775	323.977	296.577	249.352	260.770	264.865	58.095	57.319	55.628
P=30 GPa	412.346	389.102	404.421	324.350	333.764	323.586	61.343	69.648	63.133
P=35 GPa	451.109	420.389	422.159	372.694	360.017	359.319	61.977	57.517	58.506
P=40 GPa	445.345	464.399	466.860	388.261	390.107	390.386	60.815	61.717	63.658
P=45 GPa	456.919	550.976	486.596	389.842	369.250	396.620	126.722	77.395	101.663
P=50 GPa	438.615	545.255	545.707	385.169	384.538	422.414	84.626	68.148	67.492
P=55 GPa	450.838	597.716	585.436	401.415	400.298	447.837	96.043	73.690	74.758
P=60 GPa	637.837	473.739	633.512	423.994	478.282	423.212	79.932	104.531	85.649
P=70 GPa	653.407	601.443	620.491	522.807	520.559	509.222	85.184	94.210	95.136
P=90 GPa	797.046	821.423	806.981	657.458	643.240	654.788	122.093	110.962	125.777
P=100 GPa	852.228	834.603	873.546	665.708	687.621	679.488	131.292	137.473	116.422

Table 4.6: Computed isothermal elastic constants as a function of the pressure at T = 400 K in the pressure range $0 - 100$ GPa.

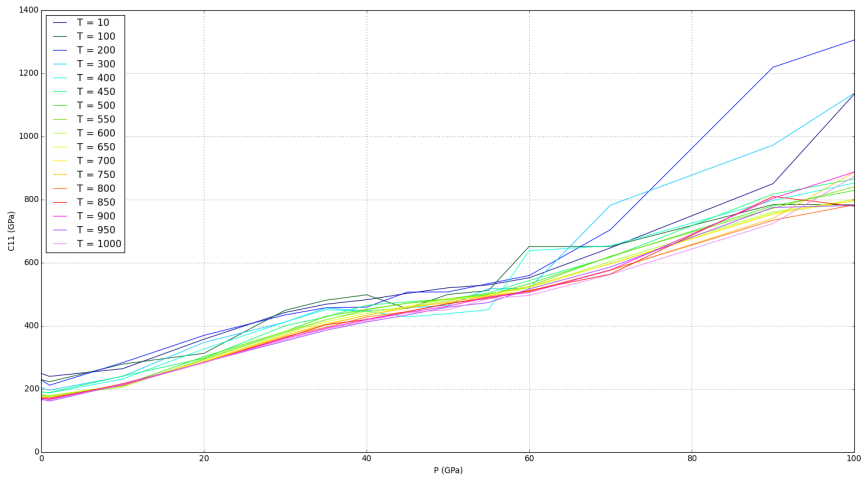

Figure 4.10: Isothermal behavior of elastic constant C_{11} as a function of the pressure for increasing temperature: each curve refers to a different constant value of T from 10 K to 1000 K.

see from the plot. For each temperature it is important to check whether or not the system is stable through equations (4.2)-(4.11), which we have done finding the criteria are always satisfied, therefore the system is stable. We do not have any data here to compare with, but we can emphasize that the increase with the pressure is expected. We can also notice that very often when the temperature rises for a given pressure value the elastic constant decreases.

4.1.4 Isobar behavior of elastic constants in the pressure range 10 GPa-100 GPa

We now want to look at the isobar behavior of the same system. To do so, we analyze and look at the isobar curves in Figure 4.11: each curve represents the C_{11} constant as a function of the temperature at a given external pressure the system comes in equilibrium with. This means that

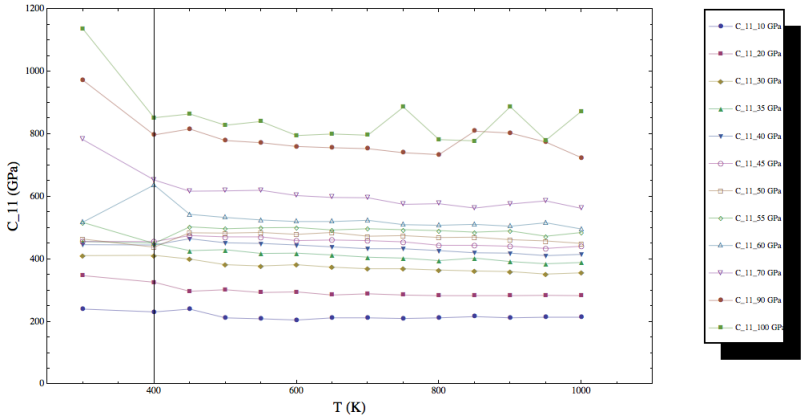

Figure 4.11: Comparison of isobar C_{11} behavior as a function of the temperature.

we always study a bcc uranium crystal with lattice constant $a = 3.493$ Å. We use a NPT simulation to let the crystal reach the desired pressure and then we print the values of the constant for a given temperature. From the graph in Figure 4.11 we can see that: if the temperature is raised, the elastic constant tends to become smaller. Besides, when the system is driven to around 100 GPa, it experiences the highest deformation (the difference between C_{11} at T = 300 K and at T=1000 K is the highest). We only report here as a sample this analysis for C_{11}, but we have done it for all the elastic constants, even though we don't report them all since they are more importantly embedded in the polycrystalline moduli analysis which we shall now present.

4.1.5 Polycrystalline moduli

Once the elastic constants are computed we can use these quantities to study polycrystalline elastic properties of bcc uranium. The quantities we are interested in are:

- the bulk modulus

$$B = \frac{[2(C_{12} + C_{13} + C_{23}) + C_{11} + C_{22} + C_{33}]}{9} \tag{4.12}$$

- the shear modulus

$$G = \frac{1}{2}\left[\frac{C_{11} - C_{12} - 3C_{44}}{5} + \frac{5C_{44}(C_{11} - C_{12})}{4C_{44} + 3(C_{11} - C_{12})}\right] \tag{4.13}$$

- the Young modulus

$$E = \frac{9BG}{(3B + G)} \tag{4.14}$$

The bulk modulus and its temperature and pressure dependencies are essential thermophysical properties because through them we can study the reliability of the equations of state valid over a wide range of temperature and pressure. The EOS play a central role in the study of a material for they bind the pressure, temperature and volume and important compressibility properties can be inferred. Once we have established that such an uranium crystal in this configuration is stable up to these pressure and temperature, we can now study the variation of the bulk modulus in both cases, isothermal and isobar.

We first compute all these quantities at T = 300 K and P = 0 GPa and compare them with [150] and [135] and the experimental work [151]. In Table 4.7 we report the values of bulk modulus, the shear modulus and Young modulus of uranium under these conditions. We need to highlight that

	Exp. [151]	Li *et al.* [150]	% error	Smirnova *et al.* [135]	% error	this work	% error
B (GPa)	113.05	133.47	18 %	149	25 %	114.54	1 %
G (GPa)	84.37	85.43	1 %	-	-	58.19	-32 %
E (GPa)	202.69	211.42	4 %	-	-	149.302	-27 %

Table 4.7: Comparison of the bulk modulus B, shear modulus G and Young modulus E at T = 300 K and P = 0 GPa between the experimental data [151] and the theoretical works: [150] using COMB potential, [135] using EAM potential and this work. The percentage error is computed from the experimental values. All units are in GPa.

the experimental value of the bulk modulus for uranium is still controversial as shown in [73], since at least ten values are reported as measured in the range from $\sim$ 100 GPa to $\sim$ 150 GPa. However the percentage error for the values we have computed is around $\sim$ 1% for the bulk modulus and the

highest is $\sim |30|\%$. Like we said before, it seems to us that the deviation of any theoretical work from the experimental values is the most significant parameter.

In Table 4.8 we can see the polycrystalline properties at T = 300 K in the pressure range P = 0 GPa $\rightarrow$ 100 GPa. In Appendix B all values are reported for each temperature we spanned. In this work we use molecular dynamics simulation to predict the isothermal bulk modulus at high pressure. To an-

	B (GPa)	G (GPa)	E (GPa)
T=300 K			
P=0 GPa	114.54	58.19	149.30
P=10 GPa	199.57	56.87	155.81
P=20 GPa	287.80	56.65	159.50
P=30 GPa	353.73	63.25	179.08
P=35 GPa	384.77	67.82	192.17
P=40 GPa	406.90	63.91	182.20
P=45 GPa	422.87	83.74	235.66
P=50 GPa	441.04	67.83	193.58
P=55 GPa	460.08	70.92	202.38
P=60 GPa	477.45	84.88	240.41
P=70 GPa	576.08	95.91	272.61
P=90 GPa	743.91	128.95	365.73
P=100 GPa	800.30	176.50	493.26

Table 4.8: Bulk modulus B, shear modulus G and Young modulus E of bcc uranium crystal at T = 300 K.

alyze the values we obtain, let's look at the **isothermal behavior of the bulk modulus**: in Figure 4.12 the behavior of isothermal bulk modulus as a function of the pressure is shown. Each curve represents an isothermal one in the range T = 10 K $\rightarrow$ 1000 K. **This is the pressure dependence of the isothermal bulk modulus at different temperatures: the bulk modulus increases with the increase of the pressure and tends to decrease with the increase of the temperature**.

Comparison with [68]

We now want to compare the quantities we have found with those found in [68] at T = 0 K. In [68] in fact the polycrystalline properties are studied at T = 0 K from 0 up to 100 GPa. Figure 4.13 shows a comparison of the MD-calculated isothermal bulk modulus with *ab initio* density functional theory using PAW method calculation [68] combined with this work. Both works show that the bulk modulus increases with increasing pressure: in [68] it is

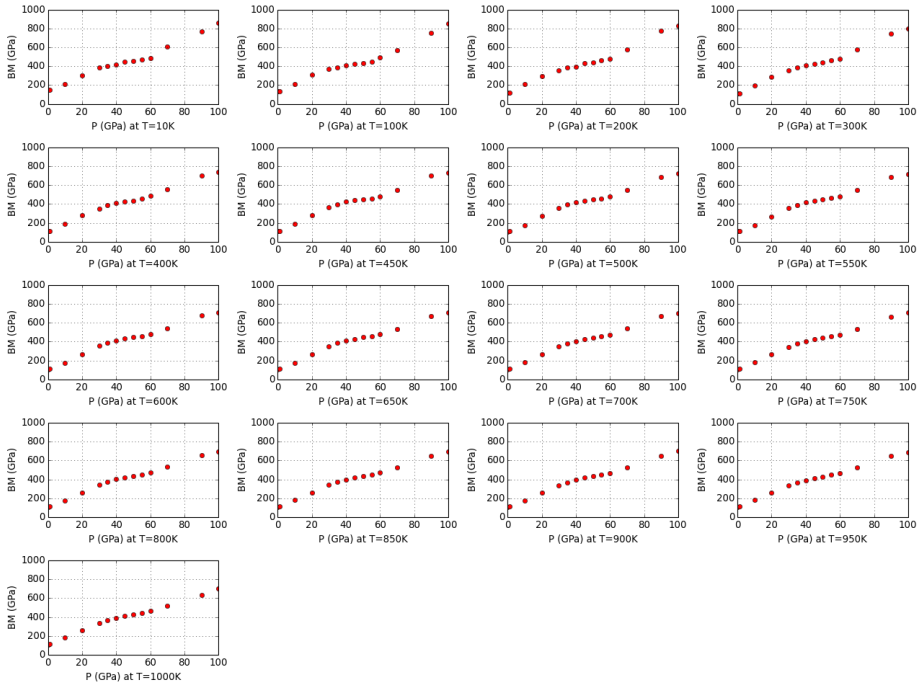

Figure 4.12: Isothermal behavior of bulk modulus of a bcc uranium as a function of the pressure at T = 10 K, 100 K, 200 K, 300 K, 400 K, 450 K, 500 K, 550 K, 600 K, 650 K, 700 K, 750 K, 800 K, 850 K, 900 K, 950 K, 1000 K.

reported an almost linear behavior whereas the values we have computed rise less smoothly. We can see that the discrepancy tends to increase for increasing pressure, showing differences in the potential in such a wide range. In Table 4.9 we show the comparison of the bulk modulus, shear modulus and Young modulus between this work and [68].

In Figure 4.14 we plot the comparison of the bulk modulus B, the shear modulus G and the Young modulus E between this work and [68]. All these quantities increase as the pressure increases and this is perfectly coherent with their physical meaning: we know that the higher the value of Young's modulus the stiffer the material is, so uranium is becoming more and more stiffer in agreement with what is found in [68]. Besides, one should be aware of the Poisson's ratio which is related to the volume change of materials during deformation. It is expressed as $\sigma = (3B - 2G)/(2(3B + G))$. A value that is less than 0.5 indicates that the system is stable against the shear.

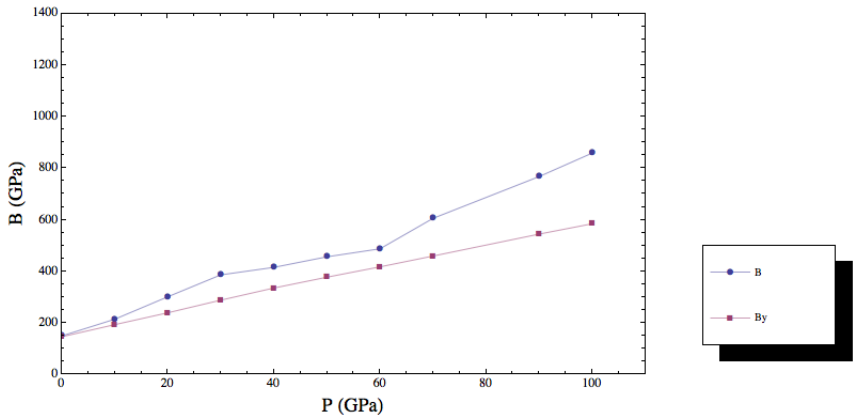

Figure 4.13: Comparison of isothermal bulk modulus as a function of the pressure at T = 0 K from [68] (B_y) and this work T $\sim$ 10 K.

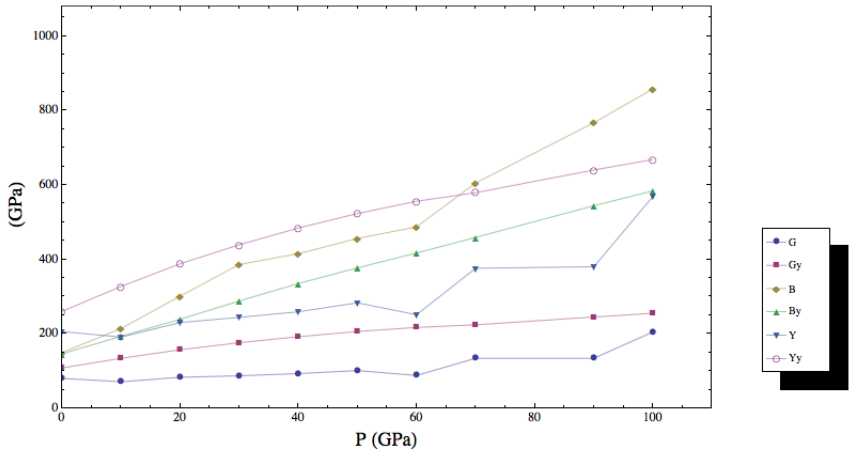

Figure 4.14: Comparison of isothermal bulk modulus B, the shear modulus G and the Young modulus E as a function of the pressure between [68] at T = 0 K (B_y, G_y, Y_y) and this work at T $\sim$ 10 K.

This is in fact the case up to 100 GPa of the system we have studied and is in agreement with [68].

We also study the **isobar behavior** of the bulk modulus that is shown in Figure 4.15. The system is brought to an external pressure it comes to equilibrium with and we compute the bulk modulus for each value of pressure

P (GPa)	B (GPa)	G (GPa)	E (GPa)	B (GPa) [68]	G (GPa) [68]	E (GPa) [68]
0	149.837	81.398	206.755	146.767	108.177	260.523
10	214.069	71.001	191.799	193.044	134.586	327.621
20	301.161	83.859	230.211	239.912	157.735	388.142
30	386.344	87.61	244.364	288.800	176.554	439.999
40	415.831	93.066	259.816	335.091	192.324	484.315
50	456.380	101.543	283.597	377.116	206.507	523.894
60	487.196	88.965	251.582	417.546	217.713	556.428
70	605.463	134.953	376.859	459.035	224.476	579.042
90	767.005	134.213	380.449	544.436	245.731	640.787
100	858.479	205.091	569.892	584.715	255.203	668.371

Table 4.9: Calculated bulk modulus B, shear modulus G and Young modulus E in GPa at T $\sim$ 10 K for uranium compared with [68] at T = 0 K.

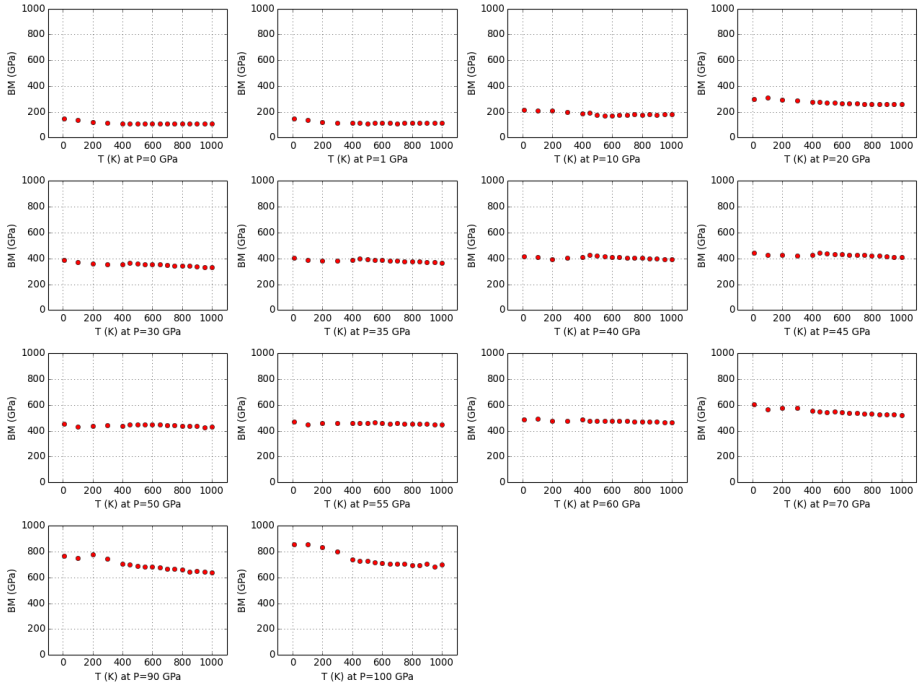

Figure 4.15: Isobar behavior of the bulk modulus B as a function of the temperature at different external pressure P = 0 GPa, P = 1 GPa, P = 10 GPa, P = 20 GPa, P = 30 GPa, P = 35 GPa, P = 40 GPa, P = 45 GPa, P = 50 GPa, P = 55 GPa, P = 60 GPa, P = 70 GPa. P = 90 GPa. P = 100 GPa.

for several temperatures. We can see that the bulk modulus increases with the increase of the external pressure imposed. And once again we can see a tendency to decrease with increasing temperature.

4.1.6 Uranium compounds and other radioactive elements contribution

As mentioned before the contribution to the total heat flux coming from the inside of the Earth (47 ± 1 TW) is due to two sources: the cooling of the planet and the heat produced by the decay of the long-lived isotopes, such as ^{238}U, ^{235}U, ^{232}Th and ^{40}K [2]-[33]. Such elements have in fact a half-life comparable to the age of the planet, the energy of their decays is converted in heat and they are sufficiently abundant: so all of these three conditions are fulfilled by the up-mentioned isotopes. Hence we started up by studying U alone as a pioneering step. But we need to highlight that looking at the mantle elemental contribution for example, K is much more abundant than U [2]: in fact potassium concentration is around 70 p.p.m. by weight compared to the one of uranium which accounts for 0.025 p.p.m. by weight; whereas Th concentration is around 0.087 p.p.m. by weight. The the next step in the research, after studying U itself, will be to carry out the same analysis with for K and Th as well. This will be mandatory to corroborate such a study, since individual contributions are relevant to the overall process.

Another follow-up study to be mentioned is the study of uranium compounds: we do know that U is mainly present in the crust as a compound with other constituents such as oxygen and silicon. So, once the analysis for U itself will be completed we will start the same pattern to study U compounds. For example uranium and thorium dioxide UO_2 and ThO_2 behavior under high pressure has been largely studied experimentally e.g. in [69] with diamond-anvil cell techniques up to $\sim$ 80 GPa, showing their elastic and mechanical behavior and compressibility. Whereas uranium and thorium silicide behavior has been investigated for example in [70]. So it will be necessary to use the same approach we used in this work to link the results we get from the simulations with the experimental data available.

4.2 The simulation structure: NVE

To reach the equilibrium to a theoretical temperature we build and run a set of NVE simulations describing a microcanonical ensemble with total number of particles N, volume V and total energy E conserved. The goal of

such a kind of simulations is to let the system reach the equilibrium after an appropriate number of time steps, during which the particle velocities and positions are updated while energy and forces are minimized at each time step. Such a process lets us optimize the structure under study and gives very good long-term predictivity. This means that the thermodynamical quantities involved have to reach a stable value after awhile. In the program we set the temperature we want to reach with the command "temp/rescale" and the temperature will remain approximately constant: we will distinguish between the temperature (imposed) and the "temp real" which is the value the system is dragged to. We also want to check how many time steps we need to reach the stability since uranium has such a high atomic number. Let's see this in detail.

Running the simulation.
The simulations are divided in modules: in the first part we need to create a three-dimensional bcc cubic *box* with four atoms in the unit cell and then such a structure is repeated to build a *region* which sets the total number of atoms (see Figure 4.16). The parameters set in the "region" command are chosen so that the total number of atoms is at least[4] $\sim 10^3$ like in other works e.g. [67] or [135]. The lattice parameter for the potential we choose

```
# ---------- Create Atoms ---------------------
lattice     bcc ${latconst}
region      box block 0 10 0 10 0 10
create_box  1 box


create_atoms 1 box
replicate 1 1 1
```

Figure 4.16: First module in the NVE simulation: creating the atoms.

to use [135] is set to be $a = 3.493$ Å, but since we want to study the system stability, we actually take different lattice constants (which implies different volumes) and perform a simulation for each of them and in a wide range of temperature. So we study the system changing a over the interval

$$a \, \epsilon \, [3.0, \ldots, 3.9] \text{ Å} \tag{4.15}$$

in steps of 0.5 Å, and for each of these we change the temperature over the interval

$$\mathrm{T} \, \epsilon \, [0, \ldots, 1000] \, K \tag{4.16}$$

[4]We also check that if too few atoms are taken the fluctuations in the quantities we simulate are too high showing high standard deviations compared to their mean values.

in steps of 100 K to investigate its stability at high temperature. So we perform $19 \times 11 = 209$ simulations. All of them run 100000 steps in order to reach the equilibrium[5].

We then take the potential from [135] and set all the necessary parameters such as the neighbor list as shown in Figure 4.17.

```
# ---------- Define Interatomic Potential ---------------------
pair_style eam/alloy
pair_coeff * * U.eam.sss2012.alloy U
neighbor 0.3 bin
neigh_modify delay 10 check yes
```

Figure 4.17: How the simulation reads the potential and sets the parameters.

The last part is to let the system evolve and run for a number of time steps. Then with the *thermo_style* command we print the following quantities: the step (*step*), the potential energy (*pe*), the kinetic energy (*ke*), the temperature[6] (*temp*), the volume (*vol*) and the pressure (*press*).

```
# ---------- Dynamics ---------------------
fix 1 all nve
fix 2 all temp/rescale 10 ${tempconst} ${tempconst} 1.0 0.5
thermo 10
thermo_style custom step pe ke temp vol press
run 100000
```

Figure 4.18: The *fix* command to run the simulation.

Stability of the system: the temperature

For each value of the lattice constant a we perform a 100000 time step simulation and study the system stability. The software expands and contracts the region (depending on whether $a < 3.493$ Å or $a > 3.493$ Å), optimizing the structure and searching for the energy and the forces minimization. First of all we can look at the temperature behavior at every time step. We can see e.g. in Figure 4.19 how the system reaches the stability for the desired temperature T = 400 K for a box of lattice constant $a = 3.5$ Å. To check the stability we calculate the mean value and the standard deviation of the temperature: with the cut of the first 60000 time steps the mean temperature is

[5] we have run simulations with more time steps up to 5×10^6. However we have checked that the fluctuations of the quantities involved are the same once we applied the cut that will be described in the next sections

[6] as noted before we set a temperature value but the system undergoes a few transformations so this value is reached approximately. This is why it is important to print the "real" temperature of the system.

400.00 K with standard deviation equal to 1.29.

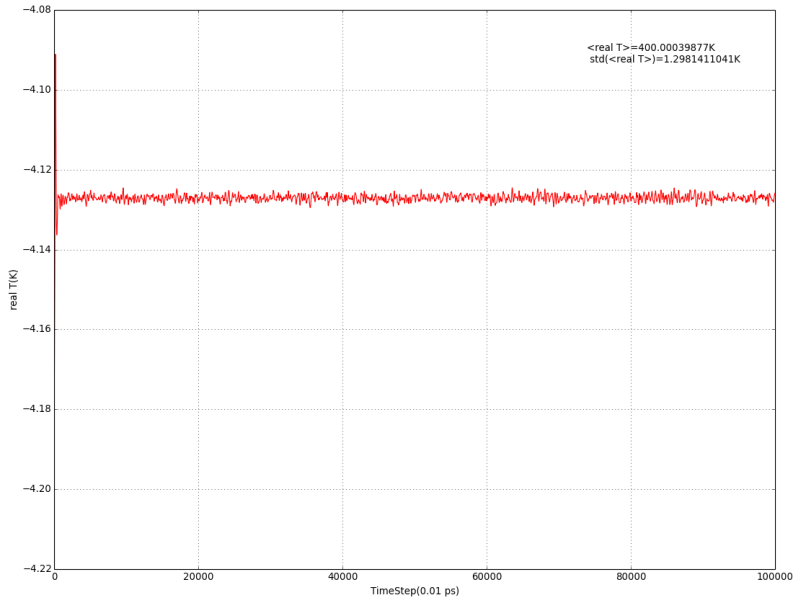

Figure 4.19: How the simulation drags the system to T = 400 K, as a function of time step (1 time step = 0.001 ps) for a bcc uranium with lattice constant $a = 3.5$ Å.

For each value of the lattice constant a we also plot the quantity $(T - Tr/T)$ which is the difference between the temperature we impose (T) and the "temp real" (Tr) normalized to the T for all the values of the temperature we study: from T = 100 K to T = 1000 K in steps of 100 K. We show in Figure 4.20 these quantities for a bcc uranium with $a = 3.5$ Å. In Appendix C one can find these quantities for each value of a. *These graphs show how the system behaves: in fact we can see that the quantity* $(T - Tr/T)$ *shows a spike when the simulation starts at* $t = 0$ *s because all the parameters have to reach the set condition and then approaches 0 within a few time step until the program runs.*

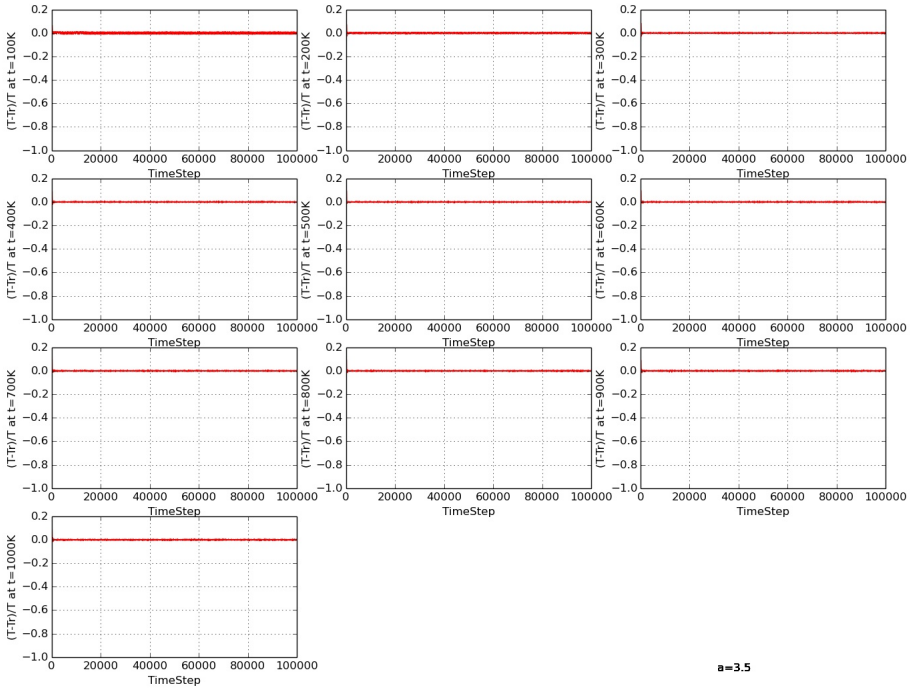

Figure 4.20: (T-Tr)/T as a function of time step (1 time step = 0.001 ps) for a bcc uranium with lattice constant $a = 3.5$ Å for each temperature from T = 100 K to T = 1000 K (in steps of ΔT= 100 K).

4.2.1 NVE results

Stability of the system: the energy per atom.
We now want to check whether we are able to gauge the other variables of the system: energy per atom and pressure[7] of the system. So for $a = 3.4$ Å, $a = 3.5$ Å and $a = 3.6$ Å we also show the energy per atom as a function of the time step for all the temperatures from T = 100 K to T= 1000 K. We choose to do this because $a = 3.5$ Å is the closest value to the lattice parameter set in the EAM potential for uranium: 3.493 Å (Figure 4.21-Figure 4.23). We only report these values here to study this atom configuration around the value $a = 3.5$ Å. In Appendix C all values for each lattice constant are

[7]during the NVE simulation the volume is constant.

reported. *We can see that the energy per atom tends to a stable value: this*

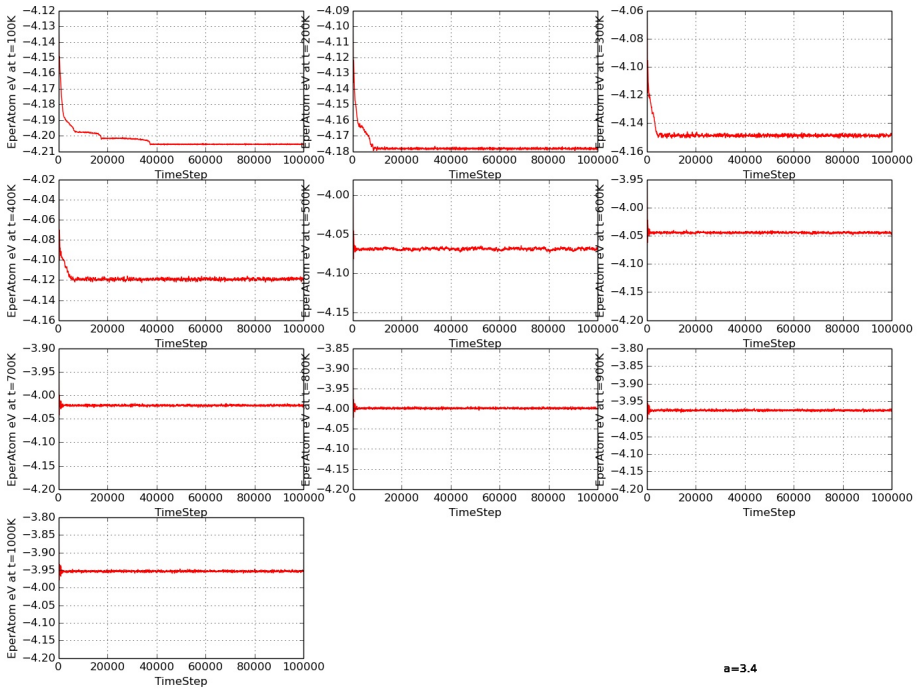

Figure 4.21: Energy per atom (in eV) as a function of time step for a bcc uranium with lattice constant $a = 3.4$ Å in the temperature interval T = 100 K $\rightarrow$ T = 1000 K with ΔT= 100 K. Each plot refers to a constant value of T.

is in fact expected and can be considered a good test for the NVE simulations whose goal is to represent a microcanonical ensemble. Like in the previous section we check the mean total energy and the standard deviation after 60000 time steps.

Once we made sure to be able to control all these physical quantities, let's have now a better look at the energy per atom as a function of the temperature: in Figure 4.24 we show all the curves for all the lattice constants. The more the system is compressed the higher the energy per atom gets, and when it is too relaxed ($a > a_{eq} = 3.493$ Å) the energy fluctuates more than in the range $a \sim a_{eq}$. We can compare our results with the theoretical work

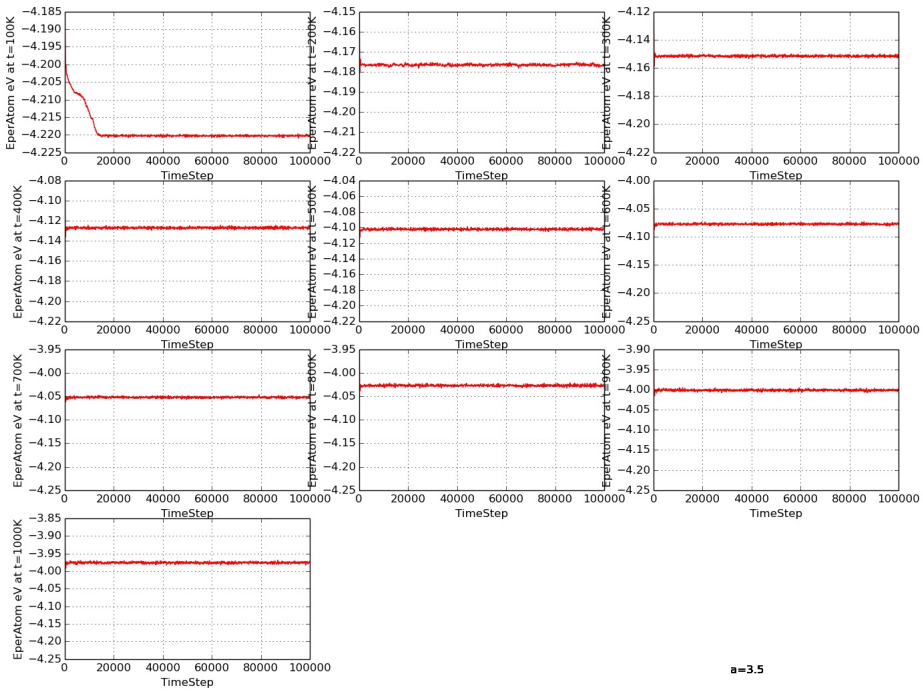

Figure 4.22: Energy per atom (in eV) as a function of time step for a bcc uranium with lattice constant $a = 3.5$ Å in the temperature interval T = 100 K $\rightarrow$ T = 1000 K with ΔT= 100 K.

[154] and the experimental work [155] both about bcc γ-U. In both these papers the temperature range varies between 800 K and 2000 K, whereas we study here the system between 100 K and 1000 K. So we can only compare a few values. However, we find that the energy per atom is within 1 eV/atom of experimental values and has approximately the same slope versus temperature. Our values are higher than theirs, and this difference is probably due to the choice of the potential. In fact Beeler *et al.* [154] use a MEAM potential and find lower values compared to the experimental data, showing once again some dependence of the work from the choice of the potential.

Stability of the system: the pressure.
We also want to check how the pressure changes after a certain number of

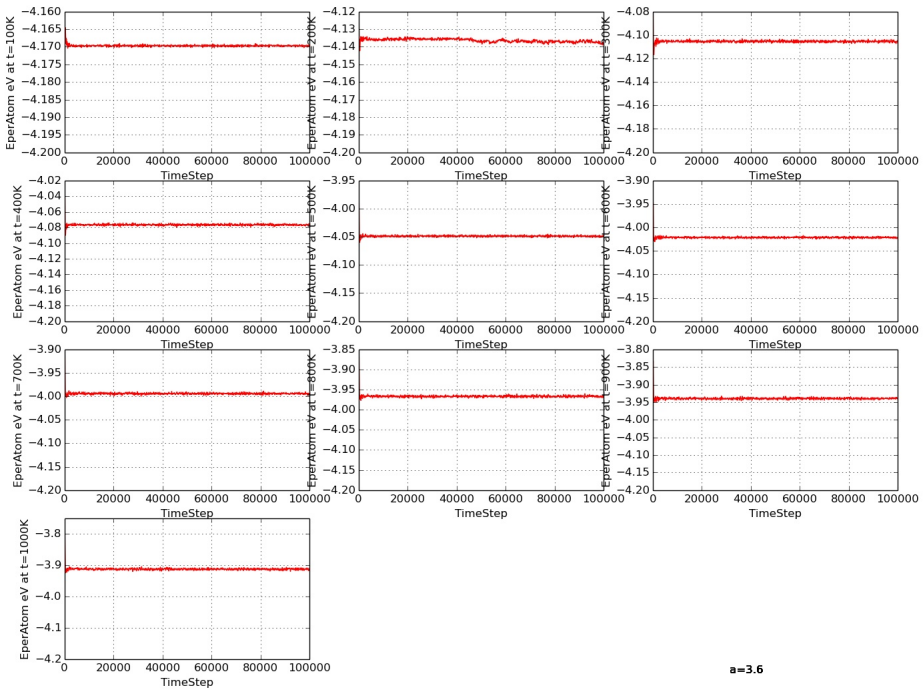

Figure 4.23: Energy per atom (in eV) as a function of time step for a bcc uranium with lattice constant $a = 3.6$ Å in the temperature interval T = 100 K $\rightarrow$ T = 1000 K with ΔT= 100 K.

time steps. For the pressure we do not set any value in the NVE simulation: however we find that this variable becomes stable after a certain amount of time steps. So we present the behavior of the pressure at each time step for the values of lattice constant $a = 3.4$ Å, $a = 3.5$ Å and $a = 3.6$ Å (Figure 4.25-Figure 4.27). The pressure of the system is positive when $a = 3.4$ Å because the crystal is contracted; it is close to 0 GPa when the lattice constant is $a = 3.5$ Å because the relaxation constant is equal to $a = 3.493$ Å; and it is negative when the system is dilated ($a = 3.6$ Å) (Figure 4.25-Figure 4.27). In Appendix C we can see these graphs for all the values of the lattice constant. We can see that as the temperature rises the pressure gets coherently higher.

And last we can see in Figure 4.28 the pressure behavior as a function

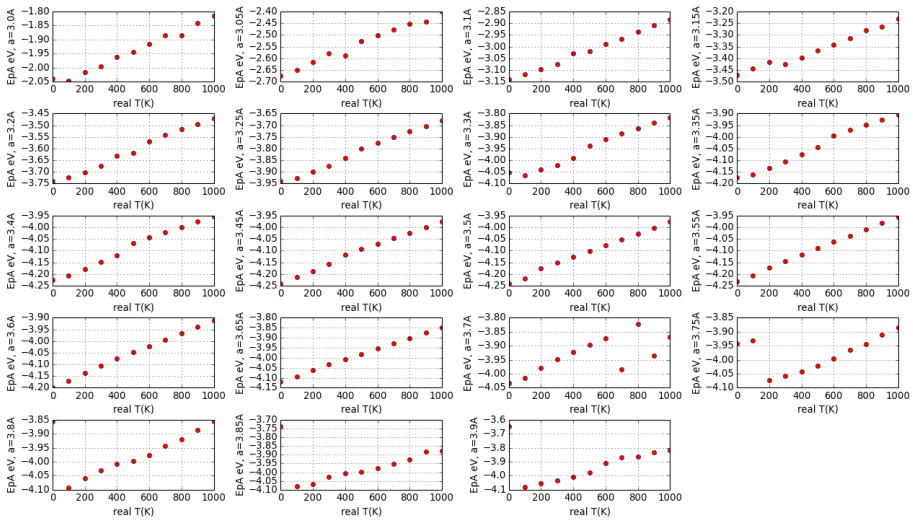

Figure 4.24: Energy per atom (in eV) as a function of the temperature. Each curve refers to a lattice constant from $a = 3.0$ Å to $a = 3.9$ Å.

of the volume of the region: each curve is an isothermal. The pressure decreases with increasing volume.

Lattice constant and cohesive energy.
A very important result is to study where the energy minimum is reached. We want to do this for three sample temperatures since we need to study the system over such a wide range of temperature. It is in fact expected that the minimum energy configuration is the one corresponding to the closest lattice parameter to $a = 3.493$ Å and we want to see whether this happens $\forall$ T. So for the temperature T = 100 K, T = 400 K and T = 700 K we show the curves of the energy per atom as a function of the lattice parameter. Since the system experiences some fluctuations during the minimization process we choose as a cutoff[8] value Λ for the time step

$$\Lambda_{\text{timestep}} > 60000 \tag{4.17}$$

In Figure 4.29-Figure 4.31 we can see the energy per atom as a function of the lattice parameter a: since for every a we let the system evolve for 100000 time step, these values here are average values over the interval $60000 <$ **timestep** ≤ 100000. Also the standard deviation is shown [136]. The

[8] we have checked the standard deviation of the mean for values below Λ and above Λ

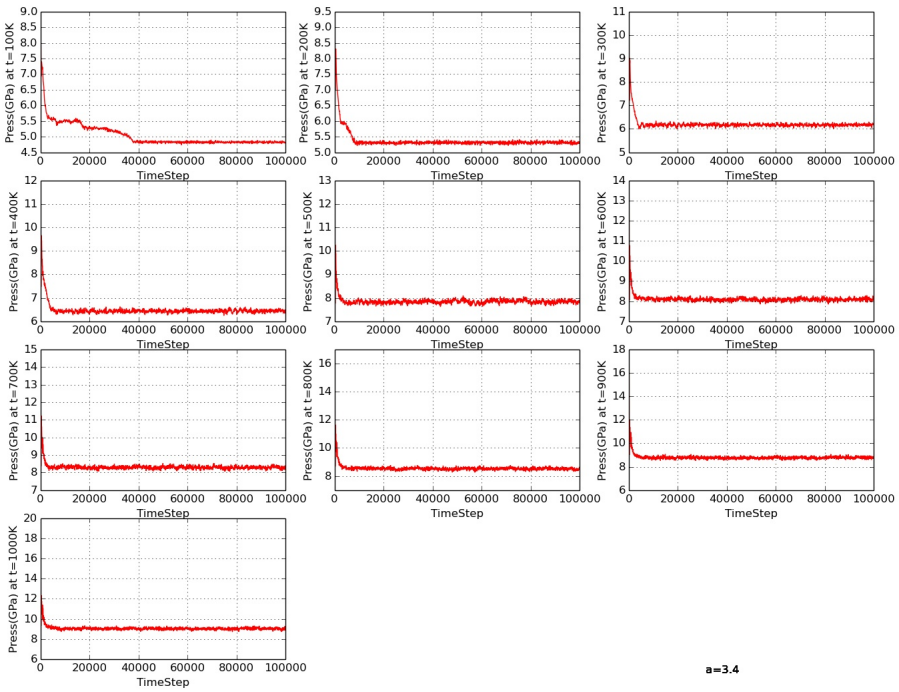

Figure 4.25: Pressure in GPa as a function of time step for a bcc uranium with lattice constant $a = 3.4$ Å, in the temperature interval between T = 100 K and T = 1000 K with ΔT = 100 K. Each plot refers to a constant value of T.

standard deviation is computed with the package *numpy* in [139]. At T = 100 K the minimum configuration energy per atom is reached for $E_{min} = -4.22$ eV at $a = 3.5$ Å; at T = 400 K the minimum configuration energy per atom is reached for $E_{min} = -4.12$ eV at $a = 3.5$ Å; and at T = 700 K the minimum configuration energy per atom is reached for $E_{min} = -4.05$ eV at $a = 3.5$ Å. This value is the closest one to the "real" lattice parameter: this configuration is the most stable. **This means the system under study is stable up to this temperature**. In each of these graphs we can see that around $a = 3.7$ Å the system experiences a rise of the energy and this phenomenon seems to happen at smaller a as the temperature increases. This may be due to the fact that the potential reliability starts to decrease since uranium is such a

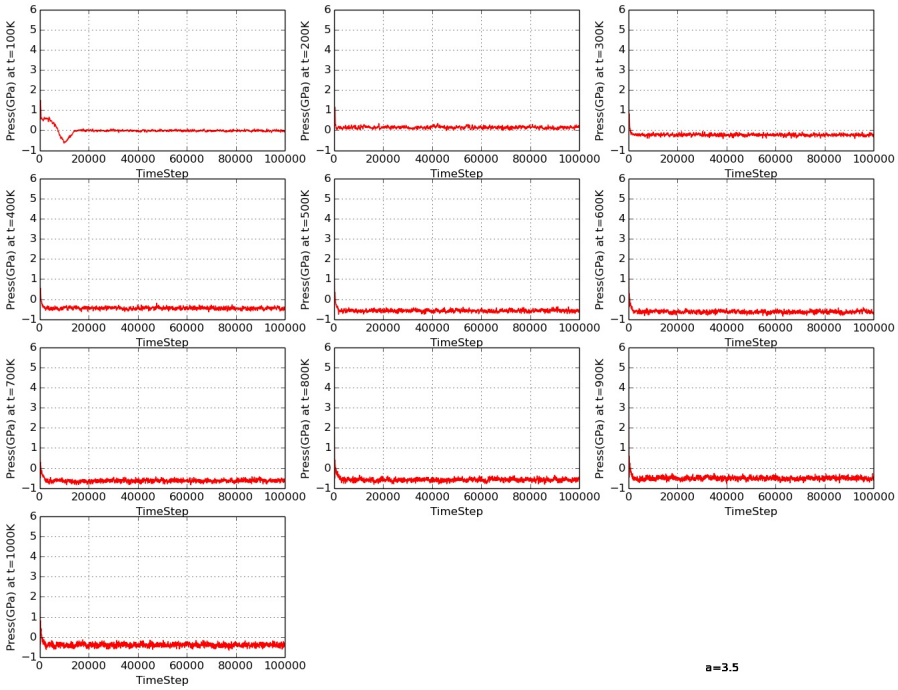

Figure 4.26: Pressure in GPa as a function of time step for a bcc uranium with lattice constant $a = 3.5$ Å, in the temperature interval between T = 100 K and T = 1000 K with ΔT = 100 K.

heavy element and this value of the lattice parameter is getting far from the one the potential is set for, while T is rising. Besides, even though the most stable configuration is the one at $a = 3.5$ Å, as the temperature rises the energy increases, as expected.

Accuracy of the simulations.

We highlight that every time we compute a mean value we always check the standard deviation associated to be sure that the quantity we are computing doesn't show high fluctuations. In fact for sufficiently small time steps the method of molecular dynamics provides the right accuracy. Numerical errors are always associated to a numerical method but we always make sure to check that the mean and the variance can be brought into agreement with the expected values.

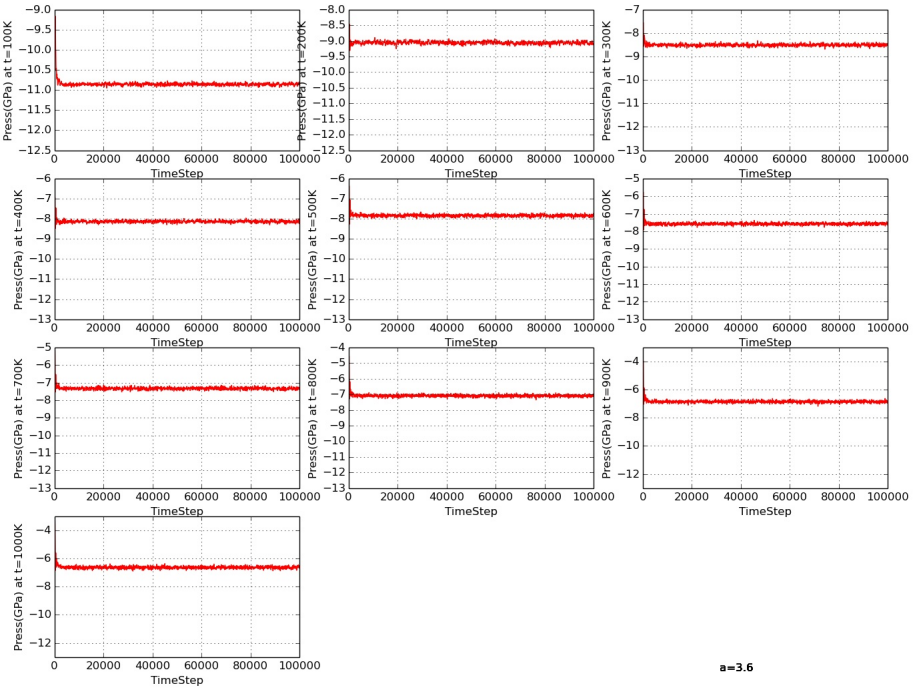

Figure 4.27: Pressure in GPa as a function of time step for a bcc uranium with lattice constant $a = 3.6$ Å, in the temperature interval between T = 100 K and T = 1000 K with ΔT = 100 K.

4.3 The simulations structure: NPT

We are now interested in studying the system under predictable conditions of pressure. Such a situation can be reached through a NPT simulation. In fact in the NVE ensemble no thermostat nor barostat is introduced to regulate the temperature or the stress. We made sure that the time step is appropriate and the numerical integrator is then implemented correctly. The NPT integration is a method that creates an isothermal-isobaric ensemble during which the positions and the velocities are updated at each time step in a group of atoms, using a Nosé-Hoover integrator [147]. We first perform NVE simulations and then NPT simulations because we are interested in studying the system under these conditions separately. Once the equilib-

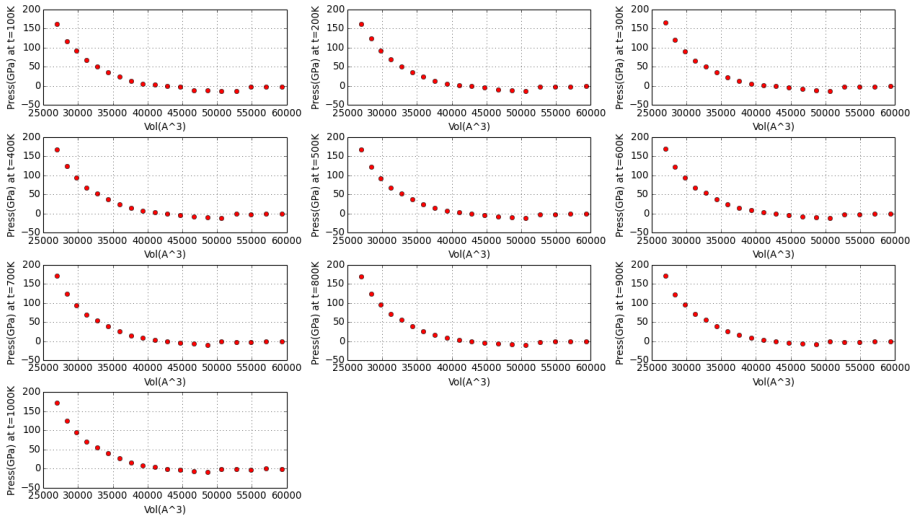

Figure 4.28: Pressure in GPa as a function of the volume of the region. Each curve refers to a constant value of the temperature.

rium is reached after 100000 time steps with the NVE, all the configurations are saved in a data file which is then read at the start of the NPT run. In this way we make sure the system is in a predictable state whose parameters (such as volume, pressure, energy per atom and temperature) we do know. The NPT runs 400000 time steps because we check for all the configurations that this amount of time step is appropriate to drag the box to the P and T desired. The thermostat/barostat works as follow: at each time step the temperature/pressure are ramped values and it is possible to specify a starting value and a stop value and how fast the variables have to be relaxed (in time units).

For what concerns this work we are studying a region filled with 2000 uranium atoms that is at first dragged to a stable state with a NVE simulation. Then we are exposing it to an external pressure and an external temperature the system will come to equilibrium with within a number of time step. We are focusing on how such a region of space behaves under these extreme conditions. And we want to see whether we can find any physical quantity to use as a marker for any variation.

Once again we study the system changing a over the interval

$$a \, \epsilon \, [3.0, \ldots, 3.9] \text{ Å} \tag{4.18}$$

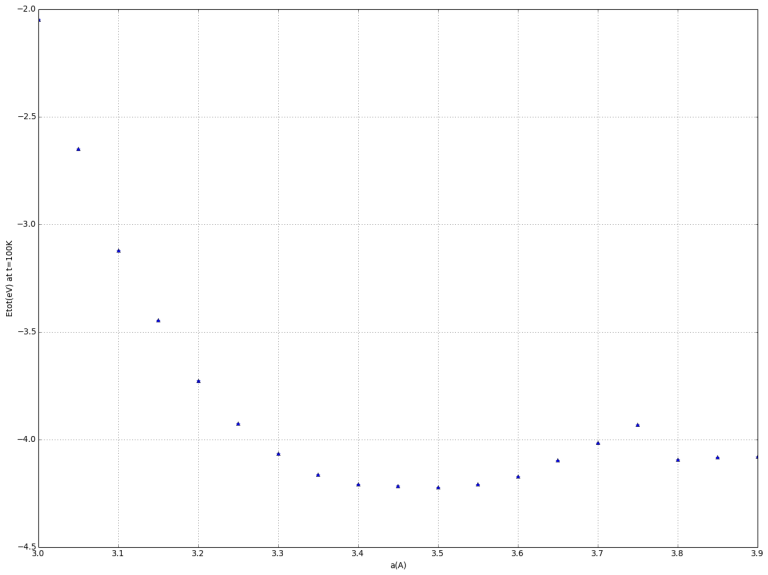

Figure 4.29: Energy per atom (potential plus kinetic) in eV as a function of the lattice constant a in Å at $T = 100$ K. Each point (with standard deviation) is the average value for that lattice parameter over the steps from 60000 to 100000.

in steps of 0.5 Å. This time though for each of these configurations we take three values of temperature imposed, i.e.

$$\mathrm{T} = 100 \text{ K},\ \mathrm{T} = 400 \text{ K},\ \mathrm{T} = 700 \text{ K} \tag{4.19}$$

and three values of external pressure imposed

$$\mathrm{P}^{ext} = 1 \text{ GPa},\ \mathrm{P}^{ext} = 20 \text{ GPa},\ \mathrm{P}^{ext} = 100 \text{ GPa} \tag{4.20}$$

So for all of the 19 configurations each corresponding to a lattice parameter a we run 3×3 simulations for a total of $19 \times 3 \times 3 = 171$.

Each run starts by reading the corresponding final NVE configuration. Clearly if at the beginning the system finds itself in a configuration such that $a < 3.493$ Å it will be initially compressed, when in fact in the case $a > 3.493$ Å it will be dilated and its reaction to an external pressure will vary consequently. We now show a sample of the results. In this case for a given lattice parameter a (corresponding to a volume) we set the temperature and let the system reach the desired pressure. In Figure 4.32 we can see the pressure (in GPa) of the system as a function of the time step for $a = 3.0$

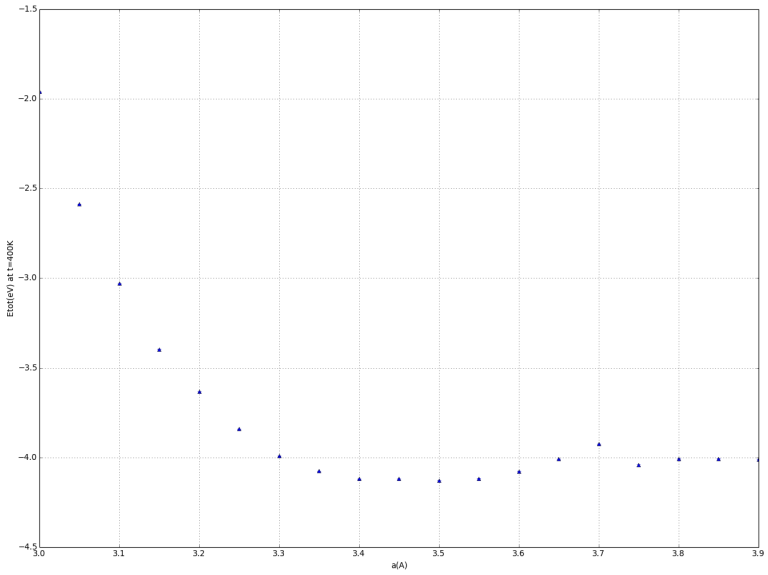

Figure 4.30: Energy per atom (potential plus kinetic) in eV as a function of the lattice constant a in Å at $T = 400$ K. Each point (with standard deviation) is the average value for that lattice parameter over the steps from 60000 to 100000.

Å. The three graphs on the left from upside to downside correspond to the three values of the temperature (100 K, 400 K, 700 K). Moving from left to right, for a given temperature, the external pressure to be reached varies: 1 GPa, 20 GPa, 100 GPa. We first notice that the system is always driven to the desired value of external pressure within 400000 time steps (the time step scale is divided by a factor 10^3). We can also see, by looking at the angle between the curve and the P axis, that the higher the temperature is the more smoothly the system reaches the pressure imposed. This is because if the particles are already excited it takes less effort to get to the desired pressure. In this case the region is very compressed compared to its "natural" state (i.e. $a = 3.493$ Å): this means that any perturbation leads to a big change in the system. So the pressure drops quickly as in an elastic rebound and then approaches the desired value. For the same configuration we also show in Figure 4.33 and Figure 4.34 the energy per atom and the real temperature versus the time step. We must highlight that the temperature is slightly different than the one imposed. We can see that consequently to a drop of pressure the energy per atom increases in absolute value and

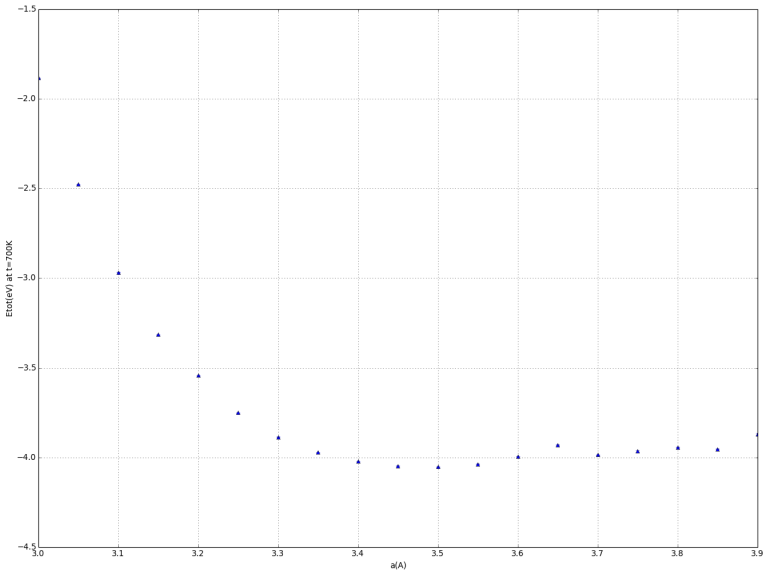

Figure 4.31: Energy per atom (potential plus kinetic) in eV as a function of the lattice constant a in Å at $T = 700$ K. Each point (with standard deviation) is the average value for that lattice parameter over the steps from 60000 to 100000.

then decreases. The real temperature is calculated by rescaling the velocities and the positions of the particles involved every N time steps and is then a discrete operation: a target temperature is set and rescaling happens only if the difference between the current temperature and the desired one is above a threshold value that is also set by the user. We also show the dilatation of the system corresponding to this transformation: in Figure 4.35 the length of the box versus the time step is shown. In Appendix D we report all these graphs for all the lattice parameters. We show here a sample of all these quantities for $a = 3.0$ Å, $a = 3.5$ Å and for $a = 3.7$ Å corresponding respectively to a value below the relaxation lattice constant, one close to it and one above.

When we get closer to $a = 3.493$ Å the system finds itself in equilibrium in its natural state and we are exposing it to an external pressure. The response of such a configuration is that the system opposes to this transformation and so it oscillates as we can see in Figure 4.36. This phenomenon is faster (and so the curve is less thick) when the external pressure grows, since the region has to approach a higher value in the same amount of time steps. In Figure 4.37

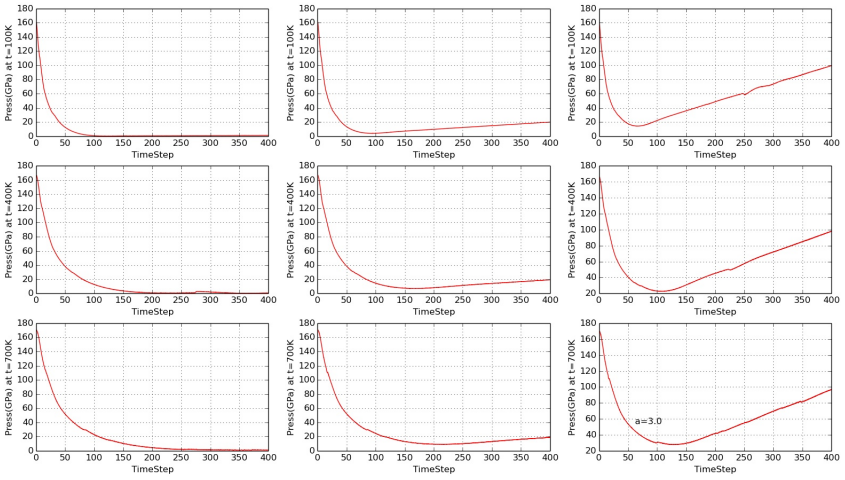

Figure 4.32: Pressure (GPa) as a function of the time step (divided by 10^3) for a system with $a = 3.0$ Å. The temperature is fixed going from left to right, whereas moving from upside to downside the behavior with fixed external pressure varying the three temperature imposed is shown.

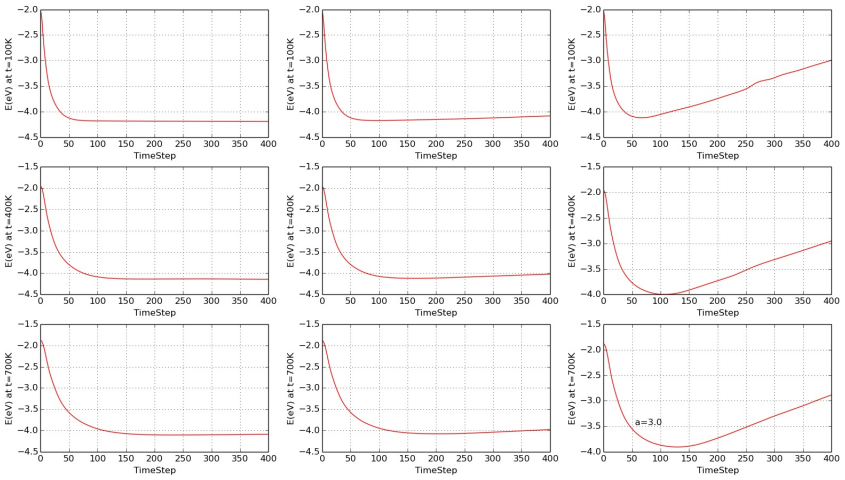

Figure 4.33: Energy per atom (in eV) as a function of the time step (divided by 10^3) for a system with $a = 3.0$ Å.

we can see the energy per atom. In Figure 4.38 we show the temperature real: once again the temperature swings. The higher the pressure, the less the box stays close to the temperature imposed, coherently. And in Figure 4.39 we

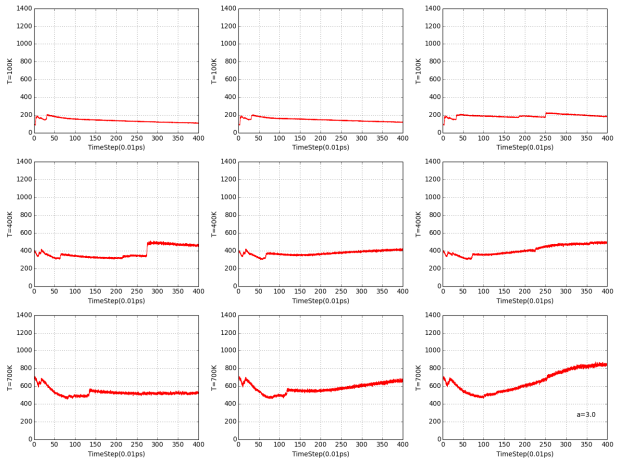

Figure 4.34: Real temperature (in K) as a function of the time step (divided by 10^3) for a system with $a = 3.0$ Å.

see the box length that will contract as the pressure rises. For the case $a = 3.7$ Å we report the same graphs: Figure 4.40 shows all the graphs for the pressure. This time it is pretty clear that the system is very much relaxed and is brought to a higher value of pressure. The corresponding energy per atom in Figure 4.41 increases when the pressure drops and decreases when the pressure rise. The temperature swings again, Figure 4.42. It is important that when we study the system we keep in mind what the real temperature is. And last in Figure 4.43 we can see the corresponding change in the length of the box.

4.4 Bulk moduli as markers during transient states

So far we have computed the bulk modulus of a box of 2×10^3 atoms of uranium with an external pressure applied under different temperature conditions. So we have produced the isothermal/isobaric curves previously seen. We now want to analyze the *transient states*, which means we are interested in the difference between several equilibrium states. When studying such a system of atoms we have described a box replicated every time starting from different initial conditions and exposed to different physical conditions. All these boxes are non-interacting. But to better understand the differences between the equilibrium states we bring them to, it is useful to study how the bulk modulus varies between different equilibrium states. i.e. **we mean**

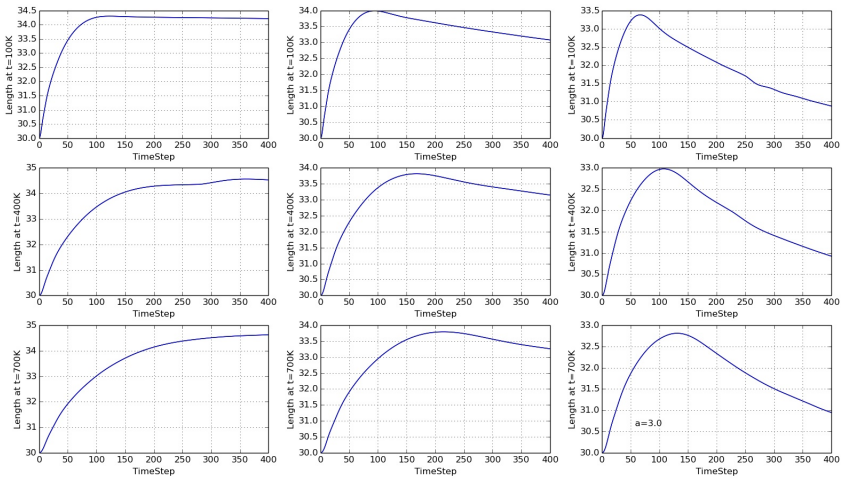

Figure 4.35: Box side length (in Å $\times 10$) as a function of the time step (divided by 10^3) for a system with $a = 3.0$ Å

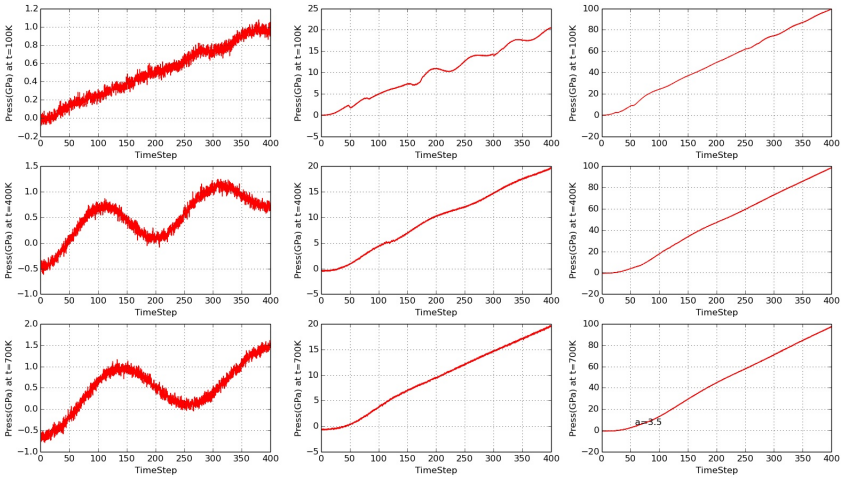

Figure 4.36: Pressure (GPa) as a function of the time step (divided by 10^3) for a system with $a = 3.5$ Å.

to use the bulk modulus as a marker of the response of the system to an applied gradient of pressure or temperature.

In order to actually see how this marker at a given temperature has changed from a configuration to another when an external pressure is applied we now plot the difference between the bulk modulus at a given pressure and

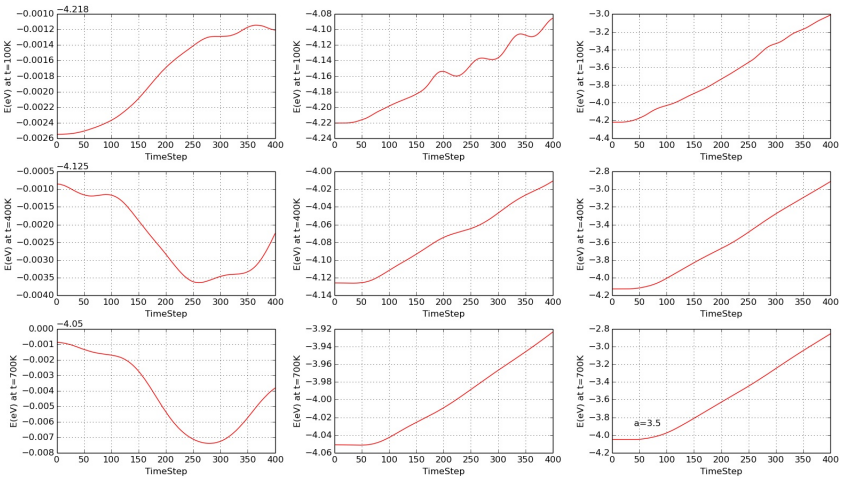

Figure 4.37: Energy per atom (in eV) as a function of the time step (divided by 10^3) for a system with $a = 3.5$ Å.

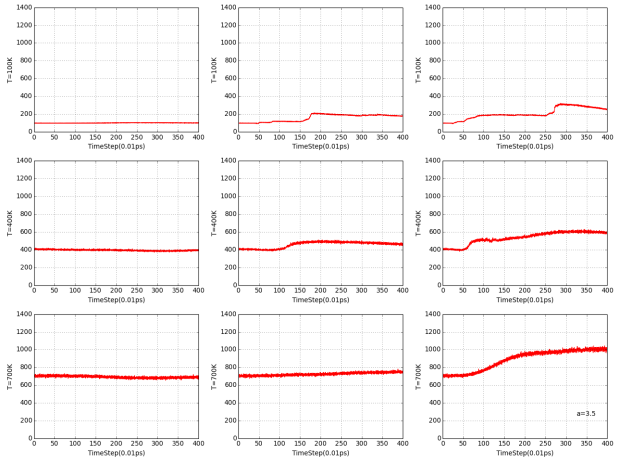

Figure 4.38: Real temperature (in K) as a function of the time step (divided by 10^3) for a system with $a = 3.5$ Å.

the bulk modulus at a different pressure normalized to the latter, i.e.

$$\frac{\mathrm{B(P}_i) - \mathrm{B(P}_j)}{\mathrm{B(P}_j)} \tag{4.21}$$

where the indices i, j refer to the external values of pressure. In this way we can realize how big a change the bulk modulus has undergone and how a box

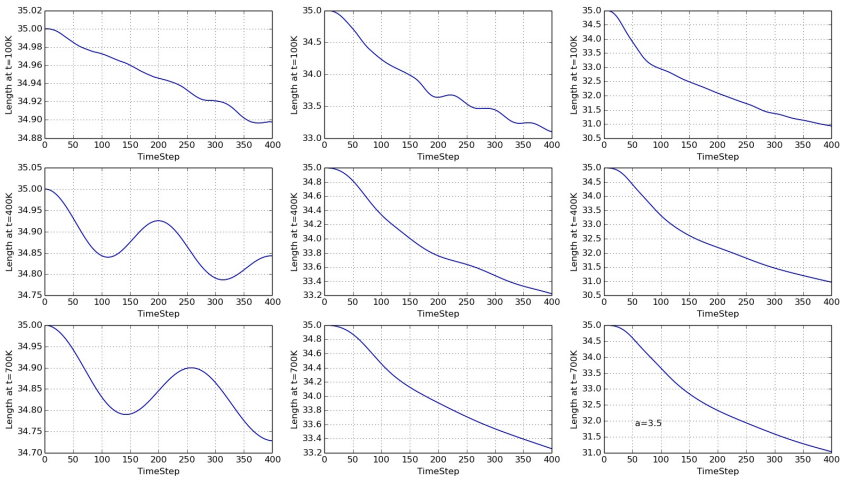

Figure 4.39: Box side length (in Å $\times 10$) as a function of the time step (divided by 10^3) for a system with $a = 3.5$ Å

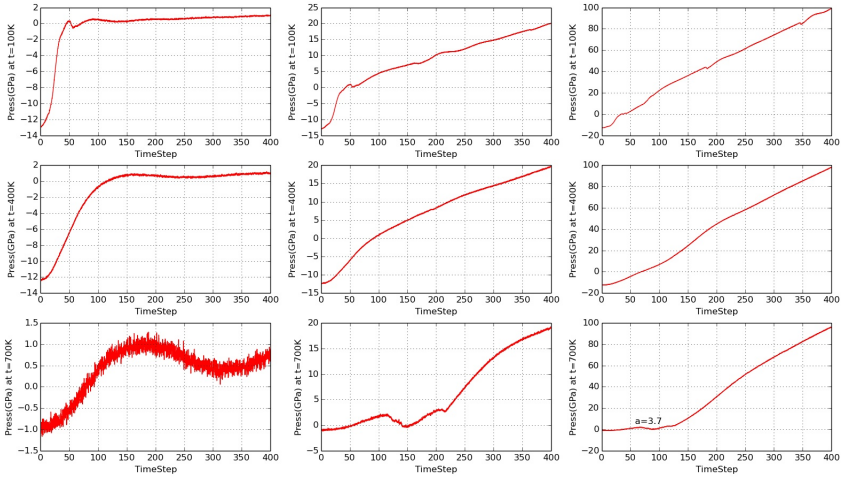

Figure 4.40: Pressure (GPa) as a function of the time step (divided by 10^3) for a system with $a = 3.7$ Å.

of uranium made up of 2000 atoms would react in going from a configuration to another under a given temperature. Since we have thirteen values of the external pressure and we compare each one with one other, we only report a few samples here for: $P^{ext} = 20$ GPa (Figure 4.44); $P^{ext} = 50$ GPa (Figure 4.45); $P^{ext} = 100$ GPa (Figure 4.46). All the other plots are reported

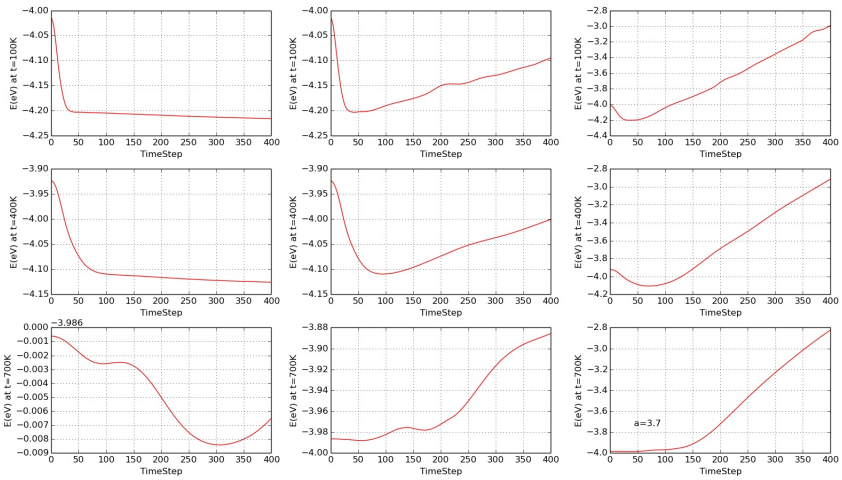

Figure 4.41: Energy per atom (in eV) as a function of the time step (divided by 10^3) for a system with $a = 3.7$ Å.

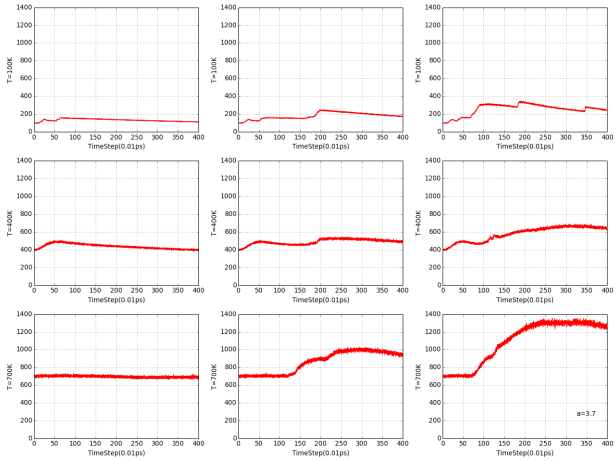

Figure 4.42: Real temperature (in K) as a function of the time step (divided by 10^3) for a system with $a = 3.7$ Å.

in Appendix E. We choose to plot these quantities because they show that for a system such as the one we simulate at a given temperature we can quantify the change in pressure. For example, let's look at Figure 4.44: we can see in the first figure up on the left that at T = 400 K the bulk modulus between a box exposed to 20 GPa and one at 0 GPa doubles. The higher

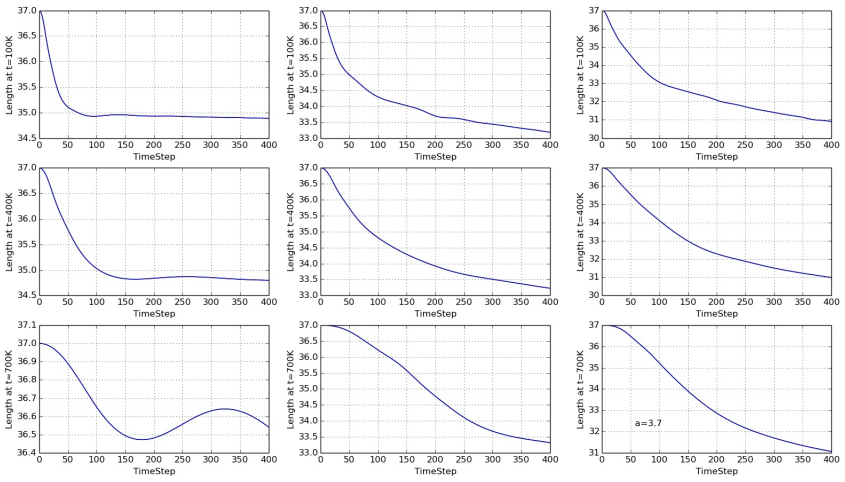

Figure 4.43: Box side length (in Å $\times 10$) as a function of the time step (divided by 10^3) for a system with $a = 3.7$ Å

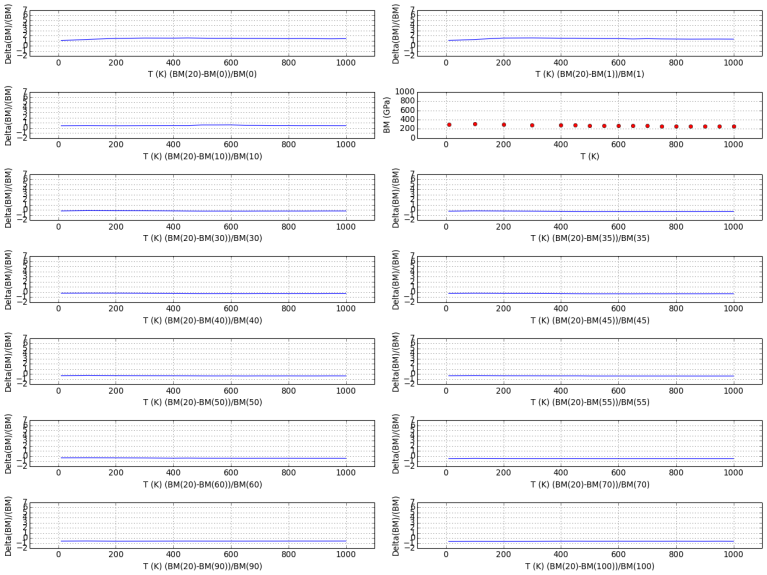

Figure 4.44: Difference between the bulk modulus of a system at $P^{ext} = 20$ GPa and the bulk values at all the other values of pressure. The graph with the red dot is the dependence of the bulk modulus from the temperature at that external pressure.

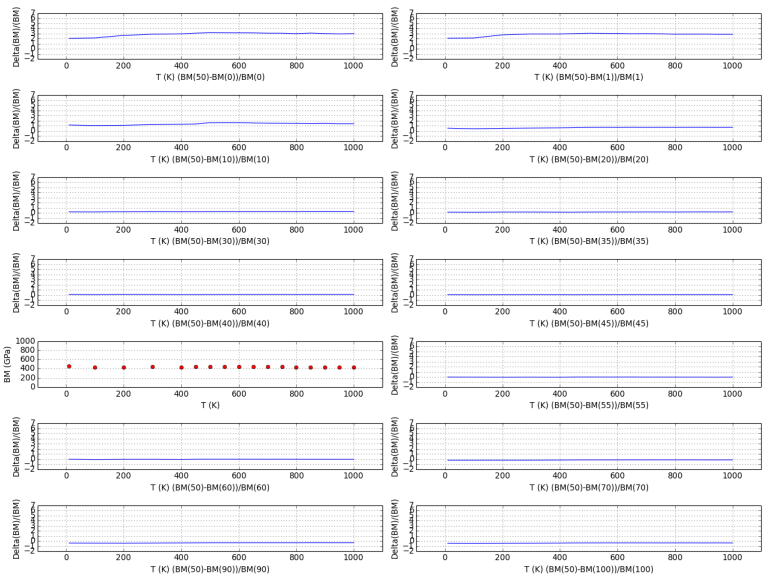

Figure 4.45: Difference between the bulk modulus of a system at $P^{ext} = 50$ GPa and the bulk values at all the other values of pressure. The graph with the red dot is the dependence of the bulk modulus from the temperature at that external pressure.

the difference in pressure is the higher the difference in the bulk is, but this not systematic. **These graphs are useful because they allow us to say that for a given temperature, if a cluster of uranium atoms finds itself in such a configuration at a given internal pressure and it is exposed to a different pressure to come to equilibrium with, it experiences a variation we can now quantify. We can hence use the bulk modulus as a marker for such a variation**.

4.4.1 Pressure distribution

We now want to look at the pressure distribution over all the simulations we have performed. For a fixed value of the lattice constant a between 3.0 Å and 3.9 Å we now show the difference between the pressure of the box and the external pressure for: P^{ext} = 1 GPa, 20 GPa, 100 GPa. We do this for the temperature values T = 100 K, 400 K, 700 K. We only report here a sample for a = 3.0 Å (Figure 4.47), a = 3.5 Å (Figure 4.48) and 3.7 Å (Figure 4.49). In Appendix E all the plots are reported. On the

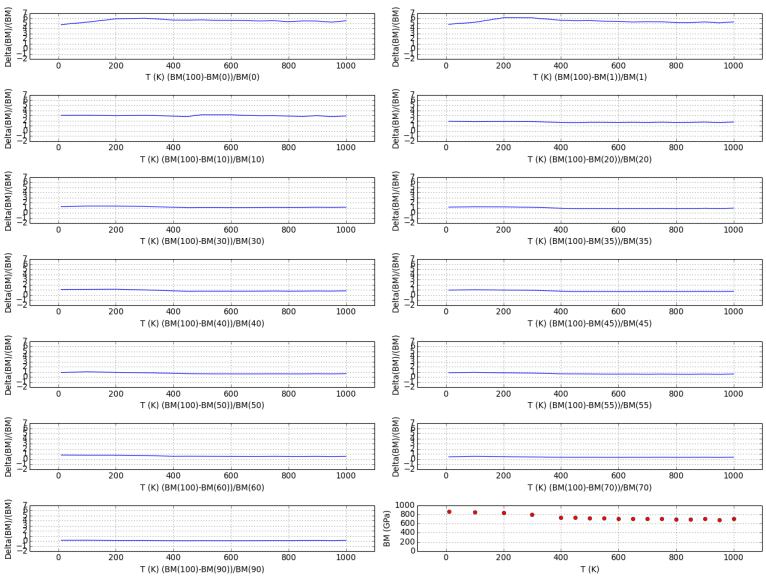

Figure 4.46: Difference between the bulk modulus of a system at $P^{ext} = 100$ GPa and the bulk values at all the other values of pressure. The graph with the red dot is the dependence of the bulk modulus from the temperature at that external pressure.

x-axis there is the distribution of the difference between the pressure of the system and the external pressure imposed. These graphs show some important issue: we can say that for example if an uranium distribution of atoms e.g. such that $a = 3.0$ Å in a region of space finds itself at 100 K and is exposed to a 100 GPa pressure there is a higher probability to find such a cluster in a different pressure state causing some gradient phenomenon than in the case at $P^{ext} = 1$ GPa. Let's look at Figure 4.48: at 100 K and $P^{ext} = 100$ GPa the bin corresponding to a difference of $|\Delta P \sim 100|$ GPa is highly populated. Clearly this ΔP can be negative or positive depending on which is the pressure of the box: let's recall that the equilibrium is around $a = 3.5$ Å so the cluster can be contracted or dilated. This scenario gives us a a quantitatively approach to the variation of pressure in such a complex environment.

We can see that when brought at 1 GPa of external pressure the system experiences the smallest variation in pressure, even though when raising the temperature these ΔP rise. At $P^{ext} = 20$ GPa the bins with higher variation start to populate consistently. For example for $a = 3.5$ Å we can see a $\Delta P =$

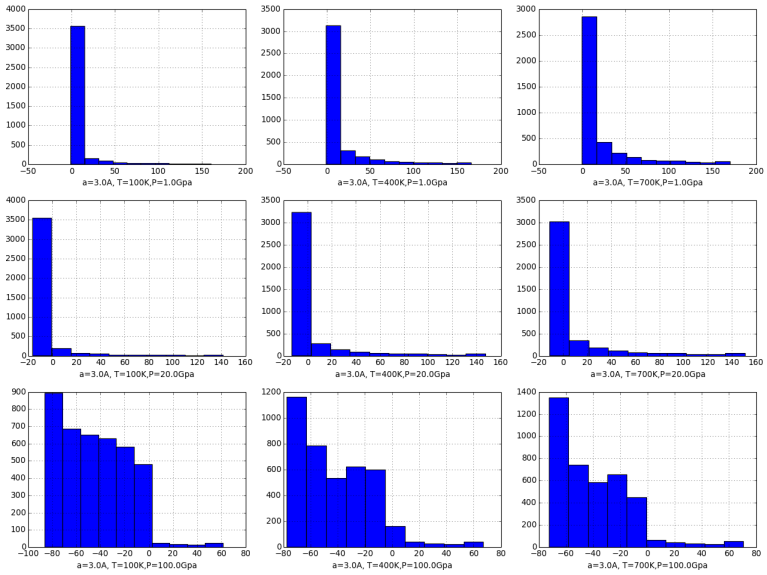

Figure 4.47: Distribution of the difference between the pressure of the box with lattice constant $a = 3.0$ Å and the external pressure at different temperature.

|20| GPa and this variation increases with increasing volume, so that at $a = 3.7$ Å it is even higher. When the box is dragged to $P^{ext} = 100$ GPa hence we can see the highest pressure variation: in all configurations of volume there is a variation of ~ 100 GPa at each temperature. From a physical point of view this means that for example if 2000 atoms of uranium gather up forming a box around the equilibrium configuration at T = 400 K and if they happen to be in a environment where the pressure is ~ 100 GPa they experience a 100 GPa variation in their pressure reaching the equilibrium with the environment. An energy gradient would definitely occur in such a change. This analysis can be done for each value of pressure/volume/temperature studied in this work which can be considered as a database of markers to look at when needed.

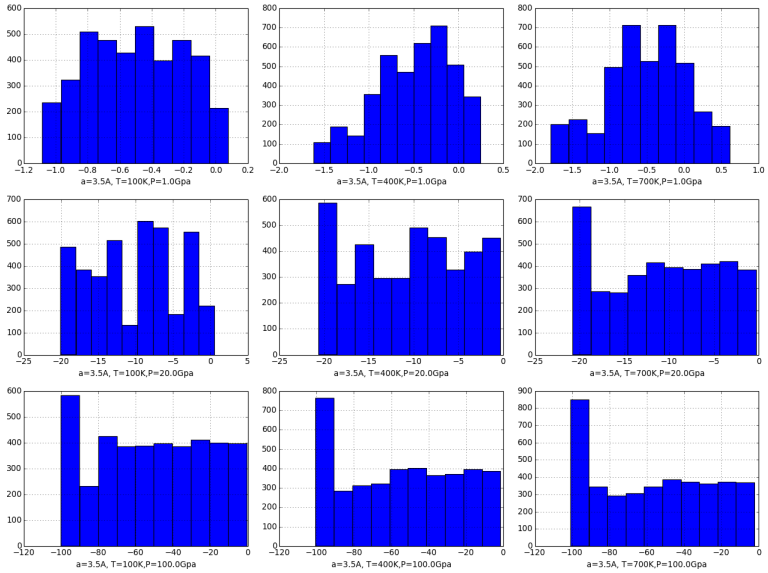

Figure 4.48: Distribution of the difference between the pressure of the box with lattice constant $a = 3.5$ Å and the external pressure at different temperature.

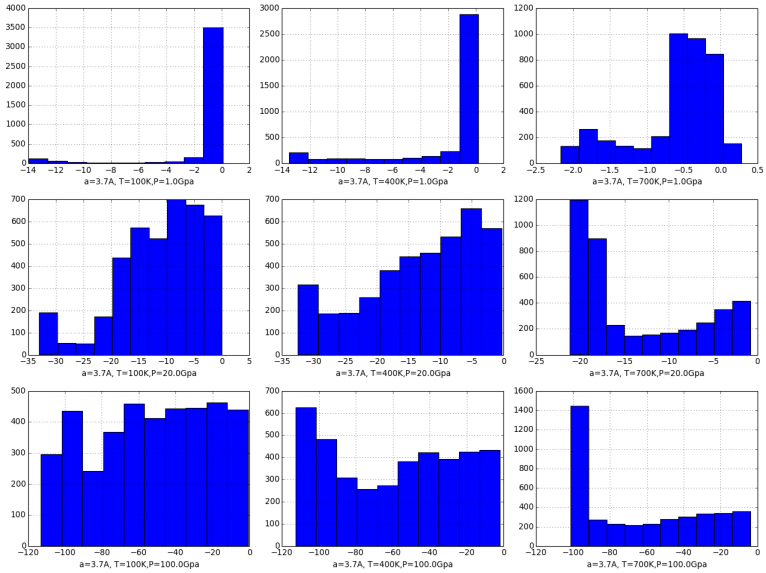

Figure 4.49: Distribution of the difference between the pressure of the box with lattice constant $a = 3.7$ Å and the external pressure at different temperature.

Chapter 5

Conclusions

The comprehension of the dynamics of earthquakes and the seismic source physics in a deterministic way is a challenging task requiring a multiple approach. There has been a huge effort to build up a constituent law of earthquakes involving all the processes occurring: such processes happen over a wide range of time and space scale sometimes overlapping, and this is why when building a numerical model, one needs to take into account that these processes can interact with each other and/or compete. Of course a phenomenological model has to be related to the available sets of surveys.

In this thesis we aimed at making some steps forward in this complex scenario toward a more complete comprehension of seismic source physics.

In fact numerical models regarding the physics of seismic source have been developed and implemented in order to gather a lot of physical and chemical processes and laboratory data. However all the phenomena studied so far haven't been considered to include any radioactive process that we do know happen in the Earth interior: in fact 70 % of the total heat flux and energy produced inside the Earth crust and mantle comes from the decays of the three mainly present radioactive elements, i.e. ^{238}U, ^{235}U, ^{232}Th and ^{40}K. Uranium itself provides $\sim 25\%$ of the total heat flux at the Earth surface and is mainly present in the mantle, even though we cannot constrain the exact distribution yet.

Besides, all the mechanisms occurring in a fault structure that have been studied so far happen over a temporal scale between $\sim 10^{-6}$ s and $\sim 10^{14}$ s and over a spatial scale between 10^{-6} m and $\sim 10^{6}$ km, such as melting, nucleation, thermal pressurization etc.

We aimed at investigating processes occurring over a time scale between $\sim 10^{-11}$ s and $\sim 10^{-9}$ s and over a space scale of up to 10^{-1} Å which seem

to happen in a blind zone yet unexplored.

We chose to perform our numerical simulations with the LAMMPS software using a Classical Molecular Dynamics simulation approach: the first step has been to pick a potential describing the interactions between the atoms in the system. In fact we simulated a cubic bcc uranium box with 2×10^3 atoms. We chose the EAM potential previously developed and tested to be valid over a wide range of temperature and pressure: this approach provides a description of the atoms interactions made up of an electron gas due to all the atoms where a particle is embedded.

It was then necessary to confirm the validity of such a potential. So we aimed at reproducing some known properties of uranium crystal. We decided to compute the elastic constants and its polycrystalline properties such as bulk modulus, Young modulus and shear modulus. Elastic constants are defined to be $C_{ijkl} = \frac{\partial \sigma_{ij}}{\partial e_{kl}}$, where σ_{ij} is the applied stress and e_{kl} is the strain tensor, whereas for a cubic system the bulk modulus is defined as $B = [2(C_{12} + C_{13} + C_{23}) + C_{11} + C_{22} + C_{33}]/9$, the Young modulus $E = \frac{9BG}{(3B+G)}$ and the shear modulus $G = \frac{1}{2}\left[\frac{C_{11}-C_{12}-3C_{44}}{5} + \frac{5C_{44}(C_{11}-C_{12})}{4C_{44}+3(C_{11}-C_{12})}\right]$. So we compared our results with a few previous theoretical works using different approaches and with the available data at T = 300 K and P = 0 GPa. We have found a little discrepancy between our work and other theoretical ones, but a good agreement result with the available data. This was a very strong test for the model we have developed: all these elastic calculations seem to be model-dependent, therefore according to what kind of approximation one uses, slightly different results can be found. The deviation from the experimental values under the same physical conditions seems to us a better parameter to quantify the reliability of such a model.

We then performed the same calculations over a wider range of temperature and pressure: between 100 K and 1000 K and 0 GPa up to 100 GPa. We then produced the isothermal and isobar bulk modulus curves, always being careful in checking the system's mechanical stability. We compared our results with previous works, but this was not always possible since for a few range of T and P we studied, there was no set of data available.

We have then considered the same bcc cubic box of uranium atoms and studied its behavior at first when brought to equilibrium and then under extreme pressure and temperature conditions. With NVE simulations we have studied the equilibrium states, varying the lattice parameter a (and so the volume of the box) looking for the minimum energy configuration. We have also studied the pressure evolution of the system, finding that not only the system is stable under these extreme temperature conditions but also

that the minimum energy is reached coherently when the lattice parameter is close to the physical value $a = 3.493$ Å $\forall$ T.

The next advancement was to investigate the extreme pressure condition behavior of the system. So we exposed the uranium box to an external pressure in the range $P^{ext} = 1$ GPa, $P^{ext} = 20$ GPa and $P^{ext} = 100$ GPa. We have seen that after an appropriate amount of time step it comes to equilibrium with the external pressure at every temperature T = 100 K, T = 400 K and T = 700 K. We have explored all the possible volumes of the box varying the lattice parameter a around 3.493 Å between $a = 3.0$ Å and 3.9 Å. Each run started by reading the previously calculated NVE equilibrium configuration: we did this because we wanted to study the box under these conditions separately, so after 100000 time steps evolution with the NVE, the results are stored in a data file that is then read by the NPT program (running for 400000 time steps) at the beginning of the simulation. So we made sure we were able to let the system evolve to a predictable state. We have also checked that for all the configurations the number of time steps was appropriate to drag the box to the desired T and/or P. We have noticed that regardless of whether the system is compressed or dilated, it is always driven to the desired conditions.

Hence after studying the pressure, temperature, box length and energy evolution curves, we focused on the transient states. We were particularly interested in these states because through them we could check any (anomalous) variation in the bulk modulus and in the pressure of the box, i.e. in the mechanical properties, to use as a marker, when exposed to external conditions. As a result we plotted all the variations in pressure between a given configuration the box finds itself in and all the others we have studied. We were therefore able to see how big a variation in pressure the system undergoes in a given volume, pressure, temperature situation. So we can now quantitatively answer the questions: which is the pressure (bulk modulus) response of such a system when exposed to several physical conditions different from the one it finds itself in? and how much time is needed for this to happen? how many atoms are necessary for a cluster to behave like this?

The aim of this work was in fact to realize whether any process related to uranium could occur during an earthquake. Uranium is present in the mantle and can then be found in clusters in there. Therefore it was necessary to relate it to the pressure and temperature conditions typical of the mantle and crust and to study its behavior. However it has to be highlighted that the contribution to the radiogenic heat development is due to other elements as well: for example looking at the mantle concentration [2], the contribution

of K is 70 p.p.m by weight, the contribution of Th is 0.087 p.p.m. by weight and the one of U is only 0.025 p.p.m. by weight. Which means that this study can only be considered as a pioneering step in this field: it will be mandatory to replicate such a study with the main elements present in the crust and in the mantle, to check for individual contribution and behavior.

Besides, we know that in the Earth crust U is present as a compound with other elements such as oxygen as silicon, so as a follow-up study it'll be necessary (and is being done) to study U clusters bounded with these other elements.

Clearly this investigation is yet to be completed. We still need to check whether any difference occur if we increase the number of atoms, or what happens if we vary the geometry of the system from cubic to any other kind of clusterization. But so far clear indications of strong variation of pressure of such a configuration of atoms that we can see through the bulk modulus used as a marker have been demonstrated.

Appendix A

Isothermal elastic constants for uranium

In Table A.1-Table A.12 we report the values of the elastic constants of a bcc uranium at a given temperature as a function of the pressure for: T = 450 K, T = 500 K, T = 550 K, T = 600 K, T = 650 K, T = 700 K, T = 750 K, T = 800 K, T = 850 K, T = 900 K, T = 950 K and T = 1000 K.

	C_{11} (GPa)	C_{22} (GPa)	C_{33} (GPa)	C_{12} (GPa)	C_{13} (GPa)	C_{23} (GPa)	C_{44} (GPa)	C_{55} (GPa)	C_{66} (GPa)
T=450 K									
P=0 GPa	189.812	192.148	185.182	71.071	70.455	70.803	45.985	45.925	46.475
P=10 GPa	240.697	231.518	241.938	169.462	161.882	173.206	53.758	49.039	51.431
P=20 GPa	297.299	324.397	325.320	262.593	267.903	252.032	53.012	57.407	56.331
P=30 GPa	400.173	393.302	395.782	348.404	348.775	346.033	46.563	48.749	47.740
P=35 GPa	427.878	433.841	427.386	381.306	381.708	382.584	48.071	47.809	47.00
P=40 GPa	465.02	460.486	460.147	405.818	406.524	408.430	52.551	53.087	52.036
P=45 GPa	475.809	483.489	486.584	421.893	423.569	421.696	55.900	56.016	55.815
P=50 GPa	484.500	490.156	493.155	424.531	426.313	425.697	61.228	61.606	61.901
P=55 GPa	503.845	504.670	514.450	433.289	432.455	433.230	67.503	68.968	70.398
P=60 GPa	543.174	529.593	529.769	451.898	450.313	450.059	73.637	70.730	73.240
P=70 GPa	617.131	632.262	607.252	517.863	514.008	518.600	90.669	84.371	88.387
P=90 GPa	816.895	782.651	786.640	658.270	653.521	640.245	105.426	118.082	123.910
P=100 GPa	864.917	827.889	824.970	671.461	683.827	664.308	119.066	137.455	127.418

Table A.1: Elastic constants as a function of the pressure for T =450 K in the pressure range $0 - 100$ GPa.

	C_{11} (GPa)	C_{22} (GPa)	C_{33} (GPa)	C_{12} (GPa)	C_{13} (GPa)	C_{23} (GPa)	C_{44} (GPa)	C_{55} (GPa)	C_{66} (GPa)
T=500 K									
P=0 GPa	182.120	186.420	184.066	71.282	71.308	70.940	44.054	44.655	44.641
P=10 GPa	212.098	212.528	210.492	155.133	158.313	154.755	36.875	37.780	37.401
P=20 GPa	302.201	301.683	295.959	255.074	257.607	256.177	39.916	40.629	40.457
P=30 GPa	382.408	388.529	394.870	345.219	345.246	343.189	44.218	44.783	44.038
P=35 GPa	430.053	422.495	427.727	379.048	379.016	378.241	49.888	50.206	50.460
P=40 GPa	452.123	450.138	456.388	402.536	401.804	402.059	52.221	52.874	51.960
P=45 GPa	471.222	473.102	477.790	416.797	416.186	417.334	55.094	55.325	53.982
P=50 GPa	483.254	496.802	485.430	432.000	431.022	431.227	58.529	57.725	57.644
P=55 GPa	497.995	504.080	511.635	435.606	434.287	438.535	63.826	61.894	63.380
P=60 GPa	533.016	536.468	527.963	453.225	451.516	449.983	70.681	75.602	71.930
P=70 GPa	618.645	599.942	613.971	514.961	514.798	510.490	80.294	84.040	86.545
P=90 GPa	779.814	798.641	773.775	644.309	633.793	640.960	109.022	101.423	111.855
P=100 GPa	828.728	832.996	842.404	661.680	676.943	671.689	121.432	128.055	112.166

Table A.2: Elastic constants as a function of the pressure for T =500 K in the pressure range $0 - 100$ GPa.

	C_{11} (GPa)	C_{22} (GPa)	C_{33} (GPa)	C_{12} (GPa)	C_{13} (GPa)	C_{23} (GPa)	C_{44} (GPa)	C_{55} (GPa)	C_{66} (GPa)
T=550 K									
P=0 GPa	180.788	183.916	179.436	73.382	73.175	73.340	43.697	43.505	43.855
P=10 GPa	209.099	207.392	208.430	155.378	155.077	156.025	35.845	35.423	34.974
P=20 GPa	293.706	293.743	294.369	255.775	255.712	255.708	38.130	38.290	38.226
P=30 GPa	378.385	381.788	383.392	343.047	342.436	341.930	44.567	43.979	44.022
P=35 GPa	418.673	421.218	417.476	374.190	375.956	374.601	47.951	48.142	48.716
P=40 GPa	450.649	447.767	446.092	398.529	400.410	399.706	51.831	52.775	51.758
P=45 GPa	471.595	470.009	467.250	418.166	418.453	416.844	54.916	55.501	56.225
P=50 GPa	485.679	487.264	493.382	429.900	431.020	431.924	59.039	57.524	58.089
P=55 GPa	500.153	511.356	506.227	441.033	440.235	441.629	63.881	61.406	61.875
P=60 GPa	525.152	526.041	529.545	453.327	453.974	453.948	64.084	66.858	66.985
P=70 GPa	620.274	615.916	616.451	515.202	516.405	514.869	80.933	81.124	85.805
P=90 GPa	772.075	786.127	766.598	642.566	631.652	640.399	108.016	98.917	108.045
P=100 GPa	840.099	823.934	806.211	675.226	666.237	651.171	105.824	121.312	127.104

Table A.3: Elastic constants as a function of the pressure for T =550 K in the pressure range $0 - 100$ GPa.

	C_{11} (GPa)	C_{22} (GPa)	C_{33} (GPa)	C_{12} (GPa)	C_{13} (GPa)	C_{23} (GPa)	C_{44} (GPa)	C_{55} (GPa)	C_{66} (GPa)
T=600 K									
P=0 GPa	178.164	179.670	177.557	73.906	73.44	73.488	42.441	42.344	43.205
P=10 GPa	205.872	207.862	204.613	155.296	153.907	154.222	34.018	33.193	34.486
P=20 GPa	295.865	296.065	291.496	256.238	254.889	253.973	38.397	38.192	39.210
P=30 GPa	382.005	381.360	379.742	342.808	341.809	342.942	45.184	46.003	45.106
P=35 GPa	419.479	408.368	409.335	372.294	375.213	374.076	47.375	49.322	48.427
P=40 GPa	445.563	442.888	441.275	394.850	395.171	396.571	52.453	52.189	52.471
P=45 GPa	459.188	472.161	462.576	416.910	417.261	416.587	54.307	52.483	54.565
P=50 GPa	479.077	483.379	485.606	428.329	428.259	429.241	59.338	59.280	58.868
P=55 GPa	501.373	496.269	497.278	437.787	439.203	438.903	62.275	62.755	63.403
P=60 GPa	520.644	531.764	518.096	453.100	451.329	453.275	68.024	67.294	67.110
P=70 GPa	603.637	596.276	609.564	512.712	514.735	511.475	73.860	77.602	73.858
P=90 GPa	760.779	763.729	785.748	630.383	639.949	635.322	103.235	106.622	95.627
P=100 GPa	795.761	827.684	815.964	665.976	652.549	663.048	115.004	105.608	115.898

Table A.4: Elastic constants as a function of the pressure for T =600 K in the pressure range $0 - 100$ GPa.

	C_{11} (GPa)	C_{22} (GPa)	C_{33} (GPa)	C_{12} (GPa)	C_{13} (GPa)	C_{23} (GPa)	C_{44} (GPa)	C_{55} (GPa)	C_{66} (GPa)
T=650 K									
P=0 GPa	177.559	175.362	173.471	75.304	75.389	74.735	41.530	42.109	42.167
P=10 GPa	212.522	210.206	210.967	160.208	158.972	158.003	35.867	36.485	36.628
P=20 GPa	285.812	288.688	289.893	252.152	252.600	249.925	37.089	37.840	37.326
P=30 GPa	374.308	373.797	379.754	340.195	338.706	338.940	43.901	43.974	42.905
P=35 GPa	413.210	412.610	408.795	372.938	369.648	370.186	49.263	48.103	49.825
P=40 GPa	439.131	438.156	437.299	395.532	394.604	395.083	51.794	52.854	52.683
P=45 GPa	461.258	457.639	463.310	412.473	412.807	414.266	56.528	55.500	53.921
P=50 GPa	485.360	482.303	480.433	427.061	426.951	427.526	58.017	57.804	58.541
P=55 GPa	493.100	496.859	487.161	436.095	435.283	434.797	61.501	61.177	63.524
P=60 GPa	520.286	516.830	526.429	452.102	454.263	454.199	63.822	64.295	63.564
P=70 GPa	597.622	586.589	604.713	505.154	507.955	506.670	74.998	78.167	72.063
P=90 GPa	756.549	751.312	765.756	628.213	633.500	635.327	100.920	97.317	91.830
P=100 GPa	800.900	797.021	826.977	649.386	658.823	658.189	112.751	113.589	102.857

Table A.5: Elastic constants as a function of the pressure for T =650 K in the pressure range $0 - 100$ GPa.

	C_{11} (GPa)	C_{22} (GPa)	C_{33} (GPa)	C_{12} (GPa)	C_{13} (GPa)	C_{23} (GPa)	C_{44} (GPa)	C_{55} (GPa)	C_{66} (GPa)
T=700 K									
P=0 GPa	175.188	172.503	177.827	75.976	76.910	76.185	40.963	41.836	40.855
P=10 GPa	212.689	215.068	212.762	161.227	160.947	161.076	37.159	36.337	37.322
P=20 GPa	289.978	288.643	291.965	253.035	254.399	252.568	39.725	39.251	39.180
P=30 GPa	369.568	369.844	370.674	339.123	337.209	338.095	43.967	43.838	44.112
P=35 GPa	406.756	405.090	407.750	367.670	367.168	367.636	48.675	49.597	49.812
P=40 GPa	433.072	440.612	431.540	390.194	390.701	390.831	54.519	53.932	54.522
P=45 GPa	459.577	457.254	452.544	409.457	409.782	408.670	55.350	56.605	56.939
P=50 GPa	473.029	473.413	474.162	427.323	426.521	426.930	58.074	57.113	58.421
P=55 GPa	497.346	498.095	496.990	440.089	438.196	437.885	63.648	63.642	65.080
P=60 GPa	524.671	515.022	519.752	454.173	454.350	452.746	64.240	65.502	66.104
P=70 GPa	596.104	589.249	600.777	508.142	508.740	509.355	76.012	75.863	76.339
P=90 GPa	753.676	759.785	731.083	629.911	623.594	627.626	97.033	92.784	98.667
P=100 GPa	796.604	806.899	791.413	655.345	651.760	659.156	113.475	103.041	108.737

Table A.6: Elastic constants as a function of the pressure for T =700 K in the pressure range $0 - 100$ GPa.

	C_{11} (GPa)	C_{22} (GPa)	C_{33} (GPa)	C_{12} (GPa)	C_{13} (GPa)	C_{23} (GPa)	C_{44} (GPa)	C_{55} (GPa)	C_{66} (GPa)
T=750 K									
P=0 GPa	173.732	171.866	171.876	76.614	77.523	77.622	40.383	40.355	39.360
P=10 GPa	210.857	217.629	213.028	162.490	160.798	162.035	37.526	36.147	37.931
P=20 GPa	285.555	290.355	285.011	250.311	249.452	250.961	40.364	39.210	40.126
P=30 GPa	369.836	367.383	368.729	332.992	334.018	335.198	45.605	44.815	45.167
P=35 GPa	403.767	409.888	400.040	364.570	366.124	365.083	50.447	49.918	50.443
P=40 GPa	433.423	427.895	428.718	389.009	389.011	388.059	51.851	52.599	52.485
P=45 GPa	455.833	452.393	460.600	409.787	410.086	408.445	57.123	57.846	57.386
P=50 GPa	475.484	471.769	478.167	423.710	422.909	423.123	59.999	59.774	59.455
P=55 GPa	494.603	488.793	493.734	435.243	435.055	435.197	60.983	59.510	60.457
P=60 GPa	510.255	509.890	515.241	449.235	449.834	449.020	65.316	64.690	64.866
P=70 GPa	575.315	581.688	581.443	505.448	503.009	506.800	73.254	68.393	70.752
P=90 GPa	740.459	748.772	741.594	624.990	625.712	627.342	94.189	93.773	92.281
P=100 GPa	886.504	837.321	849.041	623.145	618.996	652.023	145.506	101.599	105.295

Table A.7: Elastic constants as a function of the pressure for T =750 K in the pressure range $0 - 100$ GPa.

	C_{11} (GPa)	C_{22} (GPa)	C_{33} (GPa)	C_{12} (GPa)	C_{13} (GPa)	C_{23} (GPa)	C_{44} (GPa)	C_{55} (GPa)	C_{66} (GPa)
T=800 K									
P=0 GPa	173.450	170.453	173.955	78.768	78.637	79.043	40.454	40.114	40.299
P=10 GPa	212.841	212.078	213.096	161.223	161.842	161.879	36.288	35.893	35.656
P=20 GPa	283.426	286.304	287.598	251.633	250.602	250.145	39.886	40.206	38.595
P=30 GPa	365.849	362.120	363.252	332.805	332.747	332.611	43.577	44.057	44.775
P=35 GPa	395.362	405.248	405.556	367.280	364.597	363.211	50.634	50.165	52.256
P=40 GPa	427.658	433.436	430.449	388.418	389.041	387.472	55.259	55.102	55.668
P=45 GPa	444.969	447.158	446.562	408.152	407.977	408.121	56.302	55.706	55.665
P=50 GPa	469.349	461.713	471.461	421.559	421.900	419.266	57.696	60.368	58.995
P=55 GPa	491.513	488.834	485.813	435.716	435.381	434.364	63.762	63.899	64.738
P=60 GPa	508.772	522.000	506.194	447.594	447.669	448.756	68.413	65.732	66.344
P=70 GPa	577.159	582.406	575.226	506.591	506.266	506.902	71.37	69.552	70.774
P=90 GPa	734.267	743.139	744.039	618.395	619.061	619.643	93.739	95.155	91.373
P=100 GPa	782.967	788.868	775.368	654.941	646.371	650.696	103.303	95.669	107.356

Table A.8: Elastic constants as a function of the pressure for T =800 K in the pressure range $0 - 100$ GPa.

	C_{11} (GPa)	C_{22} (GPa)	C_{33} (GPa)	C_{12} (GPa)	C_{13} (GPa)	C_{23} (GPa)	C_{44} (GPa)	C_{55} (GPa)	C_{66} (GPa)
T=850 K									
P=0 GPa	168.842	169.629	165.892	77.363	76.459	77.370	37.901	37.444	38.555
P=10 GPa	216.905	215.330	216.564	162.716	163.262	162.6696	37.354	37.513	37.522
P=20 GPa	283.328	281.590	288.215	247.712	247.366	247.576	39.314	38.738	38.837
P=30 GPa	362.414	361.132	362.033	330.907	328.410	330.530	47.420	46.116	46.826
P=35 GPa	403.477	397.646	391.077	362.354	361.159	361.951	50.383	50.068	51.581
P=40 GPa	420.148	421.560	420.574	386.358	386.590	386.626	54.230	54.338	54.168
P=45 GPa	444.525	446.140	444.195	404.680	404.722	406.3795	56.142	55.847	55.273
P=50 GPa	470.396	464.761	462.651	422.102	422.436	420.978	58.869	59.863	59.763
P=55 GPa	486.973	487.603	488.356	435.866	435.631	435.136	62.053	62.522	63.329
P=60 GPa	511.664	504.443	502.786	449.542	451.942	451.096	65.362	64.667	63.546
P=70 GPa	563.702	581.621	573.272	504.164	502.860	503.698	73.358	71.141	72.969
P=90 GPa	809.635	816.814	714.202	539.251	596.880	598.954	119.485	116.942	77.194
P=100 GPa	778.420	779.774	764.852	650.360	650.664	652.936	100.755	99.035	97.113

Table A.9: Elastic constants as a function of the pressure for T =850 K in the pressure range $0 - 100$ GPa.

	C_{11} (GPa)	C_{22} (GPa)	C_{33} (GPa)	C_{12} (GPa)	C_{13} (GPa)	C_{23} (GPa)	C_{44} (GPa)	C_{55} (GPa)	C_{66} (GPa)
T=900 K									
P=0 GPa	169.953	167.116	165.833	79.494	80.619	80.347	37.827	38.283	37.696
P=10 GPa	212.282	212.764	211.107	161.450	160.569	160.611	36.948	36.578	37.265
P=20 GPa	283.546	283.360	280.737	247.601	247.477	247.126	39.271	39.817	39.867
P=30 GPa	360.487	358.157	363.654	324.701	324.690	322.843	48.093	48.743	48.377
P=35 GPa	392.437	382.550	390.856	358.896	359.186	361.341	49.694	49.266	48.082
P=40 GPa	419.596	420.278	423.994	387.630	387.131	387.142	53.024	53.031	53.417
P=45 GPa	441.783	441.007	447.703	402.436	403.820	403.722	56.215	55.278	55.218
P=50 GPa	462.224	456.718	468.615	420.756	422.001	420.844	60.798	61.576	60.692
P=55 GPa	490.430	494.799	483.169	433.166	432.150	434.473	66.590	64.726	65.622
P=60 GPa	505.560	512.737	506.784	447.986	448.066	449.486	68.187	65.484	66.641
P=70 GPa	576.577	567.271	577.693	503.899	507.206	505.190	71.378	73.453	71.086
P=90 GPa	803.700	761.157	763.412	579.290	574.736	605.027	126.491	92.245	95.973
P=100 GPa	887.170	803.735	889.353	642.966	583.270	645.312	138.234	87.306	135.395

Table A.10: Elastic constants as a function of the pressure for T =900 K in the pressure range $0 - 100$ GPa.

	C_{11} (GPa)	C_{22} (GPa)	C_{33} (GPa)	C_{12} (GPa)	C_{13} (GPa)	C_{23} (GPa)	C_{44} (GPa)	C_{55} (GPa)	C_{66} (GPa)
T=950 K									
P=0 GPa	166.969	161.570	165.256	83.056	82.830	82.170	37.496	38.729	38.184
P=10 GPa	214.572	213.182	212.554	162.238	163.720	161.566	37.698	38.498	37.552
P=20 GPa	284.488	282.892	285.725	246.219	246.099	246.844	41.406	41.430	41.570
P=30 GPa	352.197	352.979	355.974	324.094	323.516	323.705	46.035	46.327	45.580
P=35 GPa	385.796	384.172	392.235	358.482	359.693	357.829	49.552	50.713	49.988
P=40 GPa	411.946	410.121	419.084	381.989	379.561	381.570	52.811	52.566	52.378
P=45 GPa	434.167	436.323	437.055	401.363	399.782	398.779	56.636	57.595	56.960
P=50 GPa	458.940	447.462	456.448	415.997	415.990	415.429	59.761	60.796	3 60.711
P=55 GPa	473.400	479.564	486.358	432.902	434.560	434.376	65.296	65.566	64.534
P=60 GPa	516.428	492.755	501.317	448.916	450.192	447.044	66.245	70.668	69.033
P=70 GPa	586.243	571.425	579.377	501.702	503.542	501.050	77.260	78.672	76.473
P=90 GPa	774.835	760.196	748.715	598.934	566.571	598.945	112.392	80.489	105.354
P=100 GPa	780.970	849.762	813.058	604.710	639.626	606.293	98.847	134.028	96.099

Table A.11: Elastic constants as a function of the pressure for T =950 K in the pressure range $0 - 100$ GPa.

	C_{11} (GPa)	C_{22} (GPa)	C_{33} (GPa)	C_{12} (GPa)	C_{13} (GPa)	C_{23} (GPa)	C_{44} (GPa)	C_{55} (GPa)	C_{66} (GPa)
T=1000 K									
P=0 GPa	164.983	163.119	158.628	81.737	81.537	80.755	36.234	36.885	37.345
P=10 GPa	214.506	214.978	213.422	163.108	162.638	162.354	37.297	37.545	38.442
P=20 GPa	283.675	282.460	280.381	246.145	245.403	245.485	41.331	41.229	41.762
P=30 GPa	356.132	355.113	351.644	323.320	322.808	323.233	48.267	48.413	48.733
P=35 GPa	389.973	384.085	380.457	353.421	354.526	352.831	50.608	51.056	50.635
P=40 GPa	415.874	409.234	416.348	380.258	381.243	381.054	54.123	57.013	55.072
P=45 GPa	441.228	435.885	437.134	399.718	399.243	400.296	60.179	60.523	59.826
P=50 GPa	450.798	454.819	463.341	415.779	416.785	416.508	61.762	62.523	60.955
P=55 GPa	485.686	487.495	470.418	428.615	428.451	430.473	66.795	64.277	65.430
P=60 GPa	496.268	502.944	513.777	448.353	447.564	449.648	69.943	67.908	69.375
P=70 GPa	562.344	566.372	553.967	501.778	499.676	501.833	72.430	70.857	72.435
P=90 GPa	724.146	787.534	784.208	592.089	591.025	531.1573	74.996	117.164	119.368
P=100 GPa	873.283	825.867	819.037	620.275	622.370	654.913	143.183	104.592	103.401

Table A.12: Elastic constants as a function of the pressure for T =1000 K in the pressure range $0 - 100$ GPa.

Appendix B

Polycrystalline moduli

We show here for a bcc uranium with lattice constant $a = 3.493$ Å the values of the bulk modulus B, the shear modulus G and the Young modulus E as a function of the pressure at constant temperature for T= 400 K, T = 450 K, T = 500 K, T = 550 K, T = 600 K, T = 650 K, T = 700 K, T = 750 K, T = 800 K, T = 850 K, T = 900 K, T = 950 K and T = 1000 K (Table B.1-Table B.13).

P (GPa)	B (GPa)	G (GPa)	E (GPa)
0	111.241	53.091	137.412
1	111.915	49.240	128.827
10	189.858	47.713	132.075
20	277.479	45.698	129.960
30	352.142	53.770	153.496
35	386.414	49.042	141.155
40	412.680	51.095	147.209
45	426.110	57.158	164.136
50	434.869	66.551	189.961
55	459.233	74.528	212.109
60	488.452	81.996	232.953
70	553.391	76.423	219.180
90	704.047	103.098	294.899
100	736.224	112.208	320.350

Table B.1: Bulk modulus B, shear modulus G and Young modulus E of bcc uranium crystal at T = 400 K.

P (GPa)	B (GPa)	G (GPa)	E (GPa)
0	110.201	51.331	133.297
1	112.545	48.061	126.216
10	191.473	44.819	124.726
20	279.120	44.316	126.266
30	363.965	38.347	111.138
35	397.812	38.144	110.888
40	425.245	42.527	123.466
45	442.245	45.461	131.866
50	446.766	49.698	143.765
55	457.880	56.307	162.269
60	478.564	60.206	173.349
70	550.843	73.097	210.003
90	698.918	98.427	282.042
100	728.552	110.000	314.187

Table B.2: Bulk modulus B, shear modulus G and Young modulus E of bcc uranium crystal at T = 450 K.

P (GPa)	B (GPa)	G (GPa)	E (GPa)
0	108.852	49.275	128.444
1	111.553	47.136	123.949
10	174.614	33.539	94.563
20	270.840	32.933	94.950
30	359.236	35.418	102.874
35	394.766	39.709	115.263
40	419.050	41.561	120.694
45	435.861	44.334	128.640
50	450.443	46.196	134.006
55	458.952	51.506	148.946
60	478.544	59.824	172.294
70	545.896	69.663	200.462
90	687.818	93.338	267.897
100	724.973	105.252	301.181

Table B.3: Bulk modulus B, shear modulus G and Young modulus E of bcc uranium crystal at T = 500 K.

P (GPa)	B (GPa)	G (GPa)	E (GPa)
0	109.327	47.828	125.223
1	112.152	45.493	120.224
10	173.098	31.811	89.926
20	268.468	30.571	88.359
30	355.377	34.257	99.573
35	389.652	37.803	109.858
40	415.756	40.997	119.077
45	435.087	43.688	126.820
50	450.224	46.496	134.846
55	462.615	50.422	145.963
60	478.138	54.218	156.730
70	549.511	69.984	201.401
90	683.782	90.341	259.592
100	717.279	102.689	294.035

Table B.4: Bulk modulus B, shear modulus G and Young modulus E of bcc uranium crystal at T = 550 K.

P (GPa)	B (GPa)	G (GPa)	E (GPa)
0	108.564	46.568	122.228
1	111.649	44.224	117.197
10	171.689	30.668	86.833
20	268.181	31.048	89.684
30	355.359	34.962	101.556
35	386.706	36.732	106.813
40	411.435	40.965	118.948
45	432.827	41.816	121.533
50	446.636	46.313	134.297
55	458.524	49.622	143.683
60	476.213	54.673	157.972
70	543.036	63.101	182.245
90	680.174	88.070	253.280
100	711.395	97.825	280.612

Table B.5: Bulk modulus B, shear modulus G and Young modulus E of bcc uranium crystal at T = 600 K.

P (GPa)	B (GPa)	G (GPa)	E (GPa)
0	108.584	45.226	119.137
1	113.306	43.267	115.144
10	176.452	32.230	91.142
20	263.750	29.766	86.060
30	351.505	33.491	97.379
35	384.463	37.561	109.130
40	409.448	40.091	116.472
45	429.034	42.701	123.989
50	445.686	45.976	133.344
55	454.386	48.637	140.884
60	476.075	51.869	150.153
70	536.499	62.989	181.850
90	674.189	83.119	239.514
100	706.411	96.406	276.635

Table B.6: Bulk modulus B, shear modulus G and Young modulus E of bcc uranium crystal at T = 650 K.

P (GPa)	B (GPa)	G (GPa)	E (GPa)
0	109.296	44.494	117.533
1	111.625	41.565	110.926
10	178.558	32.649	92.319
20	265.622	31.004	89.528
30	348.772	32.761	95.299
35	380.505	37.425	108.711
40	405.409	41.495	120.378
45	425.022	43.210	125.382
50	442.462	44.044	127.888
55	458.308	50.225	145.365
60	475.776	52.381	151.581
70	537.623	62.969	181.809
90	667.423	81.925	236.113
100	703.049	93.628	268.945

Table B.7: Bulk modulus B, shear modulus G and Young modulus E of bcc uranium crystal at T = 700 K.

P (GPa)	B (GPa)	G (GPa)	E (GPa)
0	109.000	43.068	114.166
1	112.496	40.883	109.396
10	179.129	32.734	92.563
20	262.486	31.287	90.273
30	345.596	34.034	98.857
35	378.361	38.023	110.371
40	402.466	39.651	115.171
45	425.052	43.839	127.145
50	440.545	46.225	133.987
55	454.236	47.633	138.072
60	470.174	51.461	148.949
70	529.885	57.359	166.085
90	665.213	79.568	229.550
100	706.800	115.727	329.213

Table B.8: Bulk modulus B, shear modulus G and Young modulus E of bcc uranium crystal at T = 750 K.

P (GPa)	B (GPa)	G (GPa)	E (GPa)
0	110.084	42.935	113.985
1	113.464	40.753	109.186
10	178.657	31.773	89.984
20	262.455	30.734	88.739
30	343.062	32.686	95.040
35	377.372	38.016	110.344
40	402.379	41.647	120.774
45	420.799	41.164	119.593
50	436.442	44.732	129.762
55	453.010	49.193	142.425
60	469.446	52.961	153.126
70	530.479	56.676	164.180
90	659.516	80.343	231.624
100	694.580	87.612	252.232

Table B.9: Bulk modulus B, shear modulus G and Young modulus E of bcc uranium crystal at T = 800 K.

P (GPa)	B (GPa)	G (GPa)	E (GPa)
0	107.417	40.992	109.097
1	113.222	39.631	106.470
10	180.678	33.155	93.731
20	259.827	30.743	88.730
30	340.586	34.455	99.993
35	373.681	37.522	108.921
40	397.937	39.395	114.409
45	418.492	41.392	120.211
50	436.538	44.519	129.166
55	452.911	48.001	139.090
60	469.340	49.803	144.305
70	526.671	57.352	166.029
90	645.647	103.095	293.656
100	692.330	83.987	242.168

Table B.10: Bulk modulus B, shear modulus G and Young modulus E of bcc uranium crystal at T = 850 K.

P (GPa)	B (GPa)	G (GPa)	E (GPa)
0	109.314	40.258	107.568
1	112.483	39.460	105.986
10	177.935	32.393	91.620
20	259.117	30.820	88.935
30	336.308	36.381	105.343
35	369.411	35.170	102.265
40	398.631	38.692	112.439
45	416.717	41.377	120.154
50	434.974	44.877	130.155
55	451.998	50.629	146.419
60	468.462	52.032	150.524
70	528.237	56.867	164.691
90	649.598	100.890	287.771
100	702.595	119.435	339.090

Table B.11: Bulk modulus B, shear modulus G and Young modulus E of bcc uranium crystal at T = 900 K.

P (GPa)	B (GPa)	G (GPa)	E (GPa)
0	109.990	39.265	105.268
1	112.228	37.547	101.339
10	179.485	32.935	93.111
20	259.048	32.478	93.524
30	333.754	33.578	97.465
35	368.246	35.798	104.022
40	391.933	38.086	110.674
45	411.933	41.413	120.211
50	428.632	43.950	127.491
55	449.223	48.245	139.733
60	466.979	52.146	150.824
70	527.738	61.865	178.614
90	645.850	94.267	269.680
100	682.784	105.339	300.561

Table B.12: Bulk modulus B, shear modulus G and Young modulus E of bcc uranium crystal at T = 950 K.

P (GPa)	B (GPa)	G (GPa)	E (GPa)
0	108.310	38.273	102.720
1	112.331	37.431	101.066
10	179.901	32.977	93.235
20	257.843	32.164	92.639
30	333.513	35.318	102.342
35	364.008	36.709	106.546
40	391.841	39.835	115.589
45	412.529	43.772	126.830
50	429.679	45.041	130.560
55	446.520	49.705	143.780
60	467.125	52.607	152.111
70	521.029	55.104	159.684
90	636.048	101.080	287.986
100	701.478	111.611	317.968

Table B.13: Bulk modulus B, shear modulus G and Young modulus E of bcc uranium crystal at T = 1000 K.

Appendix C

NVE simulations

For each value of the lattice constant a we plot the quantity $T - Tr/T$ which is the difference of the temperature we impose (T) and the "temp real" (Tr) normalized to the T for all the values of the temperature we studied: from T = 100 K to T = 1000 K in steps of 100 K. We show these quantities in Figure C.1-Figure C.18 for every a.

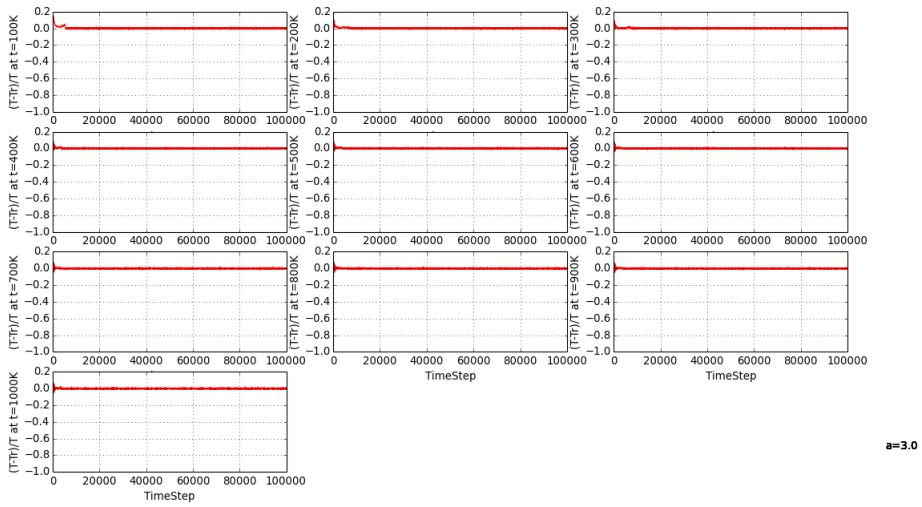

Figure C.1: (T-Tr)/T as a function of time step (1 time step = 0.001 ps) for a bcc uranium with lattice constant $a = 3.0$ Å.

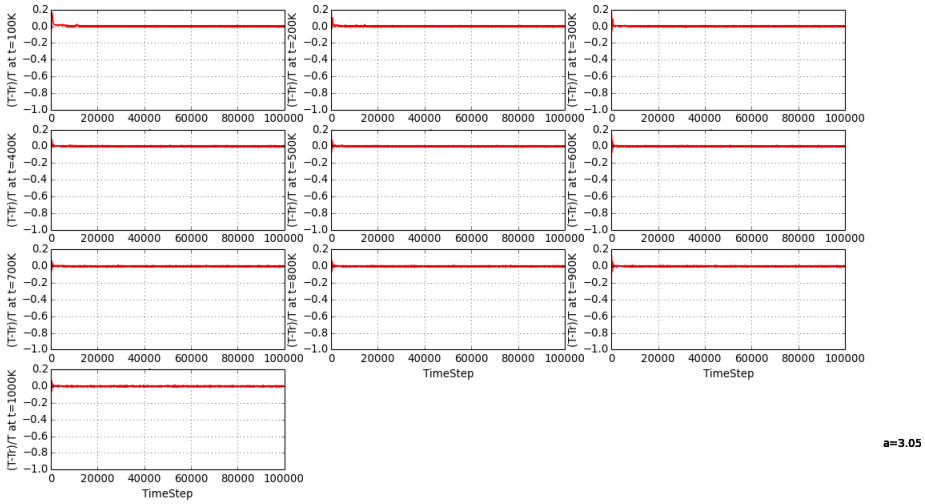

Figure C.2: (T-Tr)/T as a function of time step (1 time step = 0.001 ps) for a bcc uranium with lattice constant $a = 3.05$ Å.

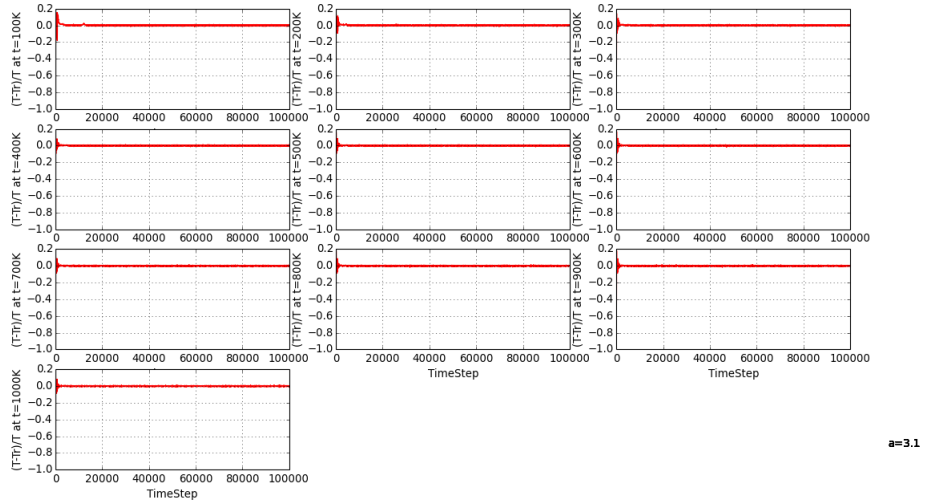

Figure C.3: (T-Tr)/T as a function of time step (1 time step = 0.001 ps) for a bcc uranium with lattice constant $a = 3.1$ Å.

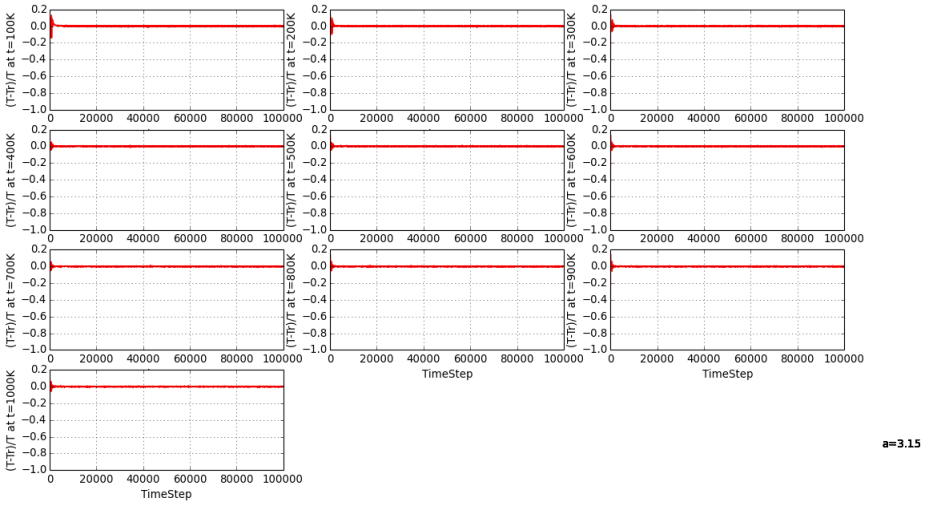

Figure C.4: (T-Tr)/T as a function of time step (1 time step = 0.001 ps) for a bcc uranium with lattice constant $a = 3.15$ Å.

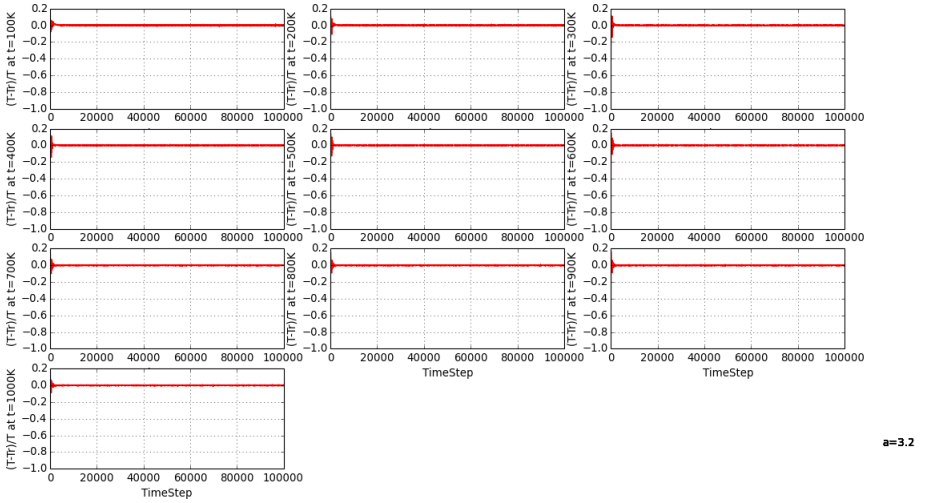

Figure C.5: (T-Tr)/T as a function of time step (1 time step = 0.001 ps) for a bcc uranium with lattice constant $a = 3.2$ Å.

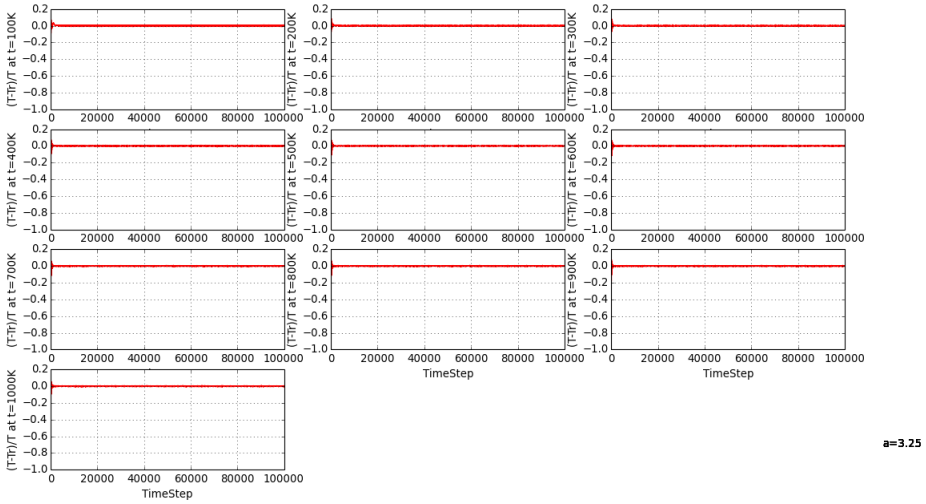

Figure C.6: (T-Tr)/T as a function of time step (1 time step = 0.001 ps) for a bcc uranium with lattice constant $a = 3.25$ Å.

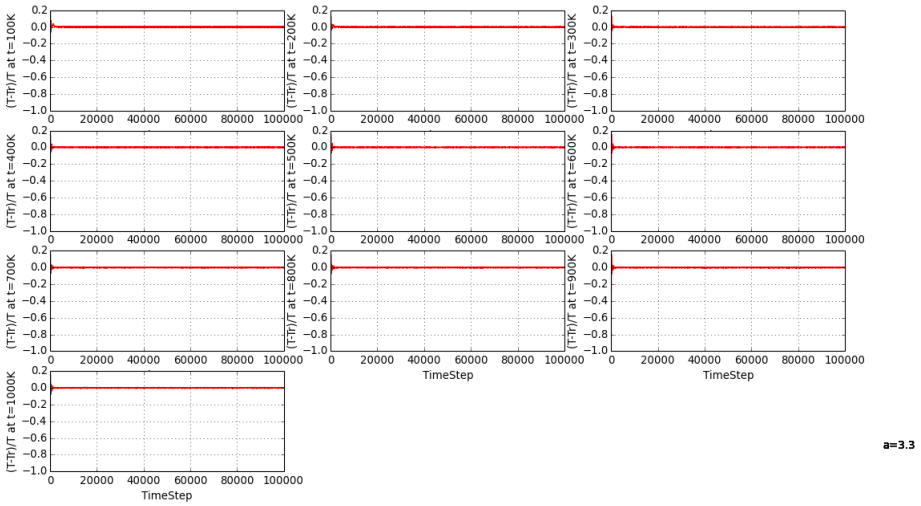

Figure C.7: (T-Tr)/T as a function of time step (1 time step = 0.001 ps) for a bcc uranium with lattice constant $a = 3.3$ Å.

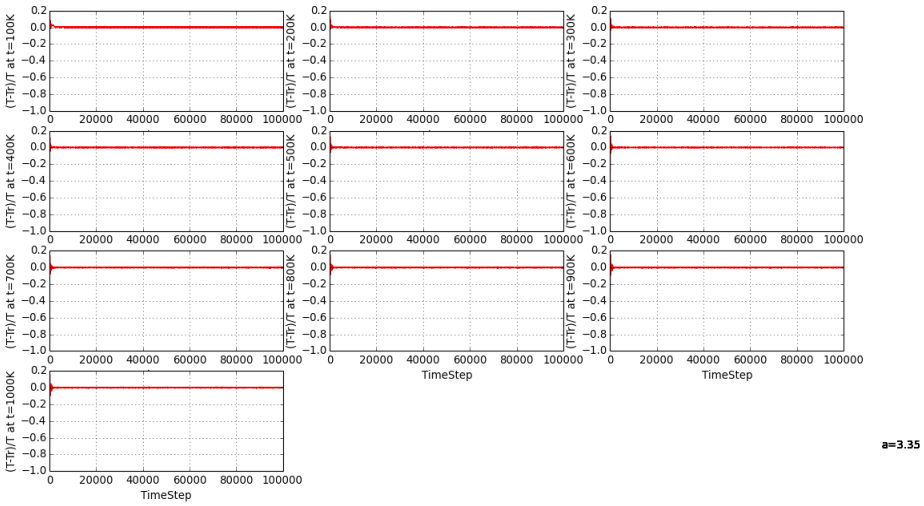

Figure C.8: (T-Tr)/T as a function of time step (1 time step = 0.001 ps) for a bcc uranium with lattice constant $a = 3.35$ Å.

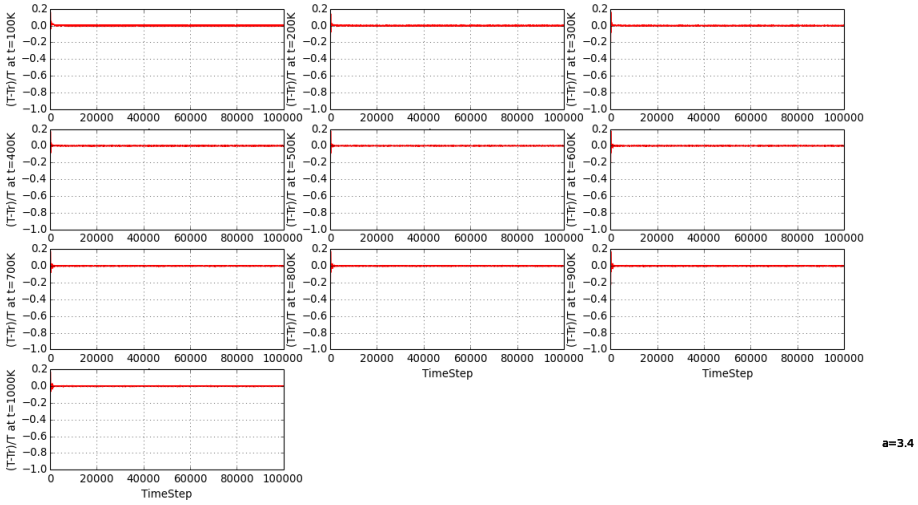

Figure C.9: (T-Tr)/T as a function of time step (1 time step = 0.001 ps) for a bcc uranium with lattice constant $a = 3.4$ Å.

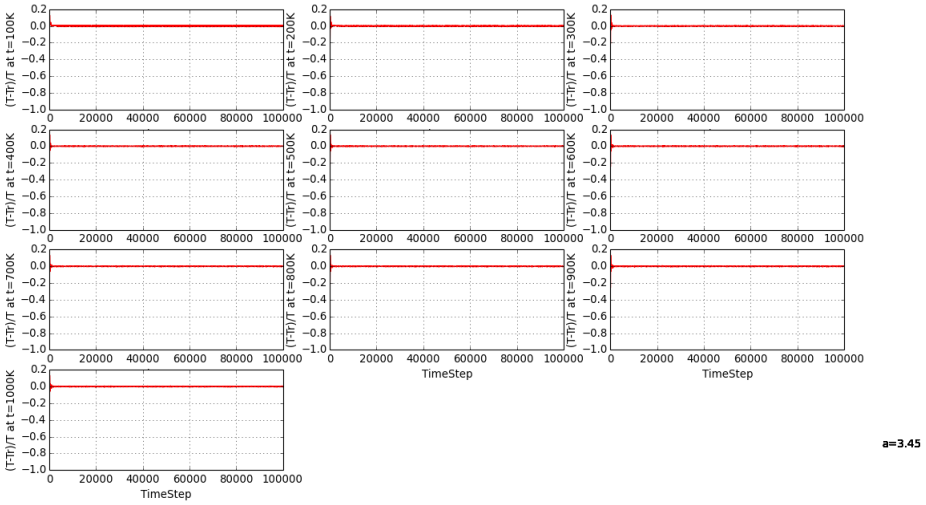

Figure C.10: (T-Tr)/T as a function of time step (1 time step = 0.001 ps) for a bcc uranium with lattice constant $a = 3.45$ Å.

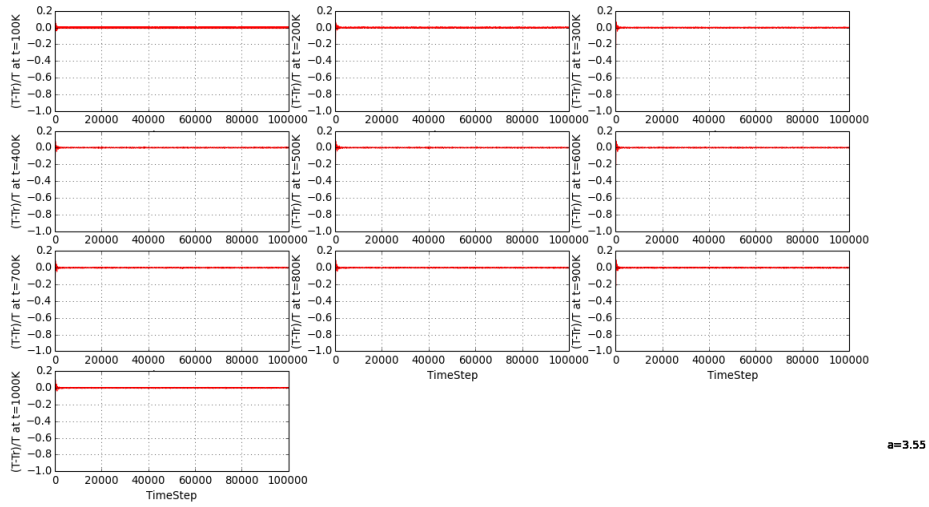

Figure C.11: (T-Tr)/T as a function of time step (1 time step = 0.001 ps) for a bcc uranium with lattice constant $a = 3.55$ Å.

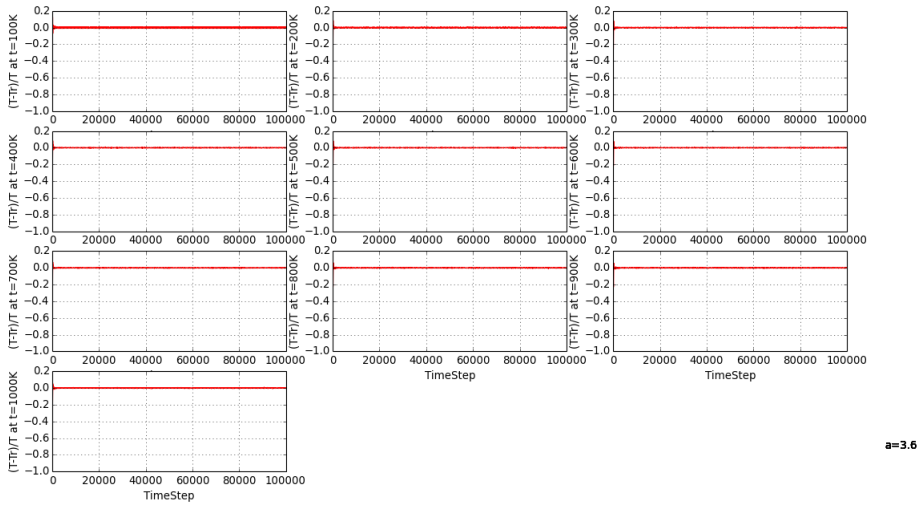

Figure C.12: (T-Tr)/T as a function of time step (1 time step = 0.001 ps) for a bcc uranium with lattice constant $a = 3.6$ Å.

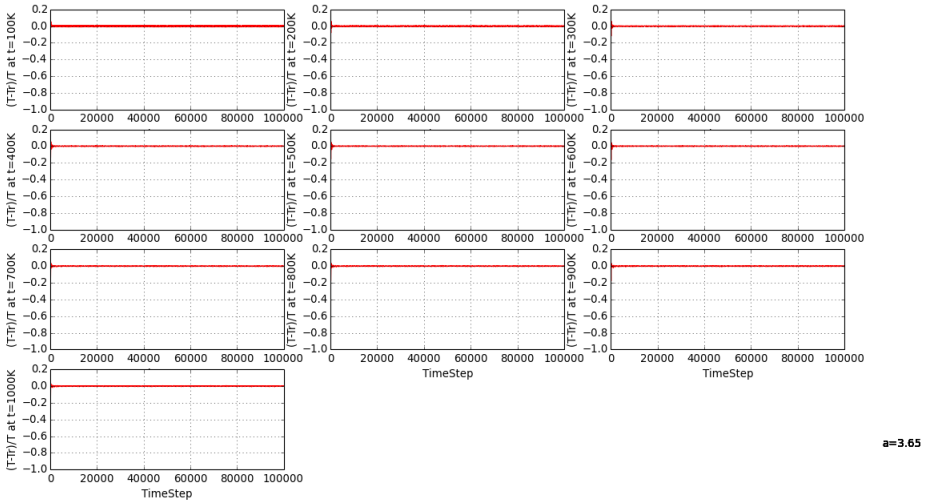

Figure C.13: (T-Tr)/T as a function of time step (1 time step = 0.001 ps) for a bcc uranium with lattice constant $a = 3.65$ Å.

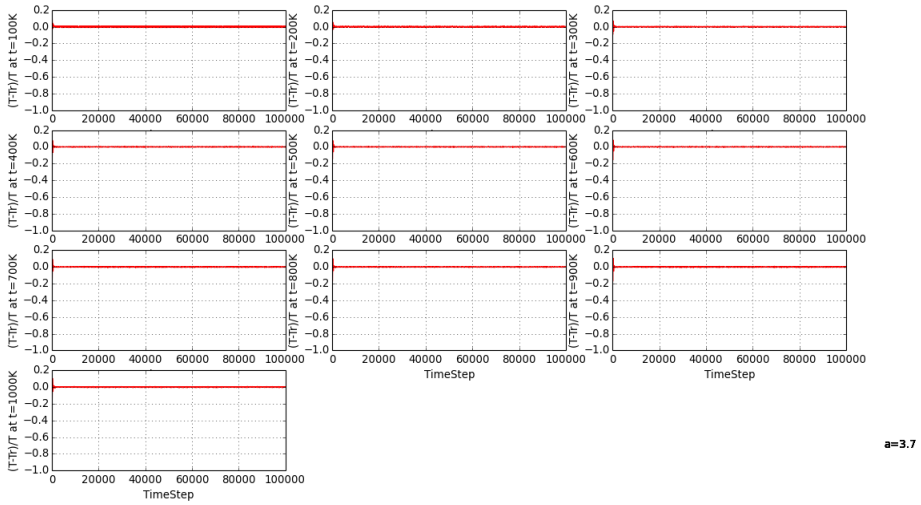

Figure C.14: (T-Tr)/T as a function of time step (1 time step = 0.001 ps) for a bcc uranium with lattice constant $a = 3.7$ Å.

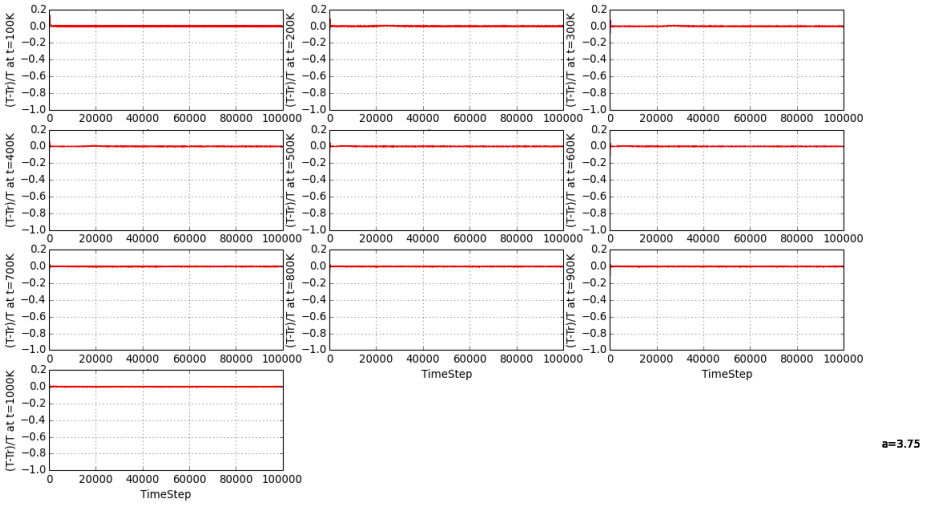

Figure C.15: (T-Tr)/T as a function of time step (1 time step = 0.001 ps) for a bcc uranium with lattice constant $a = 3.75$ Å.

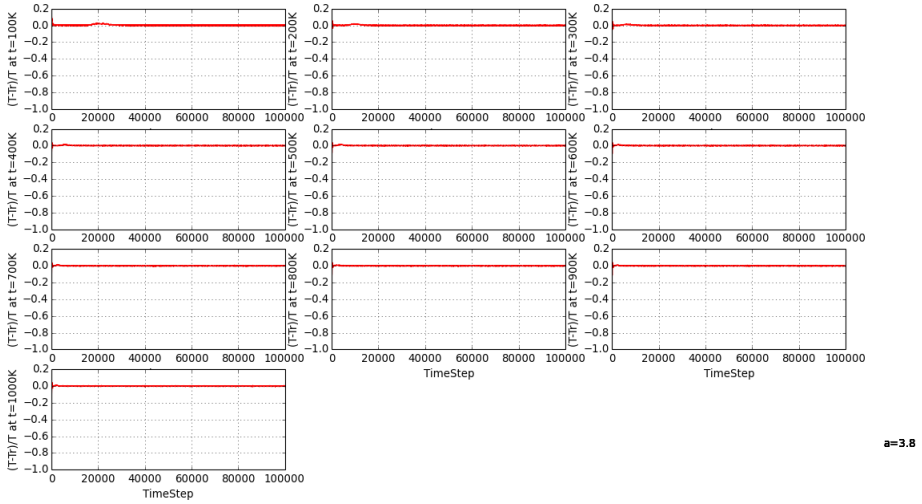

Figure C.16: (T-Tr)/T as a function of time step (1 time step = 0.001 ps) for a bcc uranium with lattice constant $a = 3.8$ Å.

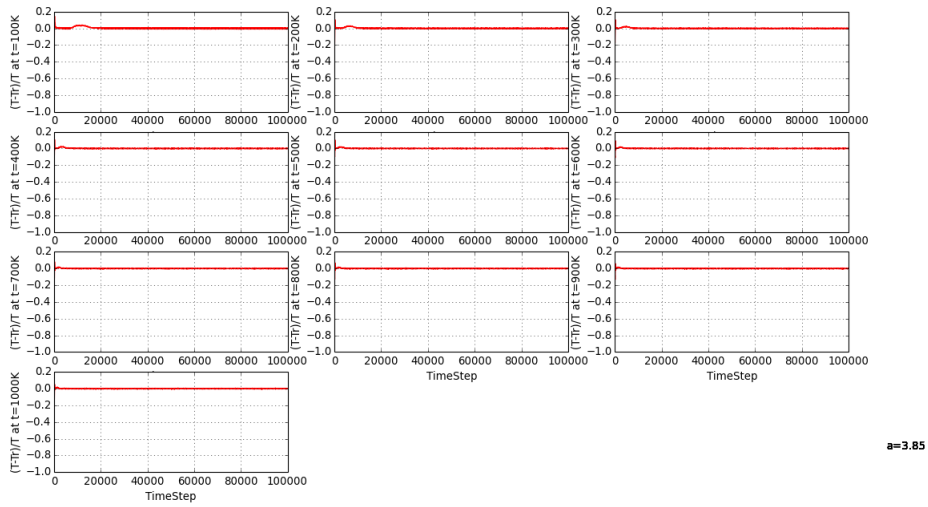

Figure C.17: (T-Tr)/T as a function of time step (1 time step = 0.001 ps) for a bcc uranium with lattice constant $a = 3.85$ Å.

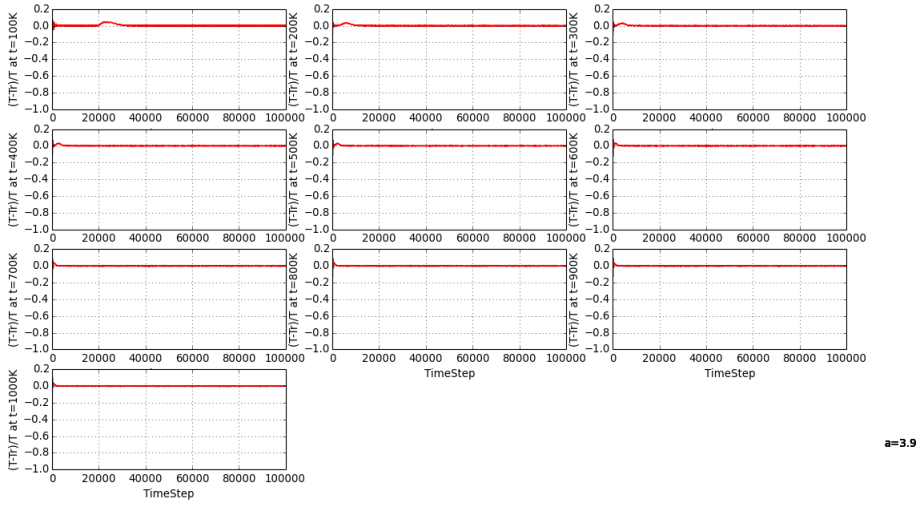

Figure C.18: (T-Tr)/T as a function of time step (1 time step = 0.001 ps) for a bcc uranium with lattice constant $a = 3.9$ Å.

We now show the graphs of the energy versus the time step for all the values of the lattice constant we have studied a: from $a = 3.0$ Å to $a = 3.9$ Å in Figure C.19-Figure C.34.

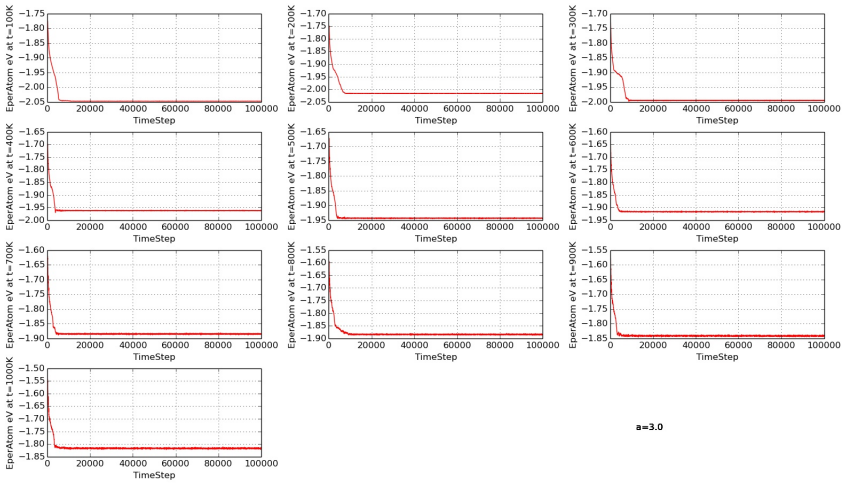

Figure C.19: Energy per atom (in eV) as a function of time step for a bcc uranium with lattice constant $a = 3.0$ Å in the temperature interval T = 100 K $\rightarrow$ T = 1000 K with ΔT= 100 K.

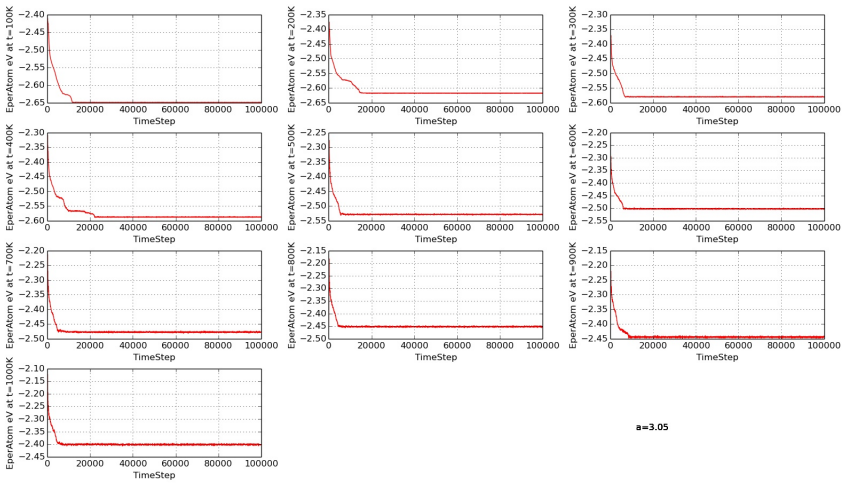

Figure C.20: Energy per atom (in eV) as a function of time step for a bcc uranium with lattice constant $a = 3.05$ Å in the temperature interval T = 100 K $\rightarrow$ T = 1000 K with ΔT= 100 K.

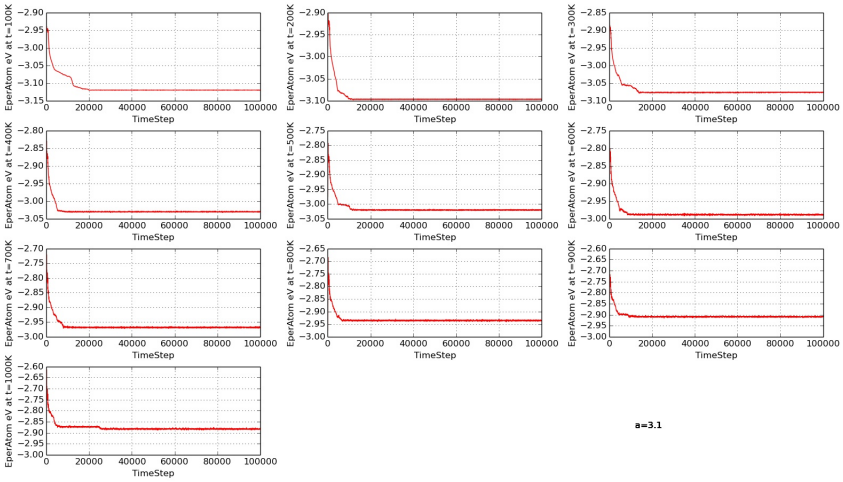

Figure C.21: Energy per atom (in eV) as a function of time step for a bcc uranium with lattice constant $a = 3.1$ Å in the temperature interval T = 100 K $\rightarrow$ T = 1000 K with ΔT= 100 K.

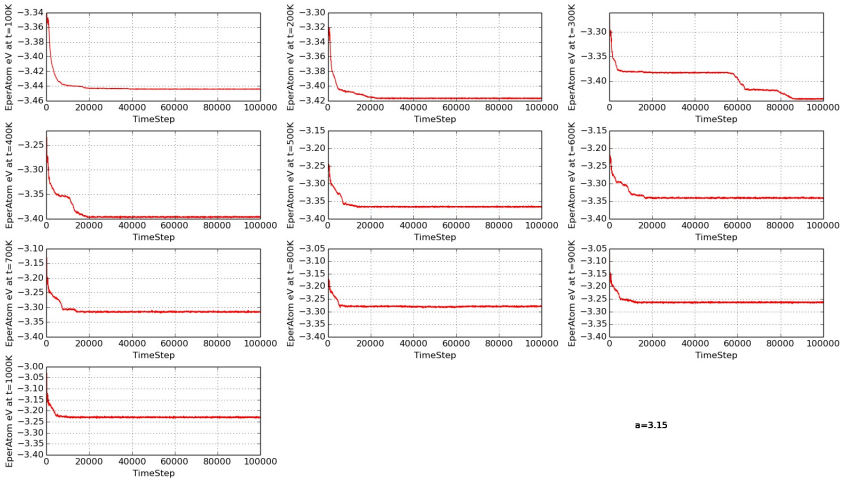

Figure C.22: Energy per atom (in eV) as a function of time step for a bcc uranium with lattice constant $a = 3.15$ Å in the temperature interval T = 100 K $\rightarrow$ T = 1000 K with ΔT= 100 K.

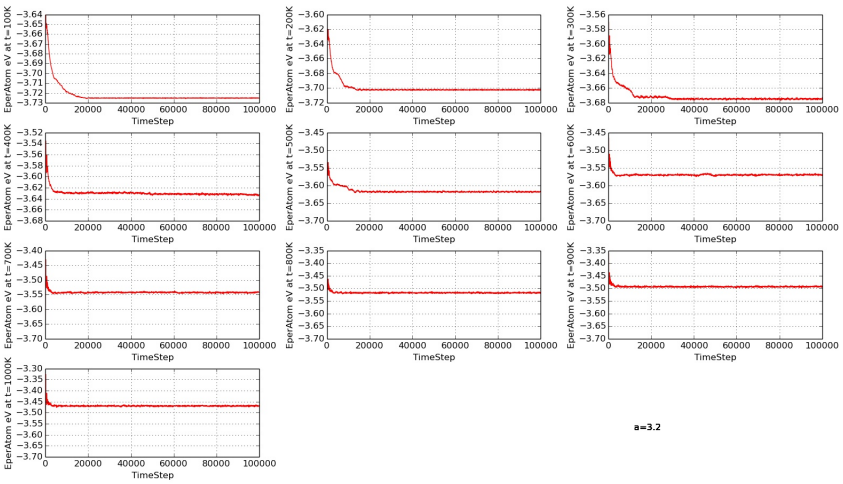

Figure C.23: Energy per atom (in eV) as a function of time step for a bcc uranium with lattice constant $a = 3.2$ Å in the temperature interval T = 100 K $\rightarrow$ T = 1000 K with ΔT= 100 K.

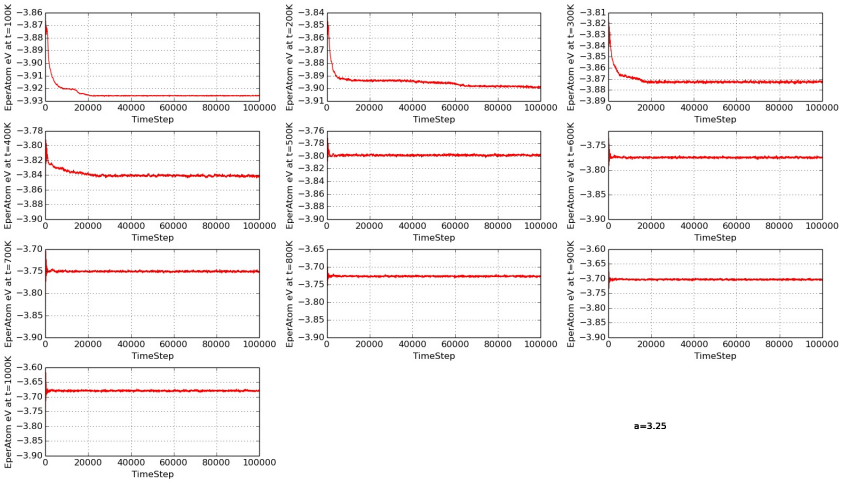

Figure C.24: Energy per atom (in eV) as a function of time step for a bcc uranium with lattice constant $a = 3.25$ Å in the temperature interval T = 100 K $\rightarrow$ T = 1000 K with ΔT= 100 K.

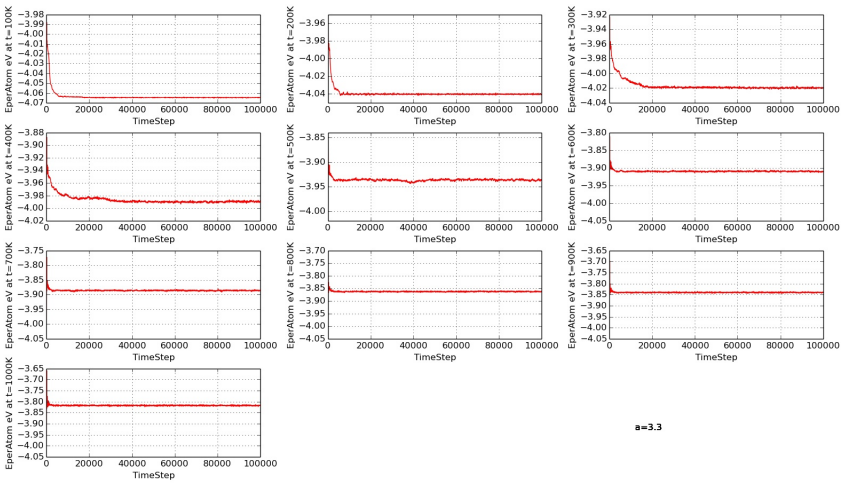

Figure C.25: Energy per atom (in eV) as a function of time step for a bcc uranium with lattice constant $a = 3.3$ Å in the temperature interval T = 100 K $\rightarrow$ T = 1000 K with ΔT= 100 K.

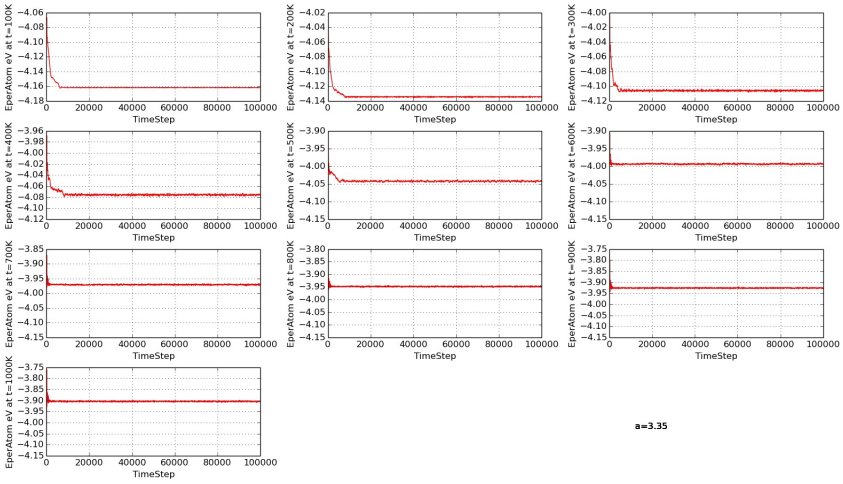

Figure C.26: Energy per atom (in eV) as a function of time step for a bcc uranium with lattice constant $a = 3.35$ Å in the temperature interval T = 100 K $\rightarrow$ T = 1000 K with ΔT= 100 K.

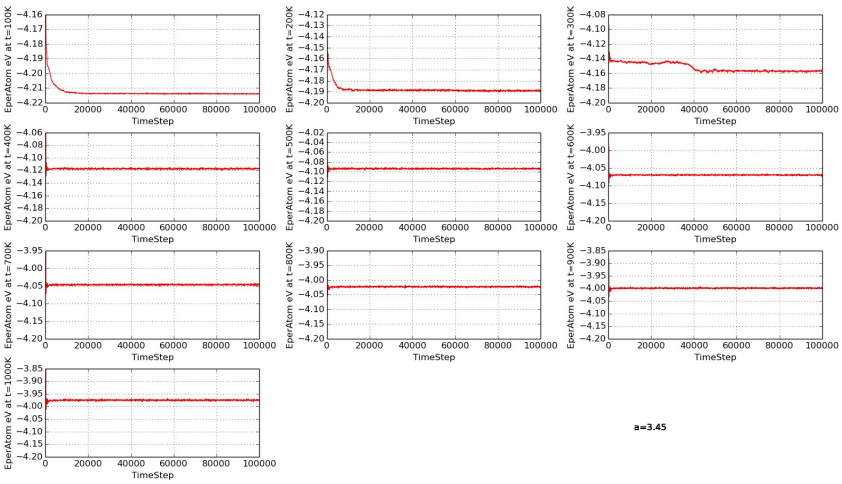

Figure C.27: Energy per atom (in eV) as a function of time step for a bcc uranium with lattice constant $a = 3.45$ Å in the temperature interval T = 100 K $\rightarrow$ T = 1000 K with ΔT= 100 K.

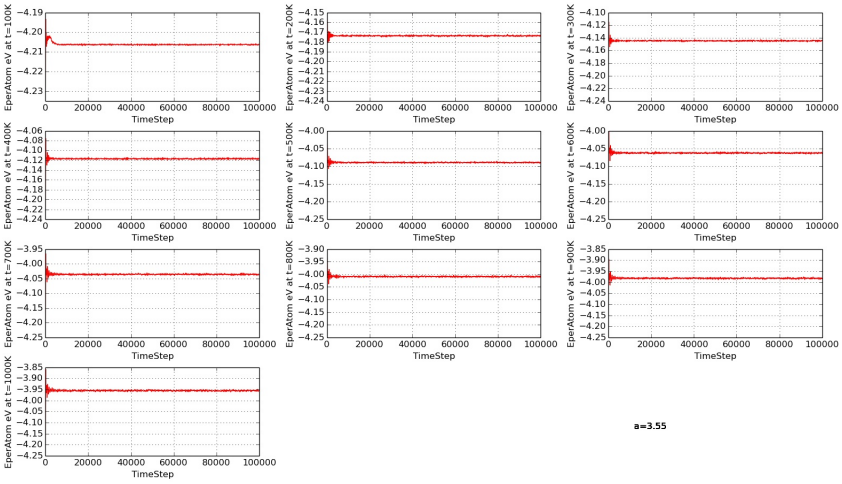

Figure C.28: Energy per atom (in eV) as a function of time step for a bcc uranium with lattice constant $a = 3.55$ Å in the temperature interval T = 100 K $\rightarrow$ T = 1000 K with ΔT= 100 K.

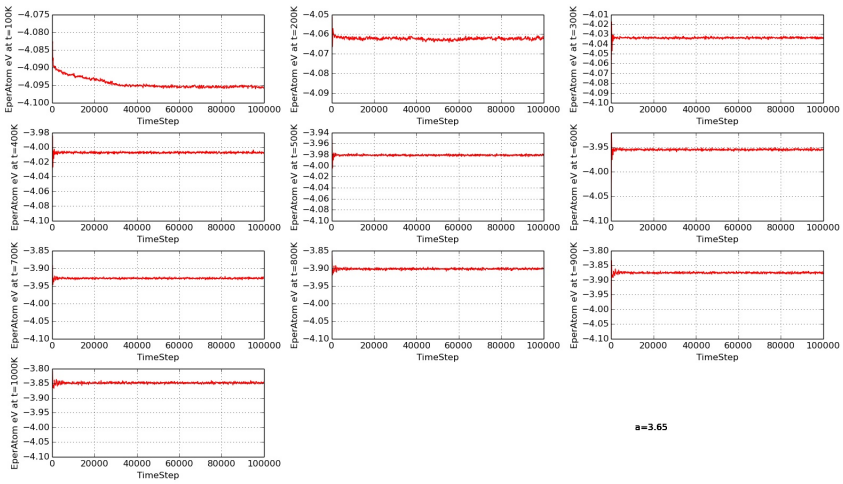

Figure C.29: Energy per atom (in eV) as a function of time step for a bcc uranium with lattice constant $a = 3.65$ Å in the temperature interval T = 100 K $\rightarrow$ T = 1000 K with ΔT= 100 K.

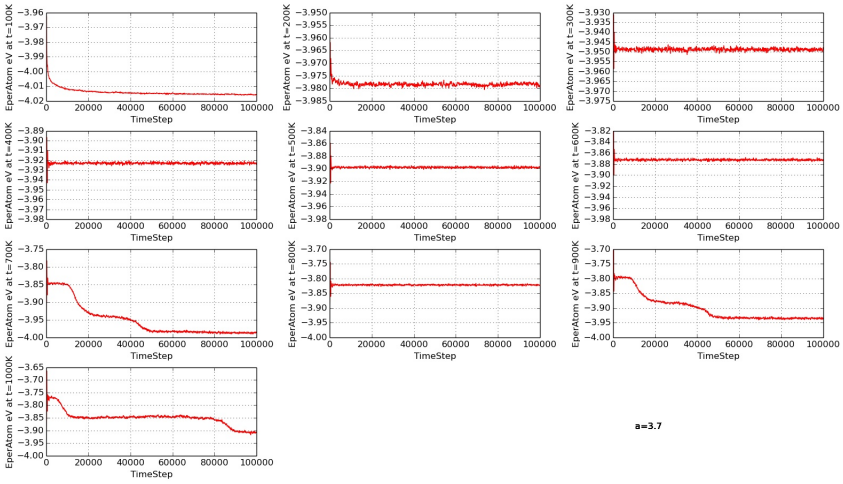

Figure C.30: Energy per atom (in eV) as a function of time step for a bcc uranium with lattice constant $a = 3.7$ Å in the temperature interval T = 100 K $\rightarrow$ T = 1000 K with ΔT= 100 K.

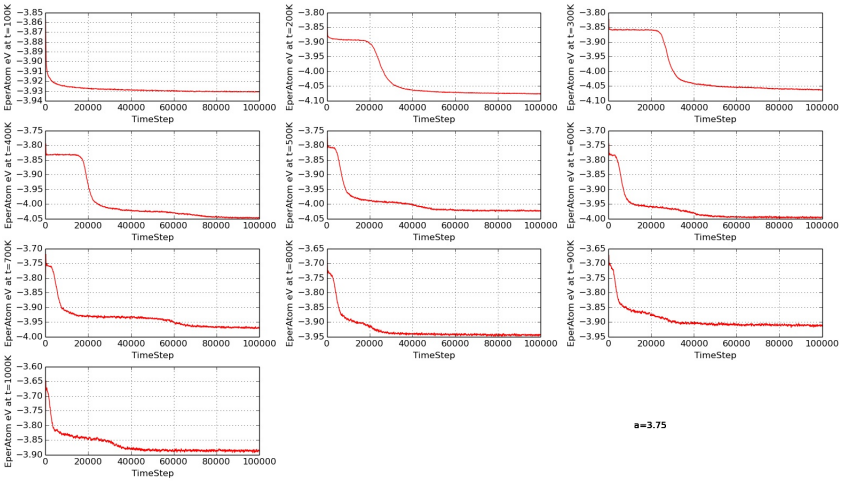

Figure C.31: Energy per atom (in eV) as a function of time step for a bcc uranium with lattice constant $a = 3.75$ Å in the temperature interval T = 100 K $\rightarrow$ T = 1000 K with ΔT= 100 K.

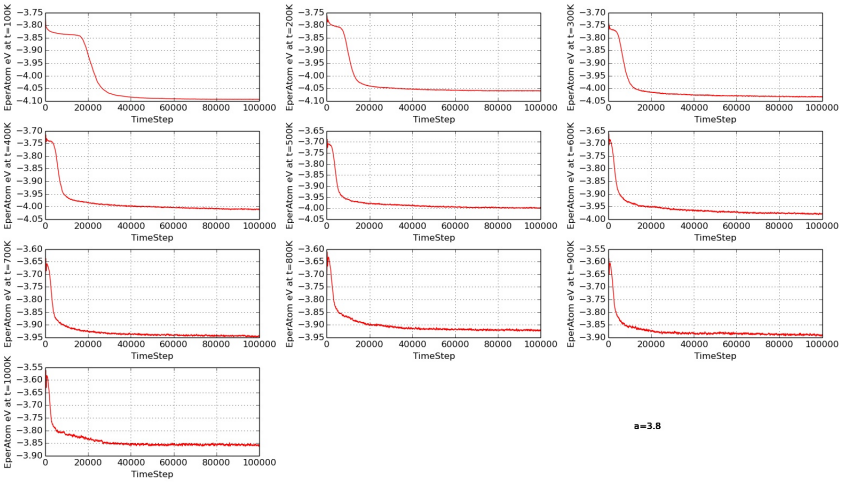

Figure C.32: Energy per atom (in eV) as a function of time step for a bcc uranium with lattice constant $a = 3.8$ Å in the temperature interval T = 100 K $\rightarrow$ T = 1000 K with ΔT= 100 K.

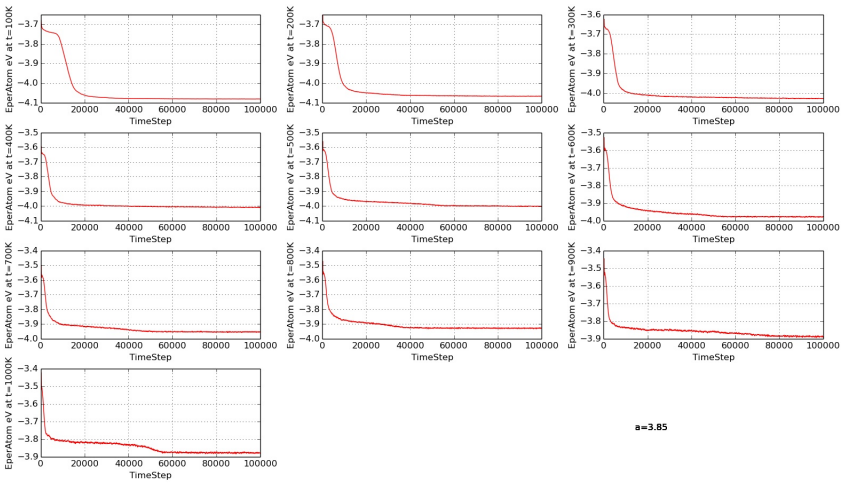

Figure C.33: Energy per atom (in eV) as a function of time step for a bcc uranium with lattice constant $a = 3.85$ Å in the temperature interval T = 100 K $\rightarrow$ T = 1000 K with ΔT= 100 K.

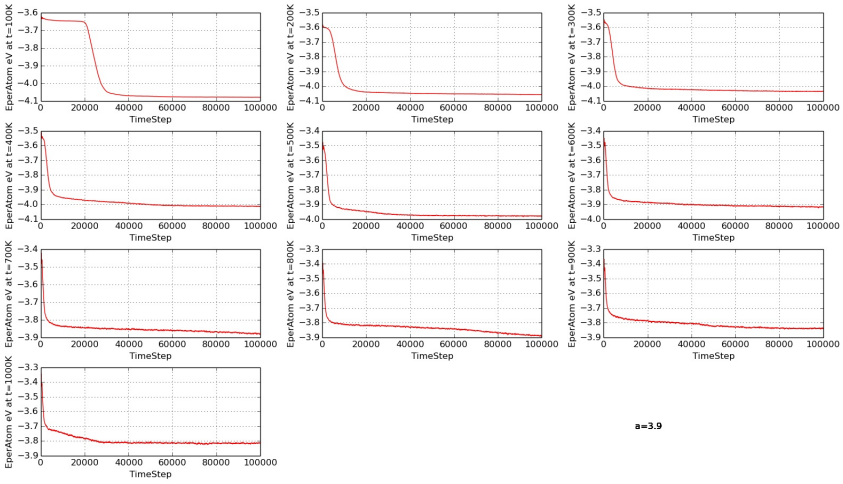

Figure C.34: Energy per atom (in eV) as a function of time step for a bcc uranium with lattice constant $a = 3.9$ Å in the temperature interval T = 100 K $\rightarrow$ T = 1000 K with ΔT= 100 K.

We now show the behavior of pressure as a function of the time step for the values of the lattice constant a from $a = 3.0$ Å to $a = 3.9$ Å for every T, in Figure C.35-Figure C.50.

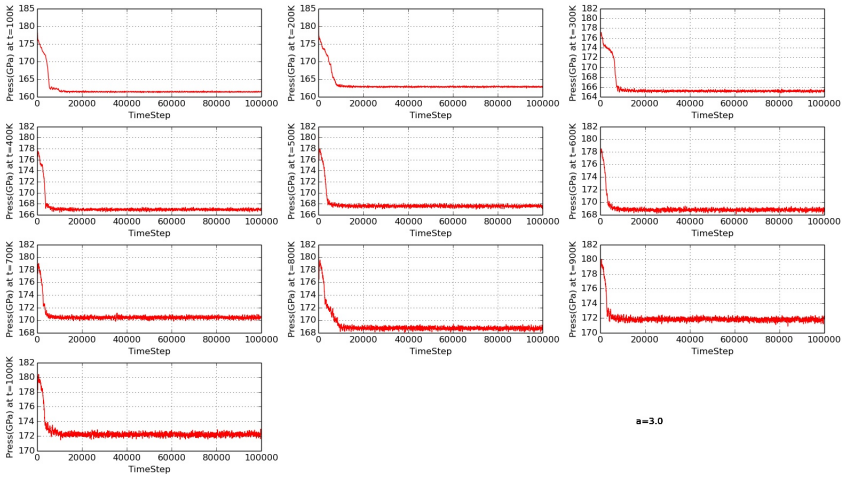

Figure C.35: Pressure in GPa as a function of time step for a bcc uranium with lattice constant $a = 3.0$ Å, in the temperature interval between T = 100 K and T = 1000 K with ΔT = 100 K.

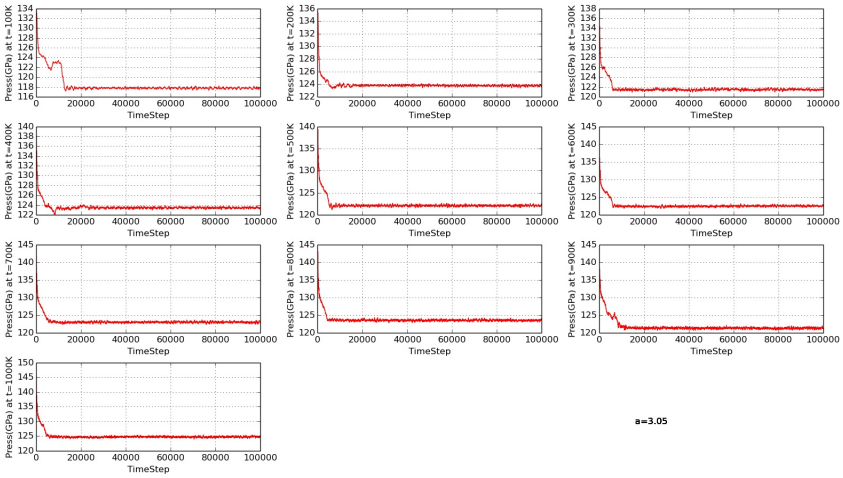

Figure C.36: Pressure in GPa as a function of time step for a bcc uranium with lattice constant $a = 3.05$ Å, in the temperature interval between T = 100 K and T = 1000 K with ΔT = 100 K.

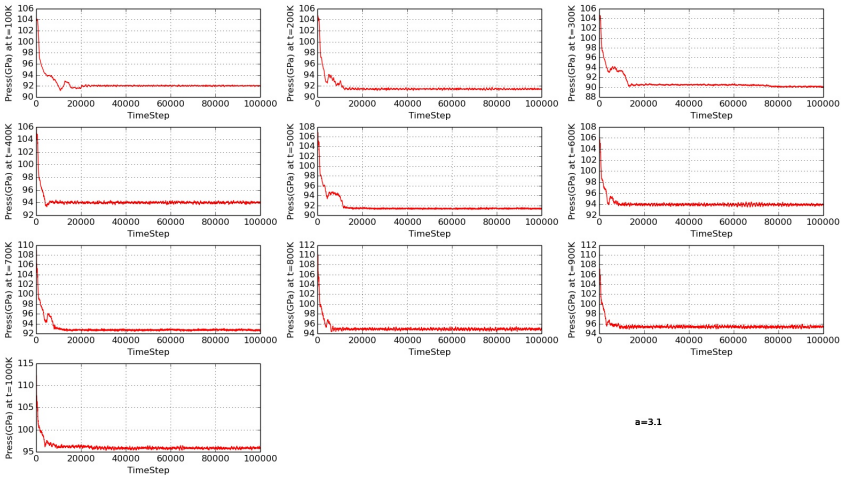

Figure C.37: Pressure in GPa as a function of time step for a bcc uranium with lattice constant $a = 3.1$ Å, in the temperature interval between T = 100 K and T = 1000 K with ΔT = 100 K.

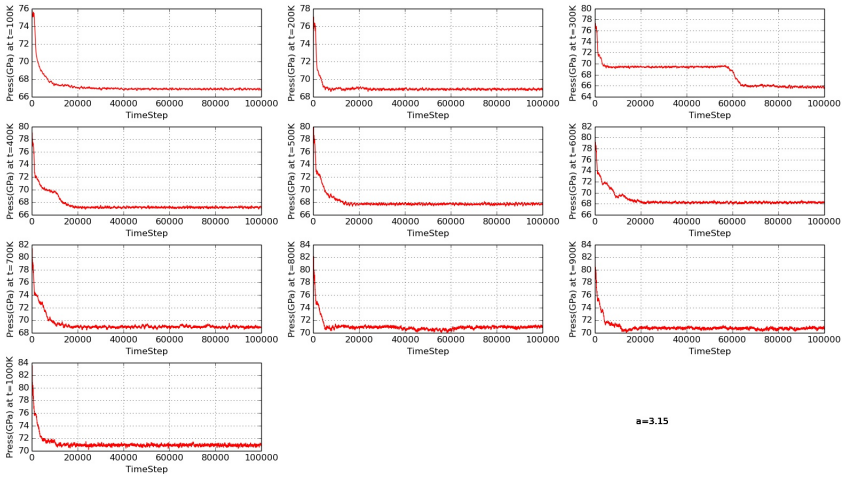

Figure C.38: Pressure in GPa as a function of time step for a bcc uranium with lattice constant $a = 3.15$ Å, in the temperature interval between T = 100 K and T = 1000 K with ΔT = 100 K.

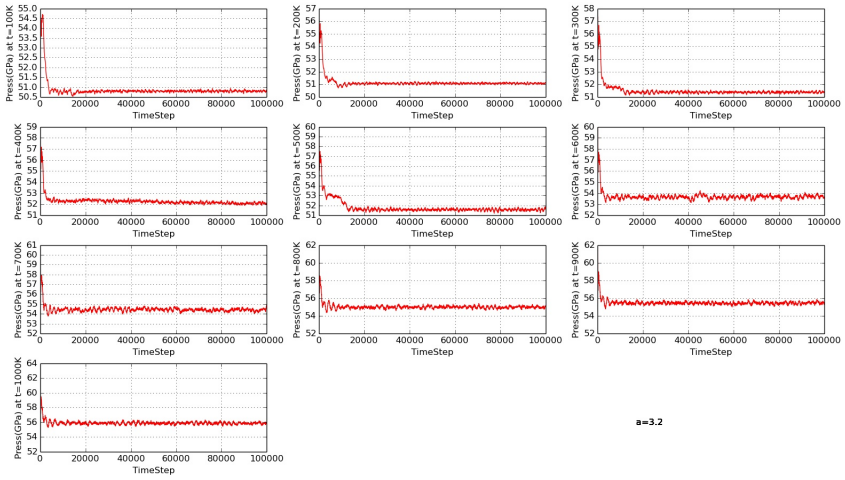

Figure C.39: Pressure in GPa as a function of time step for a bcc uranium with lattice constant $a = 3.2$ Å, in the temperature interval between T = 100 K and T = 1000 K with ΔT = 100 K.

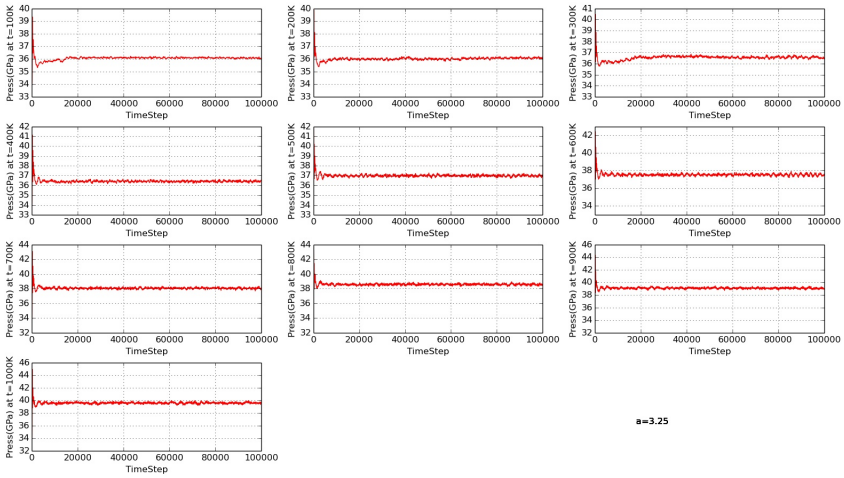

Figure C.40: Pressure in GPa as a function of time step for a bcc uranium with lattice constant $a = 3.25$ Å, in the temperature interval between T = 100 K and T = 1000 K with ΔT = 100 K.

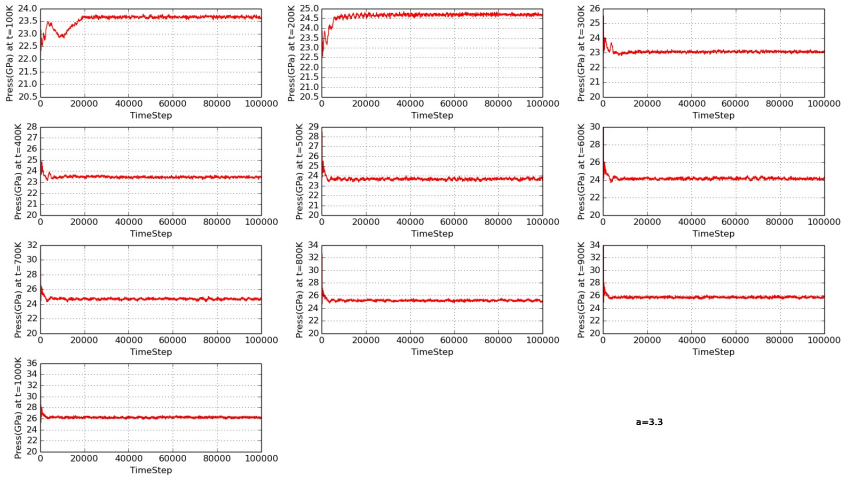

Figure C.41: Pressure in GPa as a function of time step for a bcc uranium with lattice constant $a = 3.3$ Å, in the temperature interval between T = 100 K and T = 1000 K with ΔT = 100 K.

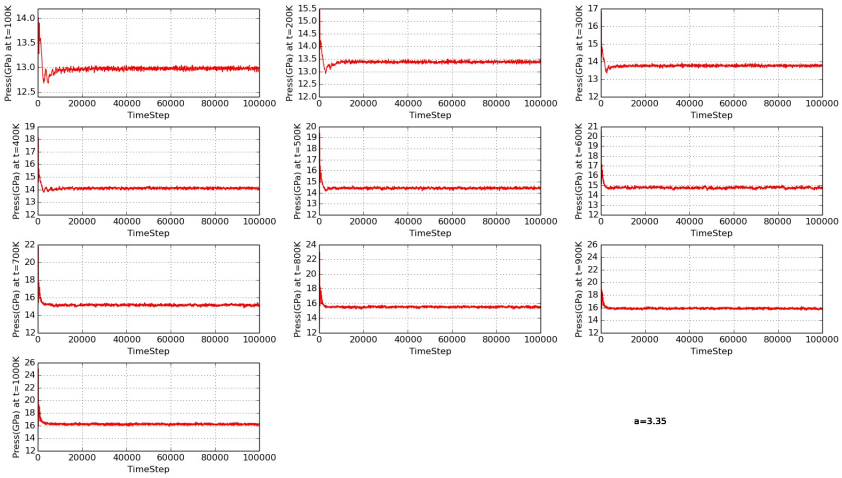

Figure C.42: Pressure in GPa as a function of time step for a bcc uranium with lattice constant $a = 3.35$ Å, in the temperature interval between T = 100 K and T = 1000 K with ΔT = 100 K.

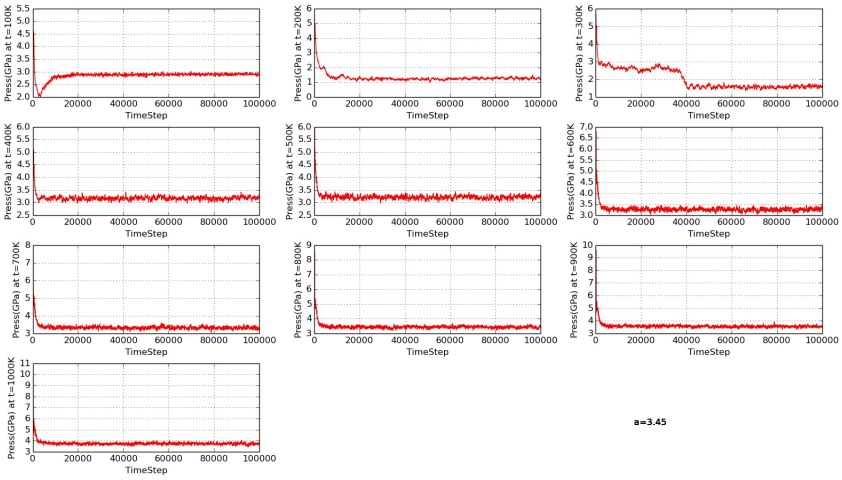

Figure C.43: Pressure in GPa as a function of time step for a bcc uranium with lattice constant $a = 3.45$ Å, in the temperature interval between T = 100 K and T = 1000 K with ΔT = 100 K.

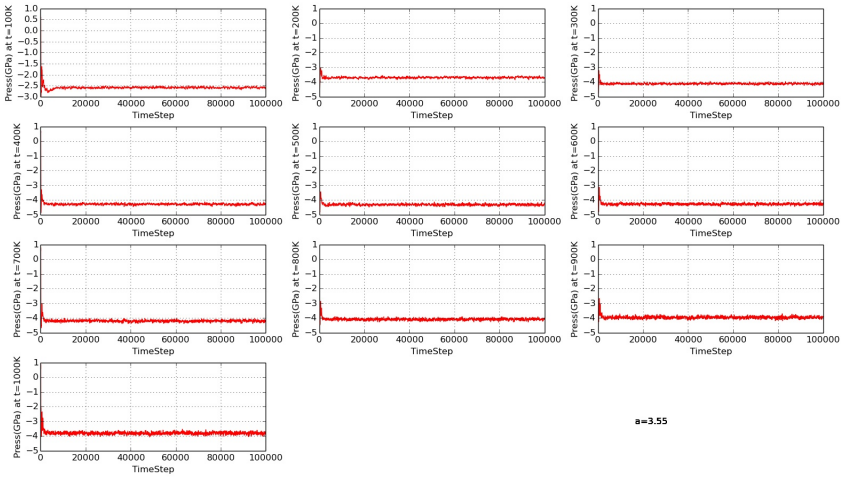

Figure C.44: Pressure in GPa as a function of time step for a bcc uranium with lattice constant $a = 3.55$ Å, in the temperature interval between T = 100 K and T = 1000 K with ΔT = 100 K.

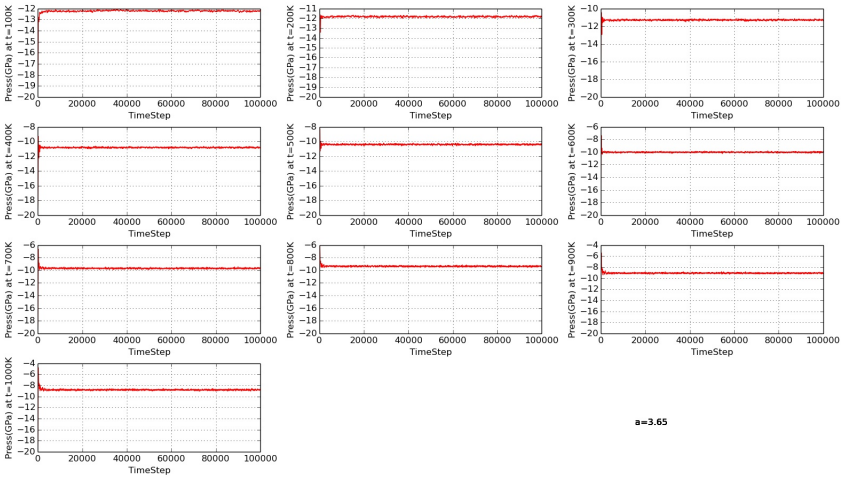

Figure C.45: Pressure in GPa as a function of time step for a bcc uranium with lattice constant $a = 3.65$ Å, in the temperature interval between T = 100 K and T = 1000 K with ΔT = 100 K.

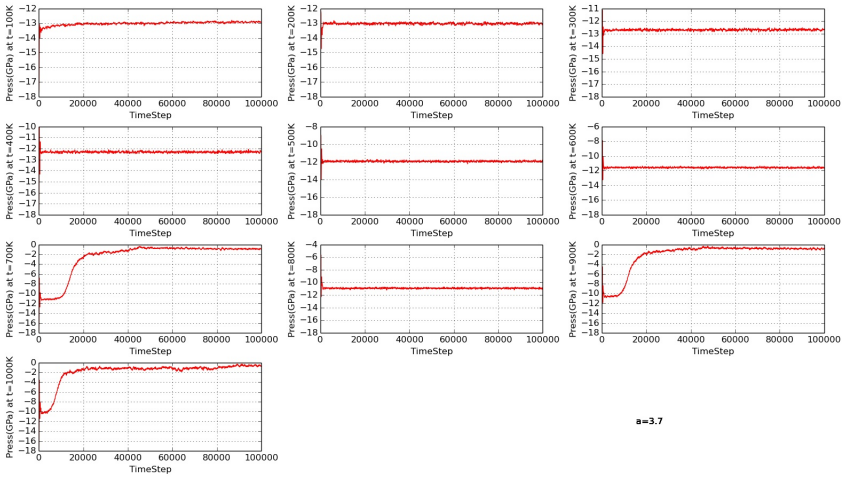

Figure C.46: Pressure in GPa as a function of time step for a bcc uranium with lattice constant $a = 3.7$ Å, in the temperature interval between T = 100 K and T = 1000 K with ΔT = 100 K.

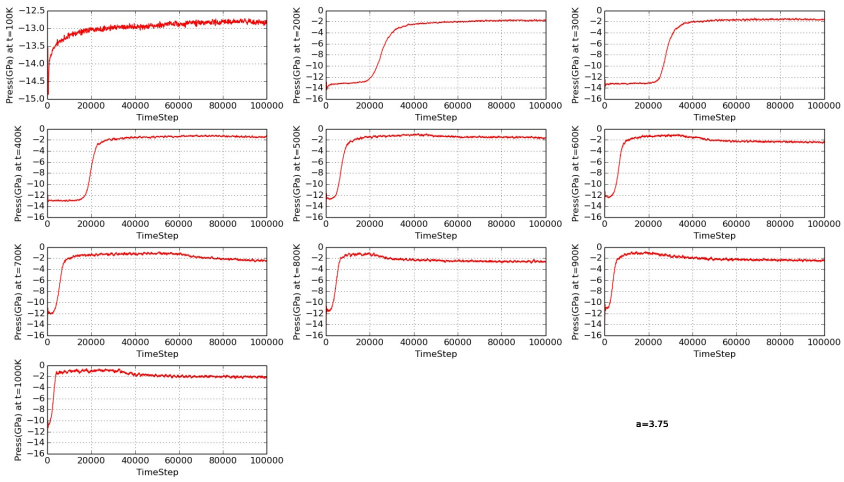

Figure C.47: Pressure in GPa as a function of time step for a bcc uranium with lattice constant $a = 3.75$ Å, in the temperature interval between T = 100 K and T = 1000 K with ΔT = 100 K.

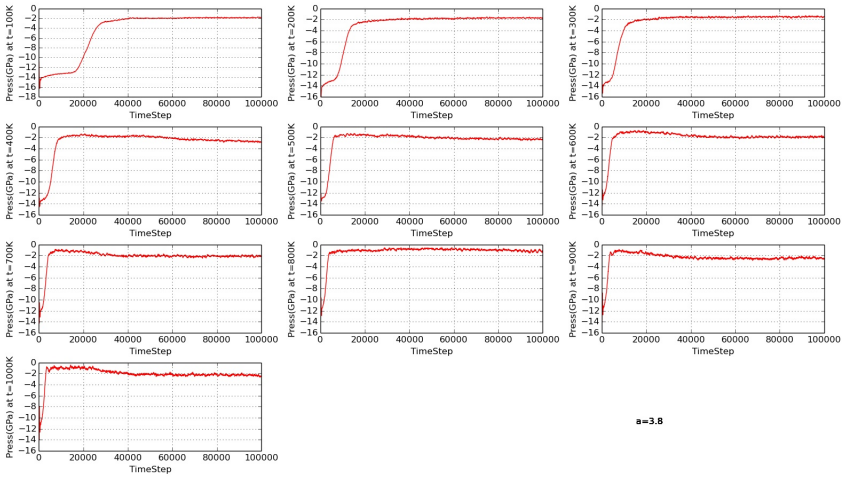

Figure C.48: Pressure in GPa as a function of time step for a bcc uranium with lattice constant $a = 3.8$ Å, in the temperature interval between T = 100 K and T = 1000 K with ΔT = 100 K.

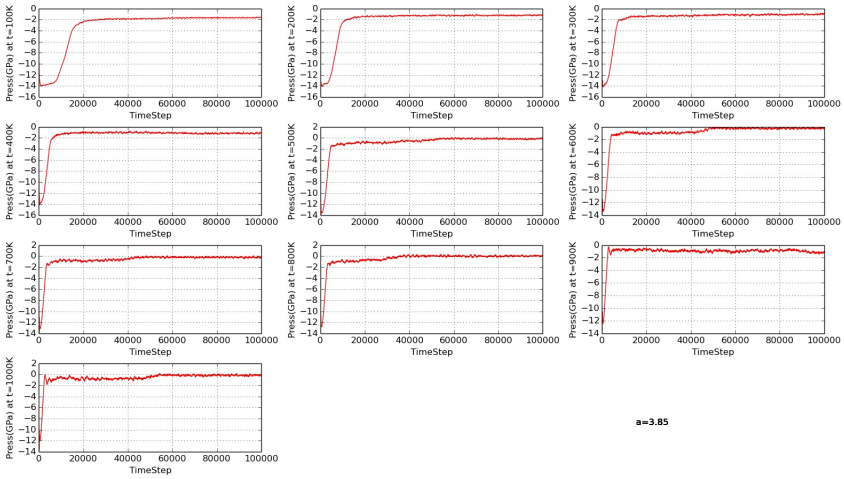

Figure C.49: Pressure in GPa as a function of time step for a bcc uranium with lattice constant $a = 3.85$ Å, in the temperature interval between T = 100 K and T = 1000 K with ΔT = 100 K.

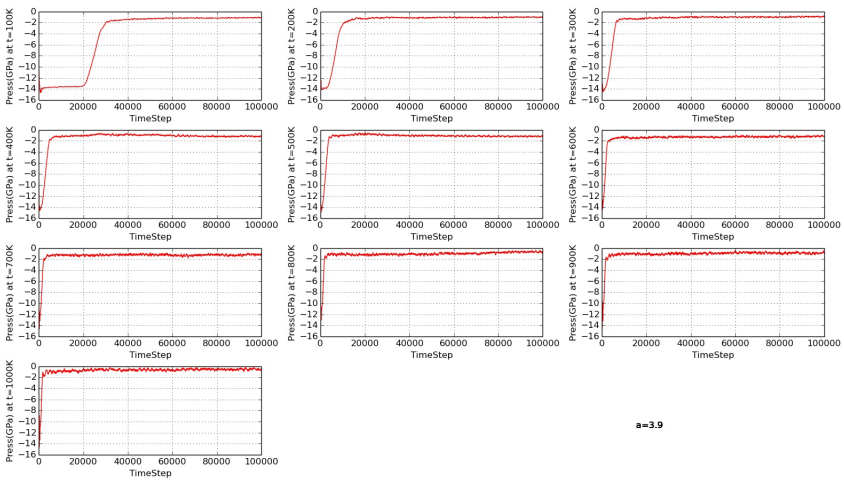

Figure C.50: Pressure in GPa as a function of time step for a bcc uranium with lattice constant $a = 3.9$ Å, in the temperature interval between T = 100 K and T = 1000 K with ΔT = 100 K.

Appendix D

NPT simulations

We show here the graphs produced by the NPT simulations. The first set is the one with the pressure versus the time step for all the lattice parameter from $a = 3.0$ Å to 3.9 Å (Figure D.1-Figure D.16). In the case of the NPT we only have three values of the external pressure, i.e. $P^{ext} = 1$ GPa, $P^{ext} = 20$ GPa and $P^{ext} = 100$ GPa the system has to come to equilibrium with, and three values of the temperature T= 100 K, T = 400 K and T = 700 K.

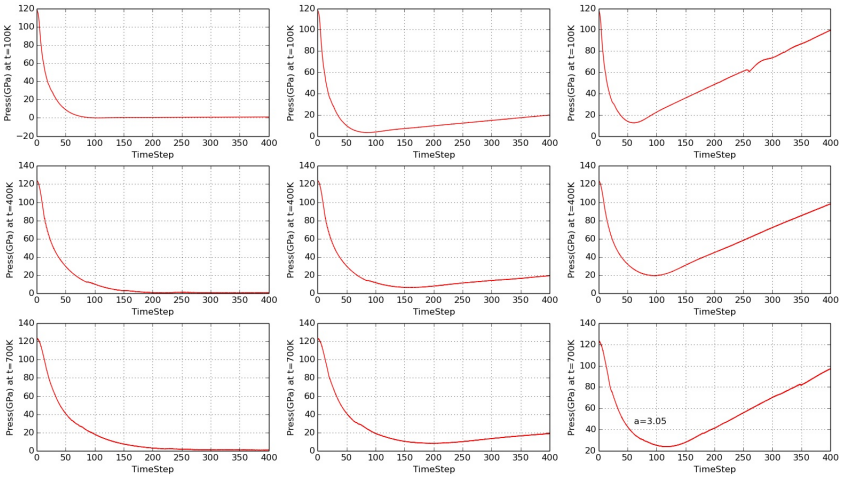

Figure D.1: Pressure (GPa) as a function of the time step (divided by 10^3) for a system with $a = 3.05$ Å. The temperature is fixed going from left to right, whereas moving from upside to downside the behavior with fixed external pressure changing the temperature is shown.

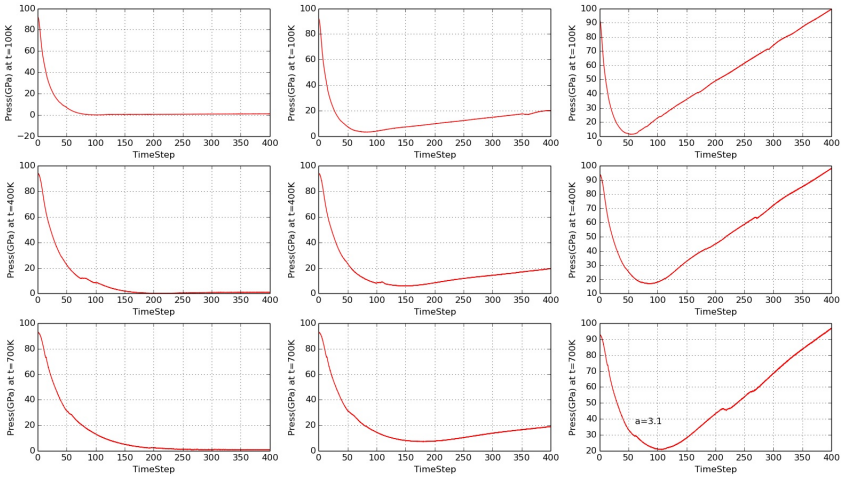

Figure D.2: Pressure (GPa) as a function of the time step (divided by 10^3) for a system with $a = 3.1$ Å. The temperature is fixed going from left to right, whereas moving from upside to downside the behavior with fixed external pressure changing the temperature is shown.

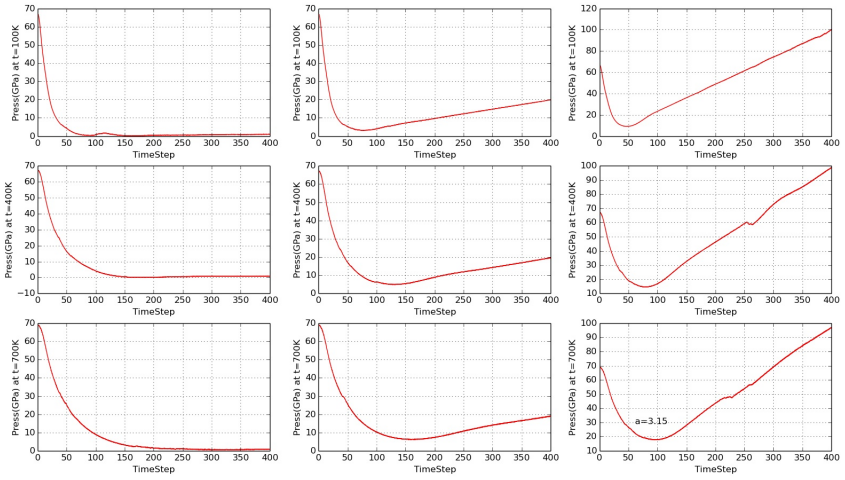

Figure D.3: Pressure (GPa) as a function of the time step (divided by 10^3) for a system with $a = 3.15$ Å. The temperature is fixed going from left to right, whereas moving from upside to downside the behavior with fixed external pressure changing the temperature is shown.

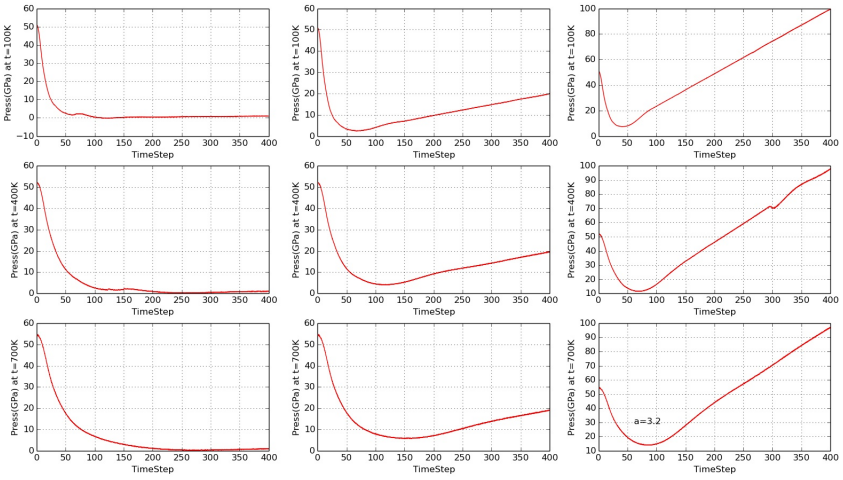

Figure D.4: Pressure (GPa) as a function of the time step (divided by 10^3) for a system with $a = 3.2$ Å. The temperature is fixed going from left to right, whereas moving from upside to downside the behavior with fixed external pressure changing the temperature is shown.

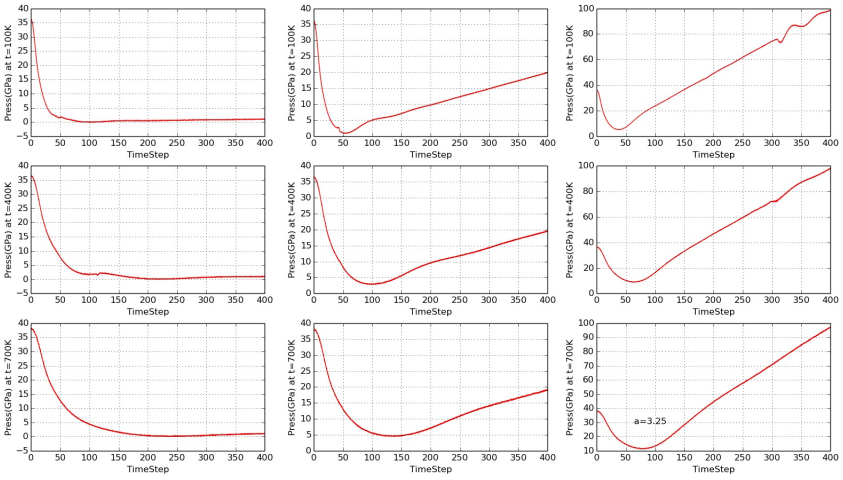

Figure D.5: Pressure (GPa) as a function of the time step (divided by 10^3) for a system with $a = 3.25$ Å. The temperature is fixed going from left to right, whereas moving from upside to downside the behavior with fixed external pressure changing the temperature is shown.

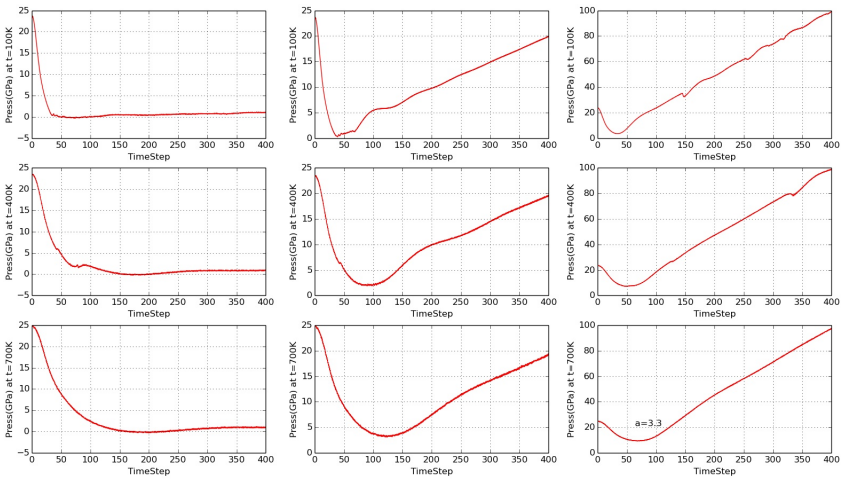

Figure D.6: Pressure (GPa) as a function of the time step (divided by 10^3) for a system with $a = 3.3$ Å. The temperature is fixed going from left to right, whereas moving from upside to downside the behavior with fixed external pressure changing the temperature is shown.

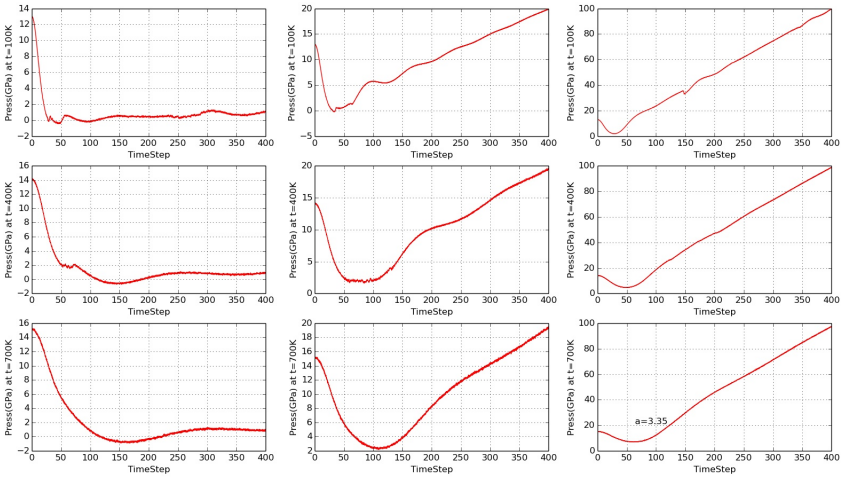

Figure D.7: Pressure (GPa) as a function of the time step (divided by 10^3) for a system with $a = 3.35$ Å. The temperature is fixed going from left to right, whereas moving from upside to downside the behavior with fixed external pressure changing the temperature is shown.

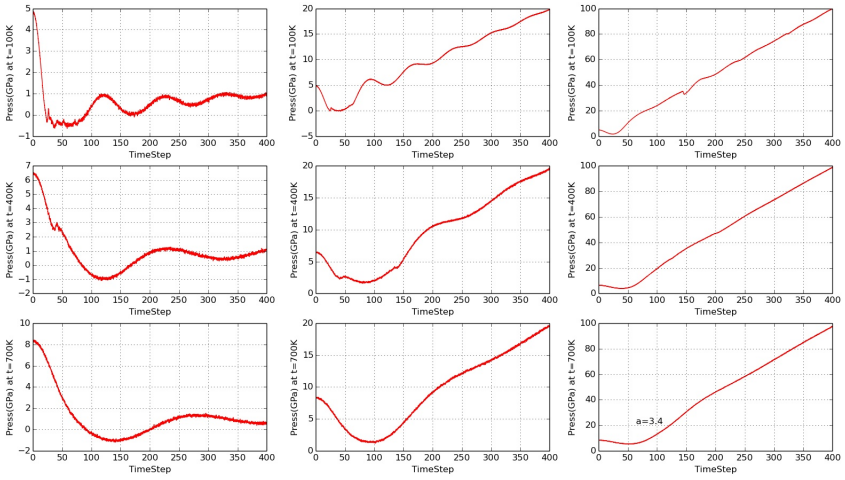

Figure D.8: Pressure (GPa) as a function of the time step (divided by 10^3) for a system with $a = 3.4$ Å. The temperature is fixed going from left to right, whereas moving from upside to downside the behavior with fixed external pressure changing the temperature is shown.

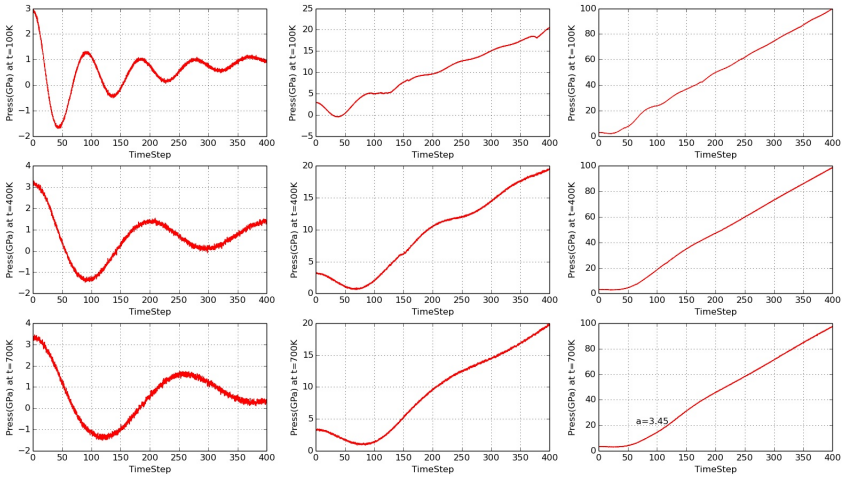

Figure D.9: Pressure (GPa) as a function of the time step (divided by 10^3) for a system with $a = 3.45$ Å. The temperature is fixed going from left to right, whereas moving from upside to downside the behavior with fixed external pressure changing the temperature is shown.

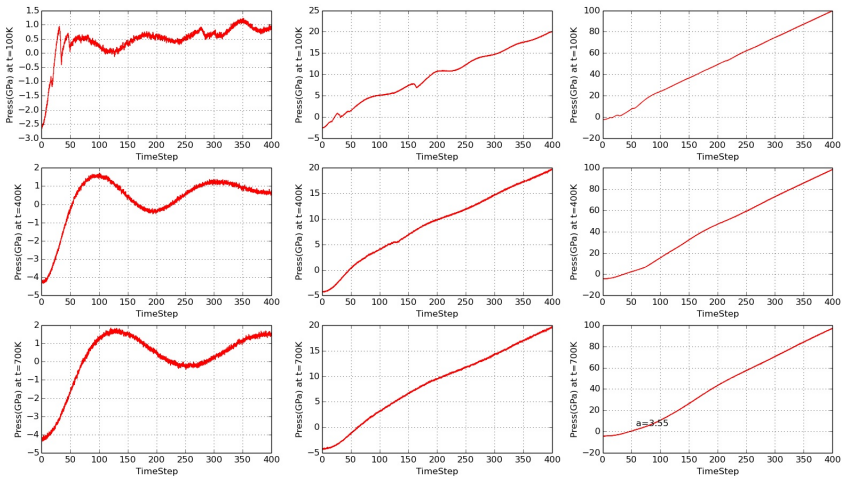

Figure D.10: Pressure (GPa) as a function of the time step (divided by 10^3) for a system with $a = 3.55$ Å. The temperature is fixed going from left to right, whereas moving from upside to downside the behavior with fixed external pressure changing the temperature is shown.

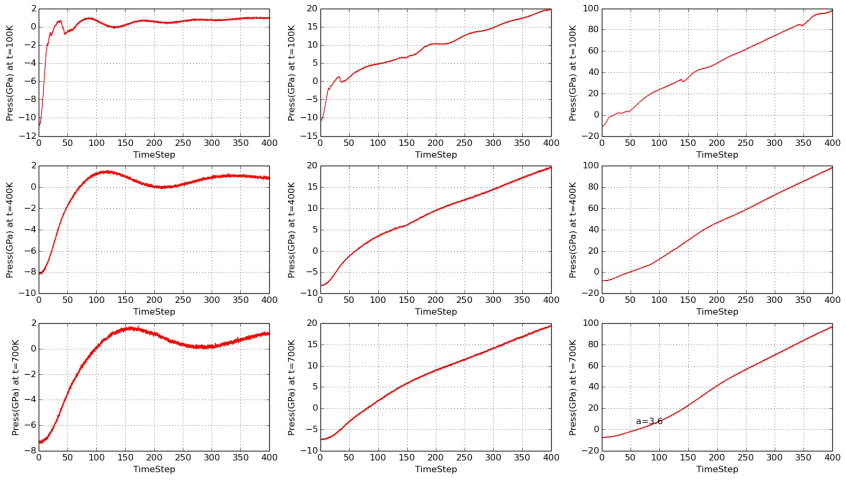

Figure D.11: Pressure (GPa) as a function of the time step (divided by 10^3) for a system with $a = 3.6$ Å. The temperature is fixed going from left to right, whereas moving from upside to downside the behavior with fixed external pressure changing the temperature is shown.

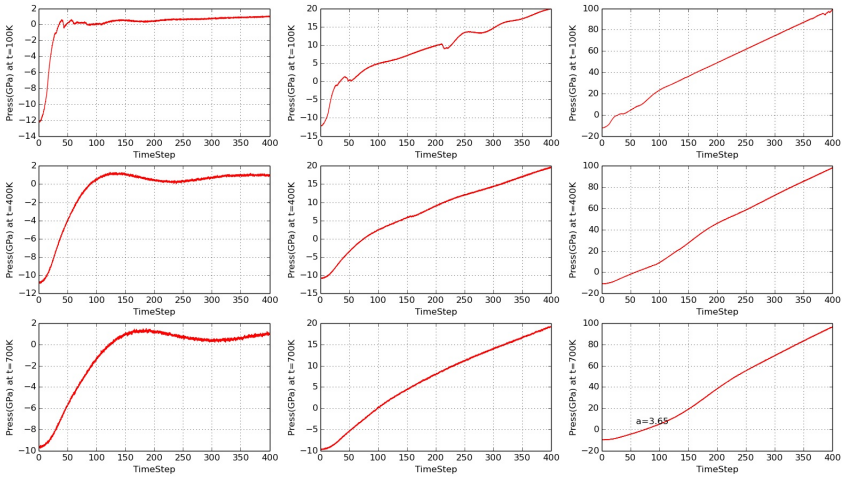

Figure D.12: Pressure (GPa) as a function of the time step (divided by 10^3) for a system with $a = 3.65$ Å. The temperature is fixed going from left to right, whereas moving from upside to downside the behavior with fixed external pressure changing the temperature is shown.

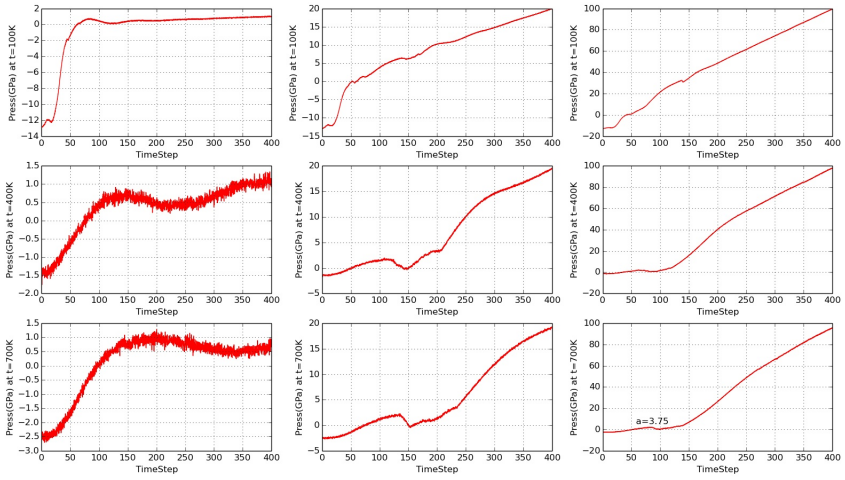

Figure D.13: Pressure (GPa) as a function of the time step (divided by 10^3) for a system with $a = 3.75$ Å. The temperature is fixed going from left to right, whereas moving from upside to downside the behavior with fixed external pressure changing the temperature is shown.

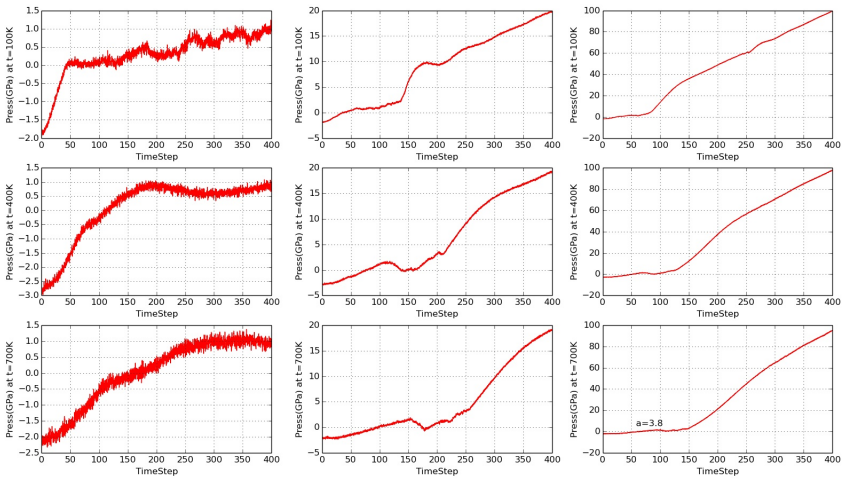

Figure D.14: Pressure (GPa) as a function of the time step (divided by 10^3) for a system with $a = 3.8$ Å. The temperature is fixed going from left to right, whereas moving from upside to downside the behavior with fixed external pressure changing the temperature is shown.

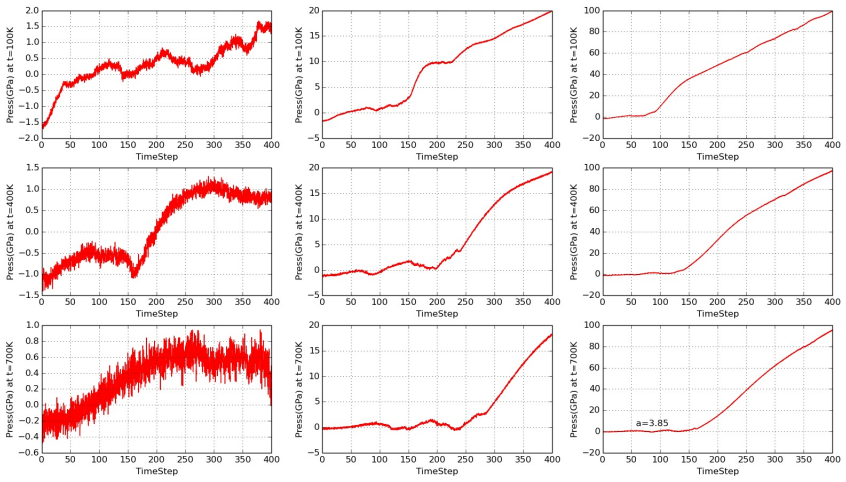

Figure D.15: Pressure (GPa) as a function of the time step (divided by 10^3) for a system with $a = 3.85$ Å. The temperature is fixed going from left to right, whereas moving from upside to downside the behavior with fixed external pressure changing the temperature is shown.

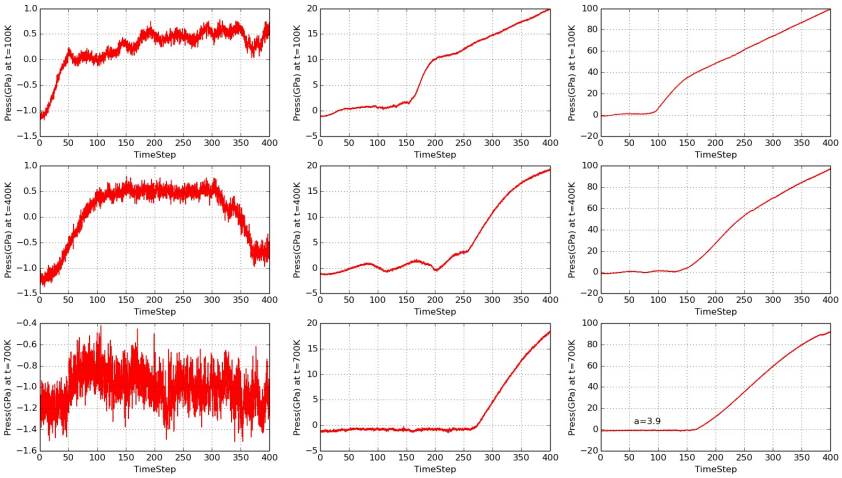

Figure D.16: Pressure (GPa) as a function of the time step (divided by 10^3) for a system with $a = 3.9$ Å. The temperature is fixed going from left to right, whereas moving from upside to downside the behavior with fixed external pressure changing the temperature is shown.

We now show the energy as a function of the time step for all the lattice parameters, in Figure D.17-Figure D.32.

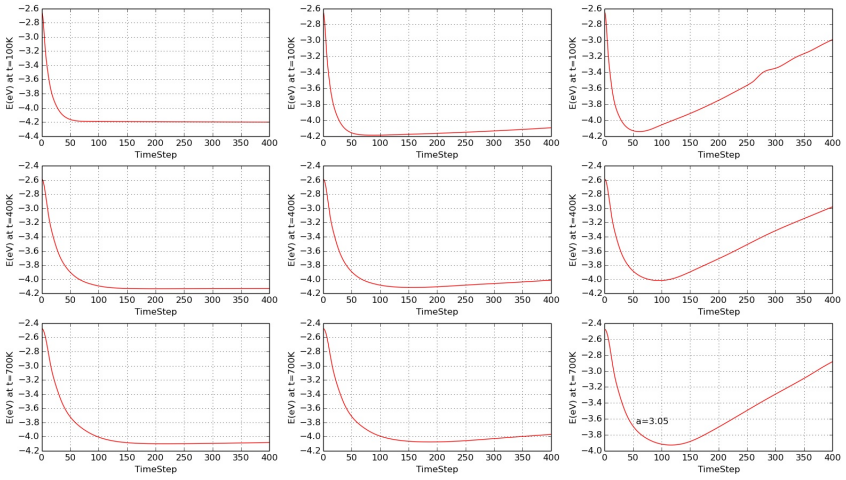

Figure D.17: Energy per atom (in eV) as a function of the time step (divided by 10^3) for a system with $a = 3.05$ Å.

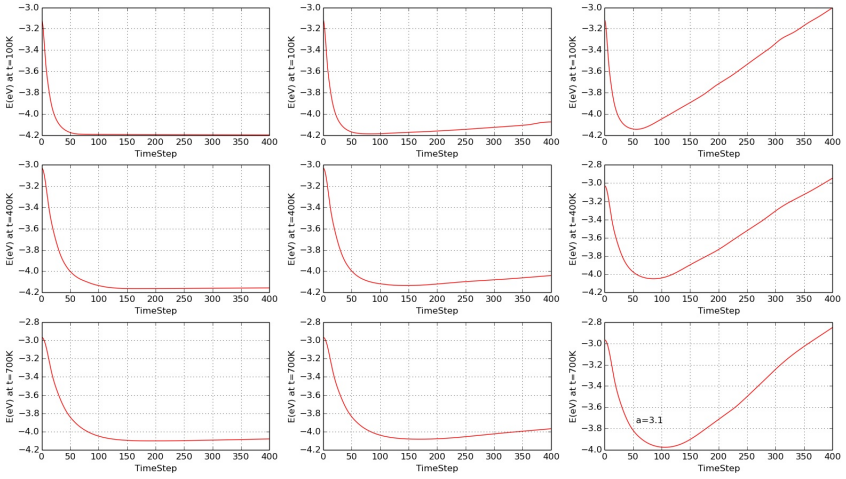

Figure D.18: Energy per atom (in eV) as a function of the time step (divided by 10^3) for a system with $a = 3.1$ Å.

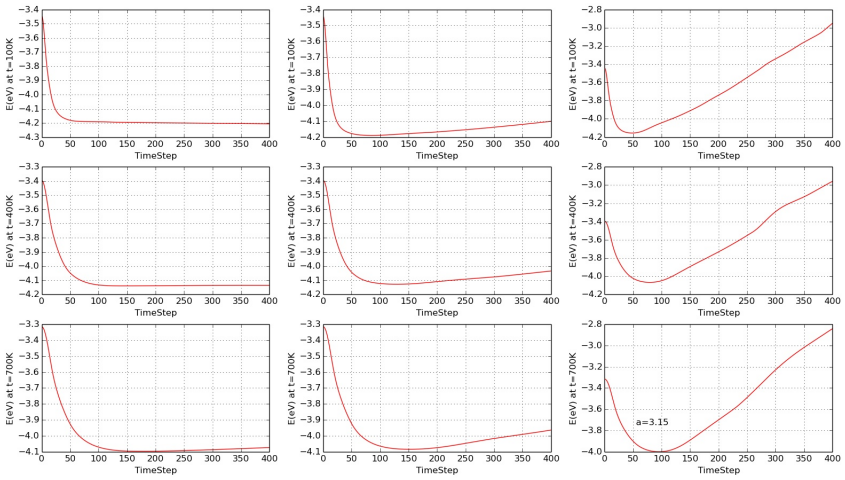

Figure D.19: Energy per atom (in eV) as a function of the time step (divided by 10^3) for a system with $a = 3.15$ Å.

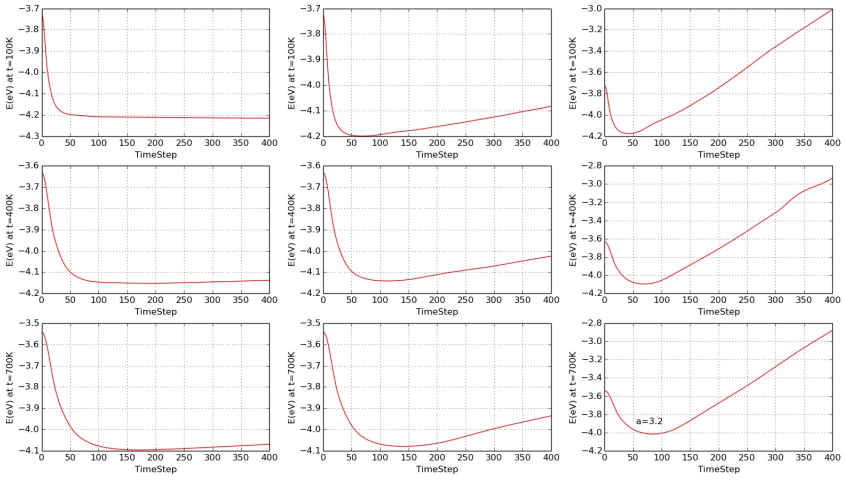

Figure D.20: Energy per atom (in eV) as a function of the time step (divided by 10^3) for a system with $a = 3.2$ Å.

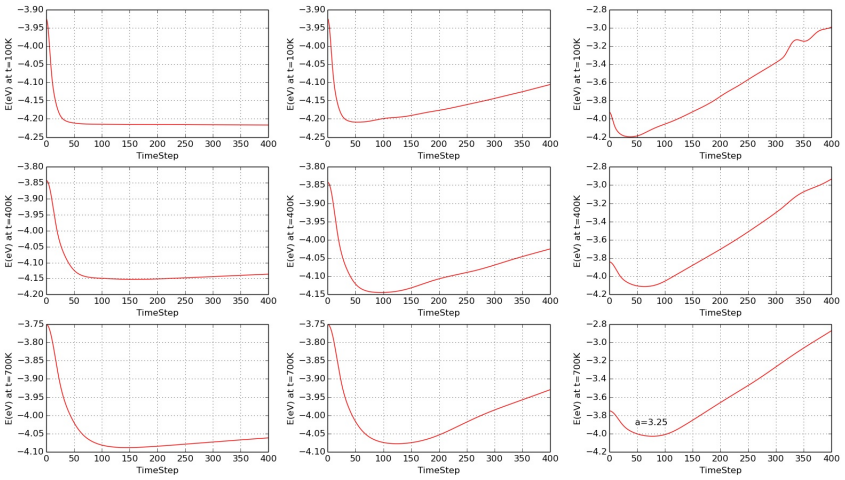

Figure D.21: Energy per atom (in eV) as a function of the time step (divided by 10^3) for a system with $a = 3.25$ Å.

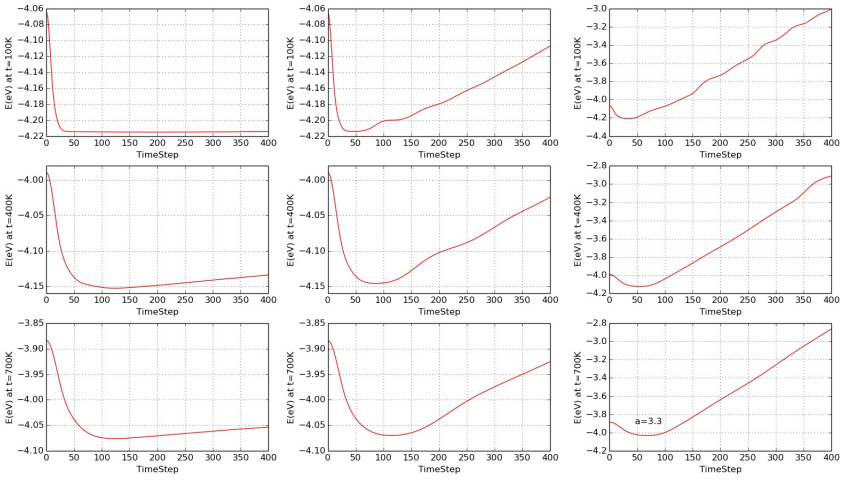

Figure D.22: Energy per atom (in eV) as a function of the time step (divided by 10^3) for a system with $a = 3.3$ Å.

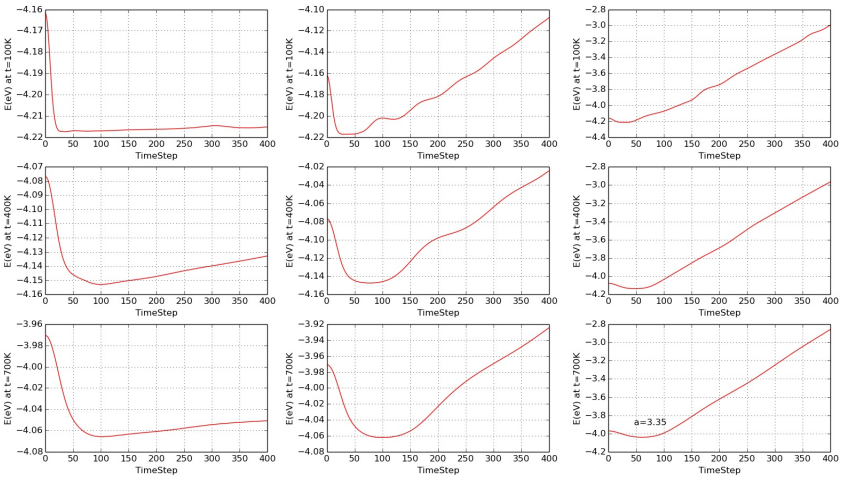

Figure D.23: Energy per atom (in eV) as a function of the time step (divided by 10^3) for a system with $a = 3.35$ Å.

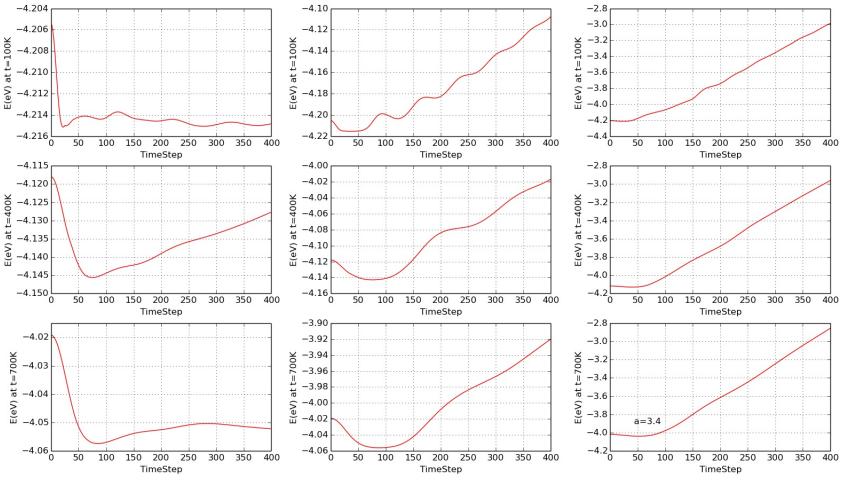

Figure D.24: Energy per atom (in eV) as a function of the time step (divided by 10^3) for a system with $a = 3.4$ Å.

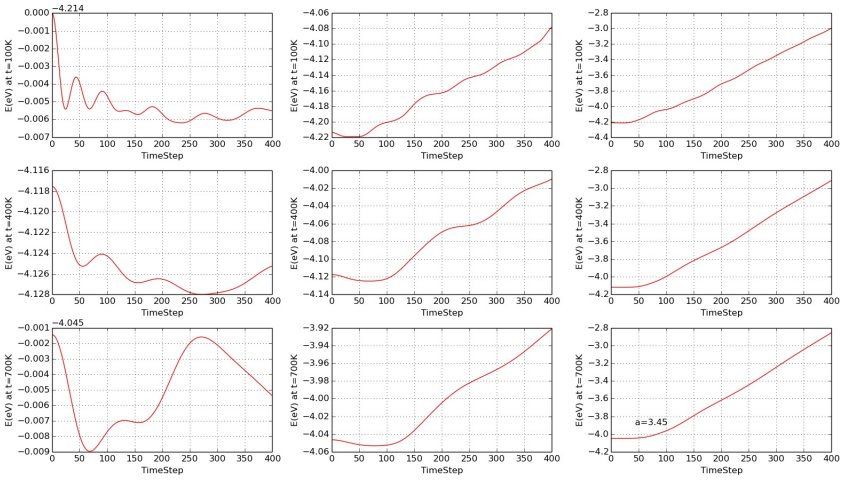

Figure D.25: Energy per atom (in eV) as a function of the time step (divided by 10^3) for a system with $a = 3.45$ Å.

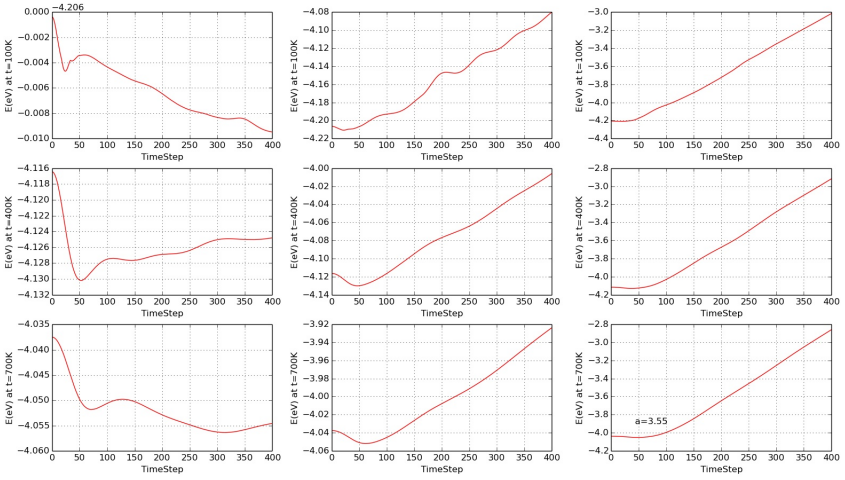

Figure D.26: Energy per atom (in eV) as a function of the time step (divided by 10^3) for a system with $a = 3.55$ Å.

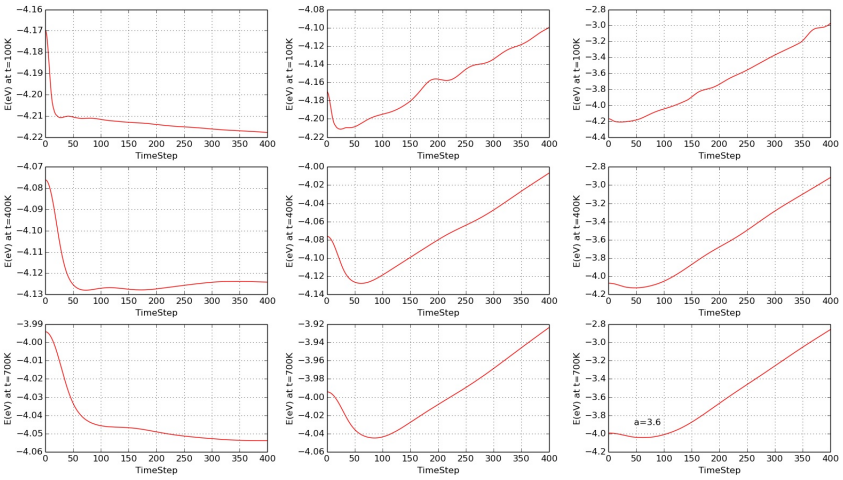

Figure D.27: Energy per atom (in eV) as a function of the time step (divided by 10^3) for a system with $a = 3.6$ Å.

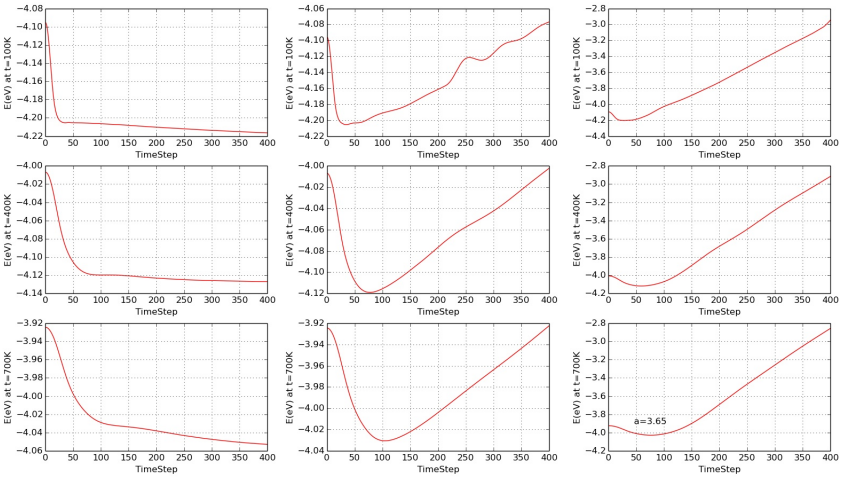

Figure D.28: Energy per atom (in eV) as a function of the time step (divided by 10^3) for a system with $a = 3.65$ Å.

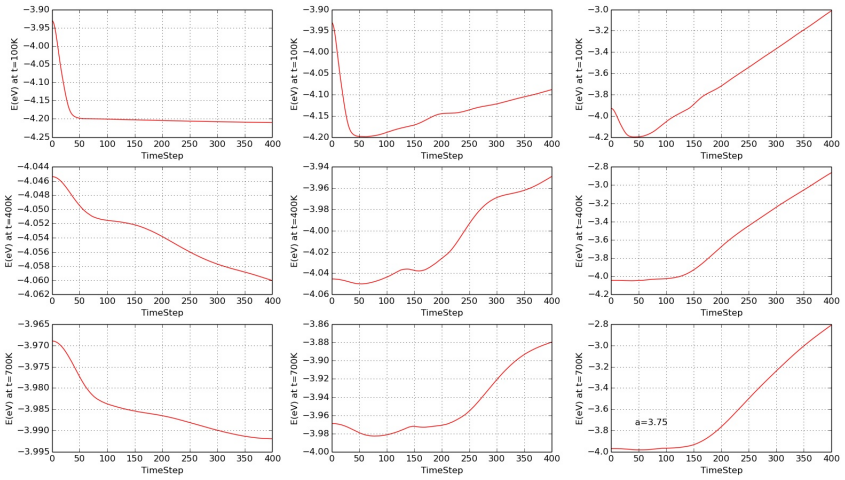

Figure D.29: Energy per atom (in eV) as a function of the time step (divided by 10^3) for a system with $a = 3.75$ Å.

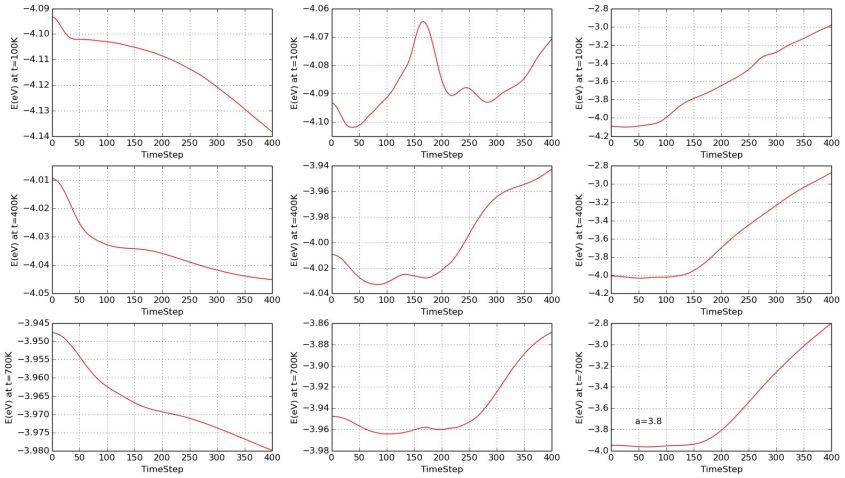

Figure D.30: Energy per atom (in eV) as a function of the time step (divided by 10^3) for a system with $a = 3.8$ Å.

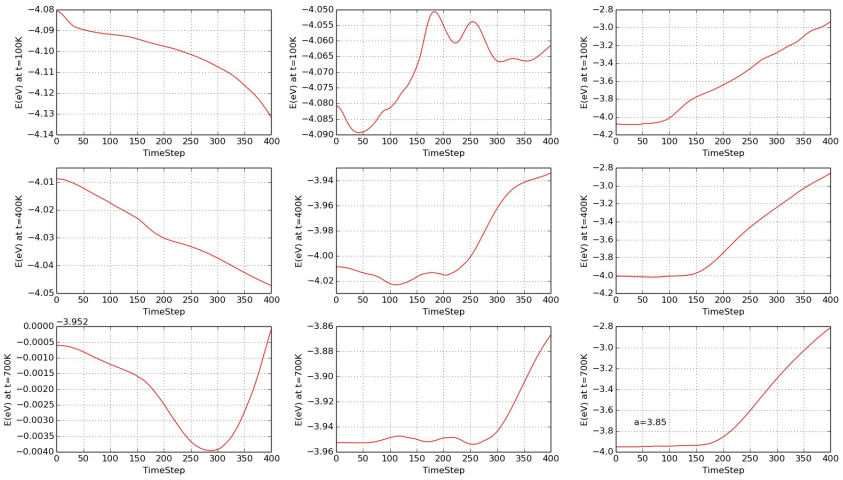

Figure D.31: Energy per atom (in eV) as a function of the time step (divided by 10^3) for a system with $a = 3.85$ Å.

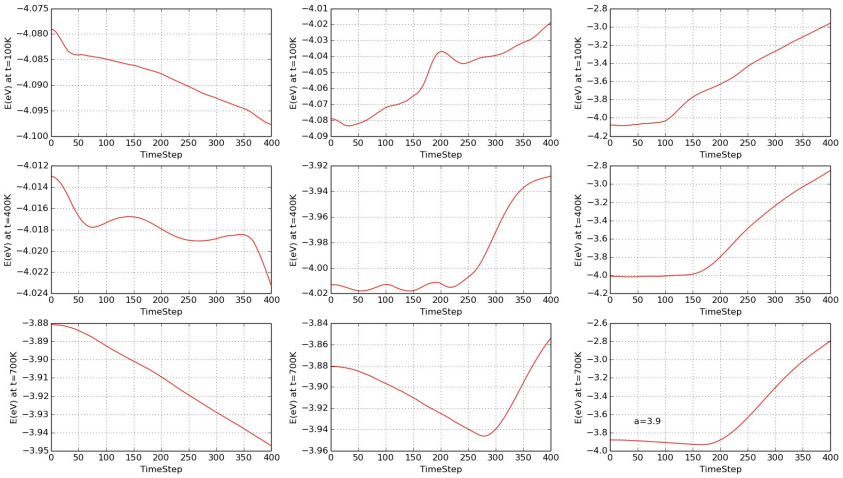

Figure D.32: Energy per atom (in eV) as a function of the time step (divided by 10^3) for a system with $a = 3.9$ Å.

Then we show here the temperature real as a function of the time step in Figure D.33-Figure D.47.

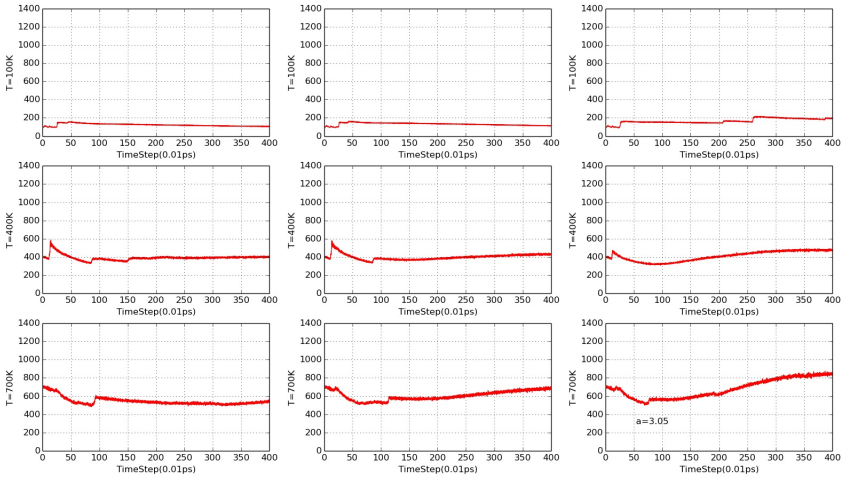

Figure D.33: Real temperature (in K) as a function of the time step (divided by 10^3) for a system with $a = 3.05$ Å.

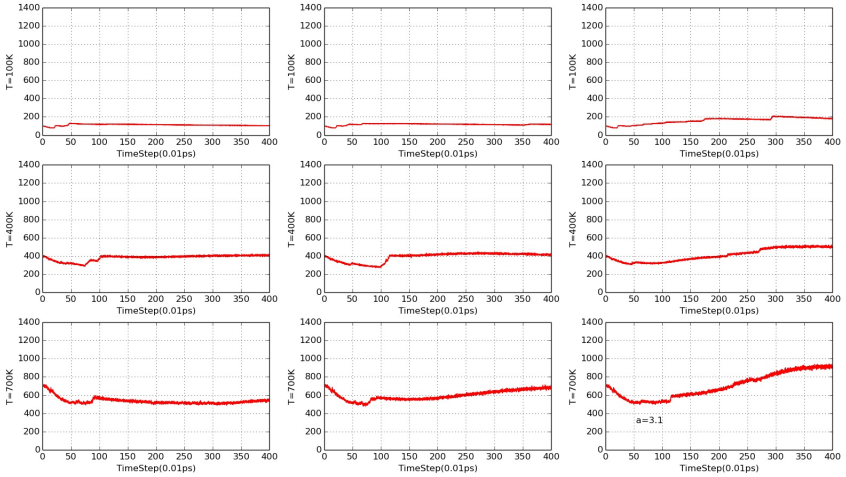

Figure D.34: Real temperature (in K) as a function of the time step (divided by 10^3) for a system with $a = 3.1$ Å.

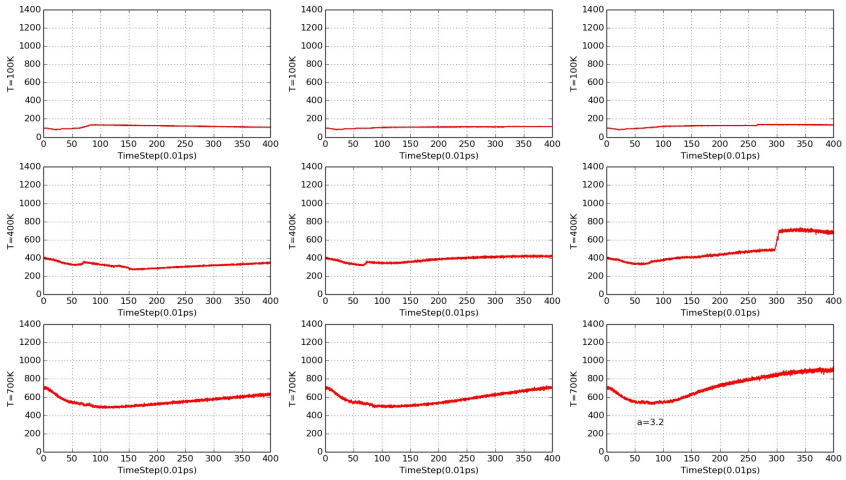

Figure D.35: Real temperature (in K) as a function of the time step (divided by 10^3) for a system with $a = 3.2$ Å.

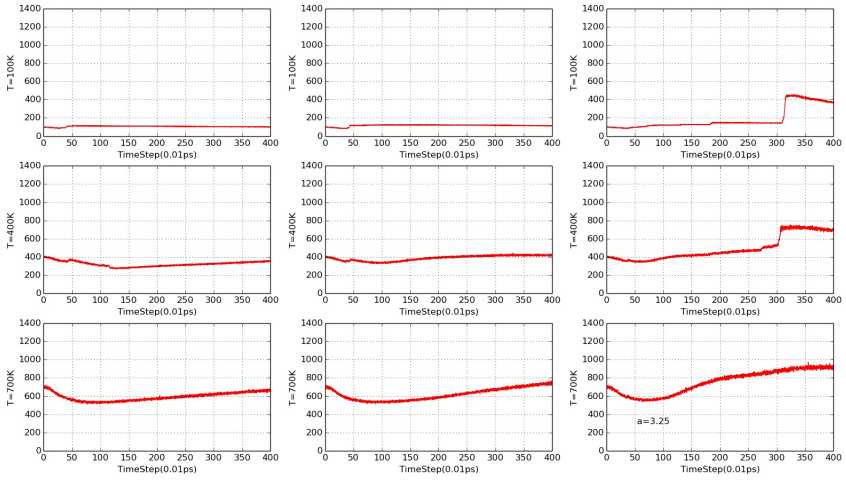

Figure D.36: Real temperature (in K) as a function of the time step (divided by 10^3) for a system with $a = 3.25$ Å.

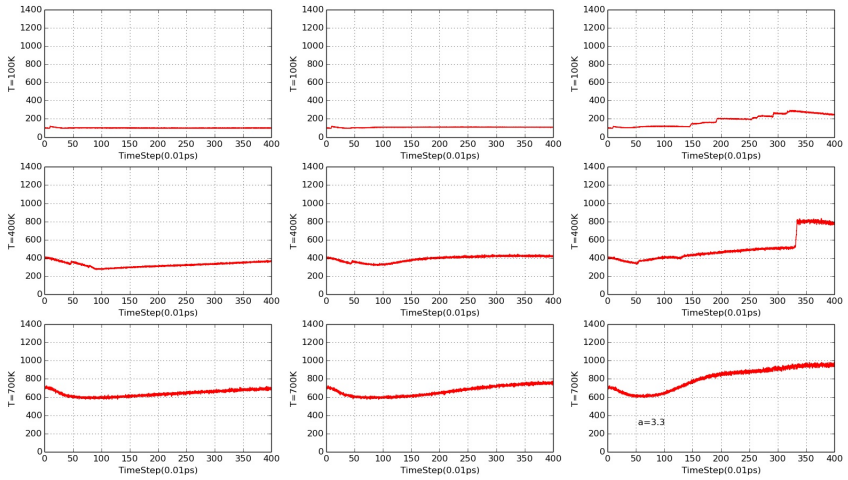

Figure D.37: Real temperature (in K) as a function of the time step (divided by 10^3) for a system with $a = 3.3$ Å.

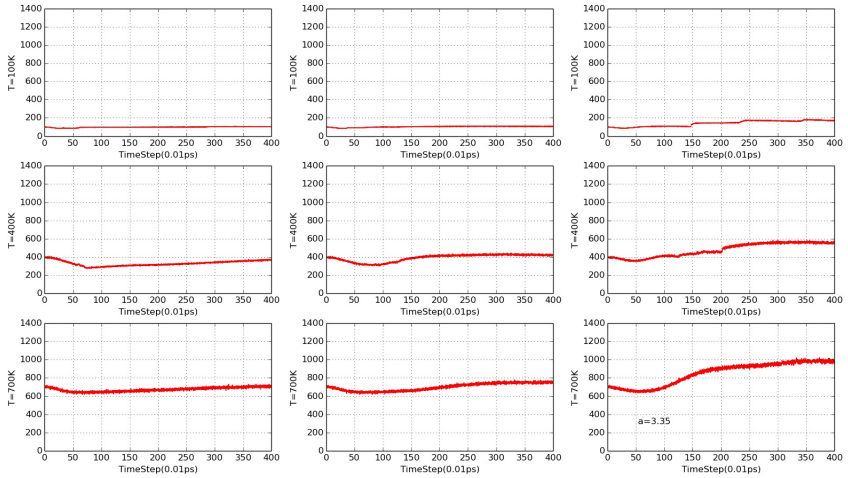

Figure D.38: Real temperature (in K) as a function of the time step (divided by 10^3) for a system with $a = 3.35$ Å.

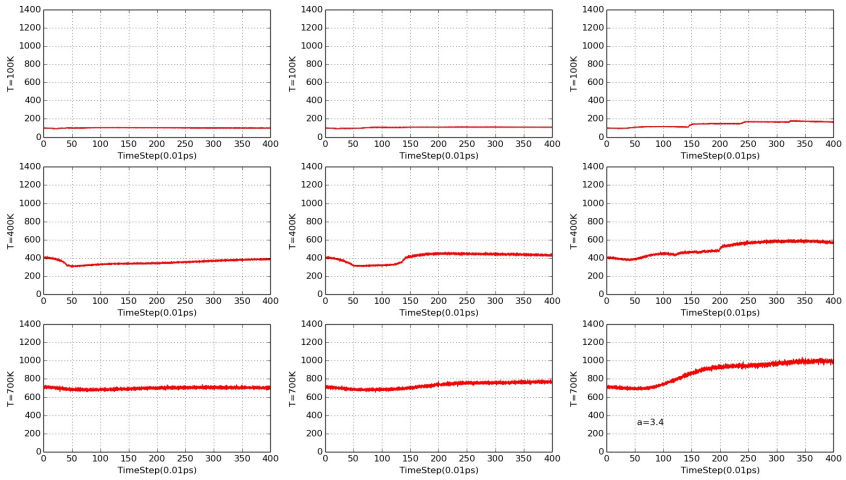

Figure D.39: Real temperature (in K) as a function of the time step (divided by 10^3) for a system with $a = 3.4$ Å.

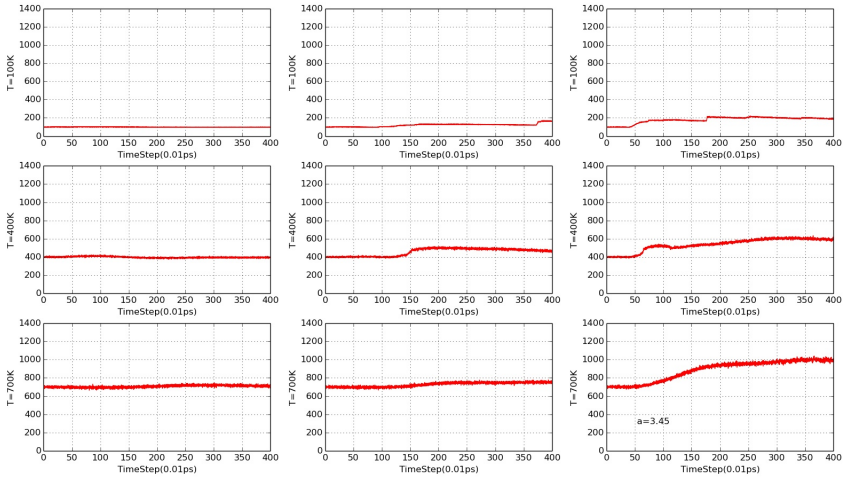

Figure D.40: Real temperature (in K) as a function of the time step (divided by 10^3) for a system with $a = 3.45$ Å.

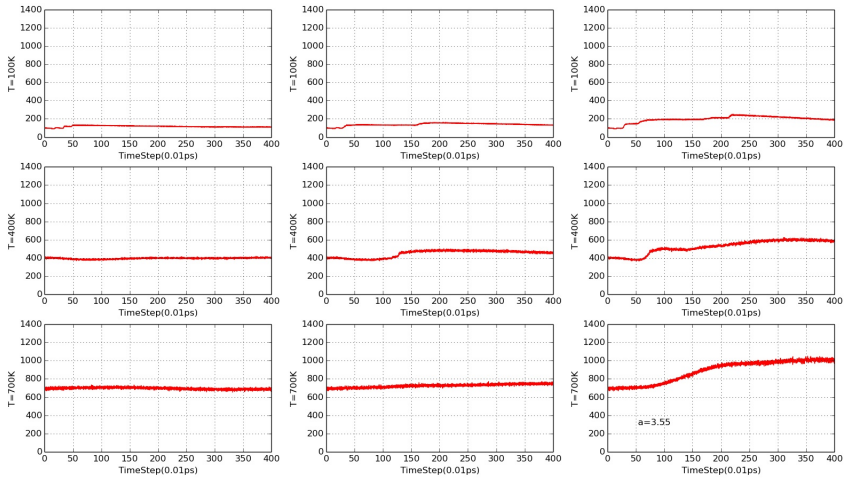

Figure D.41: Real temperature (in K) as a function of the time step (divided by 10^3) for a system with $a = 3.55$ Å.

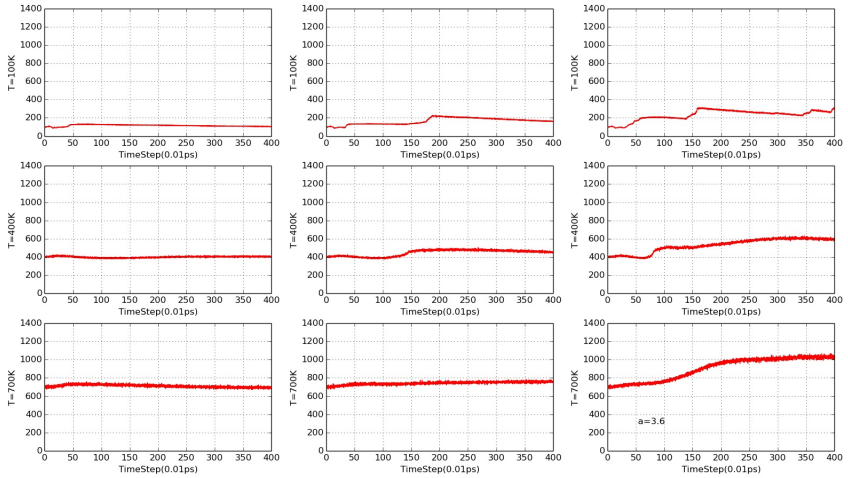

Figure D.42: Real temperature (in K) as a function of the time step (divided by 10^3) for a system with $a = 3.6$ Å.

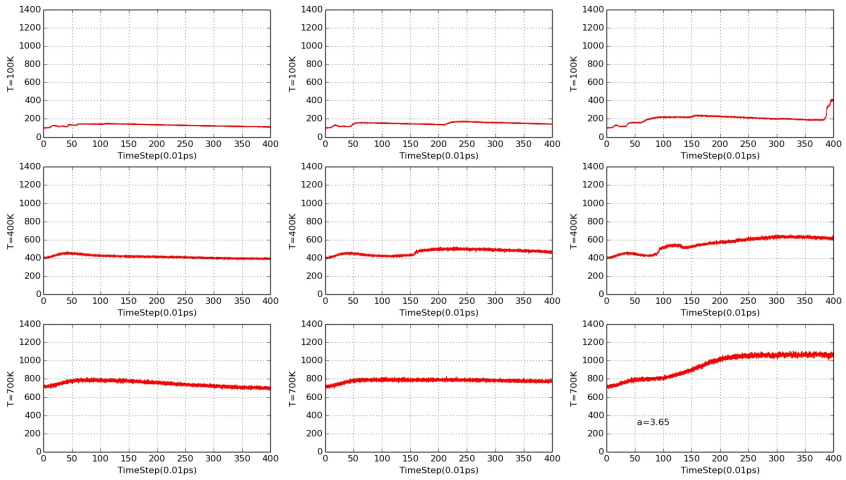

Figure D.43: Real temperature (in K) as a function of the time step (divided by 10^3) for a system with $a = 3.65$ Å.

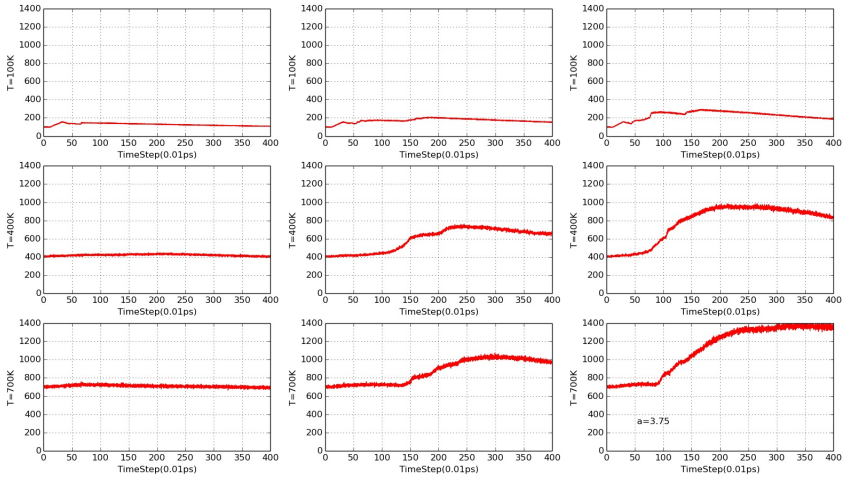

Figure D.44: Real temperature (in K) as a function of the time step (divided by 10^3) for a system with $a = 3.75$ Å.

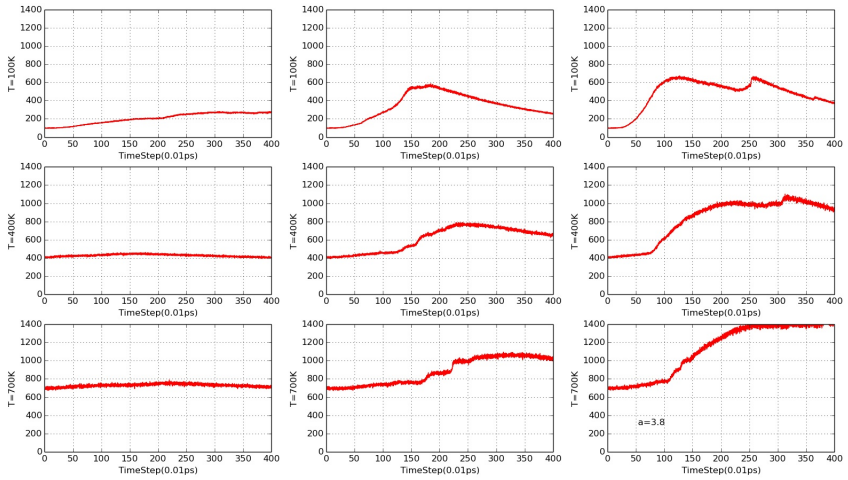

Figure D.45: Real temperature (in K) as a function of the time step (divided by 10^3) for a system with $a = 3.8$ Å.

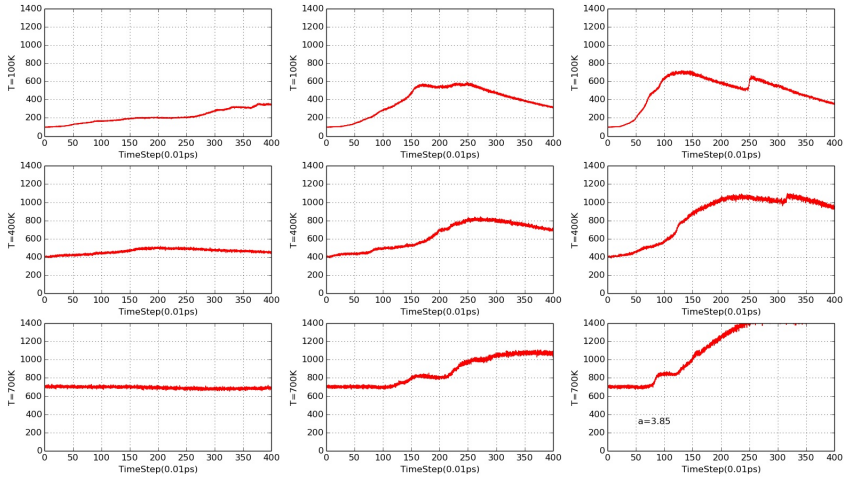

Figure D.46: Real temperature (in K) as a function of the time step (divided by 10^3) for a system with $a = 3.85$ Å.

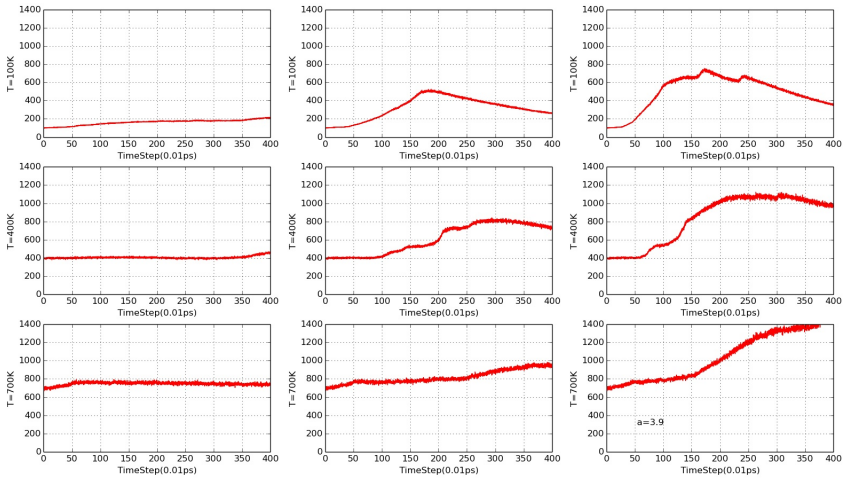

Figure D.47: Real temperature (in K) as a function of the time step (divided by 10^3) for a system with $a = 3.9$ Å.

And here are the plots of the length box as a function of the time step during the NPT simulations for all the values of the lattice parameters in Figure D.48-Figure D.63.

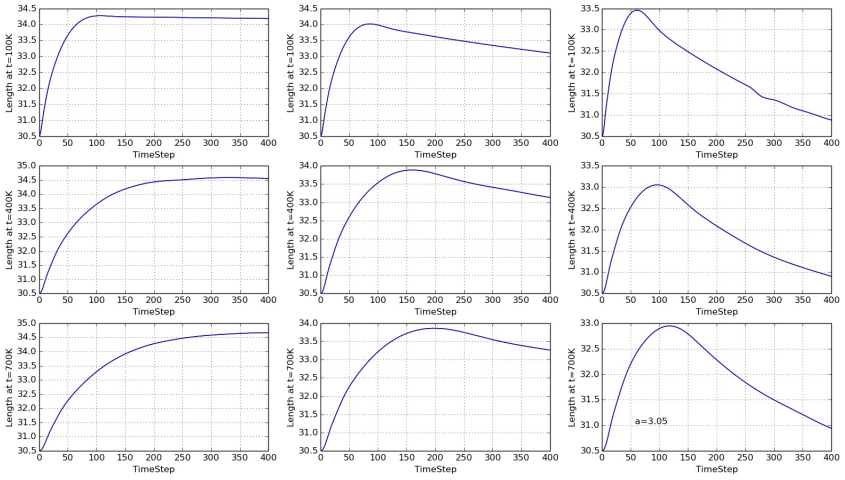

Figure D.48: Box side length (in Å $\times 10$) as a function of the time step (divided by 10^3) for a system with $a = 3.05$ Å

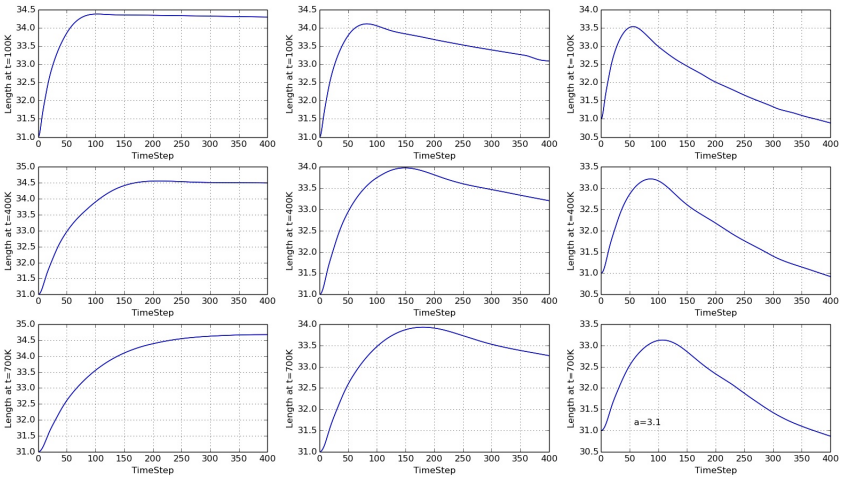

Figure D.49: Box side length (in Å $\times 10$) as a function of the time step (divided by 10^3) for a system with $a = 3.1$ Å

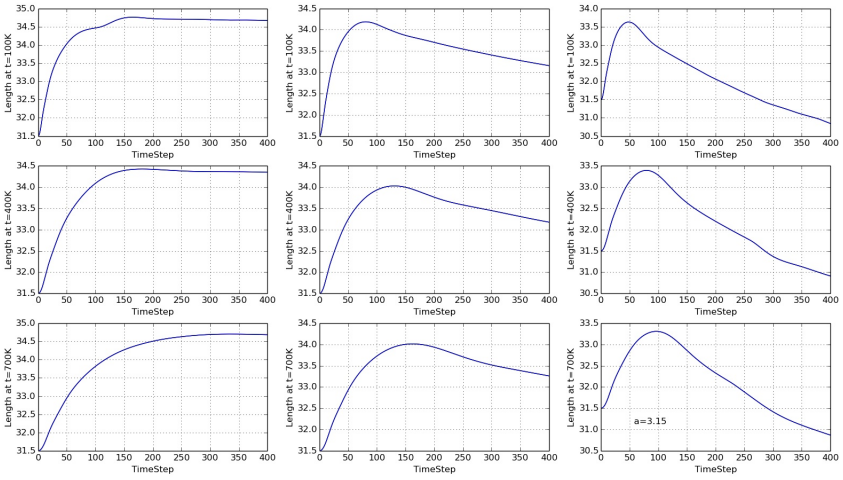

Figure D.50: Box side length (in Å $\times 10$) as a function of the time step (divided by 10^3) for a system with $a = 3.15$ Å

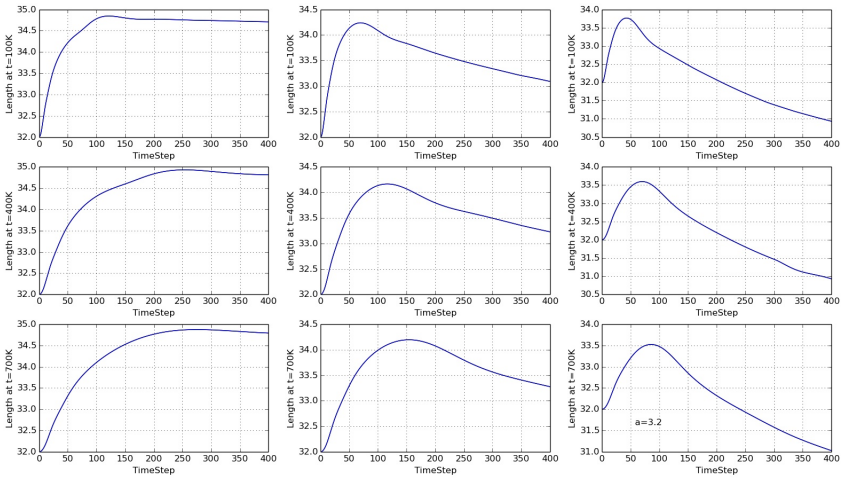

Figure D.51: Box side length (in Å $\times 10$) as a function of the time step (divided by 10^3) for a system with $a = 3.2$ Å

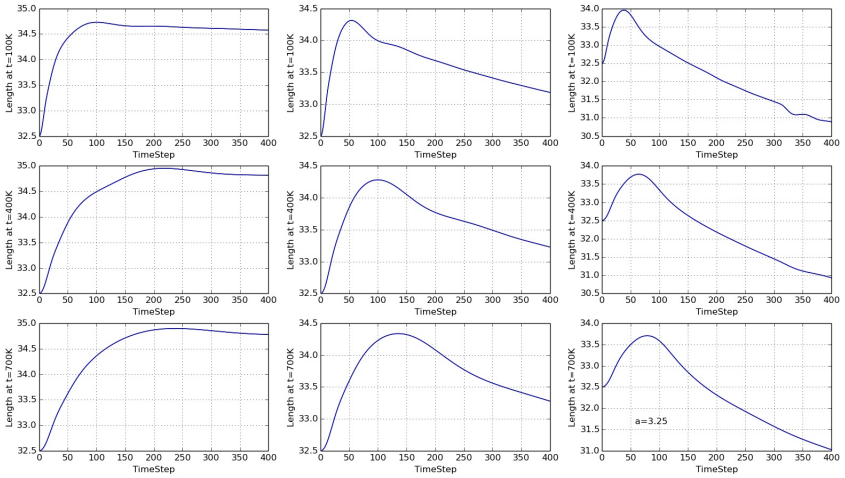

Figure D.52: Box side length (in Å $\times 10$) as a function of the time step (divided by 10^3) for a system with $a = 3.25$ Å

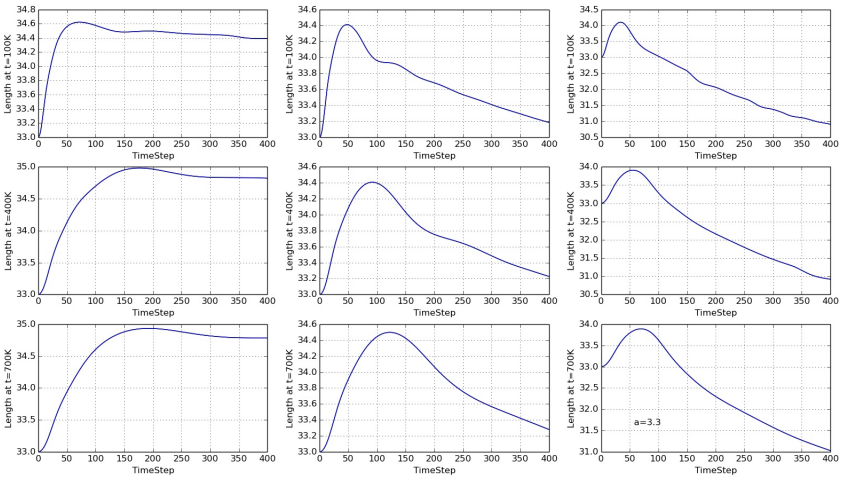

Figure D.53: Box side length (in Å $\times 10$) as a function of the time step (divided by 10^3) for a system with $a = 3.3$ Å

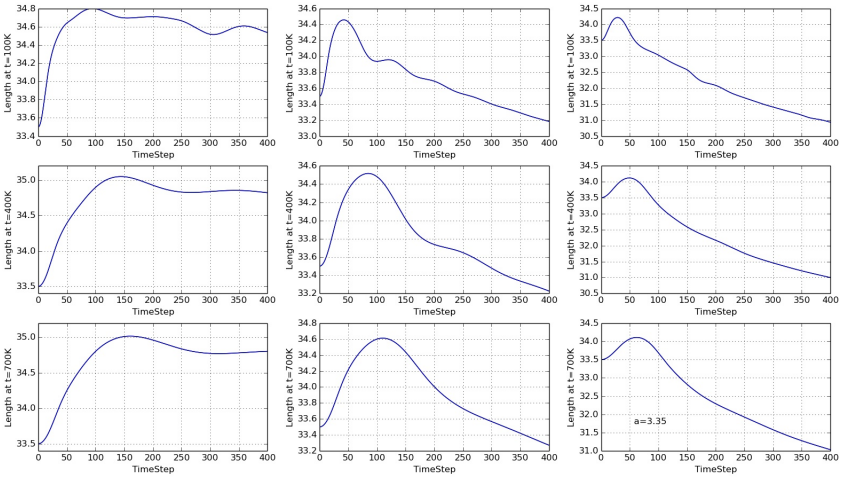

Figure D.54: Box side length (in Å $\times 10$) as a function of the time step (divided by 10^3) for a system with $a = 3.35$ Å

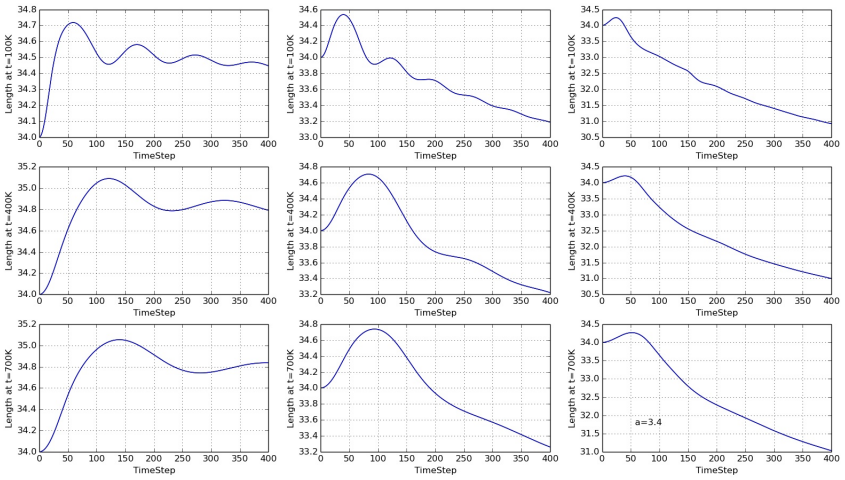

Figure D.55: Box side length (in Å $\times 10$) as a function of the time step (divided by 10^3) for a system with $a = 3.4$ Å

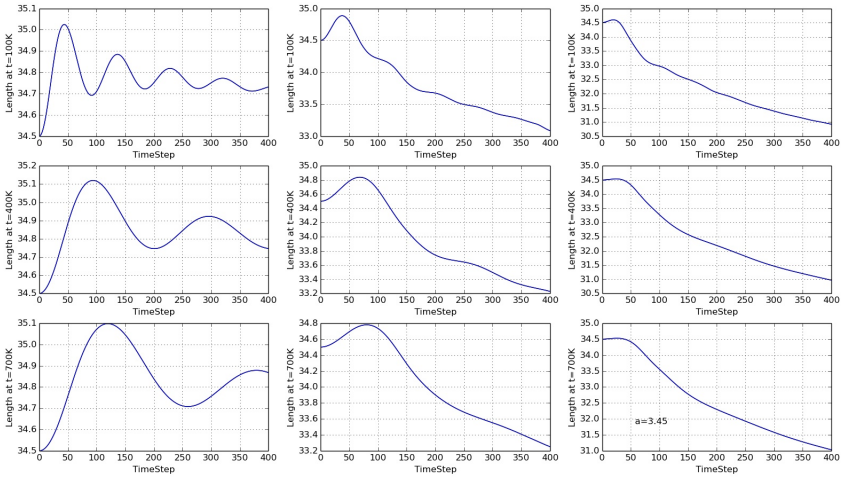

Figure D.56: Box side length (in Å $\times 10$) as a function of the time step (divided by 10^3) for a system with $a = 3.45$ Å

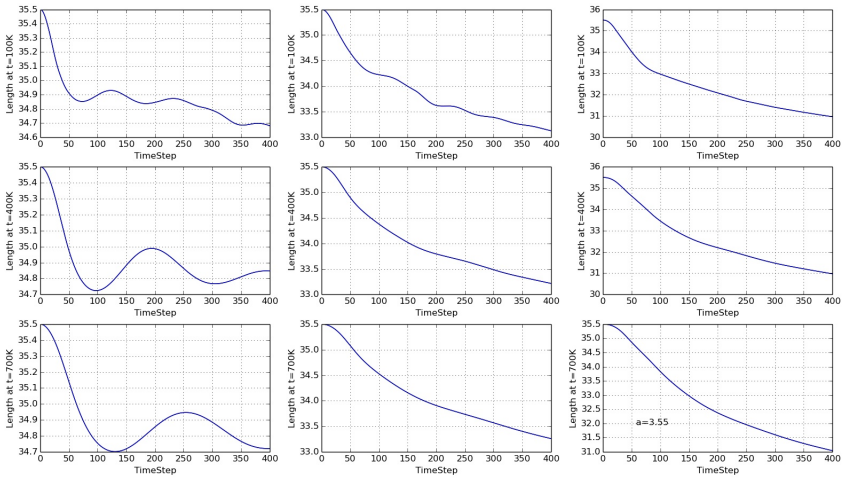

Figure D.57: Box side length (in Å $\times 10$) as a function of the time step (divided by 10^3) for a system with $a = 3.55$ Å

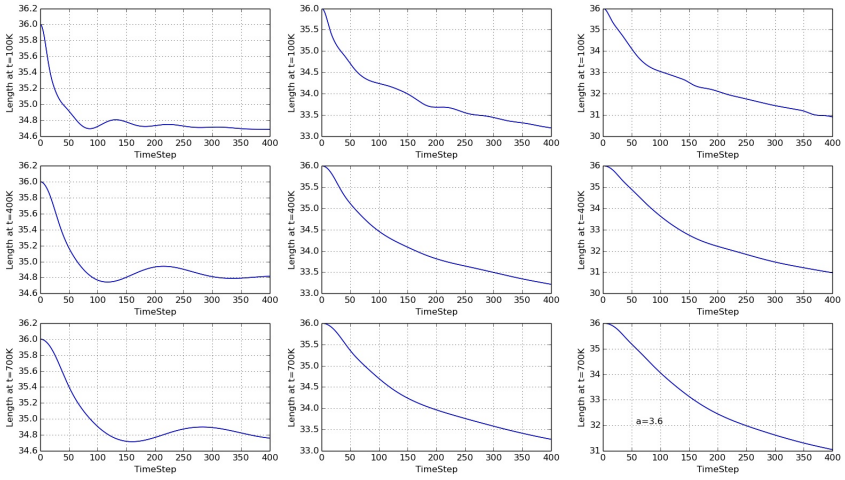

Figure D.58: Box side length (in Å $\times 10$) as a function of the time step (divided by 10^3) for a system with $a = 3.6$ Å

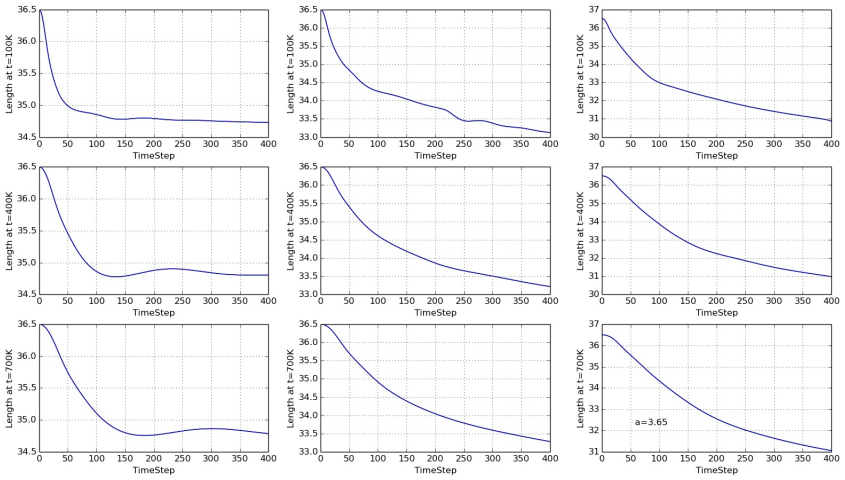

Figure D.59: Box side length (in Å $\times 10$) as a function of the time step (divided by 10^3) for a system with $a = 3.65$ Å

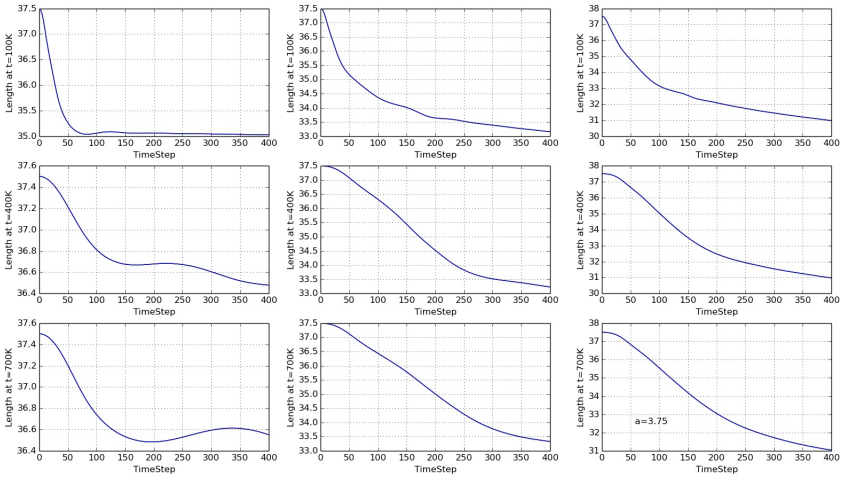

Figure D.60: Box side length (in Å $\times 10$) as a function of the time step (divided by 10^3) for a system with $a = 3.75$ Å

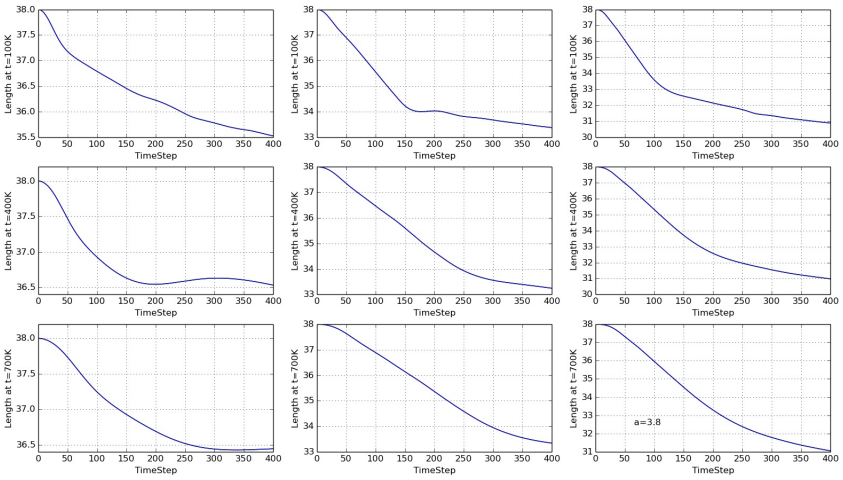

Figure D.61: Box side length (in Å $\times 10$) as a function of the time step (divided by 10^3) for a system with $a = 3.8$ Å

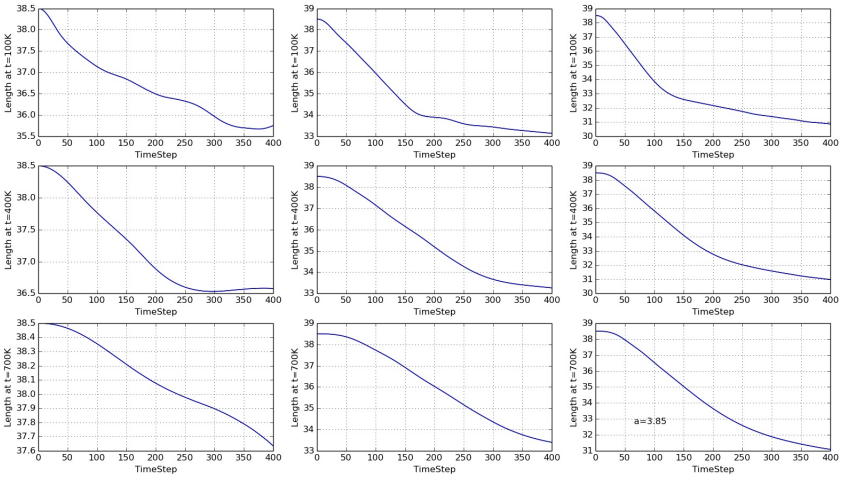

Figure D.62: Box side length (in Å $\times 10$) as a function of the time step (divided by 10^3) for a system with $a = 3.85$ Å

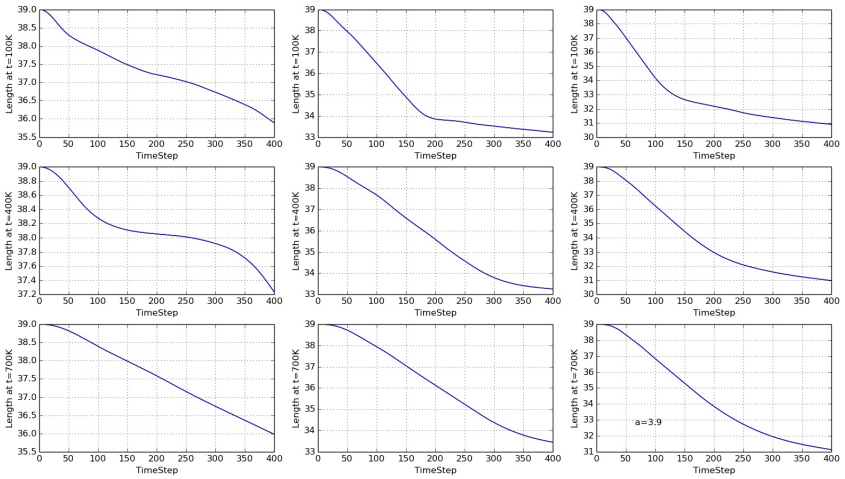

Figure D.63: Box side length (in Å $\times 10$) as a function of the time step (divided by 10^3) for a system with $a = 3.9$ Å

Appendix E

Pressure and bulk modulus distribution

We show here the difference between the bulk modulus at a given pressure and the bulk modulus at a different pressure normalized to the latter for all the values of the external pressure we have run, from $P^{ext} = 0$ GPa to $P^{ext} = 100$ GPa (Figure E.1-Figure E.10).

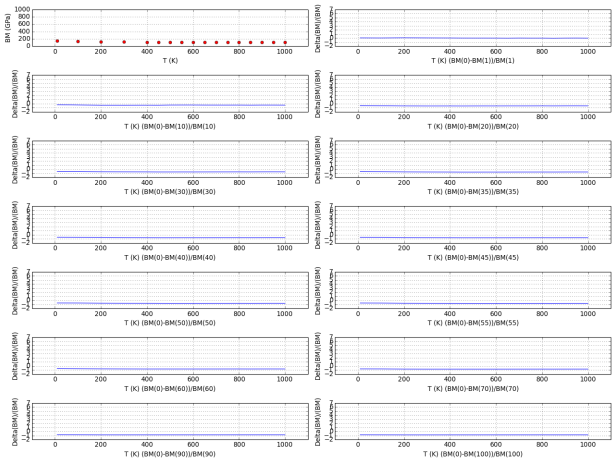

Figure E.1: Difference between the bulk modulus of a system at $P^{ext} = 0$ GPa and the bulk values at all the others values of pressure. The graph with the red dot is the dependence of the bulk modulus from the temperature at that external pressure.

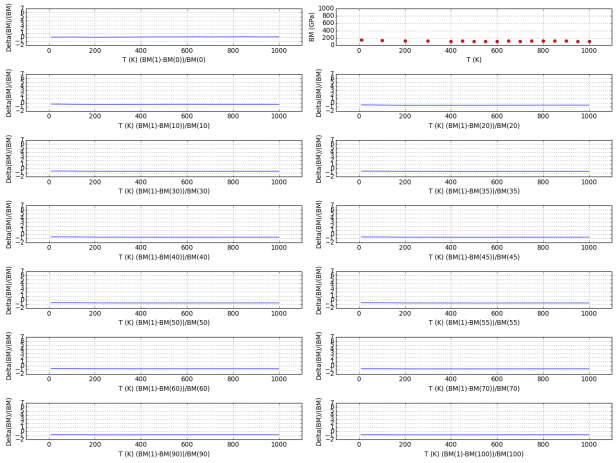

Figure E.2: Difference between the bulk modulus of a system at $P^{ext} = 1$ GPa and the bulk values at all the others values of pressure. The graph with the red dot is the dependence of the bulk modulus from the temperature at that external pressure.

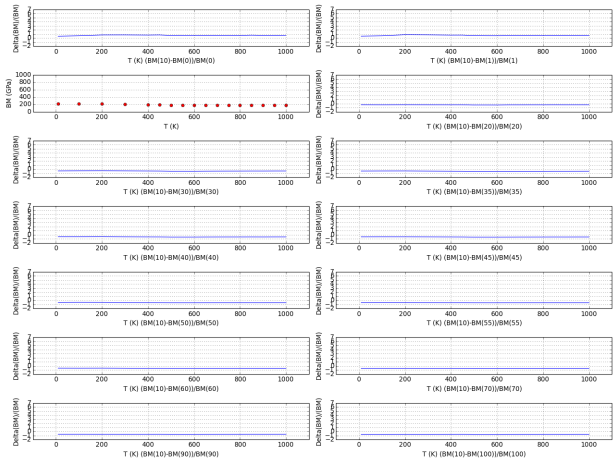

Figure E.3: Difference between the bulk modulus of a system at $P^{ext} = 10$ GPa and the bulk values at all the others values of pressure. The graph with the red dot is the dependence of the bulk modulus from the temperature at that external pressure.

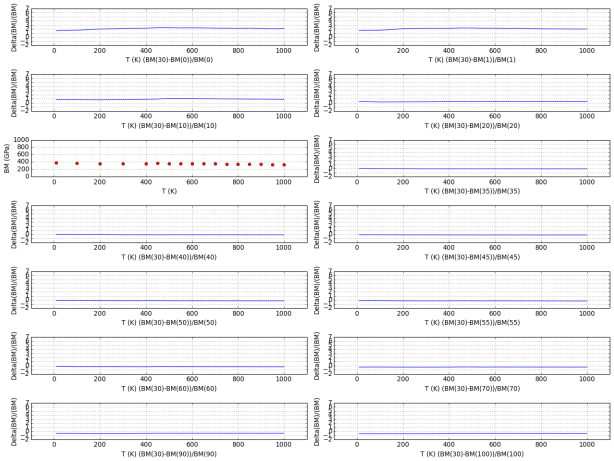

Figure E.4: Difference between the bulk modulus of a system at $P^{ext} = 30$ GPa and the bulk values at all the others values of pressure. The graph with the red dot is the dependence of the bulk modulus from the temperature at that external pressure.

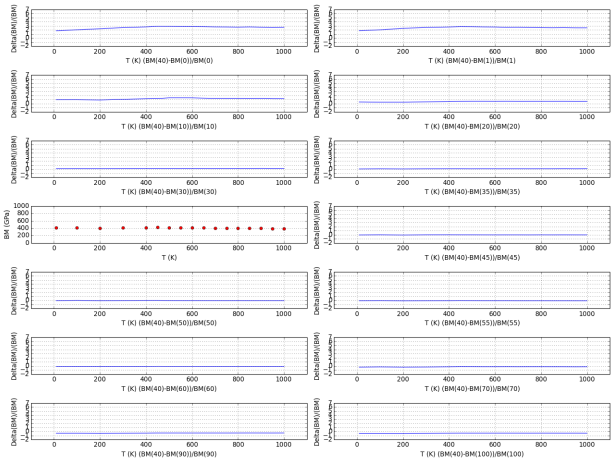

Figure E.5: Difference between the bulk modulus of a system at $P^{ext} = 40$ GPa and the bulk values at all the others values of pressure. The graph with the red dot is the dependence of the bulk modulus from the temperature at that external pressure.

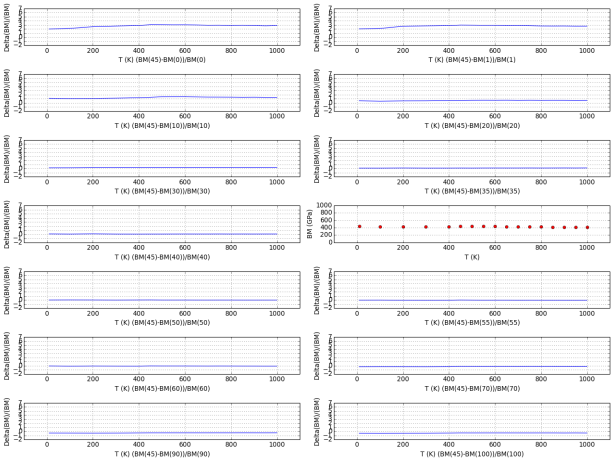

Figure E.6: Difference between the bulk modulus of a system at $P^{ext} = 45$ GPa and the bulk values at all the others values of pressure. The graph with the red dot is the dependence of the bulk modulus from the temperature at that external pressure.

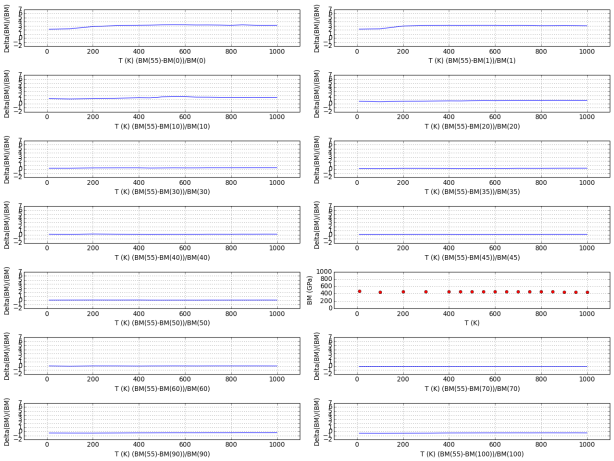

Figure E.7: Difference between the bulk modulus of a system at $P^{ext} = 55$ GPa and the bulk values at all the others values of pressure. The graph with the red dot is the dependence of the bulk modulus from the temperature at that external pressure.

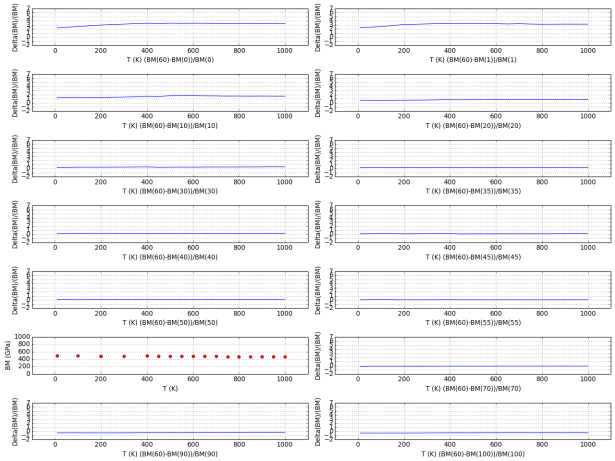

Figure E.8: Difference between the bulk modulus of a system at $P^{ext} = 60$ GPa and the bulk values at all the others values of pressure. The graph with the red dot is the dependence of the bulk modulus from the temperature at that external pressure.

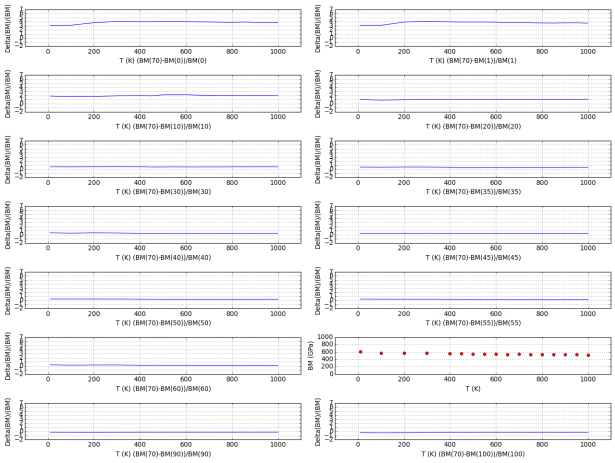

Figure E.9: Difference between the bulk modulus of a system at $P^{ext} = 70$ GPa and the bulk values at all the others values of pressure. The graph with the red dot is the dependence of the bulk modulus from the temperature at that external pressure.

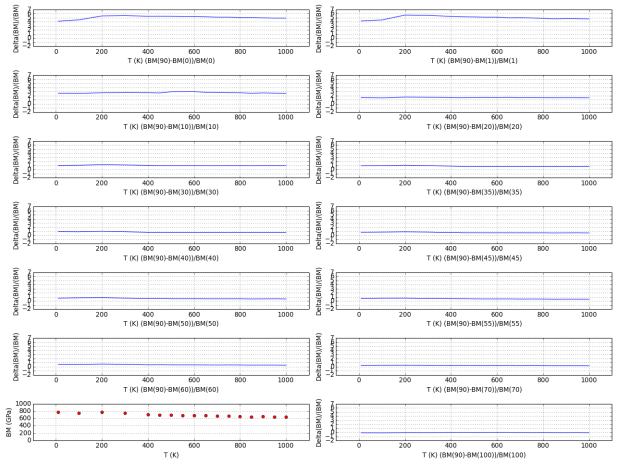

Figure E.10: Difference between the bulk modulus of a system at $P^{ext} = 90$ GPa and the bulk values at all the others values of pressure. The graph with the red dot is the dependence of the bulk modulus from the temperature at that external pressure.

Here are the plots of the population of the difference between the pressure of the box and the external pressure for: $P^{ext} = 1$ GPa, 20 GPa, 100 GPa at T = 100 K, 400 K, 700 K for all the values of the lattice parameter between $a = 3.0$ Å and $a = 3.9$ Å (Figure E.11-Figure E.26).

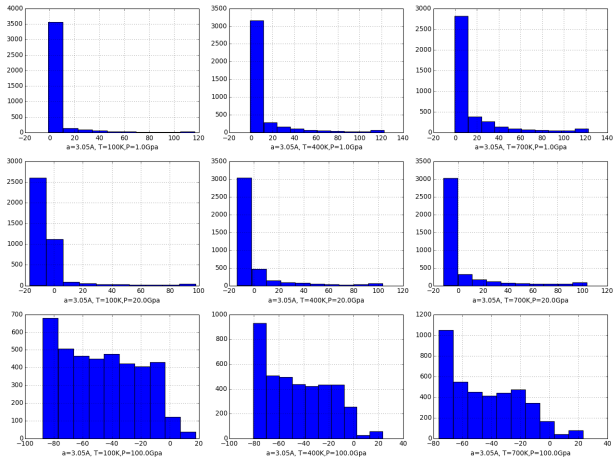

Figure E.11: Difference between the pressure of the box with lattice constant $a = 3.05$ Å and the external pressure at different temperature.

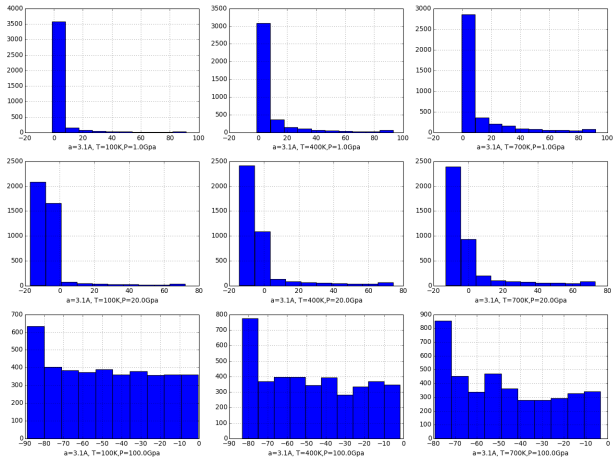

Figure E.12: Difference between the pressure of the box with lattice constant $a = 3.1$ Å and the external pressure at different temperature.

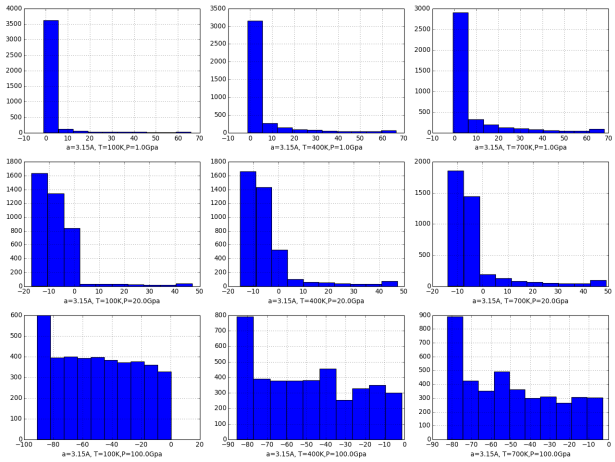

Figure E.13: Difference between the pressure of the box with lattice constant $a = 3.15$ Å and the external pressure at different temperature.

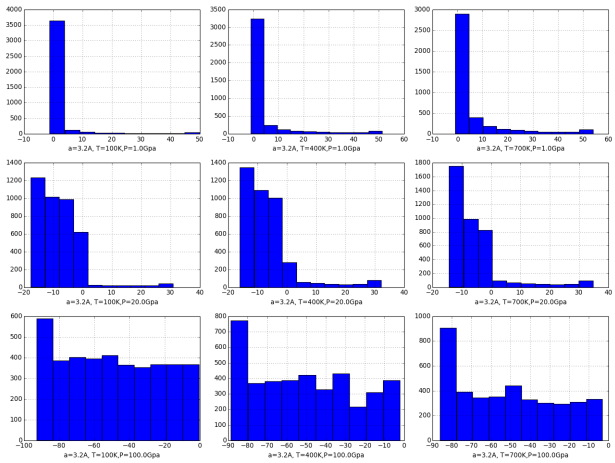

Figure E.14: Difference between the pressure of the box with lattice constant $a = 3.2$ Å and the external pressure at different temperature.

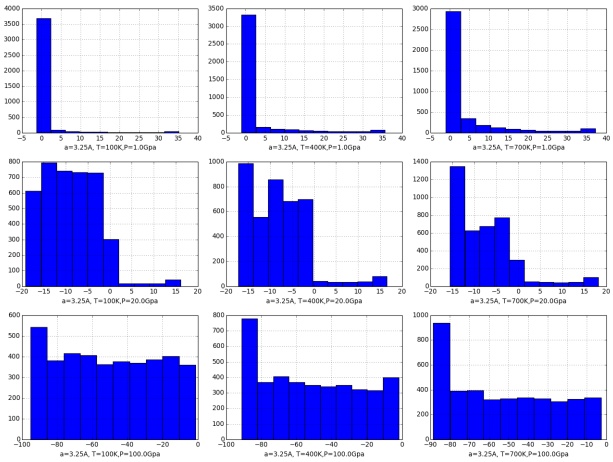

Figure E.15: Difference between the pressure of the box with lattice constant $a = 3.25$ Å and the external pressure at different temperature.

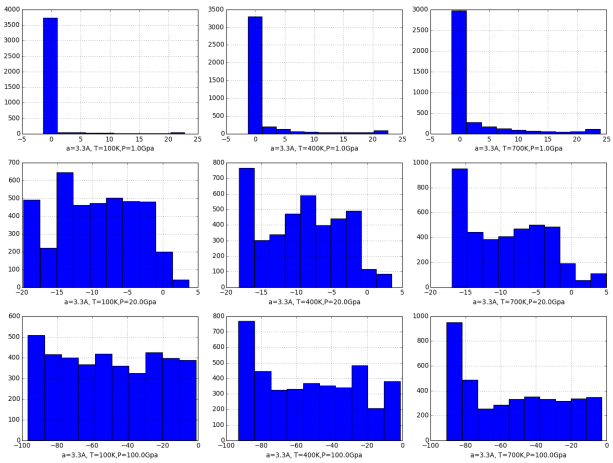

Figure E.16: Difference between the pressure of the box with lattice constant $a = 3.3$ Å and the external pressure at different temperature.

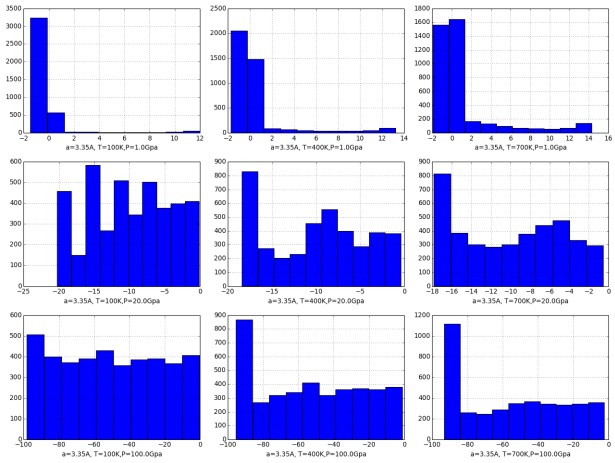

Figure E.17: Difference between the pressure of the box with lattice constant $a = 3.35$ Å and the external pressure at different temperature.

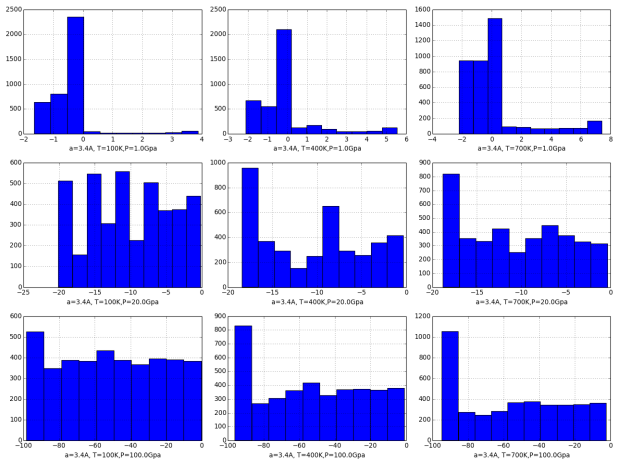

Figure E.18: Difference between the pressure of the box with lattice constant $a = 3.4$ Å and the external pressure at different temperature.

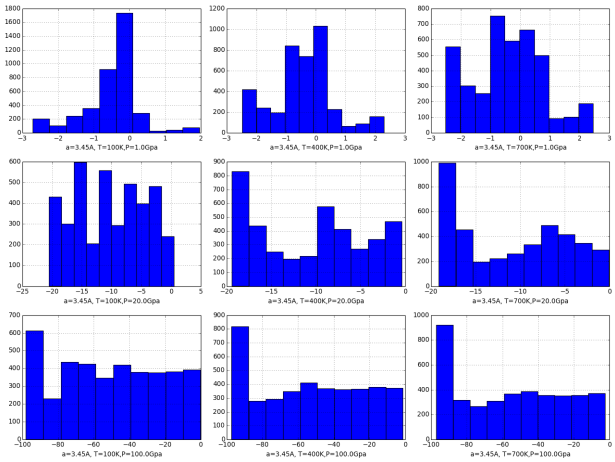

Figure E.19: Difference between the pressure of the box with lattice constant $a = 3.45$ Å and the external pressure at different temperature.

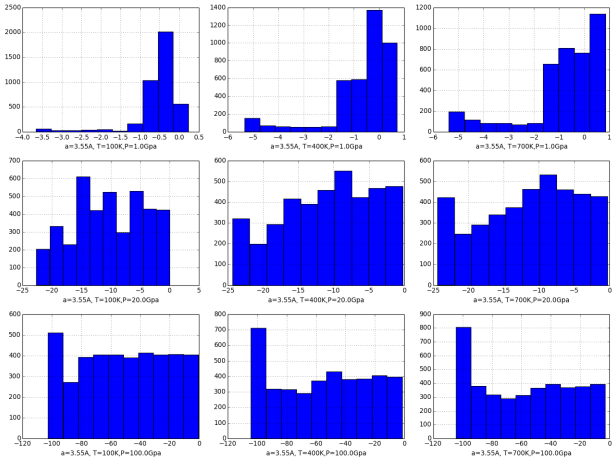

Figure E.20: Difference between the pressure of the box with lattice constant $a = 3.55$ Å and the external pressure at different temperature.

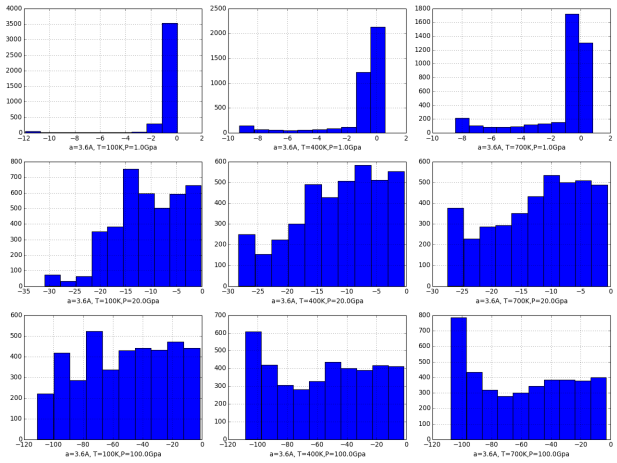

Figure E.21: Difference between the pressure of the box with lattice constant $a = 3.6$ Å and the external pressure at different temperature.

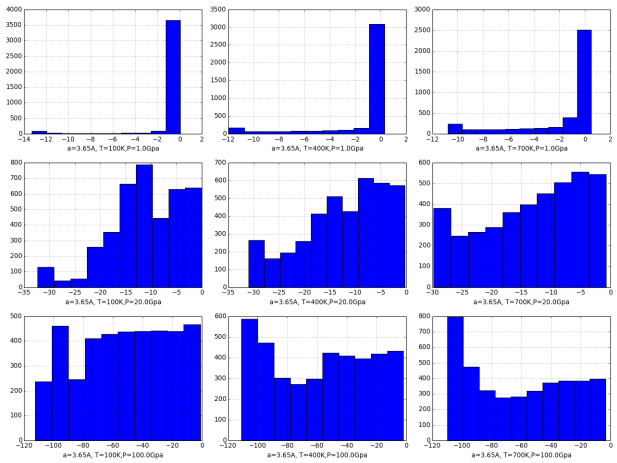

Figure E.22: Difference between the pressure of the box with lattice constant $a = 3.65$ Å and the external pressure at different temperature.

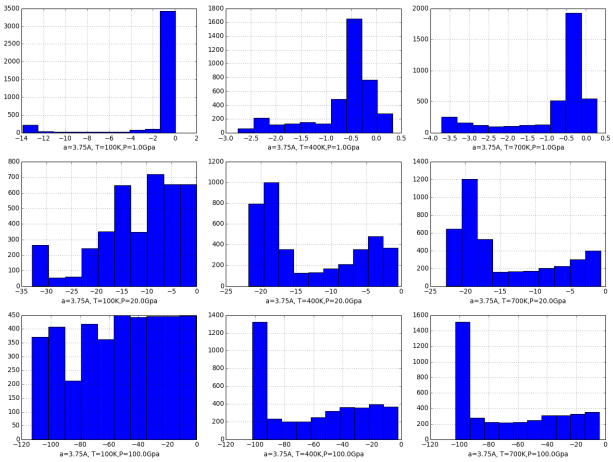

Figure E.23: Difference between the pressure of the box with lattice constant $a = 3.75$ Å and the external pressure at different temperature.

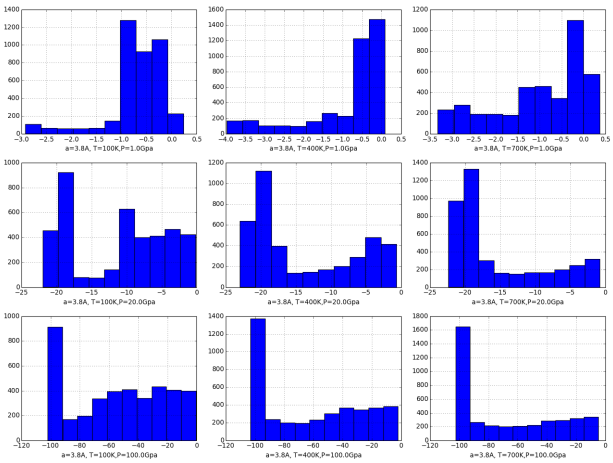

Figure E.24: Difference between the pressure of the box with lattice constant $a = 3.8$ Å and the external pressure at different temperature.

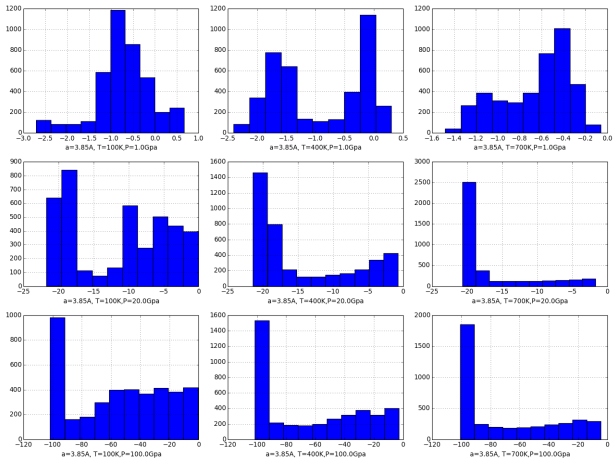

Figure E.25: Difference between the pressure of the box with lattice constant $a = 3.85$ Å and the external pressure at different temperature.

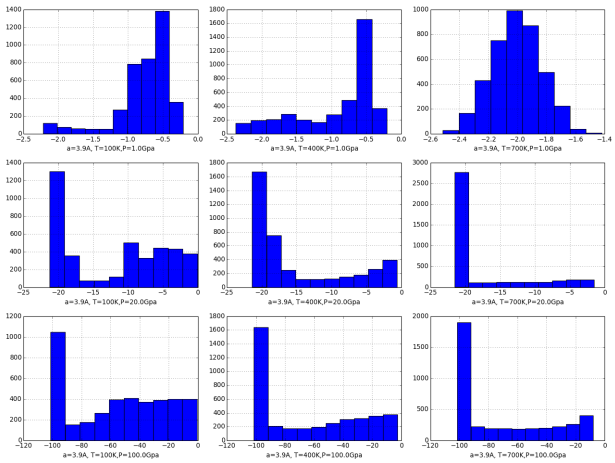

Figure E.26: Difference between the pressure of the box with lattice constant $a = 3.9$ Å and the external pressure at different temperature.

Bibliography

[1] L.D. Landau & E.M. Lifshitz, Theory of Elasticity, (1970) Pergamon Press

[2] W. Lowrie, Fundamentals of Geophysics, (2007) Cambridge University Press

[3] J.H. Dieterich, J. Geophys. Res., **77** (1972) 3771

[4] B.V. Kostrov & S. Das, Principles of Earthquake Source Mechanics, (1988) Cambridge University Press.

[5] D.C.P. Peacock *et al.*, Glossary of normal faults in Journal of Structural Geology, **22** (2000) 291

[6] A. Ghali *et al.*, Structural Analysis: a Unified Classical and Matrix Approach, (2009) CRC Press

[7] K. Aki & P.G. Richards, Quantitative Seismology, University Science Books Sausalito California (2002)

[8] L.D. Landau & E.M. Lifshitz, Relativistic Quantum Theory, (1971) Pergamon Press

[9] A. Bizzarri, Toward the Formulation of a Realistic Fault Governing Law. In: Dynamic Models of Earthquake Ruptures, (2010) Dynamic Modelling Alisson V. Brito (Ed.)

[10] J.R. Rice, J. Geophys. Res., **111** (2006) B5, B05311

[11] A. Bizzarri & M. Cocco, J. Geophys. Res., **111** (2006) B05304

[12] M.F. Linker & J.H. Dieterich, J. Geophys. Res., **97** (1992) B4 4923

[13] A. Bizzarri & P. Spudich, J. Geophys. Res., **113** (2008) B05304

[14] A. Bizzarri, Geophys. Res. Lett., **36** (2009) L11304

[15] A. Tsutsumi & T. Shimamoto, Geophys. Res. Lett., **24** (1997) 699

[16] A. Bizzarri & M. Cocco, J. Geophys. Res., **111** (2006) B05303

[17] S. Nielsen *et al.*, J. Geophys. Res., **113** (2008) B01308

[18] T. Hirose & M. Bystricky, Geophys. Res. Lett., **34** (2007) L14311

[19] R. Han *et al.*, Science, **316** (2007) 878

[20] N.H. Sleep, J. Geophys. Res., **102** No. B2 (1997) 2875

[21] N.H. Sleep, J. Geophys. Res., **100** No. B7 (1995) pp. 13,065 − 13,080

[22] P. Segall & J.R. Rice, J. Geophys. Res., **100** No. 101 (1995) pp. 22,155−21, 171

[23] D.L. Turcotte & G. Schubert, Geodynamics, (2014) Cambridge University Press

[24] J.R. Rice, Fault stress states, pore pressure distributions, and the weakness of the San Andreas Fault. In: Fault Mechanics and Transport Properties in Rocks (the Brace Volume), B. Evans & T.F. Wong (Eds.), Academic Press, San Diego CA pp. 475−503 (1992)

[25] J. Kozeny, Über kapillare Leitung des Wassers im Boden, Sitzungsber Akad. Wiss. Wien Math. Naturwiss. Kl., Abt. 2a, (1927)

[26] K.F. Ma *et al.*, G. Res. Lett., **30** 5 (2003) 1244

[27] E.E. Brodsky & H. Kanamori, J. Geophys. Res., **106** B8 (2001) 16,357−16,374

[28] T. Yamashita, Geophys. J. Int., **143** (2000) 395

[29] J. Weertman, J. Geophys. Res., **85** B3 (1980) 1455

[30] R.A. Harris & S.M. Day, Bull. Seism. Soc. Am., **87** (1997) 1267

[31] E.M. Dunham & J.R. Rice, J. Geophys. Res., **113** (2008) B09304

[32] A. Bizzarri & M. Cocco, Earth Planets Space, **58** (2006) 1525

[33] J.H. Davies & D.R. Davies, Solid Earth, **1** (2010) 5

[34] D. Porcelli, Radioactivity in the Environment, **13** (2008) 107

[35] R.L. Fleischer & R.O. Raabe, Geochimica et Cosmochimica Acta, **42** (1978) 973

[36] S. Krishnaswami *et al.*, Water Resources Research, **6** (1982) 1663

[37] A. Tricca *et al.*, Geochimica et Cosmochimica Acta, **65** (2001)1187

[38] S.D. Luo *et al.*, Geochimica et Cosmochimica Acta, **64** (2000) 867

[39] D. Porcelli & P. W. Swarzenski, Reviews in Mineralogy and Geochemistry, **52** (2003) 317

[40] G.R. Choppin, Marine Chemistry, **99** (2006) 83

[41] D. Porcelli *et al.*, Geochimica et Cosmochimica Acta, **65** (2001) 2439

[42] J.A.T. Smellie & J.S. Stuckless, Chemical Geology, **51** (1985) 55

[43] T.-L. Ku, S. Luo, B.W. Leslie & D.E. Hammond, Decay-series disequilibria applied to the study of rock−water interaction and geothermal systems. In: Uranium-Series Disequilibrium Application to Earth, Marine and Environmental Sciences (Eds M. Ivanovich and R.S. Harmon), Clarendon Press, Oxford, (1992) p. 631

[44] R.A. Freeze & J. A. Cherry, Groundwater, Prentice-Hall Englewood Cliffs (1979), New Jersey

[45] A. Tricca *et al.*, The Proceedings of the Indian Academy of Sciences, **109** (2000) 95

[46] J.K. Osmond & J.B. Cowart, U-series nuclides as tracers in groundwater hydrology. In: Environmental Tracers in Subsurface Hydrology (Eds P. Cook and A. Herczeg), (2000) Kluwer Academic Publishers, Boston p. 290

[47] T.E. Tullis *et al.*, In: Tectonic Faults: Agents of Change on a Dynamic Earth, edited by Handy M. R., Hirth G. and Hovius N. (The MIT Press, Cambridge, MA) 2007, pp. 183−204.

[48] A. Bizzarri, Rivista del Nuovo Cimento, **37** (2014) 4

[49] P. Moczo *et al.*, Bull. Seism. Soc. Am., **92** (2002) 3042

[50] F. Cotton & M. Campillo, Ann. Geofis., XXXVII (1994) 1539

[51] A. Piatanesi *et al.*, Geophys. Res. Lett., **31** (2004) L04609

[52] A. Dziewonski & D.L. Anderson, Physics of Earth and Planetary Interiors, **25** (1981) 297

[53] K.E. Bullen, Continuum Mechanics Aspects of Geodynamics and Rock Fracture Mechanics, Advanced Study Institutes Series Volume **12** (1974) 13-21

[54] C. DeMets *et al.*, Geophys. J. Int., **181** (2010) 1

[55] O. Sramek *et al.*, Earth and Planetary Science Letters, **361** (2013) 356

[56] J.J. Katz *et al.*, The Chemistry of Actinide and Transactinide Elements Vol. 1, (2008) Springer

[57] M.S.S. Brooks *et al.*, In: Handbook on the Physics and Chemistry of Actinides (vol. 1, chap. 3), A.J. Freeman & G.H. Lander, North-Holland Amsterdam

[58] C.S. Barrett *et al.*, Physical Review, **129** (1963) 625

[59] J. Akella *et al.*, Phys. Condens. Matter, **9** (1997) 549

[60] J.M. Wills & O. Eriksson, Physical Review B, **45** 13879 (1992)

[61] O. Eriksson *et al.*, Journal of Alloys and Compounds, **213** (1994) 268

[62] P. Söderlind *et al.*, Nature, **374** (1995) 524-525

[63] P. Söderlind, Physcial Review B, **66** (2002) 085113

[64] C.D. Taylor, Physical Review B, **77** (2008) 094119

[65] B. Beeler *et al.*, J. Phys.: Condens. Matter, **22** (2010) 505703

[66] J.H. Li *et al.*, Journal of Alloys and Compounds, **516** (2012) 139

[67] B. Beeler *et al.*, Journal of Nuclear Materials, **433** (2013) 143

[68] J.W. Yang *et al.*, The European Physical Journal B, **87** (2014) 130

[69] M. Idiri *et al.*, Physical Review B, **70** (2013) 014113

[70] S. Yagoubi *et al.*, Journal of Alloys and Compounds, **546** (2013) 63

[71] G.H. Lander *et al.*, Advances in Physics, **43** (1994) 1

[72] C.S. Yoo *et al.*, Phys. Rev. B, **57** (1998) 10359

[73] T. Le Bihan *et al.*, Phys. Rev. B, **67** (2003) 134102

[74] P. Söderlind, Advances in Physics, **47** (1998) 959

[75] L.T. Lloyd & C.S. Barrett, Journal of Nuclear Materials, **18** (1966) 55

[76] P.E. Armstrong *et al.*, Journal of Nuclear Materials, **45** (1976) 211

[77] A. Lawson *et al.*, Acta Cryst., **44B** (1998) 89

[78] S. Xiang *et al.*, J. Nucl. Mater., **375** (2008) 113

[79] A. Wilson & R. Rundle, Acta Cryst., **2** (1949) 126

[80] Y. Li *et al.*, J. of Phys. Conden. Matt., **25** (2013) 505401

[81] M. Born, Math. Proc. Camb. Phil. Soc., **36** (1940) 160

[82] S. Adak *et al.*, Physica B, **406** (2011) 3342

[83] P. Blochl *et al.*, Phys. Rev. B, **49** (1994) 16223

[84] G.R. Helffrich &B.J. Wood, Nature, **412** (2001) 501

[85] K. Huang, Statistical Mechanics, (1987) J. Wiley & Sons

[86] F.D. Stacey *et al.*, Geophys. Surveys, **4** (1981) 189

[87] F.D. Murnaghan, Finite Deformation of an Elastic Solid, (1967) Dover New York

[88] F.D. Murnaghan, Proc. Nat. Acad. Sci. U.S.A., **30** (1944) 244

[89] A.F. Birch & F.D. Murnaghan, Phys. Rev. B, **71** (1947) 809

[90] P. Vinet *et al.*, J. Phys. C: Solid State Physics, **19** (1986) L467

[91] J.H. Rose *et al.*, Phys. Rev. B, **29** (1984) 2963

[92] R. Jeanloz, Phys. Rev. B, **38** (1987) 805

[93] Wolfram Research, Inc., Mathematica, Version 7.0, Champaign, IL (2008)

[94] L. Morss, N. Edelstein, J. Fuger, The Chemistry of the Actinide and Trnasactinide Elements, Springer (2006) Netherlands

[95] E.S. Fisher & D. Dever, Phys. Rev., **170** (1968) 607

[96] J. Akella *et al.*, High Press. Res., **2** (1990) 295

[97] A. Dewaele *et al.*, Phys. Rev. B, **88** (2013) 134202

[98] J. Donohue, The Structure of the Elements, Wiley New York (1974)

[99] B.H. Bransden & C.J. Joachain, Physics of Atoms and Molecules, Pearson Education (2007)

[100] P. Hohenberg & W. Kohn, Phys. Rev. B, **3** (1964) 136

[101] D.S. Sholl & J.A. Steckel, Density Functional Theory A Practical Introduction, Wiley New York (2009)

[102] J.P. Perdew, In: Electronic Structure of Solids ′91, edited by P. Ziesche and H. Eschrig (Akademie Verlag, Berlin, 1991), p. 11

[103] J.P. Perdew *et al.*, Phys. Rev. Lett., **77** (1996) 18

[104] P.W. Atkins & R.S. Friedman, Molecular Quantum Mechanics, Oxford University Press UK (1997)

[105] D.A. McQuarrie, Quantum Chemistry, University Science Books, Mill Valley CA (1983)

[106] W. Koch & M.C. Holthausen, A Chemist's Guide to Density Functional Theory, Wiley-VHC Weinheim (2000)

[107] R.M. Martin, Electronic Structure: Basic Theory and Practical Methods, Cambridge University Press, Cambridge UK (2004)

[108] J.M. Haile, Molecular Dynamics Simulation, Wiley Interscience Publication (1997)

[109] F. Gatti, Molecular Quantum Dynamics, Springer (2013)

[110] L. Verlet, Phys. Rev., **159** (1967) 98

[111] M. Finnis, Interatomic Forces in Condensed Matter, Oxford University Press (2003)

[112] J.E. Jones, Proceedings of the Royal Society of London. Series A, **106** 463-477 (1924)

[113] D.V Matyushov & R. Schmid, Journal of Chemical Physics, **104** (1996) 8627

[114] P.M. Morse, Physical Review, **34** (1929) 57

[115] F.H. Stillinger & T. A. Weber, Physical Review B, **31** (1985) 5262

[116] J. Tersoff, Physical Review Letters, **56** (1986) 632

[117] J. Tersoff, Physical Review Letters, **61** (1988) 2879

[118] D.W. Brenner, Physical Review B, **42** (1990) 9458

[119] M.W. Finnis & J.E. Sinclair, Philosophical Magazine A, **50** (1984) 45

[120] J. Yu *et al.*, Physical Review B, **75** (2007) 085311

[121] M.S. Daw & M.I. Baskes, Physical Review Letters, **50** (1983) 1285

[122] M.S. Daw & M.I. Baskes, Physical Review B, **29** (1984) 6443

[123] T.R. Shan *et al.*, Physical Review B, **81** (2010) 125328

[124] B. Devine *et al.*, Physical Review B, **84** (2011) 125308

[125] T. Liang *et al.*, The Journal of Physical Chemistry A, **116** (2012) 7976

[126] F.H. Streitz & J. W. Mintmire, Physical Review B, **50** (1994) 11996

[127] A. Yasukawa, JSME International Journal A, **39** (1996) 313

[128] J.K. Nørskov & N.D. Lang, Phys. Rev. B, **21** (1980) 2131

[129] M.J. Stott & E. Zaremba, Phys. Rev. B, **22** (1980) 1564

[130] M.S. Daw, Phys. Rev. B, **39** (1988) 7441

[131] M.I. Pascuet *et al.*, Anal. AFA, **19** (2007) 40

[132] M.I. Pascuet *et al.*, Proc. Int. Conf. "Multiscale Modeling of Mircrostructure Evolution in Materials", p. 489 (2008)

[133] D.K. Belashchenko *et al.*, High Temp., **48** (2010) 363

[134] R. Li *et al.*, Chin. J. Chem. Phys., **24** (2011) 405

[135] D.E. Smirnova *et al.*, J. Phys: Condens. Matter, **24** (2012) 015702

[136] M.P. Allen, Introduction to Molecular Dynamics Simulation, in: Computational Soft Matter: From Synthetic Polymers to Proteins, Lecture Notes, NIC Series Vol. **23** (2004) 1-28

[137] F. Ercolessi & J.B. Adams, Europhys. Lett., **39** (1994) 583

[138] S. Plimpton, Journal of Computational Physics, **117** (1995) 1-19, http://lammps.sandia.gov (released 11.11.13)

[139] Python Software Foundation. Python Language Reference, version 2.7. Available at http://www.python.org

[140] C.A. Becker *et al.*, "Consideration for choosing and using force fields and interatomic potentials in materials science and engineering", Current Opinion in Solid State and Material Science, **17** (2013) 277-288. http://www.ctcms.nist.gov/potentials

[141] Z. Yao *et al.*, Comp. Phys. Commun., **161** (2004) 27

[142] T. Maximova & C. Keasar, J. Comp. Biol., **13** (2006) 1041

[143] L.G. Zhou & H. Huang, Phys. Rev. B, **87** (2013) 045431

[144] S.M. Foiles & M.I. Baskes, MRS Bull., **37** (2012) 485

[145] R. Pasianot & E.J. Savino, Phys. Rev. B, **45** (1992) 12704

[146] W. Jun *et al.*, Model. Simul. Mater. Sci. Eng, **7** (1999) 189

[147] S. Nose, S. Mol. Phys., **52(2)** (1984) 255

[148] W.G. Hoover, Phys. Rev. A, **31(3)** (1985) 1695

[149] J.W. Yang *et al.*, Physica, B **429** (2013) 119

[150] Y. Li *et al.*, J. of Phys. Conden. Matt., **24** (2012) 235403

[151] E.S. Fisher & H.J. McSkimin, Journal of Applied Physics, **29** (1958) 1473-1484

[152] J. Bouchet & R.C. Albers, J. Phys.: Condens. Matter, **23** (2011) 215402

[153] Y. Zhao *et al.*, Phys. Rev. B, **75** (2007) 174104

[154] B. Beeler *et al.*, J. Phys.: Condens. Matter, **24** (2012) 075401

[155] D. Belashchenko *et al.*, High Temp., **48** (2010) 363